

Electronic Thesis and Dissertation Repository

12-16-2019 2:00 PM

Miniature Cone Penetration Tests with Shear Wave Velocity and Electrical Resistivity Measurements in Characterization of Silica Sand

Ronit Ganguly, *The University of Western Ontario*

Supervisor: Sadrekarimi, Abouzar, *The University of Western Ontario*

A thesis submitted in partial fulfillment of the requirements for the Master of Engineering Science degree in Civil and Environmental Engineering

© Ronit Ganguly 2019

Follow this and additional works at: <https://ir.lib.uwo.ca/etd>



Part of the [Geotechnical Engineering Commons](#)

Recommended Citation

Ganguly, Ronit, "Miniature Cone Penetration Tests with Shear Wave Velocity and Electrical Resistivity Measurements in Characterization of Silica Sand" (2019). *Electronic Thesis and Dissertation Repository*. 6751.

<https://ir.lib.uwo.ca/etd/6751>

This Dissertation/Thesis is brought to you for free and open access by Scholarship@Western. It has been accepted for inclusion in Electronic Thesis and Dissertation Repository by an authorized administrator of Scholarship@Western. For more information, please contact wlsadmin@uwo.ca.

Abstract

Geotechnical engineering design and analysis require sound identification and characterization of in-situ soil. To characterize is to gather information about the engineering properties of a particular soil which will affect the performance of any structure built on it. As a result of complications associated with the retrieving of undisturbed samples of cohesionless soils, calibration chamber-based experiments under controlled laboratory settings are used for the determination of several geotechnical engineering parameters. The capability of a reduced-scale calibration chamber-based cone penetration testing system along with shear wave velocity and electrical resistivity measurements, to better characterize in-situ soil is examined in this study. Reconstituted clean sand specimens are anisotropically consolidated to different levels of consolidation relative densities to ideally simulate in-situ field conditions. This measured parameters such as cone tip resistance (q_c), sleeve friction (f_s), shear wave velocity (V_s) and bulk electrical resistivity of soil (ρ_s) at different consolidation stresses and relative densities have been used to establish improved characterization techniques for any site-specific pre-design geotechnical engineering analyses on silica-based cohesionless soil.

Keywords

Calibration chamber cone penetration test, shear wave velocity, bulk electrical resistivity of soil, K_0 consolidation

Summary for Lay Audience

This study is an attempt to characterize silica sands under different conditions of loading, vibration, etc. This behavioural analysis or characterization, therefore, provides, an insight into its overall strength, stiffness, rigidity, etc. in the form of engineering parameters. The obtained parameters are again correlated with each other to develop new relationships for a particular soil type or to compare them with previous relevant studies to confirm the potency of the methods that were used to obtain them. This study is one such example of laboratory-controlled testing of a particular sand.

Soil specimens are prepared to a particular uniform dimension. The mass of soil used in the specimens is varied in order to obtain loose, medium dense and dense specimens. Following a water saturation process, the specimens are exposed to high pressures. During the pressurization, the specimen loses a certain amount of water and as a result of the decrease in pore volume, the height of the specimen decreases. Under such stresses, a thin metallic rod with a cone at its tip is mechanically pushed into the soil as we record the resistances felt by the cone penetrometer. During the penetration, resistance is felt at the tip of the cone (q_c) and along the sidewalls of the probe due to the friction it overcomes while on its way (f_s). If we cause a vibration in the form of a wave, on the top layer of the specimen, the bottom layer will experience the force wave as it is transmitted through the adjacent particles, and the corresponding speed of travel is known as shear wave velocity (V_s). Moreover, if we apply a source of electric current to pass through a soil specimen, the charge will be transmitted across the specimen through the pore water between the particles, unlike the V_s , giving a measure of the electrical resistivity of the soil specimen (ρ) at that particular loading condition.

Therefore, these parameters have been investigated and explored in detail in this study to have a better understanding of the behaviour of the tested material under different conditions of loading.

Co-Authorship Statement

This thesis has been prepared in accordance for an Integrated-Article format thesis stipulated by the School of Graduate and Postdoctoral Studies at the University of Western Ontario and has been co-authored as:

Chapter 3: Miniature Cone Penetration Test on Silica Sand

All experimental work contributing to the completion of the concerned chapter was completed by Ronit Ganguly under the supervision of Dr. Abouzar Sadrekarimi. A paper co-authored by Ronit Ganguly and Abouzar Sadrekarimi will be submitted to the Journal of Geotechnical and Geoenvironmental Engineering, ASCE.

Chapter 4: Non-Destructive Testing with Electrical Resistivity and Shear Wave Velocity Measurements on Silica Sand

All experimental work contributing to the completion of the concerned chapter was completed by Ronit Ganguly under the supervision of Dr. Abouzar Sadrekarimi. A paper co-authored by Ronit Ganguly and Abouzar Sadrekarimi will be submitted to the ASTM Geotechnical Testing Journal.

Acknowledgments

Throughout the writing of this dissertation I have received a great deal of support and assistance. I would first like to thank my supervisor, Dr. Abouzar Sadrekarimi, whose consistent guidance and expertise were invaluable in formulating the progress of the research and methodology.

I would also like to thank our laboratory supervisors, Melodie Richards and Aiham Adawi as well as my fellow research colleagues at Western University, for both their technical insight and friendship through thick and thin.

In addition, I would like to thank my parents for their wise counsel and empathetic ear. Finally, there are my friends, who were of great support in times of need, as well as providing a happy distraction to rest my mind outside of my research.

Table of Contents

Abstract.....	ii
Summary for Lay Audience.....	iii
Co-Authorship Statement.....	iv
Acknowledgments.....	v
Table of Contents.....	vi
List of Tables.....	x
List of Figures.....	xi
List of Appendices.....	xvii
List of Abbreviations, Symbols and Nomenclature.....	xix
Chapter 1	1
1 Introduction.....	1
1.1 Background.....	1
1.2 Research Objectives.....	3
1.3 Thesis Outline.....	4
Chapter 2	5
2 Literature Review.....	5
2.1 Background of Miniature Cone Penetration Test.....	5
2.2 Background of Shear Wave Velocity.....	10
2.3 Background of Electrical Resistivity Test.....	12
Chapter 3	18
3 Miniature Cone Penetration Tests on a Silica Sand.....	18
3.1 Introduction.....	18
3.2 Design of the Calibration Chamber.....	19
3.3 Tested Material.....	33

3.4	Mechanism of the Miniature Cone Penetration Test	36
3.4.1	Specimen Preparation	36
3.4.2	Seating, Docking, Flushing and Saturation.....	39
3.4.3	K_0 Consolidation.....	44
3.4.4	Cone Penetration.....	49
3.5	Factors Affecting MCPT Calibration Chamber	49
3.5.1	Scale Effect	49
3.5.2	Penetration Rate Effect	50
3.5.3	Effect of Particle Crushing.....	51
3.5.4	Effect of Calibration Chamber Boundary Condition	53
3.6	MCPT Results.....	68
3.6.1	Cone penetration	68
3.6.2	Repeatability	72
3.7	Overburden Stress Normalization.....	73
3.7.1	Normalization Exponent of Cone Tip Resistance.....	73
3.7.2	Normalization Exponent of Sleeve Friction	75
3.7.3	Stress Normalization Correction Factors	76
3.8	Tip Resistance and Sleeve Frictional Resistance.....	83
3.9	Evaluation of Soil Unit Weight.....	85
3.10	Evaluation of Sand Relative Density	88
3.11	Evaluation of Constrained Modulus	92
3.12	Comparison with State Parameter.....	96
3.13	Conclusion	101
Chapter 4	104
4	Non-destructive Testing with Shear Wave Velocity and Electrical Resistivity Measurements on Silica Sand	104

4.1	Introduction.....	104
4.2	Design of the Non-destructive Testing Chamber.....	108
4.3	Tested Material	114
4.4	Mechanism of Non-destructive Testing.....	117
4.4.1	Specimen Preparation	117
4.4.2	Seating, Docking, Flushing, Saturation	118
4.4.3	K_0 consolidation.....	119
4.4.4	V_s and ER Measurements	122
4.5	Test Results.....	123
4.5.1	Shear Wave Velocity	123
4.5.2	Pore Fluid Electrical Resistivity	127
4.5.3	Summary of Results.....	130
4.6	Overburden Stress Normalization.....	131
4.6.1	Normalization Exponent of Shear Wave Velocity.....	131
4.6.2	Correction Factor (C_v) for Shear Wave Velocity.....	133
4.7	Influence of Stress on Formation Factor.....	134
4.8	Correlations and Comparisons.....	136
4.8.1	Analysis of $V_s - FF$ correlation	136
4.8.2	Analysis of $V_s - q_c$ correlation.....	138
4.8.3	Analysis of $V_s - f_s$ correlation.....	143
4.8.4	Analysis of $FF - q_c$ correlation	144
4.8.5	Estimation of Porosity.....	145
4.8.6	Estimation of Void Ratio	149
4.8.7	Estimation of Relative Density	159
4.8.8	Estimation of Unit Weight	165
4.9	Evaluation of In-Situ State.....	170

4.10 Conclusion	176
Chapter 5	179
5 Conclusion	179
5.1 Fulfillment of Research Objectives	179
5.2 Future Investigations.....	180
Bibliography	181
Appendix – A – MCPT Results	205
Curriculum Vitae	214

List of Tables

Table 3-1: Different boundary conditions summarized by Salgado et al. (1998).....	53
Table 3-2: Summary of CPT results at BC1 and BC3 boundary conditions	66
Table 3-3: Summary of measured and corrected q_c from this study.....	67
Table 3-4: Summary of MCPT results completed in this study.....	72
Table 3-5: CPT Overburden Stress Normalization methods	76
Table 3-6: M_0 - q_{cN} correlation ranges proposed by previous studies	93
Table 4-1: Calibration tests to determine pore fluid electrical resistivity.....	127
Table 4-2: Summary of ER and V_s Measurements.....	130
Table 4-3: Summary of $V_{s1} - q_{c1N}$ correlations reported by Andrus et al., (2007).....	140

List of Figures

Figure 2.1: Overview of the cone penetration test per ASTM D5778.....	6
Figure 3.1: Schematics of the MCPT chamber used in this study	21
Figure 3.2: Schematics of the structure of the miniature cone penetrometer (Damavandi-Monfared and Sadrekarimi 2015)	22
Figure 3.3: Illustration of the Internal Load Cell connected to the Miniature Cone	23
Figure 3.4: Miniature cone penetration test setup with associated forces developed during cone penetration (Damavandi-Monfared and Sadrekarimi 2015)	25
Figure 3.5: Assembly of the top chamber cap and miniature cone.....	26
Figure 3.6: Image of the base platen and its components	28
Figure 3.7: Image of the top acrylic disk and its components	29
Figure 3.8: Image showing the acrylic spacers used to initiate K_0 consolidation.....	30
Figure 3.9: Illustration showing a specimen after preparation	31
Figure 3.10: Central hole for cone penetrometer on the top cap	31
Figure 3.11: Fully set-up MCPT chamber during a test	32
Figure 3.12: Sample image of the physical appearance of Boler Sand	33
Figure 3.13: A closer look at the Boler sand particles.....	34
Figure 3.14: Particle Size Distribution of Boler Sand re-graded as Fraser River Sand.....	34
Figure 3.15: X-Ray Diffraction analysis of Boler Sand (Mirbaha 2017)	35
Figure 3.16: Aluminium split mold used in this study for specimen preparation.....	37
Figure 3.17: Assembled split mold before (left) and after (right) specimen preparation	38

Figure 3.18: Calibration test to determine frictional resistance	41
Figure 3.19: Increase in piston pressure at the point of docking	42
Figure 3.20: Decrease in the rate of water flow into the piston at the point of docking.....	42
Figure 3.21: Test on uplift calibration (Jones 2017).....	43
Figure 3.22: Illustration of the docking mechanism (Jones 2017).....	44
Figure 3.23: Volumetric strain versus axial strain during consolidation in Test CPT-65-4.	45
Figure 3.24: Development of effective stresses and K_0 state during the consolidation stage of Test CPT-65-4.....	47
Figure 3.25: Variation of pressures during a sample consolidation stage	48
Figure 3.26: Piston and specimen volume changes during a sample consolidation stage	48
Figure 3.27: Particle size distributions of the silica sand before and after cone penetration..	52
Figure 3.28: Effect of chamber size (D_c/d_c) on q_c measured in very dense and loose samples of Hokksund and Ticino sands reproduced from Jamiolkowski et al. (1985)	54
Figure 3.29: Illustration of different boundary condition mechanisms after Goodarzi et al. (2018).....	56
Figure 3.30: Correction for boundary effects based on state parameter by Been et al. (1987)	58
Figure 3.31: Correction for chamber size effect based on Jamiolkowski et al. (2001) empirical method	59
Figure 3.32: Chamber size effect resulting from the reduced vertical stress above the cone (from Wesley 2002)	60
Figure 3.33: Setup of a BC3 MCPT.....	62
Figure 3.34: Comparison of q_c at BC1 and BC3 conditions for specimens $D_{rc} = 25\%$	63

Figure 3.35: Comparison of f_s at BC1 and BC3 conditions for specimens $D_{rc} = 25\%$	63
Figure 3.36: Comparison of q_c at BC1 and BC3 conditions for specimens $D_{rc} = 45\%$	64
Figure 3.37: Comparison of f_s at BC1 and BC3 conditions for specimens $D_{rc} = 45\%$	64
Figure 3.38: Comparison of q_c at BC1 and BC3 conditions for specimens $D_{rc} = 65\%$	65
Figure 3.39: Comparison of f_s at BC1 and BC3 conditions for specimens $D_{rc} = 65\%$	65
Figure 3.40: q_c and f_s profiles for specimens with an average $D_{rc} = 27.2\%$	70
Figure 3.41: q_c and f_s profiles for specimens with an average $D_{rc} = 46.7\%$	71
Figure 3.42: q_c and f_s profiles for specimens with an average $D_{rc} = 64.8\%$	71
Figure 3.43: Variations of corrected q_c over normalized effective vertical stress	74
Figure 3.44: Variations of f_s over normalized effective stress.....	75
Figure 3.45: Comparison of C_q for q_{c1}	79
Figure 3.46: Comparison of C_q for q_{c1} with Idriss and Boulanger (2006).....	79
Figure 3.47: Comparison of stress normalization techniques for $q_{c1,net}$	81
Figure 3.48: Comparison of stress normalization technique for $q_{c1,net}$ with Olsen and Mitchell (1995).....	81
Figure 3.49: Comparison of stress normalization techniques for f_{s1}	82
Figure 3.50: Correlation between Cone Tip Resistance and Sleeve Frictional Resistance for Silica sand	85
Figure 3.51: Comparison of unit weight and q_{c1N} correlation from this study with Mayne (2007) and Mayne et al. (2010).....	87
Figure 3.52: Comparison of D_{rc} and q_{c1N} correlation from this study with previous research	89

Figure 3.53: Comparison of D_{rc} from MCPT test of this study with suggested method by Jamiolkowski et al. (2001).....	91
Figure 3.54: Correlation between D_{rc} and f_{s1N} for silica sand.....	92
Figure 3.55: Comparison of M_D - q_{cN} correlation with previous studies.....	94
Figure 3.56: $M_{max} - q_{cN}$ correlation for silica sand.....	95
Figure 3.57: CSL for Silica sand from Boler Mountain (Mirbaha 2017).....	97
Figure 3.58: Correlation of Q_p - ψ_{cs} for silica sand in comparison with previous studies.....	99
Figure 3.59: Illustration of stress level bias highlighted in this study	100
Figure 4.1: Modified top cap for electrical resistivity measurement	108
Figure 4.2: Illustration of the electrode cable on the upper side of the top cap.....	110
Figure 4.3: Special connection for the Hydra-probe to prevent leakage	111
Figure 4.4: Piezo-electric bender element	113
Figure 4.5: Schematic shape and dimensions of the Hydra-probe used in this study (Al-qaysi and Sadrekarimi 2015).....	114
Figure 4.6: Sample image of silica sand from Boler Mountain.....	115
Figure 4.7: Particle size distribution of silica sand re-graded as Fraser River sand	116
Figure 4.8: X-Ray Diffraction analyses on Boler Sand by Mirbaha (2017).....	117
Figure 4.9: Graphical representation of K_0 consolidation for Test ID ND-45-4	120
Figure 4.10: Illustration of the development of effective stresses for Test ID ND-65-4.....	122
Figure 4.11: Shear wave signal time history at D_{rc} 25.9% and $f = 3.3$ kHz	124
Figure 4.12: Shear wave signal time history at D_{rc} 47.6% and $f = 3.3$ kHz	125

Figure 4.13: Shear wave signal time history at D_{rc} 65.1% and $f = 3.3$ kHz	126
Figure 4.14: Image showing the effluent water after soaking Boler sand	129
Figure 4.15: Electrical resistivity measurements being taken on pore water	129
Figure 4.16: Variations of V_s over normalized effective vertical stress	132
Figure 4.17: Comparison of stress normalization correction factor for V_{s1} with Robertson et al. (1992).....	133
Figure 4.18: Influence of effective stresses and relative densities on formation factor	135
Figure 4.19: $V_{s1} - FF$ correlation for silica sand	137
Figure 4.20: Comparison of $V_{s1} - q_{c1N}$ correlation with other studies.....	139
Figure 4.21: G_{max} vs. Normalized effective stress	142
Figure 4.22: $G_{max1} - q_{c1}$ correlation for silica sand.....	142
Figure 4.23: $V_{s1} - f_{s1N}$ correlation for silica sand	143
Figure 4.24: $FF - q_{c1N}$ correlation for silica sand	144
Figure 4.25: Formation factor – porosity correlation for silica sand in comparison with other studies	147
Figure 4.26: Presence of iron in outcoming water from a typical silica sand specimen.....	148
Figure 4.27: Correlation of consolidation void ratio (e_c) with V_{s1}	151
Figure 4.28: Correlation of consolidation void ratio (e_c) with $F(e_c)$	153
Figure 4.29: Correlation of consolidation void ratio (e_c) with $AF'(e_c)$	155
Figure 4.30: Correlation of consolidation void ratio (e_c) with $AF''(e_c)$ for this study on silica sand	157
Figure 4.31: $FF - e_c$ correlation for silica sand	158

Figure 4.32: Comparison of correlations between V_{s1} and D_{rc} from this study with (Karray and Lefebvre 2008; Hussein and Karray 2015)	161
Figure 4.33: Comparison of V_{s1} predictive models proposed by (Karray and Lefebvre 2008; Hussein and Karray 2015)	163
Figure 4.34: FF – D_{rc} correlation for silica sand.....	164
Figure 4.35: Comparison of $\Upsilon_t - V_s$ correlation with Burns and Mayne (1996)	167
Figure 4.36: Comparison of $\Upsilon_{sat} - V_{s1}$ correlation with Mayne (2007)	167
Figure 4.37: Comparison of $\Upsilon_d - V_{s1}$ correlation with Mayne (2007).....	168
Figure 4.38: Υ_d and $\Upsilon_{total} - FF$ correlation for silica sand	169
Figure 4.39: CSL for silica sand developed by Mirbaha (2017).....	171
Figure 4.40: Normalized shear wave velocity vs. state parameter for silica sand	172

List of Appendices

Appendix A-1: MCPT cone tip and sleeve frictional resistance profile at $D_{rc} = 24.06\%$ and $\sigma'_{vc} = 71.99$ kPa	205
Appendix A-2: MCPT cone tip and sleeve frictional resistance profile at $D_{rc} = 27.81\%$ and $\sigma'_{vc} = 107.55$ kPa	205
Appendix A-3: MCPT cone tip and sleeve frictional resistance profile at $D_{rc} = 28.44\%$ and $\sigma'_{vc} = 203.55$ kPa	206
Appendix A-4: MCPT cone tip and sleeve frictional resistance profile at $D_{rc} = 28.75\%$ and $\sigma'_{vc} = 404.64$ kPa	206
Appendix A-5: MCPT cone tip and sleeve frictional resistance profile at $D_{rc} = 44.69\%$ and $\sigma'_{vc} = 76.07$ kPa	207
Appendix A-6: MCPT cone tip and sleeve frictional resistance profile at $D_{rc} = 46.88\%$ and $\sigma'_{vc} = 100.81$ kPa	207
Appendix A-7: MCPT cone tip and sleeve frictional resistance profile at $D_{rc} = 47.50\%$ and $\sigma'_{vc} = 203.51$ kPa	208
Appendix A-8: MCPT cone tip and sleeve frictional resistance profile at $D_{rc} = 47.81\%$ and $\sigma'_{vc} = 406.11$ kPa	208
Appendix A-9: MCPT cone tip and sleeve frictional resistance profile at $D_{rc} = 64.06\%$ and $\sigma'_{vc} = 75.74$ kPa	209
Appendix A-10: MCPT cone tip and sleeve frictional resistance profile at $D_{rc} = 62.19\%$ and $\sigma'_{vc} = 103.19$ kPa	209
Appendix A-11: MCPT cone tip and sleeve frictional resistance profile at $D_{rc} = 65\%$ and $\sigma'_{vc} = 201.26$ kPa	210
Appendix A-12: MCPT cone tip and sleeve frictional resistance profile at $D_{rc} = 67.19\%$ and $\sigma'_{vc} = 402.51$ kPa	210

Appendix A-13: MCPT cone tip and sleeve frictional resistance profile at $D_{rc} = 65.63\%$ and $\sigma'_{vc} = 405.07$ kPa	211
Appendix A-14: BC3-MCPT cone tip and sleeve frictional resistance profile at $D_{rc} = 68.1\%$ and $\sigma'_{vc} = 400$ kPa	212
Appendix A-15: BC3-MCPT cone tip and sleeve frictional resistance profile at $D_{rc} = 67.5\%$ and $\sigma'_{vc} = 405$ kPa	212
Appendix A-16: BC3-MCPT cone tip and sleeve frictional resistance profile at $D_{rc} = 44.4\%$ and $\sigma'_{vc} = 402$ kPa	213
Appendix A-17: BC3-MCPT cone tip and sleeve frictional resistance profile at $D_{rc} = 43.8\%$ and $\sigma'_{vc} = 400$ kPa	213

List of Abbreviations, Symbols and Nomenclature

CPT	Cone Penetration Test
MCPT	Miniature Cone Penetration Test
SCPT	Seismic Cone Penetration Test
q_c	Cone Tip Resistance
q_{c1}	Normalized Cone Tip Resistance for overburden stress
q_{cN}	Dimensionless Cone Tip Resistance
q_{c1N}	Normalized Dimensionless Cone Tip Resistance
$q_{c,net}$	Net Cone Tip Resistance
$q_{c1,net}$	Normalized Net Cone Tip Resistance
f_s	Sleeve Friction
f_{sN}	Normalized Sleeve Friction for overburden stress
V_s	Shear Wave Velocity
V_{s1}	Normalized Shear Wave Velocity for overburden stress
e_i	Initial specimen void ratio
e_c	Specimen void ratio after consolidation
D_{ri}	Initial specimen relative density
D_{rc}	Specimen relative density after consolidation
σ'_{vc}	Effective vertical consolidation stress

σ_{vc}	Total vertical stress
σ'_{pc}	Effective mean confining stress
σ'_{hc}	Effective horizontal stress
P_a	Reference atmospheric pressure
K_c	Coefficient of lateral earth pressure after consolidation
K_0	Coefficient of lateral earth pressure after K_0 consolidation
F_r	Friction Ratio
γ_d	Dry unit weight of soil
γ_t	Total unit weight of soil
γ_{sat}	Saturated unit weight of soil
I_c	Soil classification index
n	overburden stress normalization exponent
c	stress normalization exponent
Q_{tn}	Normalized total cone tip stress
G_{max}	Maximum shear modulus
ρ_f	Pore fluid electrical resistivity
ρ_b	Bulk electrical resistivity
F.F.	Formation Factor
B	Skempton's pore water pressure parameter
D	Diameter of calibration chamber

d_c	Diameter of miniature cone
DSS	Direct Simple Shear
CDSS	Cyclic Direct Simple Shear
a_n	Net cone area ratio
BC	Boundary conditions
d_{50}	Mean particle size
e_{max}	Maximum void ratio
e_{min}	Minimum void ratio
f	Signal frequency
F.C.	Fines Content
f_E	External load cell reading
f_I	Internal load cell reading
f_{v1}	Frictional force by V-ring located in top cap of specimen
f_{v2}	Frictional force by V-ring located in top plate of calibration chamber
G_s	Specific gravity of soil solids
g	Acceleration due to gravity
h	Height of specimen
LVDT	Linear Variable Differential Transformer
R^2	Coefficient of determination

SEM	Scanning Electronic Microscopic Images
SPT	Standard Penetration Test
ϵ_a	Axial Strain
ϵ_r	Radial Strain
ϵ_v	Volumetric Strain
XRD	X-Ray Diffraction
ER	Electrical Resistivity
u	Pore water pressure
u₁	Pore water pressure measurement near tip of cone penetrometer
u₂	Pore water pressure measurement at shoulder of cone penetrometer
kPa	Kilo Pascals
MPa	Mega Pascals
L_{tt}	Tip-to-Tip Length of Bender Elements
κ	Electrical Conductivity
S/m	Siemens/meter, unit of electrical conductivity
ohm·m	ohm·m, unit of electrical resistivity
ϵ_r	Dielectric constant
n	Porosity
a, m	Fitting parameters based on pore volume and soil cementation

Chapter 1

1 Introduction

1.1 Background

Difficulties in obtaining undisturbed high quality cohesionless soil samples has encouraged geotechnical engineers to look for alternative methods to determine soil parameters, such as empirical correlations with in-situ penetration tests. The cone penetration test (CPT) is often regarded as the most efficient tool to assess and predict a liquefaction event for a given location and to characterize the subsurface, in terms of soil classification and stability analysis. As it does not directly measure any soil property, extensive research has been conducted to develop empirical correlations to determine several soil parameters including unit weight of soil, relative density of soil, ageing and cementation behaviour, shear modulus, and shear strength characteristics of an in-situ soil. The cone penetration test (CPT) is simple, relatively fast and reliable, and can provide continuous data of subsurface soil response. The recorded response to the penetration of a cone on the cone tip and its adjacent steel shaft is measured and converted into useful parameters such as the cone tip resistance (q_c) and sleeve friction (f_s) using empirical equations suggested by ASTM D5778-12 (2012) standard procedure for CPT testing. The need to develop empirical correlations with these factors has motivated the worldwide development of calibration chamber-based penetration tests or miniature cone penetration tests (MCPT) which, over time, have proven to be less cost intensive than field-scale in-situ penetration tests (Been et al. 1987; Schmertmann 1978; Parkin et al. 1980; Baldi et al. 1981 ; Villet and Mitchell 1981). The calibration chambers however, come with their own set of challenges as they are significantly large in dimensions, often 1 m in height and 1.5 m in diameter as summarized by Holden (1991). This large scaling produced a series of significant issues including the handling of large quantities of soil, intensive labour, long sample preparation time, inconsistency of relative densities of specimens, and verification of saturation as mentioned by Ghionna and Jamiolkowski (1991).

A more convenient approach in developing CPT systems in a laboratory setting have been brought about by the development of miniature cone penetration tests which can accommodate cone penetrometer probes with smaller diameters than the conventional 35.7 mm diameter cone penetrometer specified by ASTM D5778-12 (2012). However, with a reduction in dimension, calibration chambers do tend to attract several other issues such as boundary and scale effects which will be discussed later in detail. One such MCPT calibration chamber using a triaxial testing cell and load frame was developed at Western University, London, Canada by Damavandi-Monfared and Sadrekarimi (2015). The apparatus was later upgraded by Jones (2017) to measure small-strain soil stiffness and impose anisotropic consolidation on soil samples.

The mechanical behavior and shear strength of cohesionless soils are primarily controlled by their density and porosity (Sadrekarimi 2014). Therefore, determination of the in-situ density of sands is essential for predicting the in-situ shearing strength and liquefaction susceptibility behavior, densification control, as well as determining seepage characteristics of cohesionless soils. However, direct measurement of these parameters is challenging due to difficulties in obtaining undisturbed samples for laboratory testing and the vulnerability of cohesionless soil samples to disturbance caused by borehole excavation, sampling, transportation, sample extrusion and handling. Disturbance could result in an incorrect estimation of soil porosity and density. Moreover, the inherent variability of in-situ soil deposits makes it further challenging to adequately characterize an in-situ soil deposit. These limitations have disorged widespread research to develop reliable and economical in-situ testing methods. One such geophysical technique to determine the in-situ porosity of an in-situ soil is by measuring the electrical resistivity ρ (ohm·m) of soil, which is a measure of how well the material allows the flow of electrical current through it. The inherent ability to transmit charged ions is primarily governed by the electrical resistivity, a basic property of all materials. Existing studies (Keller and Frischknecht 1966; Parkhomenko 1967; Arulanandan and Muraleetharan 1988; Mazac et al. 1990; Thevanayagam 1993) have found that the electrical resistivity of soils depends on several factors such as its porosity, electrical resistivity of the pore fluid, soil mineralogical composition, degree of saturation, particle shape and orientation, and pore structure. A further addition to the penetration-based approaches is the introduction of small-strain

shear wave velocity (V_s) measurements (Andrus and Stokoe 2000; Kayen et al. 2013). The empirical relationships based on cone tip resistance (q_c), sleeve friction (f_s) and shear wave velocity (V_s) obtained from seismic cone penetration tests (SCPT) have improved the accuracy of predicting engineering properties of soils. A series of 20 MCPT alongside 12 shear wave velocity and electrical resistivity measurements, have been carried out in this study using a triaxial load frame at Western University in conjunction with an electrical resistivity probe equipped with 4 parallel stainless-steel electrodes to address the research objective described in the next section.

1.2 Research Objectives

The main objective of this study is to establish an improved approach for characterizing engineering properties of in-situ soils based on combined measurements of cone penetration resistances, shear wave velocity, and electrical resistivity of a natural sand through advanced experimental techniques under controlled laboratory settings. Within this configuration, the following objectives have been explored:

- a. Production of an extensive database of MCPT results on a silica sand using the recently upgraded CPT calibration chamber at Western University. This is accomplished by performing a large set of MCPT experiments in the calibration chamber by recreating in-situ stress conditions.
- b. Investigating the effect of chamber boundaries by comparing experimental results with different boundary conditions and developing corrections for sample boundary effect.
- c. Investigating the application of geophysical techniques including shear wave velocity and electrical resistivity measurements for characterizing a silica sand. This is achieved by conducting experiments on saturated samples of a natural silica sand consolidated under a wide range of stress conditions and relative densities.

- d. Establishing an improved method for characterizing a silica sand by combining shear wave velocity and electrical resistivity measurements.

1.3 Thesis Outline

This thesis has been prepared as an “Integrated-Article” format. It is organized into 5 chapters with Chapter 1 introducing the reader to the background of the thesis, Chapter 2 presenting a thorough review of relevant literature, Chapter 3 describing the findings from the series of MCPT completed in this study, Chapter 4 presenting a series of empirical correlations developed from electrical resistivity and shear wave velocity measurements along with the cone penetration results, and Chapter 5 summarizing and concluding the thesis. Brief descriptions of Chapters 3 and 4 are provided below:

Chapter 3: Miniature Cone Penetration Test on Silica Sand

This chapter presents the results of a series of MCPTs performed on silica sand at a variety of effective consolidation stresses and relative densities for the recorded parameters of q_c and f_s . The results are presented alongside a discussion of operational considerations of the MCPT calibration chamber including repeatability, scale effect, calibration chamber boundary conditions, effect of particle crushing, etc.

Chapter 4: Non-destructive Testing with Shear Wave Velocity and Electrical Resistivity Measurements on Silica Sand

This chapter presents the results of multiple electrical resistivity and shear wave velocity measurements. Besides the test results, general empirical correlations have been developed between electrical resistivity and shear wave velocity measurements alongside the MCPT results to estimate various engineering properties of soil which is important in analyzing soil strength.

Chapter 2

2 Literature Review

This chapter presents a thorough review of literature that has been referred to, in this study for comparison and validation purposes.

2.1 Background of Miniature Cone Penetration Test

Geotechnical engineering analyses and design projects require sound identification and characterization of in-situ soil. The popularity and reliability of computer-based software programs have led to the development of numerous sophisticated numerical methods to assess the behaviour of in-situ soil which can be further used for construction projects. However, the primary design parameters used in these programs are derived from empirical correlations developed from conventional in-situ testing. For example, difficulties in obtaining undisturbed high quality cohesionless soil samples encouraged geotechnical engineers to look for better alternatives, such as penetration based in-situ tests. Cui (2011) rightly highlights that as an in-situ test method for site characterization, the cone penetration test (CPT) is simple, fast and reliable, and can provide continuous data of subsurface soil. The cone penetration tests (CPT), are often regarded as one of the most efficient tools to assess and predict a liquefaction event for a given location. According to ASTM D5778-12 (2012), CPT is conducted by pushing a metallic cone probe into the ground at a controlled rate of 2 cm/s. The standard CPT cone has a 60° apex angle and a diameter of 35.7 mm which corresponds to a projected cone base area of 10 cm². The standard cone has a friction sleeve with a surface area of 150 cm² for the 10 cm² cone. An illustration of the conventional CPT system presented by ASTM D 5778 is shown in Figure 2.1. However, CPT does not measure soil property directly. Under any imposed stress condition, the applied load response on the cone and its adjacent steel shaft is measured and converted into parameters like cone tip resistance (q_c) and sleeve friction (f_s) using empirical equations suggested by ASTM D5778-12 (2012).

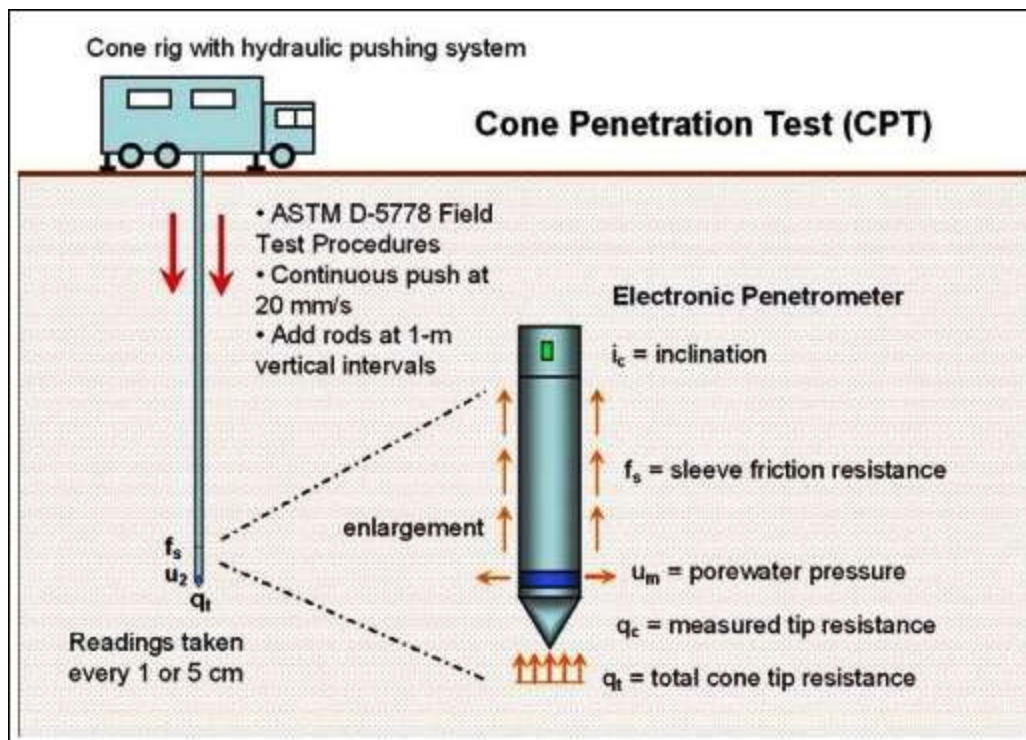


Figure 2.1: Overview of the cone penetration test per ASTM D5778

Subsequent advances added simultaneous measurement of pore water pressure either behind the cone or on the cone face, hence the term CPT_u emerged. Pore pressure measurements at different locations were made by various researchers and practitioners and piezometer cones became the most common in-situ testing tool. These obtained measurements can be effectively used for soil identification, classification, and evaluation of different soil properties such as strength and deformation characteristics. Thus, the CPT can be used for a wide range of geotechnical engineering applications. As the CPT directly does not measure any soil property, extensive research has been conducted to develop empirical correlations to determine unit weight of soil, relative density of soil, ageing and cementation behaviour. The CPT in its conventional form has proven to be expensive or may not be available to access remote sites. There have been numerous attempts in studying the effects of cone penetration test in laboratory-controlled setting to create an alternate, less expensive model of the penetration-based tests, which are known as calibration chambers. Fundamentally, a calibration chamber is a cylindrical mass of soil specimen

which is prepared at a known density and loaded at known stress levels. Thereafter, a cone penetrometer is pushed into the soil specimen at a controlled rate and down to a certain depth.

For example, Been et al. (1987) constructed a calibration chamber with a specimen height of 1 m and diameter of 1.4 m. In fact, Holden (1991) and Ghionna and Jamiolkowski (1991) summarizes the dimensions of various calibration chambers across the world. The Materials Research Division, Melbourne, first established a calibration chamber in 1969 with a specimen height of 0.91 m and diameter of 0.76 m. Subsequently, the University of Florida, Gainesville in 1971, Monash University, Melbourne in 1973, Norwegian Geotechnical Institute, Oslo in 1976, Italian National Electricity Board (ENEL) in 1978, ISMES Laboratory, Bergamo in 1981 and many more of such prestigious research institutions across the world, developed the first-generation calibration chambers all of which had specimen height more than 1.5 m and diameter 1.2 m. Several other researchers developed their attention in quantifying the relationships between sand relative density, effective stress level and CPT tip resistance by using large-scale chamber tests done by (Schmertmann 1978; Parkin et al. 1980; Villet and Mitchell 1981; Jamiolkowski et al. 1985). The calibration chambers however, came with their own set of challenges as they were significantly large in dimensions, often 1 m in height and 1.5 m in diameter as summarized by Holden (1991). The calibration chambers are reasonably large in dimensions because they involve a conventional CPT (diameter = 35.7 mm) for the penetration process. This large scaling produced a series of significant issues including the handling of large quantities of soil, intensive labour, long preparation time, inconsistency of relative densities of specimens, and verification of saturation as mentioned by Ghionna and Jamiolkowski (1991).

A more convenient approach in developing CPT systems in a laboratory setting have been brought about by the development of miniature cone penetration tests which can accommodate cone penetrometer probes with smaller diameter than the conventional 35.7 mm - 43.7 mm diameter cone penetrometers specified by ASTM D5778-12 (2012). For example, Abedin (1995) conducted extensive research on sandy clay/loam soil in a miniature calibration chamber which involved specimens with a diameter of 100 mm and

a height of 185 mm. A 10 mm diameter cone was pushed into the specimen at a rate of 0.012 mm/sec down to a depth of 55 mm. This miniature calibration chamber was successfully developed within a modified triaxial chamber at the University of Newcastle upon Tyne where Abedin (1995) performed soil tank experiments using standard sized cones to validate the MCPT performed in this study. Later, the CPT data were used to predict density of unsaturated loam soils Abedin and Hettiaratchi (2002). Kokusho et al. (2011) modified a triaxial apparatus to prepare specimens with diameter 100 mm and height 200 mm and a 6 mm cone penetrometer was pushed into the soil at a rate of 2 mm/sec down to a depth of 25 mm. A series of experimental study with MCPT and subsequent cyclic loading tests were carried out to investigate aging effect on liquefaction resistance by cementation and by prior loading, with fines content as a key parameter. They determined that both types of aging effects increased liquefaction strength under the same magnitude of penetration resistance, however, fines content was shown to possess a greater influence on cementation. Kumar and Raju (2008) studied penetration resistances in silty sands using a calibration chamber of diameter 91 mm, height 133.5 mm and 19.5 mm cone penetrometer was pushed into the soil at a rate of 0.021 mm/sec to a depth of 55 mm. The significant development in this study was the incorporation of K_0 stress conditions to replicate in-situ behaviour of soil. They established correlations between shear strength parameters and miniature cone tip resistance. Kumar and Raju (2009) extended the work for sand-fly ash mixtures. In 2009, they increased the diameter of the specimen to 180 mm to achieve a higher D_c/d_c ratio. Moreover, in their earlier works, the piston shaft was smaller in diameter than the cone diameter so that not much resistance was offered by the shaft. However, later Kumar and Raju (2009) made both the diameters equal. Through their investigations on tip resistance, friction angle and overburden stress for loose to dense sand specimens, the authors concluded, that miniature cone penetration tests resulted in reasonable predictions when compared with conventional field test results, although slightly a little conservative estimate. Baxter (2010) developed a miniature calibration chamber using an electric piezocone of 1.13 cm diameter, from FUGRO Engineers B.V. in Netherlands and a modified triaxial chamber. Soil specimens of 560 mm in height and 450 mm in diameter were prepared using Providence silt. The rate of penetration for these tests have been recorded as 20 mm/s as recommended by the ASTM standards for in-situ CPT

tests. The objective of this study was to critically evaluate the applicability of CPT based liquefaction resistance approaches to non-plastic silts commonly found in Rhode Island. MCPTs were performed on Providence silt to determine a relationship between relative density and tip resistance. Combining the findings of the mini-cone tests with cyclic resistance measurements, further comparisons were made with different liquefaction triggering analyses. Pournaghiazar (2011) prepared 840 mm high specimens of Sydney sand having 460 mm of diameter. A miniature cone probe of 16 mm was driven into unsaturated coarse samples down to a depth of 600 mm. To study the effects of negative pore pressure on cone resistance, later a suction mechanism was installed to the calibration chamber reported by Pournaghiazar et al. (2013). It was reported by the study that suction has a significant influence on cone penetration resistance. However, the empirical correlations developed in this study were essentially proposed for dry, unsaturated specimens, which may not predict accurate results for saturated sands. Cui (2011) developed a calibration chamber from a soil compactor and prepared soil specimens collected from Beijing which had a height of 200 mm and a diameter of 190 mm. A 20 mm cone probe was penetrated according to ASTM standards i.e. 20 mm/s. This study was intended to characterize the shallow subsurface soil. To calibrate the miniature cone penetration system for its application in the design of small size shallowly embedded piles under lateral loads, a series of MCPTs and loading tests in silty clay were carried out. Cui (2011) reported that miniature cone penetrometer provided reasonable results to be employed for the design of the small size piles. Some of the other prominent MCPT studies across the globe were done by Franzen (2006) and Jasinski (2008). The advantages of calibration chambers are that the type of sand, consolidation stresses, direction of applied stress and density are totally controlled under laboratory setting (Houlsby and Hitchman 1988). However, it is evident from literature, that with gradual decrease in size of the calibration chambers and the cone penetrometer probes, boundary conditions and scale effects of calibration chambers are often challenged for validity, which will subsequently be discussed.

2.2 Background of Shear Wave Velocity

An important supplement or contribution to the penetration-based approaches is the introduction of in-situ measurements of small-strain shear wave velocity (V_s) (Andrus and Stokoe 2000; Kayen et al. 2013).

A geophone is placed inside a standard 10 cm² cone probe by which seismic wave velocities are measured during cone penetration. In general, a geophone system uses a pair of bender elements, a source and a receiver, to send S waves or P waves through a soil specimen. The first type of body wave is a Primary or P wave (often referred to as 'Pressure' waves). This is a longitudinal wave in which the direction of motion of the particles is in the direction of propagation. This motion is irrotational and the wave is propagated with speed V_p . P waves apply volumetric strains to the soil, and hence P-wave velocity is controlled by the bulk modulus of the ground. On the other hand, body waves can also be Secondary or S waves (also referred to as 'Shear' waves). This is a transverse wave in which the direction of motion of the particles is perpendicular to the direction of propagation where the shear distortion is applied. The S wave velocity is therefore constant regardless of the rate of applied loading, hence no drainage as a result of volumetric loading is required. The motion is rotational and propagated with speed V_s . Since $V_p > V_s$, the first waves to arrive from any earthquake vibration will always be P-waves. P waves can be transmitted through a fluid such as pore water or through the soil skeleton, hence the saturation of the media may change the value of V_p significantly. The bulk modulus of water could be up to 50 times the value in the soil skeleton. In which case the first arrival P-wave velocity will be seen to be solely transmitted through the water at between 1400 and 1500 m/sec depending on temperature (Kaye and Laby 1982), hence the skeletal velocity of the material may be masked. Shear waves however, are almost completely unaffected by saturation of the media due to the negligible shear modulus of water. Therefore, a correct assessment of shear wave velocity can provide the operator with significant engineering parameters required in a geotechnical engineering analysis. Shear waves are created by a large force acting at ground level which sends sinusoidal waves propagating through the soil and, eventually, being received by the geophone located near the head of the cone. Shear wave velocity is measured by the distance from the source of

the large force to the location of the geophone divided by the time the shear wave requires to reach the geophone. Shear wave velocity represents a low strain measurement as its field measurement (in-situ) does not require disturbance of the soil matrix unlike CPT. The addition of measurement of shear wave velocity to the conventional cone penetration test, i.e. the seismic cone penetration test (SCPT) provides an advanced evaluation of soil characteristics and in particular liquefaction potential. Shear wave velocity is often used in constitutive models to determine small-strain response of soils to estimate the in-situ stress state of cohesionless soils (Robertson et al. 1995), for ground deformation prediction, for seismic classification in many design codes including the current National Building Code of Canada and the Canadian Highway Bridge Design Code. V_s and the time averaged V_s of the upper 30 meters (V_{s30}) is the current seismic predictor for seismic site classification in NBCC and CHBDC. (Andrus et al. 2004; Clayton 2011) studied site-response for evaluating seismic hazard, and assessing liquefaction potential in cohesionless soils. Hardin and Black (1966) and Robertson et al. (1995) studied dynamic characteristics of Ottawa sand. Kokusho (1980) studied the behaviour of Toyoura sand. Shear wave velocity and shear modulus (G) are two of the most fundamental parameters for characterizing soils in geotechnical engineering design practice. Shear wave velocity not only represents a measure of soil elasticity but also soil stiffness in terms of shear modulus (G), which is expressed as shown in Equation 2.1.

$$G_{max} = \rho \cdot V_s^2 \quad (2.1)$$

where, G_{max} is the maximum shear modulus corresponding to very small values of strain ($\gamma < 10^{-5}$) and ρ is the density of the soil. Low strain shear modulus like shear wave velocity, is an important parameter to determine site response characteristics for seismic events. Shirley and Hampton (1978) performed the first study to use bender elements in soil testing for determining shear modulus. V_s can be measured both in the laboratory (e.g. bender element tests, resonant column tests and ultrasonic tests) and in the field by down-hole, cross-hole and suspension logging.

Bender elements, and their interpretation and analysis have been studied extensively, often in triaxial setups with bender elements located on disks confining the bottom and top of

the sample (Viggiani and Atkinson 1995; Leong et al. 2005). Commonly used laboratory devices like triaxial shear by (Bates 1989; Brignoli et al. 1996; Jones 2017) direct simple shear by (Dyvik and Madshus 1985; Jones 2017; Mirbaha 2017), and ring shear apparatuses by (Youn et al. 2008; El Takch et al. 2016) modified to record shear wave velocity measurements alongside the conventional test results from the devices. However, the interpretation of shear wave velocity measurements can be very challenging as the determination of the time difference between the incipient and received wave requires some sound precision. There are many studies done previously which showcase research on various time and frequency domain models to interpret shear wave velocity (Lee and Santamarina 2005; Camacho-Tauta et al. 2015). Prior studies on shear wave velocity measurements propose setting the maximum wavelength of the shear waves (λ) to less than twice that of the bender tip to tip distance (i.e. the height of the specimen minus the height of the bender elements) to avoid near-field effects (Marjanovic and Germaine 2013). A general advantage of shear wave velocity tests is that they can be used for sites underlain by soils that are difficult to penetrate or sample (e.g., gravels, cobbles, and boulders).

2.3 Background of Electrical Resistivity Test

The mechanical behavior and shear strength of cohesionless soils are primarily controlled by their density and porosity (Sadrekarimi 2014). Therefore, determination of in-situ porosity and density of sands is essential for predicting the in-situ shearing strength and liquefaction susceptibility behavior, densification control, as well as determining seepage characteristics of cohesionless soils. However, direct measurement of these parameters is challenging due to the difficulties in obtaining undisturbed samples for laboratory testing and the vulnerability of cohesionless soil samples to disturbance caused by borehole excavation, sampling, during transportation, sample extrusion and handling. The disturbances result in an incorrect estimation of soil porosity and density. Moreover, inherent variability of the stratigraphy of in-situ soil deposits makes it further challenging to correctly analyze their strength behaviour. The challenge is further severed in case of sampling saturated cohesionless soil samples. Hence, these limitations have disgorged widespread research to develop reliable and economical in-situ testing methods. Electrical

methods of geophysical exploration gained popularity in 1927 when Conrad Schlumberger showed that electrical resistivity of oil wells could distinguish between productive and non-productive rocks. This development stimulated extensive research on electrical resistivity measurements as an indicator of physical and chemical properties of the subsurface. Electrical conduction in saturated sediments occurs through the interstitial water as the soil grains have extremely high orders of resistivity. The electrical resistivity is therefore determined by the amount of water present in the soil-water medium, its salinity and the manner in which the water is distributed across the medium. The porosity of the medium determines the amount of water that can be present in the system. However, salinity can be different in different types of soil-water formations depending on the concentration of conductive materials present in the water. To compare resistivities of different samples, it is necessary to normalize the resistivity values. This is generally done by calculating the formation factor (FF) which is defined as the ratio of bulk electrical resistivity (ρ_b) of the sample to the electrical resistivity of the pore fluid (ρ_f), shown in Equation 2.2 developed by Archie (1942).

$$FF = \frac{\rho_b}{\rho_f} \quad (2.2)$$

The relationship between electrical properties and porosity has been a very important subject of investigation in the oil and gas/petroleum industry for many years. It has also been proven to be of fundamental importance for geotechnical engineers for in-situ ground characterization. Sundberg (1932) postulated a relationship between porosity and a “resistivity factor” which is defined as the ratio of the resistivity of fully saturated granular media to the resistivity of the interstitial water. However, Archie (1942) presented strong empirical evidence towards the correlation and remodelled the resistivity factor as “formation factor”. The formation factor approach was recognized as more reasonable because it is determined by the formation characteristics of the soil medium rather than by fluid characteristics. Therefore, Archie (1942) proposed,

$$FF = n^{-m} \quad (2.3)$$

where “ n ” is the porosity fraction of the soil and “ m ” is the slope of the line representing the relationship under discussion.

Archie (1942) described “ m ” to be dependent on the pore volume geometry. The equation comes with a boundary condition that at 100% porosity, formation factor will be equal to unity. Atkins and Smith (1961) pointed out that “ m ” is strongly dependent on the shape of grains and pores. The authors reported that the dependence of “ m ” on the degree of cementation is not as strong as its dependence on the grain and pore properties, shape and type of grains, and shape and size of pores and pore throats. Therefore, it was suggested that m should be called the “shape factor” instead of “cementation factor”. The term “Archie shape factor” or “shape factor” is used for “ m ”, unless otherwise indicated.

The inherent ability to transmit charged ions is primarily governed by the electrical resistivity, a basic property of all materials. Similar findings on marine sediments were reported by (Kermabon et al. 1969; Erchul and Nacci 1971; Erchul 1972). Subsequently, Wheatcroft (2002) used an in-situ resistivity probe to measure the near-surface porosity of shallow-water marine sediments off Florida and Bahamas. Multi-electrode cells were built to measure bulk electrical resistivity in sand-clay mixtures at different volumetric water content by Bryson and Bathe (2009) Similarly, a four-electrode resistivity probe was used to study the variation of porosity according to different consolidation stages in a kaolinite clay and crushed sand mixture by Kim et al. (2011). The shape factor “ m ” indicates reduction in the number and size of pore openings. It has been widely used in hydrocarbon and groundwater exploration and in porous-media engineering studies (Archie 1942; Winsauer et al. 1952; Wyllie and Gregory 1953; Hill and Milburn 1956; Towle 1962; Helander and Campbell 1966; Waxman and Thomas 1974; Windle and Worth 1975; Jackson et al. 1978; Biella and Tabbacco 1981; Sen et al. 1981; Wong et al. 1984; Givens 1987; Brown 1988; Donaldson and Siddiqui 1989; Ruhovets 1990; Salem 1992; Tiab and Donaldson 1996). Keller (1982) summarized several values for “ m ” showing that it is a function of lithology, porosity and compaction. Wyllie and Rose (1950) and Wyllie and Gregory (1953) proposed that “ m ” lies between the limits of 1.3 to 3. Erchul and Nacci (1971) reported that Atkins and Smith (1961) found the factor “ m ” ranging from 1.6 for clean sands to 3.28 for sodium montmorillonite. The shape factor “ m ” is 1 for completely

porous material and increases with decreasing porosity. Kermabon et al. (1969) found a more limited range of 1.8 – 2. Smith (1971) conducted several electrical resistivity experiments of North Atlantic deep sea cores around Wales, England and developed 99 formation factor-porosity relationships and found that the data clearly grouped into two classes. For clay and silt, “m” was found to be approximately 2, and for sands and gravel “m” was around 1.5. Salem (2001) reported a summary of fitting factors for different classes of soil and rock as found by Salem and Chilingarian (1999) and it is for example, 1.09 for porous dolomites, 1.3 for glass spheres, 1.3 – 1.6 for homogenous clean sands, 1.5 – 2.3 heterogenous sediments, 1.8 – 3.0 for compacted sandstones and limestones and 1.8 – 4.2 for shaly sandstones and siltstones. Therefore, many researchers have developed their formation factor-porosity models based on the first equation developed by Archie (1942).

Archie (1942) while developing his model assumed that his batches of materials were essentially clean, i.e. there was no presence of clay or shaly minerals. Worthington (1993) highlights that the study also involved experiments using a very high concentration of brine solution as the electrolyte that would suppress the electrical manifestation of clay constituents. (Keller and Frischknecht 1966; Parkhomenko 1967; Arulanandan and Muraleetharan 1988; Mazac et al. 1990; Thevanayagam 1993) have found that for soils, electrical resistivity depends on many factors such as porosity, electrical resistivity of the pore fluid, composition of the solids, degree of saturation, particle shape and orientation, and pore structure. A comprehensive geophysical well logging was completed through 1961 by Dakhnov (1962) who summarized the factors that affect electrical resistivity of a porous media, which were: amount of clay/silt in the sediment, the porosity of the sediment, the degree of saturation of the sediment, temperature of the sediment, cation exchange capacity of the soil minerals and resistivity of the interstitial water. Bouma et al. (1971) and Chmelik et al. (1969) developed laboratory and in-situ electrical resistivity instruments to work on marine sediments. Their objective was to develop correlations between lithology and geotechnical engineering properties. Properties such as pH, water content, carbonate content, grain size analysis, X-ray radiographs, photographs, cone penetrometer and vane shear measurements were compared with electrical resistivity measurements and it was found that electrical resistivity was indirectly proportional to porosity of a sediment and directly proportional to the percentage of clay minerals presents. Ehrlich et al. (1991)

concluded that the cementation factor “*m*” varies with many other factors like shape of grains, sorting and packing of grains, tortuosity, overburden pressure, wettability of grain surfaces, pore geometry and most importantly fines content i.e. size of particles. Jackson et al. (1978) claimed that the constant “*m*” is a function of shape of the soil grains while Ransom (1984) claimed it is the pore geometry that affects the value of “*m*”. Salem (2001) mentioned that higher angularity or less sphericity and higher percentages of clay content increases “*m*”. An increase in specific surface area due to abundance of fine-grained sediments increases the factor “*m*”. Salem (2001) also mentions that in micro-porous systems with many dead-end pores, and in porous materials with grains of irregular shapes as well as in rocks characterized by complexity of electrolytic paths, electric current encounters more resistance, resulting in higher values of tortuosity and “*m*”. Jackson et al. (1978) performed electrical resistivity tests on unconsolidated marine sands and found a porosity-formation factor relationship according to Equation 2.3. They also found that “*m*” directly depends on the angularity of the particles in a deposit. Erickson and Jarrard (1998) performed electrical resistivity tests on shallow silica sediments from the Amazon Fan and reported that muds and sands exhibit different trends of porosity and formation factor due to differences in pore volume. All these reasons made several investigators develop more correlations involving formation factor and porosity. Winsauer et al. (1952) introduced the generalized form the Archie’s first equation which is given by,

$$FF = a \cdot n^{-m} \quad (2.4)$$

This equation has been termed as the “humble” relation or the Archie – Winsauer equation. In this equation, Winsauer et al. (1952) introduced the tortuosity factor “*a*” which is a function of tortuosity and mentioned that “*a*” is not equal to unity but varies with type of material. This factor generally decreases with an increase in compaction, consolidation, age or cementation of soil mass. Therefore, “*a*” was termed as cementation factor. Winsauer et al. (1952) assigned a value of 0.62 for “*a*” and 2.15 for “*m*”. But the magnitude of these factors has varied widely for different researchers. Keller and Frischknecht (1966) demonstrated a value of 1.0 for “*a*” in case of materials having intergranular porosity. Parkhomenko (1967) derived a value of 0.4 for “*a*” after working on resistivity experiments on consolidated sandstones. For shaly sandstones, Salem and Chilingarian (1999) found a

value of 0.44 for “a”. Boyce (1968) performed electrical resistivity tests at 43 locations around Bering Sea with each location being 600 miles away from the other. He reported a value of 1.3 for “a” and 1.45 for “m” on sediments which had porosities from 58.3 – 87.4 %. Al-qaysi and Sadrekarimi (2015) provided a detailed account of inter-relationships between soil electrical resistivity, porosity, hydraulic conductivity and consolidation behaviour of saturated Ottawa sands of two different gradations and natural Boler sand. They found that formation factor increased with increase in fines content, the cementation factor “a” increased with increase in fines content and formation factor. There have been more investigations, where the operators have found that both “a” and “m” can vary for a similar material owing to several other factors. For sandstones, Hill and Milburn (1956) showed that the “a” varies from 0.47 – 1.8 and “m” varies from 1.64 – 2.23, Carothers (1968) showed that “a” varies from 0.62 – 1.65 and “m” varies from 1.3 – 2.15, Carothers and Porter (1971) reported that “a” varies from 1 – 4 and “m” varies from 0.57 – 1.85. However for carbonates, Hill and Milburn (1956) reported a range of 0.73 – 2.3 for “a” and 1.64 – 2.10 for “m”, Carothers (1968) claimed a range of 0.45 – 1.25 for “a” and 1.78 – 2.38 for “m”, Schon (1983) reported that “a” varies from 0.35 – 0.8 and “m” varies from 1.7 – 2.3. There are several other mathematical models involving formation factor and porosity developed by investigators according to their material and testing condition. Mostly variabilities have been observed by studies that were conducted in-situ. The studies that were done experimentally such as (Erchul and Nacci, 1971) has shown to conform with the predictive model proposed by Archie (1942). Erchul and Nacci (1971) performed electrical resistivity tests on different types of soil (illite clay, kaolinite clay, Providence silt, Ottawa sand with rounded particles, glacial sand with angular particles and marine sediments) at different concentrations of pore water salinity and suggested that porosity can be determined from formation factor by laboratory testing with a minimal percentage of error. In fact, Worthington (1993) in attempt to re-examine the formation factor-porosity relationship, concluded that the first equation (Equation 2.3) proposed by Archie (1942) is well-suited for clean sands. Therefore, it can be understood that, in case of laboratory-controlled experiments on reconstituted specimens of clean coarse material, where the gradation of the material can be controlled, the first equation of Archie (1942) serves as a more reasonable model in correlating formation factor and porosity.

Chapter 3

3 Miniature Cone Penetration Tests on a Silica Sand

This chapter presents the results of a series of MCPTs performed on a silica sand at different effective consolidation stresses and relative densities and the measurement of q_c and f_s . The results are presented alongside a discussion of operational considerations of the MCPT calibration chamber including repeatability, scale effect, calibration chamber boundary conditions, effect of particle crushing, etc. MCPT results are compared with other calibration chamber test results.

3.1 Introduction

Geotechnical engineering analyses and design projects require sound identification and characterization of the in-situ soil. The popularity and reliability of computer based software programs have led to the development of numerous sophisticated numerical methods to assess the behaviour of an in-situ soil which can be further used for construction projects. However, the primary design parameters used in these programs are often derived from empirical correlations developed from conventional in-situ testing. For example, difficulties in obtaining undisturbed high quality cohesionless soil samples has encouraged geotechnical engineers to look for better alternatives, such as penetration based in-situ tests. CPT can be used for a wide range of geotechnical engineering applications in particular for characterizing saturated loose to medium-dense cohesionless soils due to the susceptibility of these soils to static or cyclic liquefaction and their potential for liquefaction flow failure. Extensive research has been conducted to develop empirical correlations of CPT measurements with soil type and engineering properties (including unit weight, relative density, and modulus) using laboratory calibration chamber experiments (Schmertmann 1978; Villet and Mitchell 1981; Baldi et al. 1986; Jamiolkowski et al. 1988, 2001; Huang and Hsu 2005). These experiments can provide reliable results for developing CPT-based correlations as the entire procedure including sample preparation, consolidation, and cone penetration is conducted in the laboratory and can be readily

monitored and controlled. However, carrying out a controlled CPT calibration chamber test with a standard cone (with a diameter of 35.7 mm) requires a large diameter (typically more than 1.2 m) chamber. Such an experiment can be expensive and time-consuming, as sample preparation involves placing a large volume of sand in the testing chamber at a controlled density. The control of sample uniformity and external stresses can also become difficult (Parkin and Lunne 1982). Due to these challenges, several studies have employed miniature cones and reduced-scale calibration chamber devices (Abedin 1995; Huang and Hsu 2005; Franzen 2006; Kumar and Raju 2009; Pournaghiazar 2011; Kokusho et al. 2012) in cohesionless soils. One such MCPT calibration chamber using a triaxial load frame was developed at Western University, London, Canada by Damavandi-Monfared and Sadrekarimi (2015). The apparatus was later upgraded by Jones (2017) to measure small-strain soil stiffness and impose anisotropic consolidation on soil samples.

3.2 Design of the Calibration Chamber

The calibration chamber designed and used in this study was modified at Western University, London Ontario, Canada, from a large triaxial compression testing cell manufactured by Trautwein Soil Testing Equipment Co., Texas, USA. Previously, several successful cone penetration tests were performed with this device. The calibration chamber was initially developed by Damavandi-Monfared and Sadrekarimi (2015) and upgraded by Jones (2017).

A schematic of the cone penetration testing chamber used in this study is presented in Figure 3.1. Each individual component is described in this section with a reference to Figure 3.1 for a better understanding to the reader.

The triaxial cell used for this study was able to fit a specimen with a height of 190 mm and a diameter of 150 mm. The top acrylic cap that rests on the specimen was drilled at the centre to allow the passage of a 6 mm diameter miniature cone penetrometer probe. The hole has been designed to accommodate a V-ring which provides sealing of the cone with the top specimen cap and is lubricated to provide smooth movement of the cone into the

specimen. The apex angle and the net area ratio (a_n) of the cone is 60 degrees and 0.75, respectively.

The subtraction type penetrometer (Figure 3.2), has been built in a way that the cone and the steel shaft both transfer the compressive forces on two load cells connected in series. The cone is connected to a thin metallic rod that passes through a hollow shaft of the cone penetrometer. This metallic rod transfers the load response from the cone to a properly calibrated internal load cell which has a maximum loading capacity of 889.6 N. The hollow steel shaft is directly connected to a metallic piston rod which exits the top cap of the triaxial cell to transfer the total load to an external load cell which has a maximum capacity of 8,896 N. An illustration showing the structure of the miniature cone is presented in Figure 3.2.

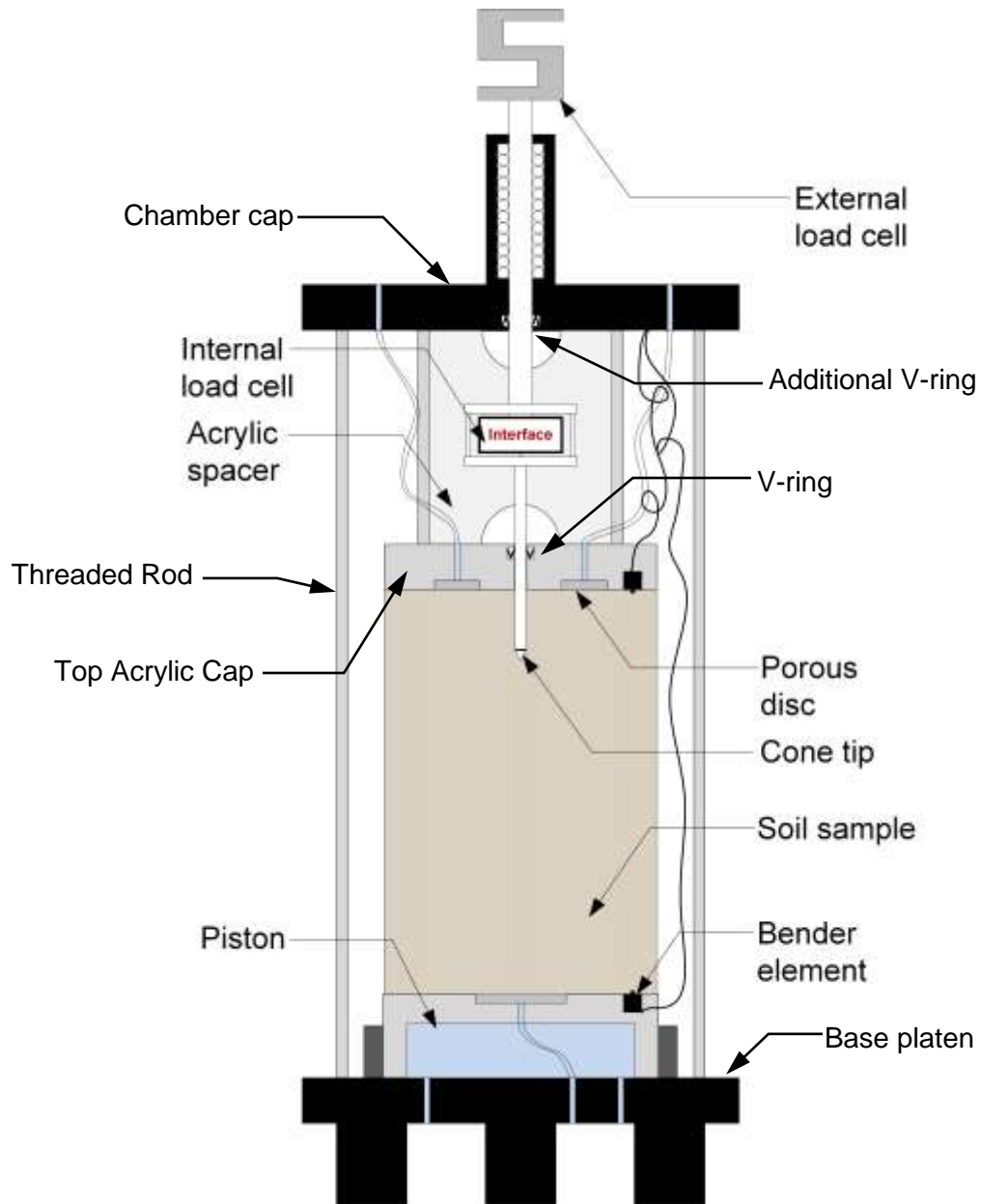


Figure 3.1: Schematics of the MCPT chamber used in this study

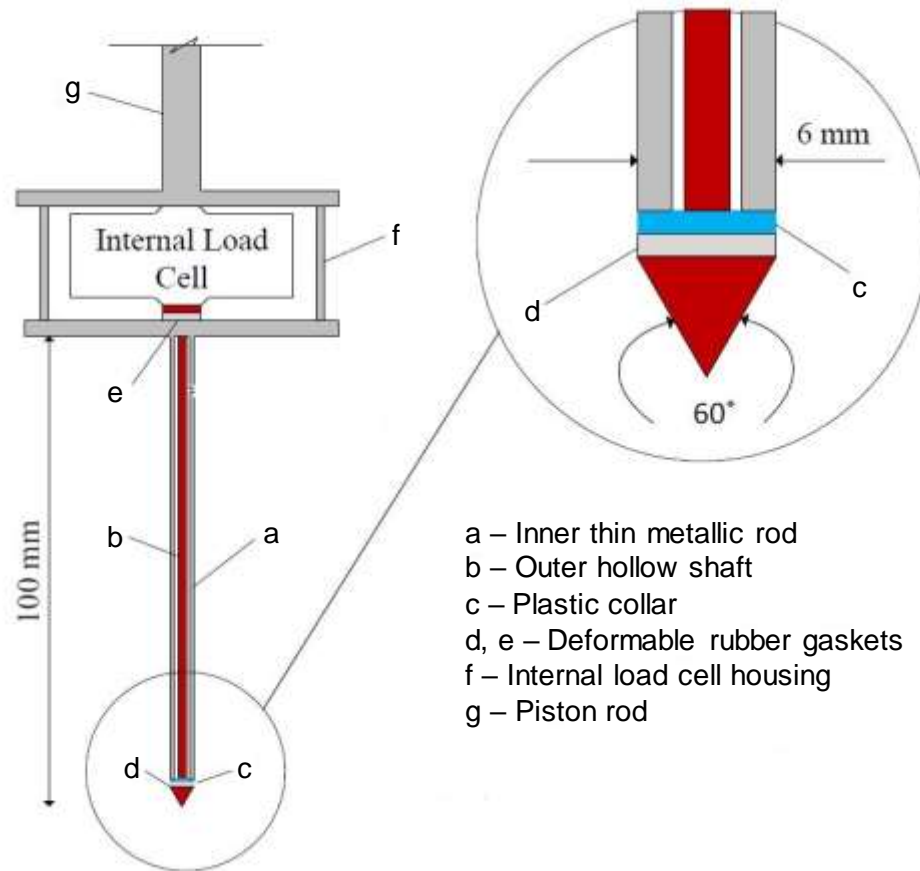


Figure 3.2: Schematics of the structure of the miniature cone penetrometer (Damavandi-Monfared and Sadrekarimi 2015)

An additional V-ring (Figure 3.1) is accommodated inside the hole of the chamber cap around the piston rod to ensure that no cell fluid leaks out during the testing process.

The triaxial load frame was used to generate an upward movement of the bottom loading platen, which in turn would lift the calibration chamber and push the piston rod against the external load cell and cone probe into the soil specimen. A rubber gasket (Figure 3.3) was inserted right above the cone tip to ensure that the stresses at the cone tip were effectively transferred to the internal load cell without being partially carried by the hollow shaft.

During the penetration of the cone into the specimen, the internal load cell directly measures the cone tip resistance, q_c which is mathematically obtained using the following Equation 3.1.

$$q_c \text{ (MPa)} = \frac{f_I \text{ (N)}}{A_c \text{ (mm}^2\text{)}} \quad (3.1)$$

Where, f_I (N) is the load recorded by the internal load cell; and A_c (mm²) is the projected area of the cone, which is 28.3 mm² for the miniature cone used in this study.

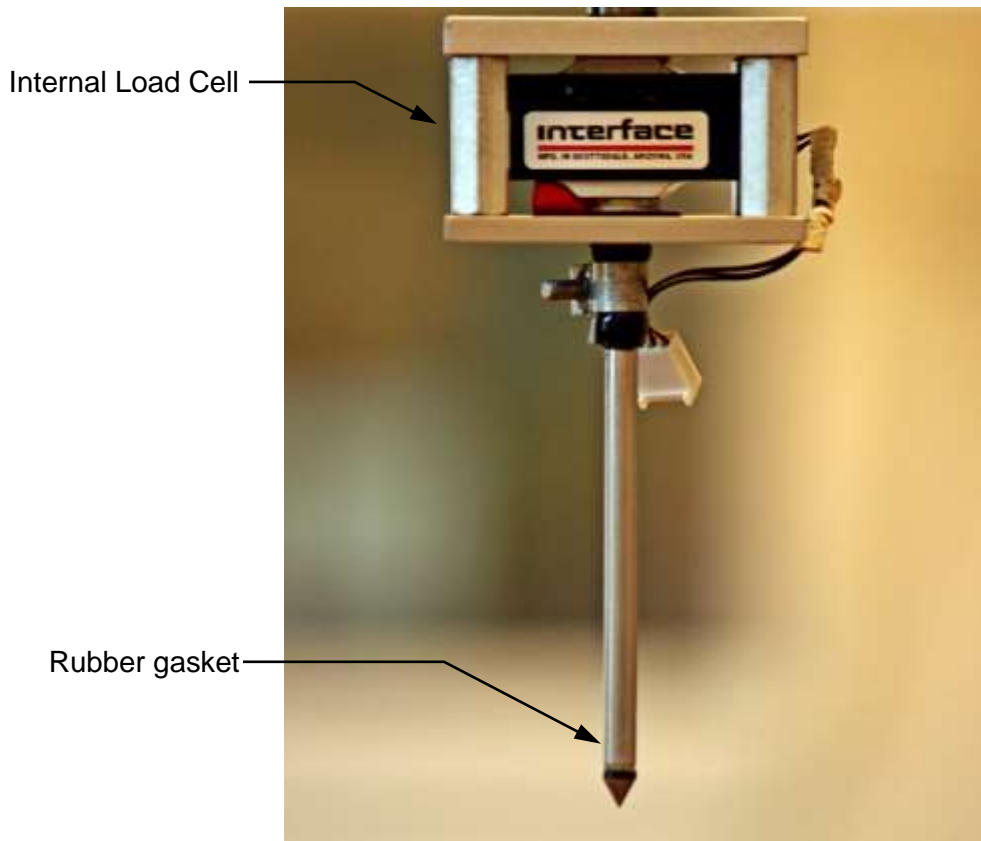


Figure 3.3: Illustration of the Internal Load Cell connected to the Miniature Cone

The external load cell (Figure 3.1), measures the total load response from the cone penetration process, which includes the cone tip resistance, the friction developed on the

sleeve of the cone penetrometer as well as the friction generated by the two rubber V-rings on the acrylic cap and the top cap of the calibration chamber. Therefore, the sleeve friction f_s is calculated according to Equation 3.2.

$$f_s \text{ (kPa)} = \frac{Q_s \text{ (kN)}}{A_s \text{ (mm}^2\text{)}} = \frac{f_E - f_I - (f_{v1} + f_{v2})}{A_s \text{ (mm}^2\text{)}} \quad (3.2)$$

where, Q_s is the frictional load response on the cone sleeve, f_E (N) and f_I (N) are the load responses on the external and the internal load cells, respectively, f_{v1} and f_{v2} are the frictional forces developed by the V-rings and A_s (mm²) is the surface area of the friction shaft.

Calibration tests by previous studies have shown that the sum of the frictional forces developed by the two V-rings, ($f_{v1} + f_{v2}$) is approximately equal to the load difference measured by the external and the internal load cells, ($f_E - f_I$) for the first 2 mm of cone penetration (Damavandi-Monfared and Sadrekarimi 2015; Jones 2017). Hence for all MCPTs, the sleeve friction values were zeroed after the first 2 mm of cone penetration.

The triaxial load frame was equipped with an encoder which recorded its travel distance automatically during the penetration. The maximum travel rate of the load frame is 0.423 mm/s which is used in this study for cone penetration. This rate of penetration is much lower than the recommended penetration rate of 20 mm/sec for an in-situ CPT test by the ASTM standard. Nevertheless, previous research has examined the effect of penetration rate on cone resistance, but no effect was recorded at least for coarse-grained soils (Dayal and Allen 1975; Abedin 1995; Eiksund and Nordal 1996; Huy et al. 2005; Damavandi-Monfared and Sadrekarimi 2015).

The University Machine Shop at Western University had fabricated the miniature cone calibration chamber which could be accommodated properly within the Sigma-1 Triaxial load frame. The calibration chamber assembly consists of a circular metallic base platen on which a finely machine-polished acrylic cell (412 mm in height and 190 mm internal diameter) and a metallic top cap is placed. The base platen and the top cap are held together tightly by three threaded rods (Figure 3.1), to ensure that the acrylic cell is tightly held in

between the two plates. Two well-greased O-rings are placed at the contacts of the acrylic cell and the two plates so that the rubber O-rings prevent leakage during the test.

During MCPTs, the acrylic cell was filled with pure silicone oil to generate cell pressure. The purpose of using silicone oil was to ensure that the electrical connections inside the chamber were safe against any electrical shortcuts during the test. A servo-controlled fluid pressure pump manufactured by Trautwein Soil Testing Company, with a pressure capacity of 1,379 kPa and a total volume of 170 mL was used in this study to generate cell fluid pressure.

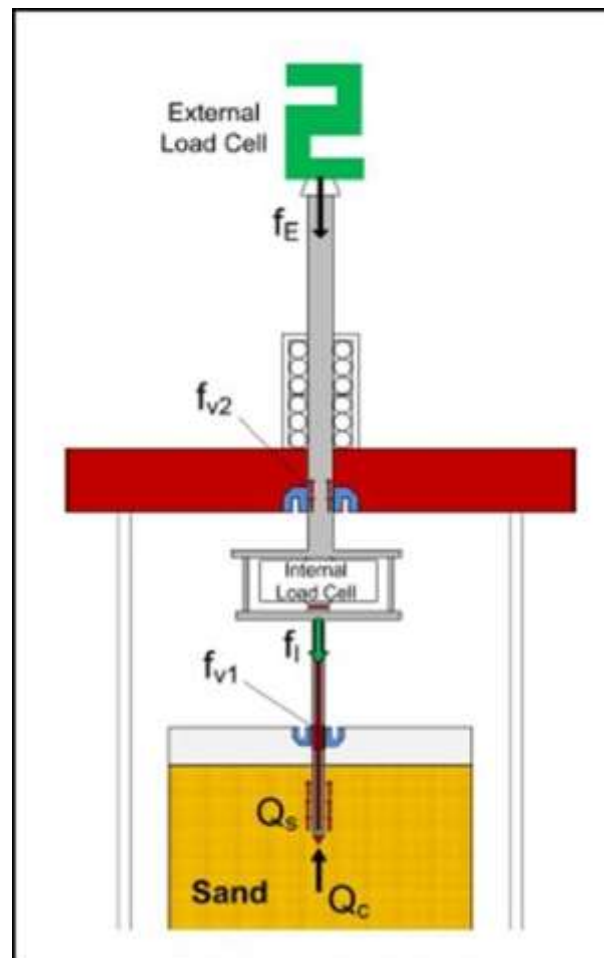


Figure 3.4: Miniature cone penetration test setup with associated forces developed during cone penetration (Damavandi-Monfared and Sadrekarimi 2015)

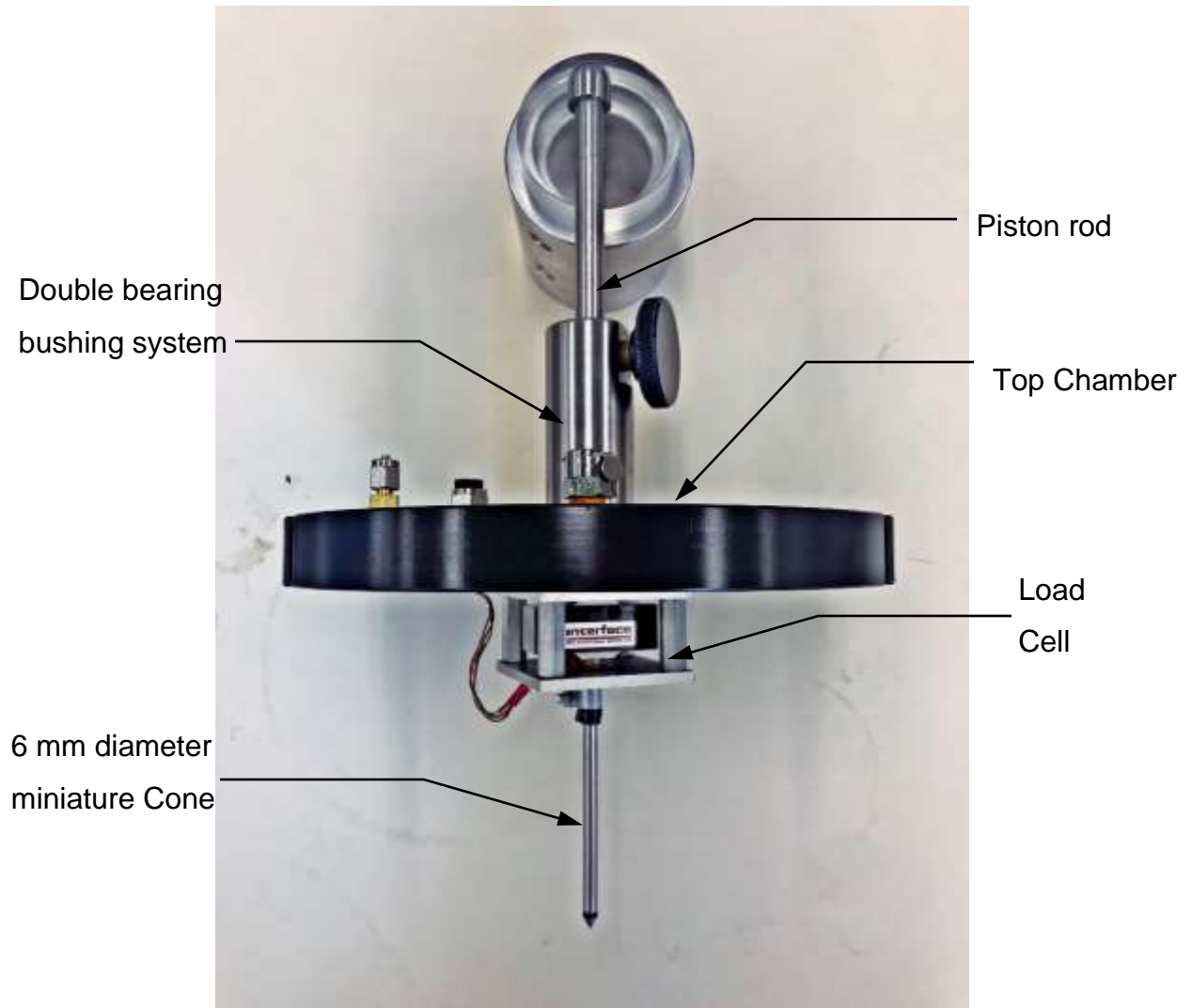


Figure 3.5: Assembly of the top chamber cap and miniature cone

On top of the base platen (Figure 3.6), a 150 mm diameter acrylic disk was placed on a hydraulic piston. The base platen is equipped with a hydraulic piston to enable the independent application of vertical stress on the specimen and develop any anisotropic consolidation states such as a K_0 stress state. K_0 represents the ratio of horizontal stress (σ'_{hc}) to that of vertical stress (σ'_{vc}) after consolidation, during which, the specimen undergoes zero lateral strain. This stress anisotropy and boundary condition are attempts to replicate an in-situ level ground stress condition.

The hydraulic piston is controlled by another fluid pressure pump like that of the cell fluid pump, mentioned above. The fluid from the pressure pump flows into the piston to generate hydraulic pressure and ultimately enables the uplift of the bottom disk situated on the piston. The metallic piston has an external ring which is screwed to the base platen and acts as the exterior wall of the piston. The bottom acrylic disk as well as the prepared soil specimen rested on the moving piece of the piston which is sealed against the stationary outer wall by a series of O-rings which run all along the circumference of the moving piece to prevent leakage of cell fluid into the piston cavity or vice-versa. Hence, the fluid pressure inside the cavity must overcome the friction developed by the O-rings, the imposed weight of the specimen and the cell fluid pressure, to enable uplift of the piston relative to the calibration chamber. From several calibration tests, the frictional force developed inside the piston cavity was found to be around 19.5 – 20 kPa.

The metallic base platen was equipped with 6 pressure line connections to control drainage, pore water pressure, cell pressure and piston pressure. An illustrative description of the bottom acrylic disk and the various components of the base platen is presented in Figure 3.6.

A 50 mm in diameter porous disc was embedded into the bottom acrylic disk to provide drainage for the specimen. A servo-controlled pressure pump with a volume of 75 mL was used to generate and measure pore water pressure inside the specimen through the drainage lines shown in Figure 3.6.

A 0.5 mm thick latex rubber membrane held in place by multiple O-rings around the bottom disk, surrounded the specimen, therefore creating a flexible boundary. The membrane was long enough to enclose the entire height of the specimen as well as the bottom and top acrylic caps. The top acrylic cap was specially designed for the top of the specimen, which has a central hole (Figure 3.7) for the passage of the cone penetrometer. As discussed earlier, a V-ring was installed inside this hole which sealed the contact circumference between the cone probe and the top cap to maintain differential pressure between the cell fluid and the pore water.

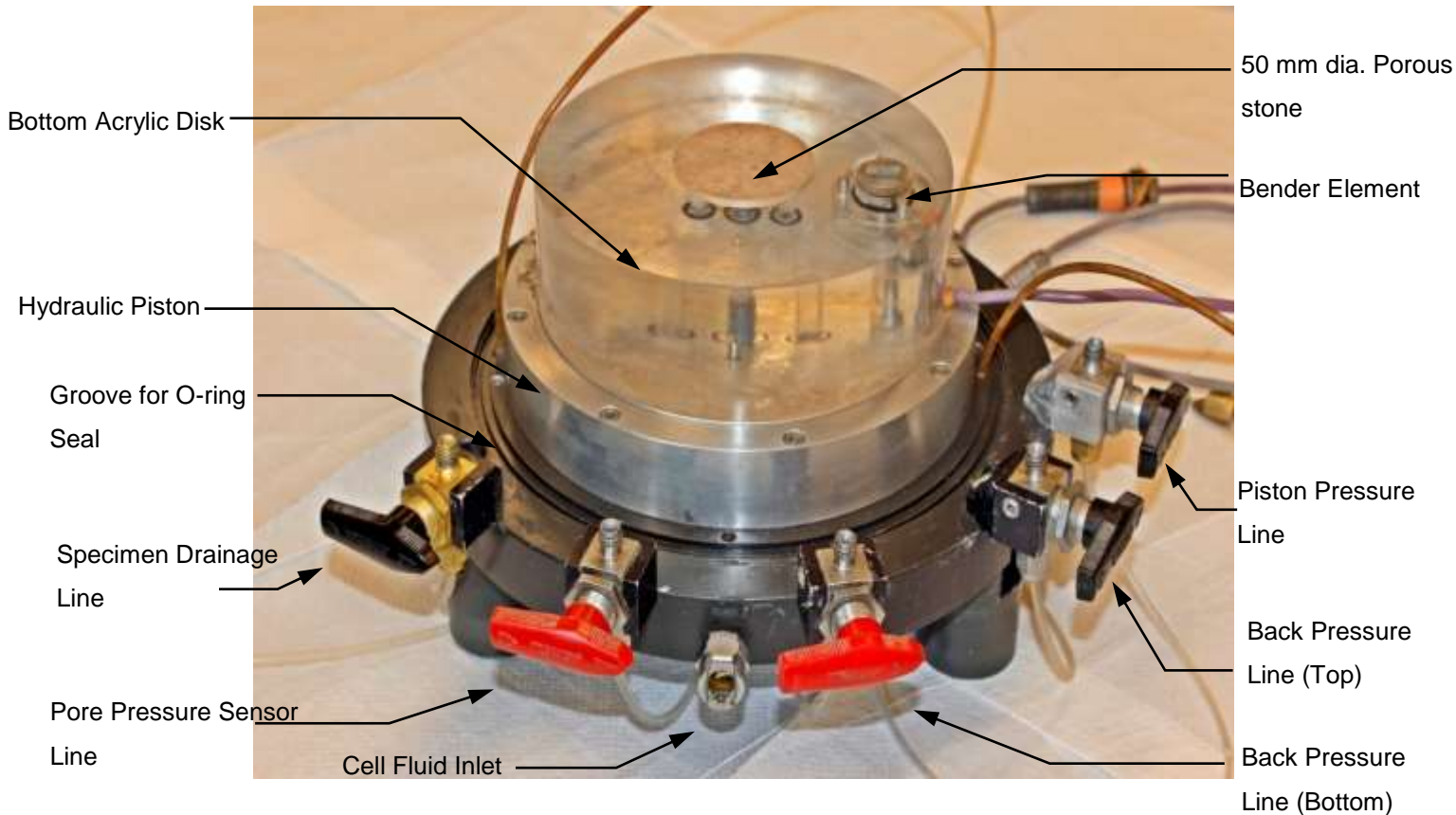


Figure 3.6: Image of the base platen and its components

As shown in Figure 3.7, two 50 mm in diameter porous stones were installed in the inner (bottom) surface of the top acrylic disk on either side of the hole, to connect the specimen to drainage lines. The two porous stone were again internally connected so that the distribution of pore water pressure throughout the specimen is uniform. Similar to the bottom disk, the top cap was also secured by two O-rings to seal the latex membrane tightly against the top cap.

A split cylindrical hollow acrylic spacer (Figure 3.8) was placed on top of the specimen, resting on the top acrylic cap inside the calibration chamber. The spacer was built in a way to allow accessibility for the drainage lines around it and other wires that connected to the internal load cell. The purpose of this spacer was to provide axial reaction force to the specimen. Initially, at the beginning of the test, a small gap existed between the top of the acrylic spacer and the top metallic cap of the calibration chamber. As the pressure inside

the piston cavity increased and upward movement of the specimen was initiated, the gap started to close. Ultimately, at some point, the acrylic spacer came in contact with the top cap of the chamber. This phenomenon is called “docking” in this study, as the spacer was then docked to the roof of the chamber. Hence, during anisotropic consolidation, further pressure from the piston cavity would axially compress the specimen generating a vertical stress.

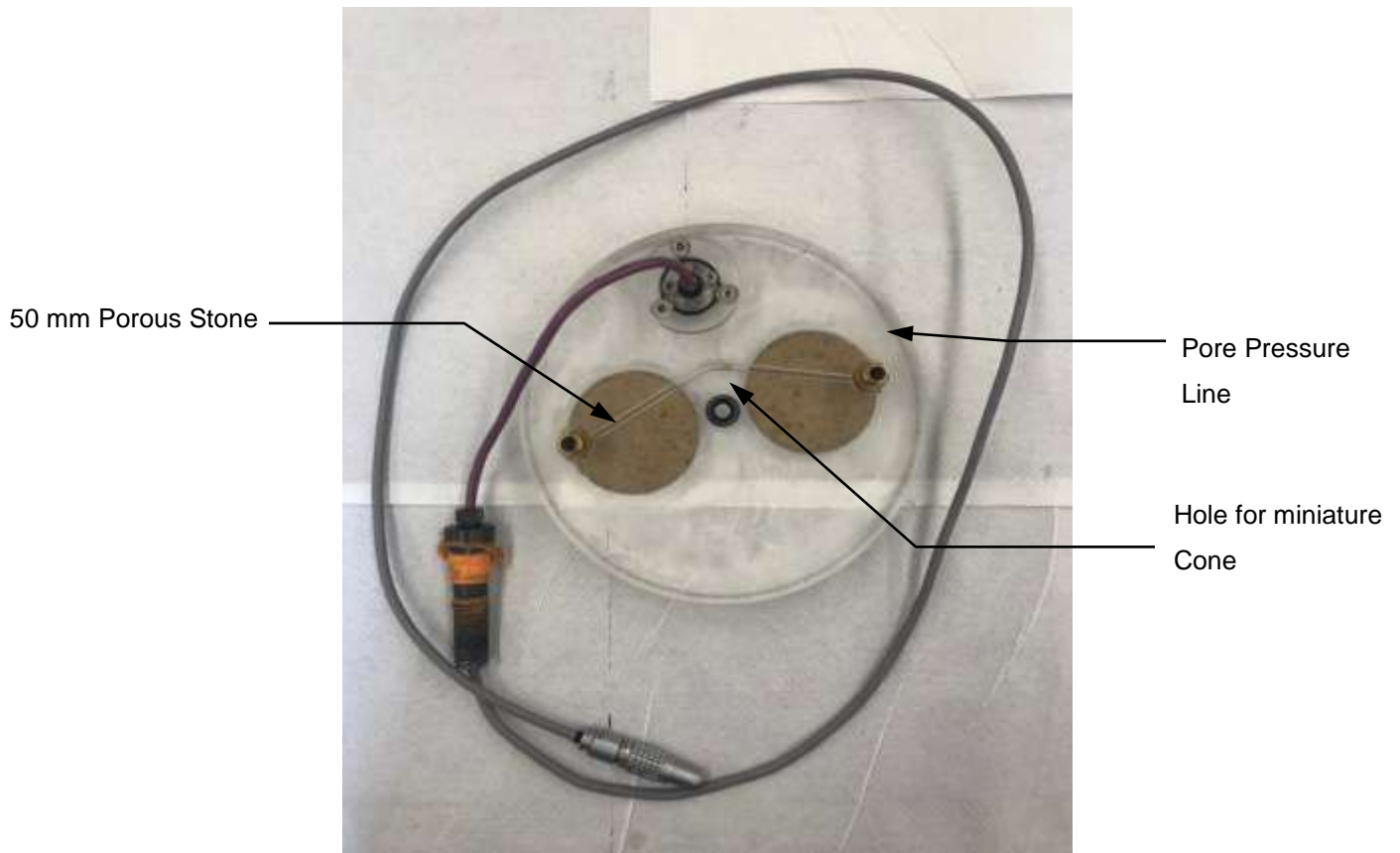


Figure 3.7: Image of the top acrylic disk and its components



Figure 3.8: Image showing the acrylic spacers used to initiate K_0 consolidation

A series of illustrations are hereby presented in this section for the reader to have a holistic visual understanding of the MCPT chamber at different stages.



Figure 3.9: Illustration showing a specimen after preparation



Figure 3.10: Central hole for cone penetrometer on the top cap



Figure 3.11: Fully set-up MCPT chamber during a test

3.3 Tested Material

Reconstituted specimens of a local silica sand were prepared and tested in this experimental program. This sand is labeled as “Boler Sand” in this study as it was collected from the Boler Mountain in London, Ontario. The natural Boler sand contains about 11% fine particles (Mirbaha 2017). However, for the experiments of this study, the segregated particles of Boler sand were re-graded to match the gradation of Fraser River sand, following the ASTM Standard procedure D6913M-17 (2017). The Fraser River sand collected by GeoPacific Consultants Ltd., from a site near the north arm of Fraser River in Richmond, B.C., had shown a fines content of approximately less than 1% (Jones 2017). Hence, to focus on the behaviour of a clean sand, the Boler sand was graded according to Fraser River sand. Figure 3.14 presents the particle size distribution curves for natural Boler sand, re-graded Boler sand and the reference Fraser River sand.



Figure 3.12: Sample image of the physical appearance of Boler Sand



Figure 3.13: A closer look at the Boler sand particles

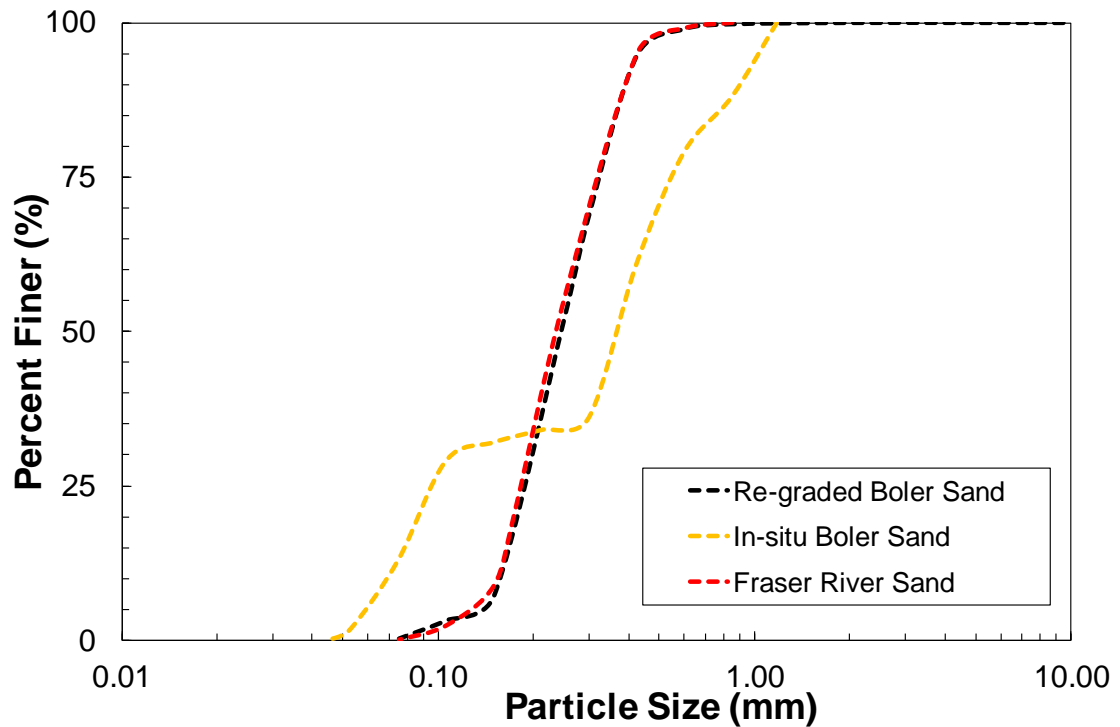


Figure 3.14: Particle Size Distribution of Boler Sand re-graded as Fraser River Sand

A specific gravity (G_s) of 2.67, maximum (e_{max}) and minimum (e_{min}) void ratios of respectively 0.845 and 0.525 were measured following ASTM Standard procedures (ASTM D854-14 2014; ASTM D4253-16 2016; ASTM D4254-16 2016). According to the

Unified Soil Classification System (USCS), the regraded Boler sand is classified as a poorly-graded sand (SP). Scanning Electron Microscopic images and X-Ray Diffraction analyses were carried out previously by Mirbaha (2017) to determine particle shapes and mineralogy of the sand. These tests show that Boler sand is primarily composed of quartz (SiO_2) minerals with sub-angular to angular particle shapes. An acid dissolution method was carried out to determine the carbonate content of the tested sand material. 50 gm of sand was soaked in 200 mL of hydrochloric acid for 24 hours. Tests were performed using both concentrated HCL, and 1N HCL. Overall, a carbonate content of 13% was determined at the end of the tests. Because of the high silica content, this sand is named as a silica sand in this study. Figure 3.15 presents the X-ray diffraction results for the test material.

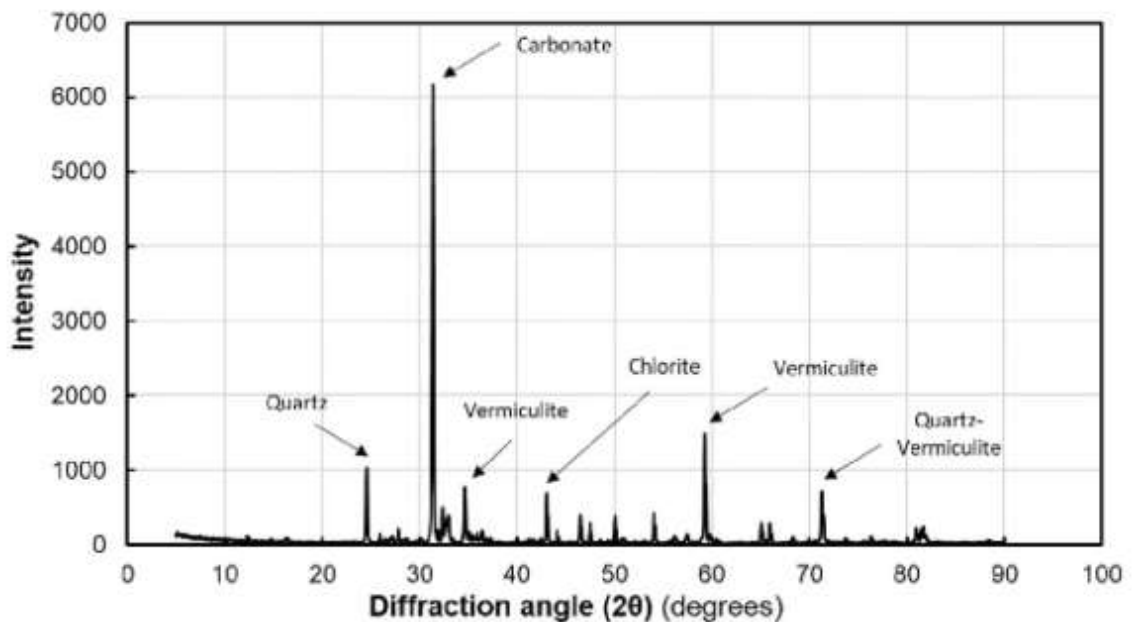


Figure 3.15: X-Ray Diffraction analysis of Boler Sand (Mirbaha 2017)

3.4 Mechanism of the Miniature Cone Penetration Test

3.4.1 Specimen Preparation

All specimens prepared in this study had a height of 190 mm and a diameter of 150.2 mm excluding the 0.5 mm thickness of the latex membrane. The thickness of the membrane conforms to the ASTM Standards for triaxial shear tests ASTM D7181-11 (2011) to provide minimum restraint to the specimen. The latex membrane was secured around the top and bottom acrylic disks with multiple O-rings to provide an effective seal and completely confine the soil specimen within the membrane. Before the preparation of the specimen, an aluminium split mold with a porous strip running along its internal mid-section was installed around the latex membrane. The mold was connected externally by two hose pipes to a suction line. The excess length of the latex membrane above the mold was stretched and flipped over the mold. As the suction was turned on, a vacuum was generated through the porous strip which pulled the membrane tightly towards the inner walls of the mold. This mechanism ensured a cylindrically uniform specimen shape. Figure 3.16 presents the illustration of the split steel mold which was used to prepare the specimens of this study. Boler sand specimens tested in this study were prepared by the process of under-compaction as suggested by Ladd (1978) in order to achieve a uniform density throughout the specimen. This method involves preparation of the specimen in layers of predetermined volume and relative density using a tamping mechanism. The under-compaction method accounts for the increased density of the lower layers by compaction of the upper layers of the soil. Therefore, in this technique the lower layers were tamped to a lesser density than the target global density of the specimen, whereas the upper layers were tamped using a higher a relative density, so that the ultimate global density of the specimen was uniform. The amount of density change was calculated prior to tamping each sublayer. The difference in density of the successive layers is called “under-compaction ratio” (Ladd 1978). Boler sand was initially wetted by 5% moisture content (distilled water) which was adequate for moist tamping (Park 1999). This ensured that a suction was generated within the soil matrix that would hold the specimen in-place

during setting up of the calibration chamber, until a certain magnitude of effective seating stress was applied by the surrounding cell fluid.

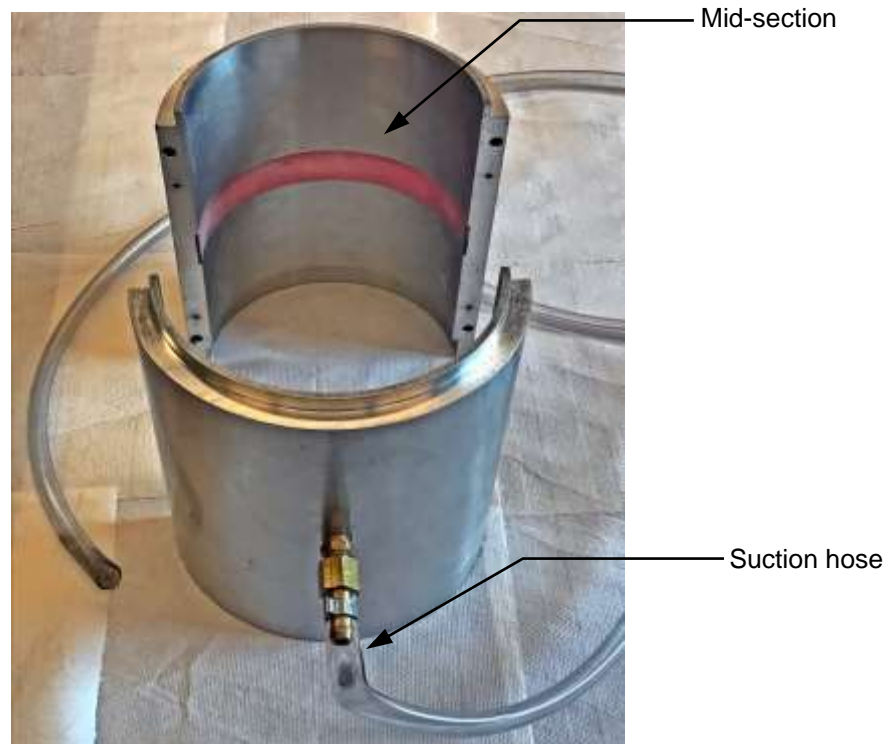


Figure 3.16: Aluminium split mold used in this study for specimen preparation

The required amount of soil for each layer was calculated using an under-compaction ratio of 10%. The soil mixed with 5% moisture was placed into the steel mold and tamped in 10 layers, each layer being 1.9 cm thick. Subsequently, the height of each layer was manually checked after tamping using a ruler. The diameter and height of each specimen were carefully measured after preparation to achieve an accurate initial void ratio (e_i) and relative density (D_{ri}). Specimens were prepared to three different categories of consolidation relative densities (D_{rc}), the average values of which were 27.2% (loose), 46.7% (medium dense) and 64.6% (dense). In order to achieve these post-consolidation relative densities, the specimens were prepared slightly looser to account for densification of the specimens

during consolidation. An illustration of the pre- and post- sample preparation stages are represented in Figure 3.17.



Figure 3.17: Assembled split mold before (left) and after (right) specimen preparation

Specimen uniformity was also evaluated while preparing the samples for MCPT. This was done by placing three aluminium containers at three different heights along the specimen. With these containers in place, a standard specimen was prepared. After the sample was prepared, the aluminium containers were carefully excavated out from the three different layers. The undisturbed containers were kept inside the oven for 24 hours which enabled us to measure the volume of sands present in each container. After taking necessary measurements, the containers were filled with distilled, de-aired water to evaluate the total volume of the containers. Therefore, void ratio was calculated for each container and a

± 0.005 standard deviation was determined, corresponding to a relative density deviation of $\pm 0.42\%$ from top to bottom of a specimen prepared at loose condition, $D_{ri} = 20\%$.

After the specimen was prepared, the sample was transported on to the load frame. The suction around the latex membrane was turned off and the split mold was carefully removed. The acrylic cell was placed around the specimen on a properly greased O-ring. The miniature cone assembly with the metallic top chamber cap was connected to the external load cell through a steel piston rod. The rod exited the calibration chamber through a double bearing bushing system, which allowed a free vertical movement during penetration. Therefore, after preparing the specimen and assembling the cell, the tip of the cone rested just above the specimen leaving a slight gap. However, the height of the specimen ensured that the cone shaft was well within the hole in the top acrylic cap and was securely sealed by the V-ring. Finally, the cylindrical cell was filled with dyed silicone oil, through which the specimen was subjected to confining pressure. The entire assembly after being set-up is represented in Figure 3.11. The non-conductive property of silicone oil makes it a suitable fluid to be used as the cell fluid to protect the internal load cell and other electrical connections against electrical short circuits.

3.4.2 Seating, Docking, Flushing and Saturation

After the entire chamber was assembled and the cell was filled with dyed silicone oil, a seating pressure of 15 kPa was applied to maintain the specimen shape and volume during the subsequent stages of docking, flushing and saturation. The seating pressure was ramped to 15 kPa in 15 mins to ensure that a gradual pressure build up and minimize sample disturbance.

Soon after the seating pressure reached its target value, water was pumped into the piston cavity below the specimen, to initiate uplift of the piston. This was done using a specific constant pressure function as the piston had to overcome the imposed forces by the cell fluid pressure, weight of the specimen, and the frictional forces developed by the O-rings inside the piston. These forces were approximately equal to 40 kPa in piston cavity

pressure. The upward movement began as soon as the piston pressure overcame the imposed forces. This movement could be visually confirmed as beyond a certain magnitude of pressure, the piston started to move upwards. The entire process was closely monitored to properly identify the point of docking and prevent any form of unwanted axial stress on the specimen. The point at which the acrylic spacers on top of the specimen contacted the top of the chamber can also be determined graphically. Initially, as the pressure was applied, the pressure inside the piston and the flow rate of the fluid entering the piston increased. The pressure increased to counteract the applied external forces. However, as soon as uplift initiated, the piston pressure as well as the flow rate became constant, as there was no restraint against the movement of the specimen. At the instance of contact between the acrylic spacer and the chamber cap, the rate of water entering the piston cavity suddenly dropped and the pressure started increasing to the target constant pressure set initially. The pressure increased as the upward movement of the piston was hindered by the chamber cap. Hence, the point at which these two parameters started changing, is used as the precise point of docking. Any further movement resulted in the development of an axial stress on the sample and the corresponding volume change. Figures 3.19 and 3.20 present the point of docking graphically.

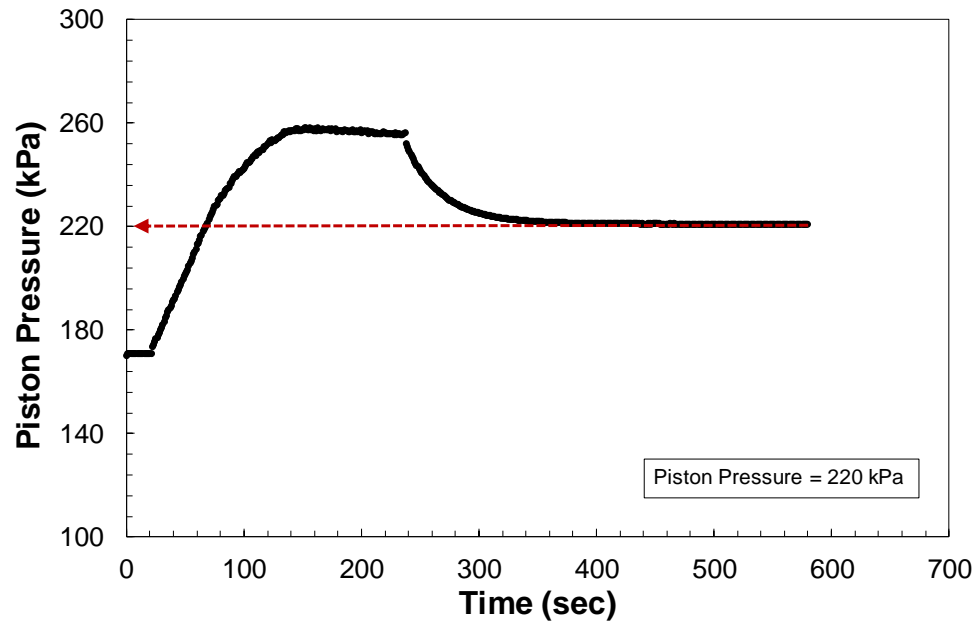


Figure 3.18: Calibration test to determine frictional resistance

The frictional forces developed by the series of O-rings along the inner circumference of the piston, the pressure by the cell fluid, and the weight of the specimen contribute to the total force that had to be counteracted by the piston to initiate uplift. A series of calibration tests were previously performed by Jones (2017) and the total resistance was found to be about 19.5 kPa equivalent piston pressure. It is imperative that this frictional force is accounted for, during the consolidation of the specimen.

In this study as well, calibrations tests were performed to verify the magnitude of this frictional resistance. This was done by assembling the triaxial cell without a specimen. The acrylic cell was filled with water and pressurized to a constant pressure of 200 kPa. The piston cavity which had been fully saturated prior to the test, was pressurized to overcome the 200 kPa pressure by the cell fluid. After a certain amount of piston pressure, uplift of the piston was visible. The piston pressure was allowed to stabilize at 220 kPa. The excess 20 kPa pressure in the piston compared to the cell fluid pressure was taken as the frictional resistance developed in the piston. Figure 3.18 shows a graphical presentation of the pressure variation inside the piston during one of the calibration tests.

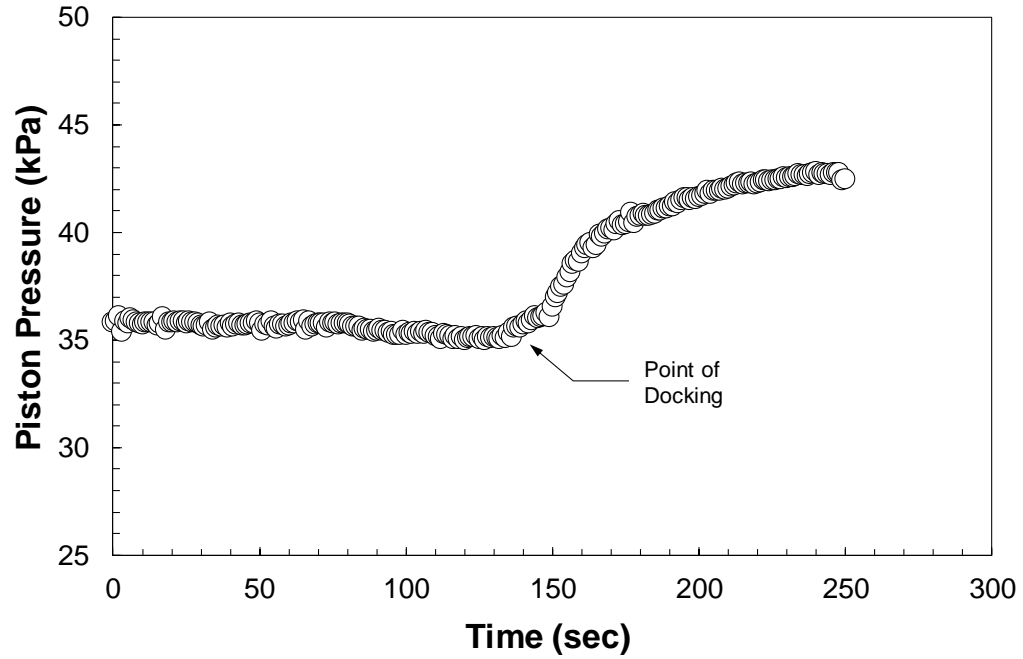


Figure 3.19: Increase in piston pressure at the point of docking

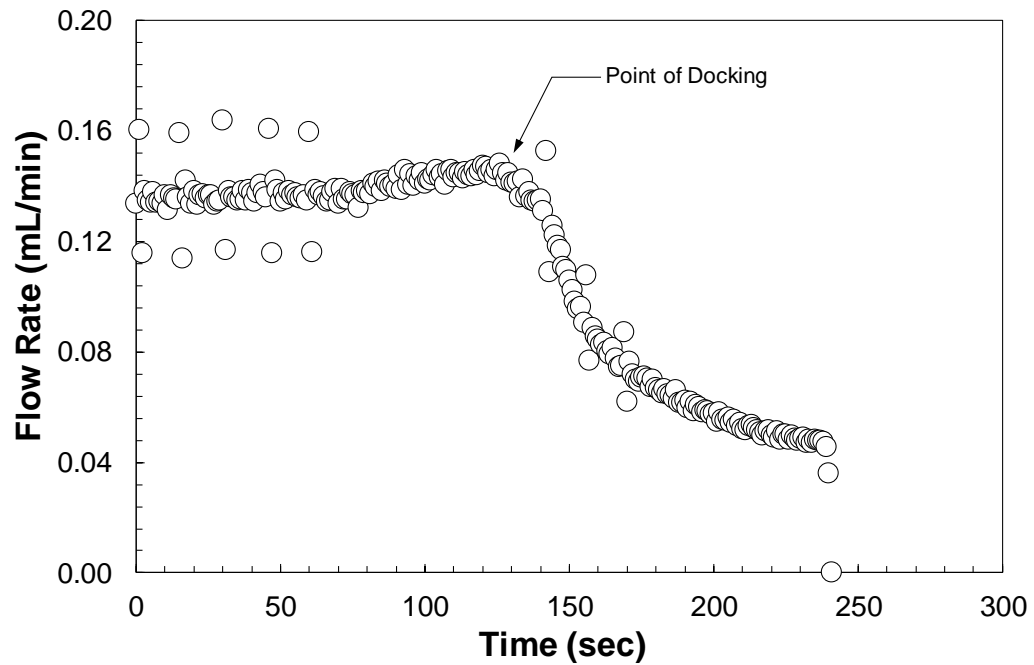


Figure 3.20: Decrease in the rate of water flow into the piston at the point of docking

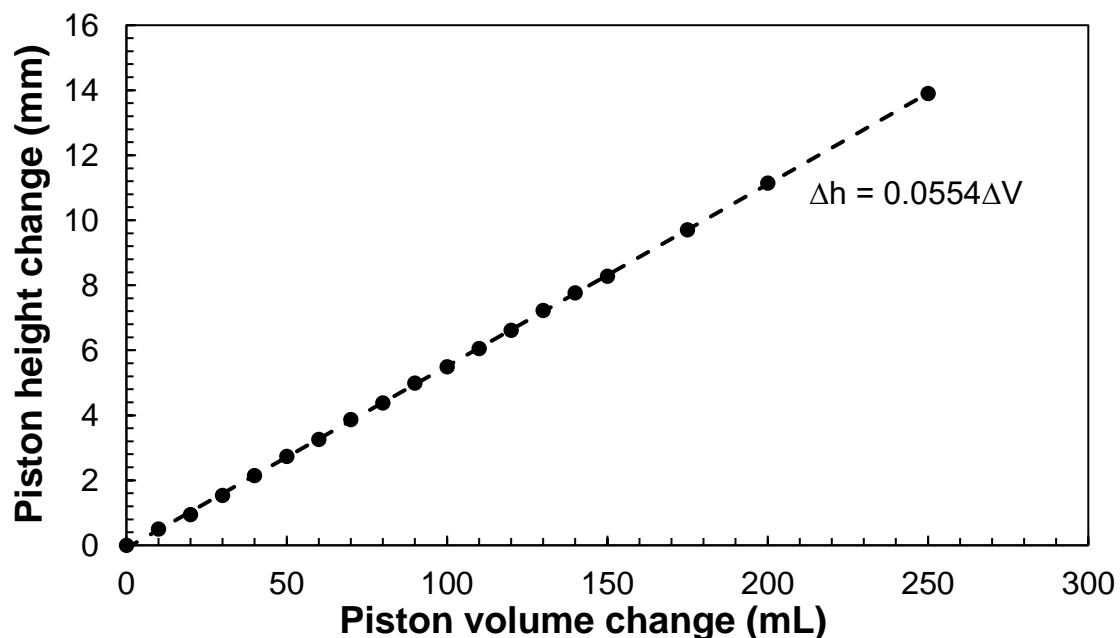


Figure 3.21: Test on uplift calibration (Jones 2017)

After docking, the specimens were flushed with carbon dioxide (CO₂) for about 45 minutes. Carbon dioxide being denser than air and highly soluble in water is an ideal gas to replace air in the sample. Subsequently, the specimens were flushed with distilled and de-aired water to achieve a high degree of saturation. Flushing was terminated once no air bubbles were seen exiting the drainage lines and the pore water pressure inside the specimen stabilized. During these stages, a constant cell pressure was maintained and any changes in cell volume were used to calculate specimen volume change during saturation.

As soon as flushing was completed, the cell pressure and back pressure were simultaneously ramped to a high pressure (~ 500 kPa) to achieve a pore pressure parameter (i.e., B value) of at least 0.96. This ensured that the specimens were properly saturated. The change in volume of the back pressure pump was monitored during this stage to determine specimen volume change.

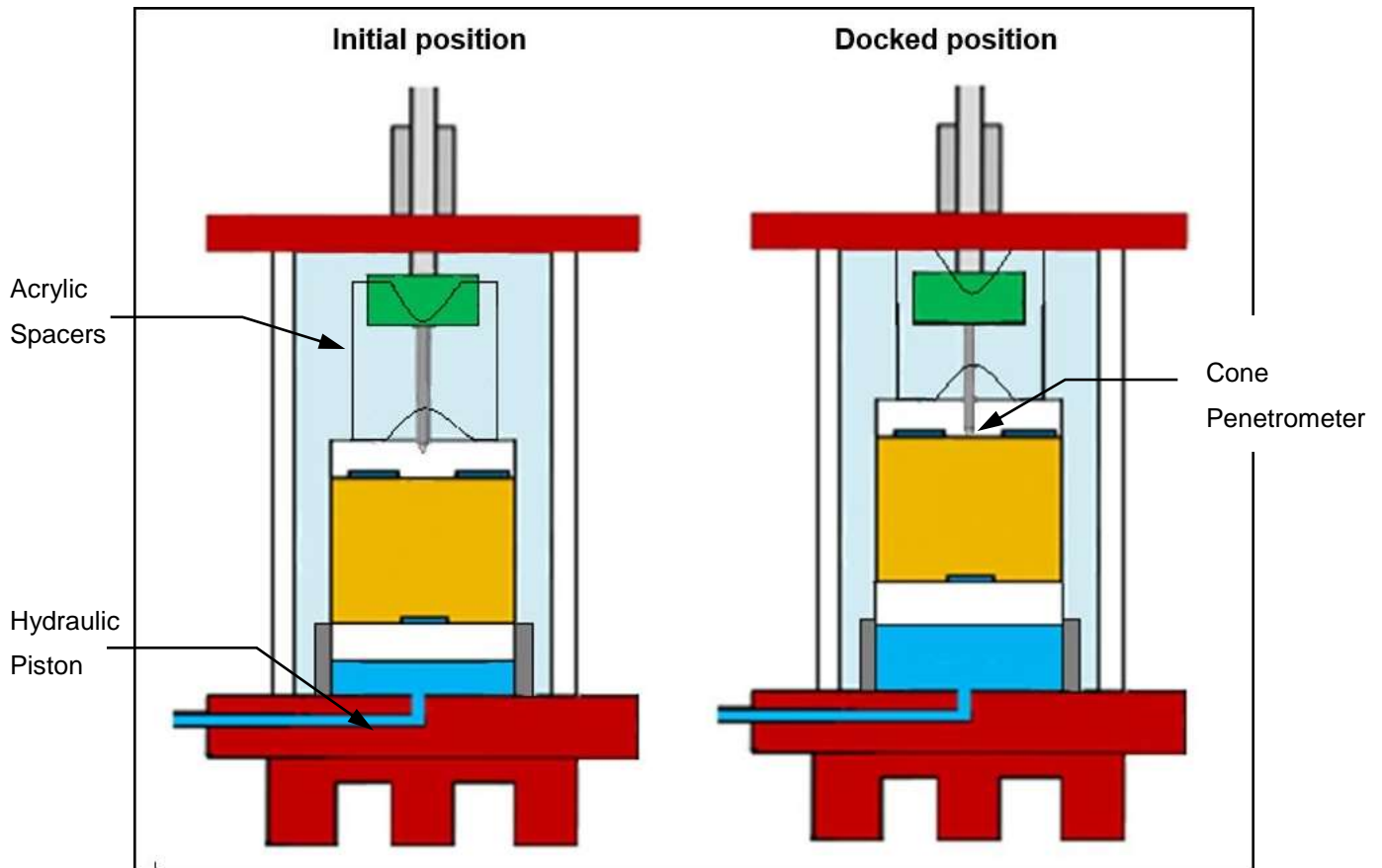


Figure 3.22: Illustration of the docking mechanism (Jones 2017)

3.4.3 K_0 Consolidation

Many research works have been carried out in the past to modify commonly used laboratory apparatuses to achieve a K_0 consolidation state. These involve K_0 -triaxial tests (Feda 1984; Eliadorani 2000) and even calibration chambers as discussed earlier (Hsu and Lu 2008; Kumar and Raju 2009).

The current study used a novel approach to induce a K_0 consolidation state through the installation of the hydraulic piston beneath the specimen. This modification was done by Jones (2017). Consolidation was carried out using a volume-control mode by extracting a certain volume of water from the specimen and simultaneously subjecting it to a specific axial deformation using the hydraulic piston. During this process, the cell pressure was

maintained at the constant value which was achieved at the end of back pressure saturation. Under such conditions equal volumetric, ε_v and axial, ε_a strains were maintained throughout the process, thus mimicking a K_0 boundary condition as described below:

$$\varepsilon_v = 2\varepsilon_r + \varepsilon_a \quad (3.3)$$

$$\text{If } \varepsilon_r = 0, \varepsilon_v = \varepsilon_a$$

Where ε_r , ε_a , and ε_v are the lateral, axial, and total volumetric strains applied to the specimen respectively during consolidation. A graphical presentation of the process in one of the experiments is shown as an example in Figure 3.23.

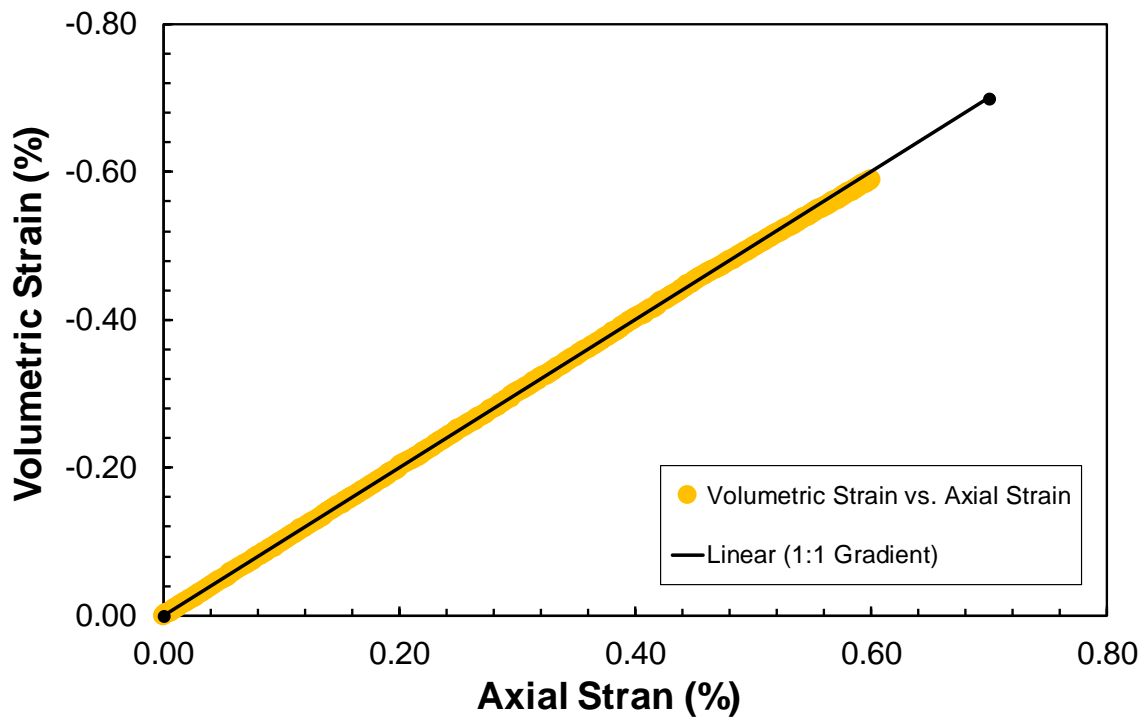


Figure 3.23: Volumetric strain versus axial strain during consolidation in Test CPT-65-4

This process of consolidating the specimen also meant that, instead of targeting a specific effective stress, a specific void ratio was being targeted. Both volume control functions were continued until a desired void ratio was reached. Consolidation occurred as the specimen's pore water pressure decreased and the piston pressure increased with respect to a constant cell pressure. Based on the respective changes in the volume of the pore pressure and the piston pressure pumps, volume and height changes of the specimen were calculated. The predetermined change of volume that was required to reach a certain void ratio was calculated by the following equations:

$$\Delta V_{pore} = \frac{e_i - e_c}{1 + e_i} (V_{sp}) \quad (3.4)$$

$$\Delta V_{piston} = \frac{e_i - e_c}{1 + e_i} (18.051)(h) \quad (3.5)$$

Where, ΔV_{pore} and ΔV_{piston} are changes in the pore pump volume and piston pump volume respectively, e_i is the initial void ratio, V_{sp} is the specimen volume, h is the specimen height, and 18.051 is the calibration factor for determining the specimen's height change (Jones 2017). After an initial adjustment phase, K_0 slowly approached a certain constant value as the target consolidation pressure was reached. This constant magnitude of K_0 represents the stress state of the specimen prior to the cone penetration stage. Figure 3.24 presents the development of effective stresses in a typical MCPT experiment.

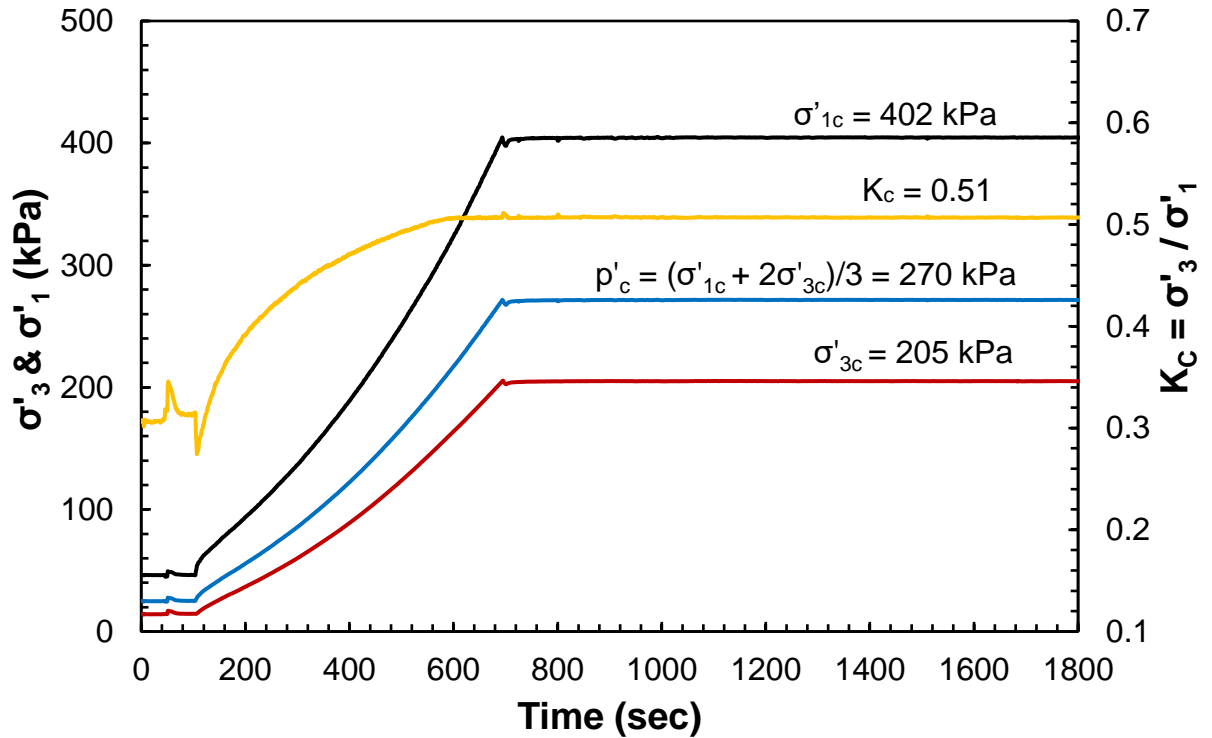


Figure 3.24: Development of effective stresses and K_0 state during the consolidation stage of Test CPT-65-4

Figures 3.25 and 3.26 present variations of fluid pressure in the piston, the cell and the specimen as well as the corresponding specimen volume change during the consolidation stage in one of the MCPT experiments.

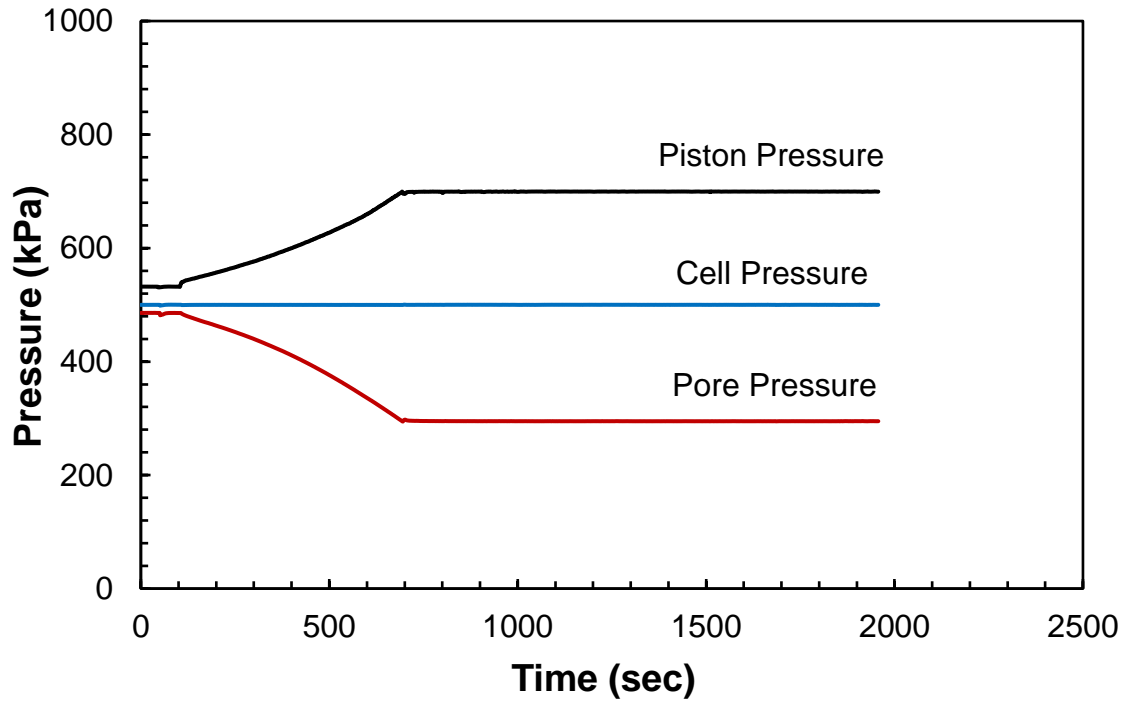


Figure 3.25: Variation of pressures during a sample consolidation stage

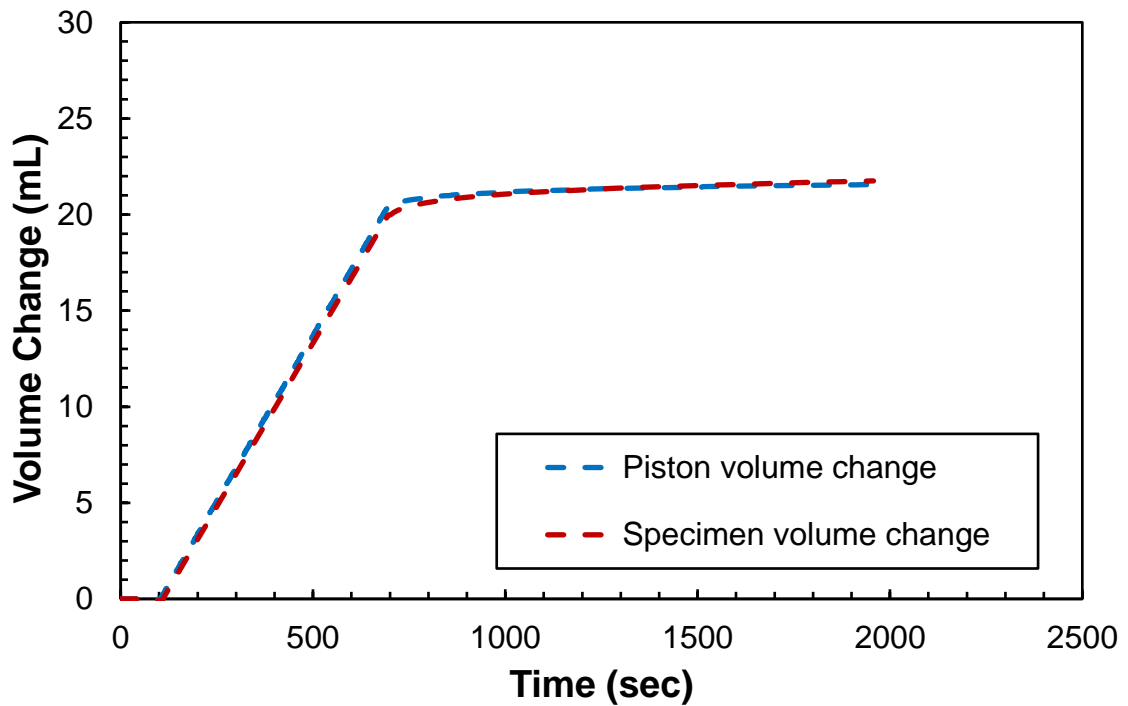


Figure 3.26: Piston and specimen volume changes during a sample consolidation stage

3.4.4 Cone Penetration

After the specimen was anisotropically consolidated to the desired stress level, the miniature cone was pushed in to the soil mass. The cone was penetrated at a rate of 25.38 mm/min, which is the maximum rate of the Sigma-1 loading frame used in this study. The depth of penetration was up to 60 mm in all tests and the specimens were allowed to drain to replicate an in-situ condition.

3.5 Factors Affecting MCPT Calibration Chamber

Since the introduction of miniature cone calibration chambers in modern research, there have been several factors that often challenge the potency of the results obtained from these tests. The effects of scaling, boundary condition, and rate, which are the most important factors affecting the results of reduced-scale cone penetration tests, are discussed in the following paragraphs.

3.5.1 Scale Effect

When a standard cone penetrometer is used for in-situ testing, the size of each individual particle and therefore, their individualistic effect on the cone tip resistance is insignificant. The resistance generated in such a scenario is a result of the soil mass acting as a unit. However, in a reduced-scale cone, since the cone tip is scaled down significantly, each particle of sand might have an appreciable contribution on the tip resistance. Several researchers have therefore studied the consequence of scale effect to better understand the results of scaled CPT experiments. The scale effect is quantified based on the ratio of cone diameter (d_c) to the average grain diameter (d_{50}) of a soil being tested. The cone penetrometer used in this study had a diameter of 6 mm and the d_{50} of the re-graded Boler sand is 0.24 mm, which correspond to a d_c/d_{50} ratio of 25. Gui (1998) carried out several tests on dense Leighton Buzzard sand. Three different particle gradations were chosen in their study, including fine ($d_{50} = 0.225$), medium ($d_{50} = 0.4$ mm) and coarse ($d_{50} = 0.9$ mm) sands. Three different miniature cones were also used with diameters of 19.05 mm, 10 mm,

and 6.35 mm. These dimensions allowed a d_c/d_{50} range of 7 to 85. Gui (1998) found no scale effect in the fine sand, some scale effect in the medium sand when $d_c/d_{50} < 20$, and the largest scale effect for the coarse sand with $d_c/d_{50} < 7$. Balachowski (2007) studied scale effect on dense Hostun sand using medium ($d_{50} = 0.32$ mm) and coarse ($d_{50} = 0.7$ mm) gradations with a cone diameter of 12 mm. This provided d_c/d_{50} ratios of 17.1 and 37.5. This study too, showed a noticeable scale effect only at $d_c/d_{50} < 20$. Sharp et al. (2010) performed miniature cone penetration tests on Nevada sand in a centrifuge physical models using sands with d_c/d_{50} ratios ranging from 30.7 to 92.3. They also found no evidence of scale effect for any of the ratios tested. More recently, Wu and Ladjal (2014) performed scale effect studies on a sand with $d_{50} = 0.9$ mm using 5 miniature cone penetrometers ranging in diameters from 0.5 to 2 mm. The primary goal of their study was to examine the dependence of cone tip resistance on penetrometer size for both loose and dense sands. It was found that changes in penetration resistance based on penetrometer size reached a limiting value for cone diameters greater than 5 times d_{50} of a sand. Since the d_c/d_{50} of 25 falls above the recorded limitations highlighted by the previous researchers, it is assumed that the scale effect was also negligible in the experiments of this study.

3.5.2 Penetration Rate Effect

According to the ASTM 5778-2012 (2012), the rate of penetration for an in-situ CPT test is 20 mm/sec. However, the triaxial load frame used in this study was limited to a maximum displacement rate of 0.423 mm/sec, which is about 50 times slower than that prescribed by the ASTM standard. Nevertheless, previous research has examined the effect of penetration rate on cone resistance, but no effect is found at least for clean sands. For example, Dayal and Allen (1975) studied the effect of penetration rate on clay and sand samples using a 10 cm² sized cone (standard size) at penetration rates ranging from 1.3 to 81.14 mm/s. No evidence of penetration rate effect was observed on the overall cone tip resistance in the sand samples tested. However, they observed that the cone tip resistance measurements in soft clays was over 6 times higher for a penetration rate of 139 mm/s compared to that with a penetration rate of 1.3 mm/s. The effect of penetration rate is generally more pronounced in fine-grained soils as the rate of penetration affects the excess pore water pressure

generation measured at the cone shoulder and increasing penetration rate produces a higher cone tip and sleeve frictional resistances. Abedin (1995) carried out MCPT experiments at penetration rates of 7.5 mm/s and 42.5 mm/s on a sandy clay loam using a 16 mm diameter penetrometer. The effect of penetration rate was found to be negligible for these tests. Damavandi-Monfared and Sadrekarimi (2015) performed 2 MCPTs on an Ottawa sand with similar relative densities and effective pressures but at two different penetration rates of 0.423 mm/s and 0.0846 mm/s, respectively. The effect of cone penetration rate for these tests was found to be insignificant. Eiksund and Nordal (1996) explored penetration rate in pile load tests in sand for incremental rates from 0.8 mm/s to 1100 mm/s. While a pile differs from a cone penetrometer in both geometry and use, the resistance mechanisms experienced at the base and along the shaft during penetration are comparable. The tests found the impacts of penetration rate to be unimportant. Huy et al. (2005) carried out pile loading tests in unsaturated sand in a calibration chamber, using a CPT cone as a model pile. Model ground was prepared by the cycle of fluidization, vibration and drainage. The loading tests consisted of four stages: constant rate test of 2 cm/s, constant rate test of 0.1 cm/s, dynamic test with 25 cm/s and static constant rate test of 0.1 cm/s. The author concluded that rate of penetration had insignificant impact on recorded resistance. Therefore, based on and previous research, it is concluded that the rate of penetration has little effect on CPT resistances measured in the clean Boler sand samples used in this study.

3.5.3 Effect of Particle Crushing

The crushing of sand particles during cone penetration can produce significant changes in CPT results as the grain size distribution instantaneously changes while being in direct contact with the cone probe. This phenomenon has been observed in calibration chamber studies on carbonate sands Belloti and Pedroni (1991). However, very little particle crushing would occur in a silica sand as observed both in calibration chamber tests (Belloti and Pedroni 1991; Porcino and Marciano 2010; Damavandi-Monfared and Sadrekarimi 2015) and Discrete Element Modelling (Falagush et al. 2015). Jones (2017) performed a study on the effect of particle crushing by sampling some of the soil, directly adjacent to where the cone penetrometer had passed through, for one of the MCPTs. Since the effect

of particle crushing would be more notable for a very dense sample at high consolidation stresses, sampling was done for a test which was in a very dense condition ($D_{rc} = 85\%$) and after having been consolidated to a high effective stress ($\sigma'_{vc} = 400$ kPa). The collected sample was sieved, and no particle crushing was observed based on the comparison with the gradation of the original sand. A similar test was performed in this study as well to investigate the effect of particle crushing. A representative sample around the cone was collected after a test was completed, oven dried and sieved. This was done for a test in which the specimen was consolidated to $D_{rc} = 65\%$ at an effective vertical stress of $\sigma'_{vc} = 400$ kPa. However, no change in gradation was noticed before and after cone penetration. Figure 3.27 presents the particle size distributions for the silica sand before and after penetration.

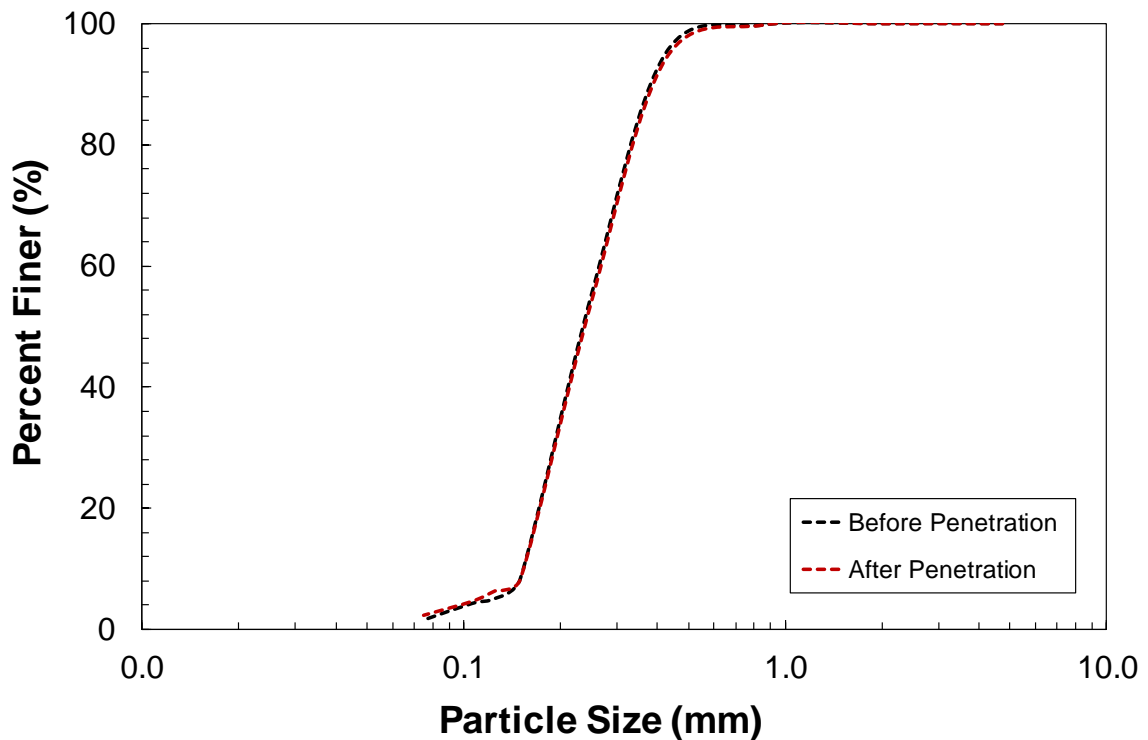


Figure 3.27: Particle size distributions of the silica sand before and after cone penetration

3.5.4 Effect of Calibration Chamber Boundary Condition

In an in-situ CPT test, the soil medium has no boundaries, as the horizontal and vertical boundaries are almost infinite. Hence, boundaries have no impact on an in-situ CPT test. However, cone resistance measured in a calibration chamber may be different from that measured in-situ because of the limited size of a calibration chamber and the imposed boundary effect on cone measurements. Hence, chamber size effect needs to be considered in predicting field performance or verifying and establishing new correlations between cone resistance and soil properties from calibration chamber test results. The effect of chamber size and boundary conditions has been examined in both numerical and experimental studies. Depending on whether stresses or displacements on the sample boundaries are kept constant, a cylindrical sample can be subjected to four different boundary conditions as summarized by Salgado et al. (1998) in Table 3-1.

Table 3-1: Different boundary conditions summarized by Salgado et al. (1998)

Boundary condition	Lateral condition	Top/bottom condition
BC1	$\Delta\sigma'_h = 0$	$\Delta\sigma'_v = 0$
BC2	$\Delta\varepsilon_h = 0$	$\Delta\varepsilon_v = 0$
BC3	$\Delta\varepsilon_h = 0$	$\Delta\sigma'_v = 0$
BC4	$\Delta\sigma'_h = 0$	$\Delta\varepsilon_v = 0$

Several researchers have previously conducted extensive studies to decipher the influence of boundary conditions on cone and sleeve resistances in a calibration chamber. The effect of sample boundaries is generally assessed based on the ratio of the calibration chamber diameter (D_c), to the diameter of the cone, d_c . In this study, with $d_c = 6$ mm and $D_c = 150$ mm, the D_c/d_c ratio is 25. In CPT calibration chamber tests in Hokksund sand, Parkin and

Lunne (1982) observed little effect of chamber size for loose samples as D_c/d_c increased from 22 to 48. However, for dense specimens, they showed that a D_c/d_c of greater than 50 was required to eliminate boundary effects as shown in Figure 3.28.

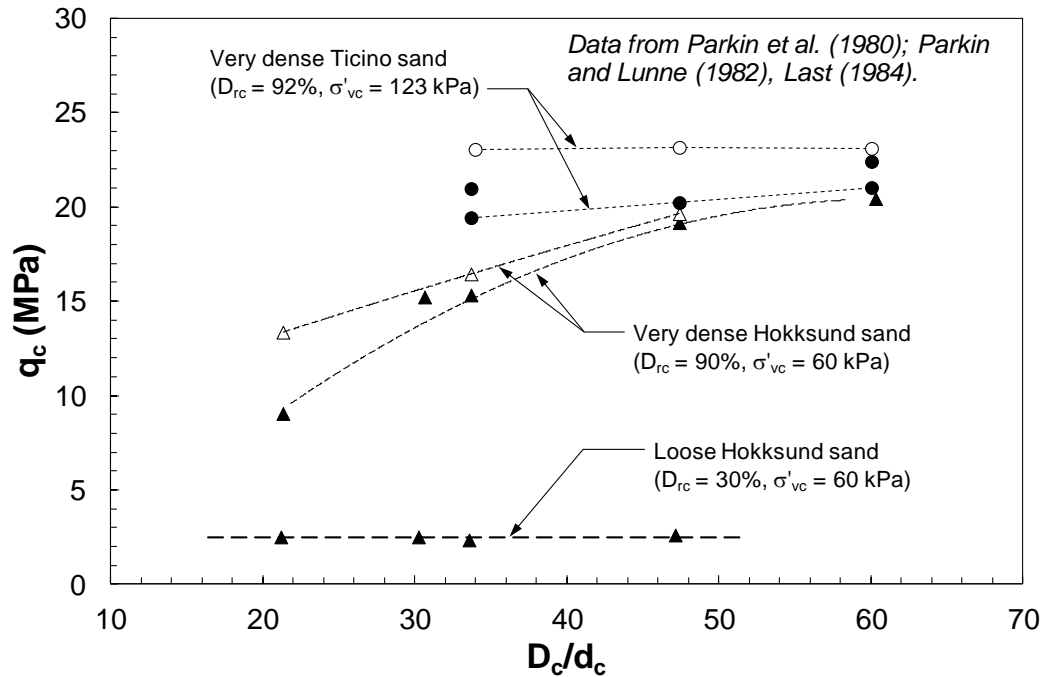


Figure 3.28: Effect of chamber size (D_c/d_c) on q_c measured in very dense and loose samples of Hokksund and Ticino sands reproduced from Jamiolkowski et al. (1985)

On the other hand, Ghionna (1984) showed little boundary effect in Ticino sand even at a relative density of 90%. This led Been et al. (1988) to argue that besides calibration chamber dimensions, the type of a sand may also have an influential role on boundary effect. Similarly, for very dense samples of Ticino sand, Bellotti (1985) demonstrated that the boundary effect diminished for $D_c/d_c = 30$ to 60. Baldi et al. (1981) performed cone penetration tests in a calibration chamber and observed that the magnitude of cone tip resistance increased in case of BC3 boundary condition, which was more pronounced for dense specimens. The authors claimed that this was due to the higher radial stress around the cone during penetration that increased the load response at the cone tip in a BC3

condition. Eid (1987) highlighted the fact that for Ticino sand (compressible), boundary effect was not as pronounced as in Hokksund sand (incompressible). He also concluded that the variation in cone tip resistance was a combined effect of cone diameter and the compressibility of the sand. A smaller cone would produce a higher cone tip resistance than that of a larger cone as less particles would be forced to move away from the shearing zone and thus the lateral boundary would have a lesser influence on the measurements. Bolton and Gui (1993) performed CPT tests in a centrifuge system and realized calibration chamber lateral boundary effects for Fontainbleau sand specimens at relative density of 76% with a D_c/d_c ratio of 21. However, when a D_c/d_c ratio range of 42 to 85 was adopted, no boundary effect was observed even at relative densities of 90%. Puppala et al. (1991) developed a calibration chamber with a flexible, double-walled membrane boundary having a D_c/d_c ratio of 42, i.e. specimen diameter and height of 63.5 cm and 178 cm respectively and a miniature cone of diameter 12.7 cm. After performing a series of tests on Monterey sand they found negligible boundary conditions effects on cone tip resistance. They even designed their testing program in a way that cone penetration was done at the center of the specimen and also closer to the periphery of the specimen. Yet, the authors reported no influence of boundary condition in either of the two locations. A negligible boundary effect was also found by Ahmadi (2000) in numerical finite difference simulations of CPT in Ticino sand at $D_{rc} = 50\%$. Similarly, Esquivel and Silva (2000) found that negligible boundary effects with D_c/d_c ratio ranging from 30 – 45. A $D_c/d_c = 24$ was deemed adequate for minimizing boundary effects by DeJong et al. (2007) as no lateral deformation was measured at the sample boundaries. Salgado et al. (1998), through a finite element study, mentioned that ideally it is not possible to maintain a zero radial strain during a BC1 condition just by the application of constant lateral stress. Therefore, cone tip resistance values are measured smaller than BC3 conditions. Huang and Hsu (2005) performed a field simulator calibration chamber test with a specimen height and diameter of 1600 mm and 790 mm respectively. The vertical boundaries were exposed to a constant stress mechanism. The lateral boundary of the specimen could experience variable stress by stacking 20 rubber rings instead of a single rubber membrane around the specimen. The cone penetration made the specimen boundary to expand as the cone tip travelled down. This boundary condition is called BC5 or simulated field boundary condition. These tests

were done on a batch of quartz sand from Da Nang, Vietnam. Two cones with diameters 17.8 mm and 35.7 mm were used which provided a D/d_c ratio of 44 and 22 respectively. Under such simulated field conditions, it was concluded from these tests that the physical lateral boundary was neither at constant stress nor under zero lateral strain during cone penetration. Goodarzi et al. (2018) performed field simulated calibration tests in a small calibration chamber developed at Center for Marine Environmental Sciences (MARUM), University of Bremen. Cuxhaven Sand was used to prepare specimens with diameter and height of 300 mm and 550 mm respectively. A 12 mm diameter miniature cone, was used in this study which resulted in a D/d_c ratio of 25 and penetrated at a rate of 2 cm/sec. Several tests were conducted under BC1, BC3 and BC5 conditions. Specimens were prepared at relative densities of 75% and 95% and tested under vertical and horizontal consolidation stresses of 300 kPa and 190 kPa respectively. LVDT sensors were connected to the lateral boundaries of the sample at calculated intervals to monitor displacement. From this study as well, BC1 condition produced low values of q_c , BC3 conditions produced very high values of q_c and BC5 provided intermediate values of q_c .

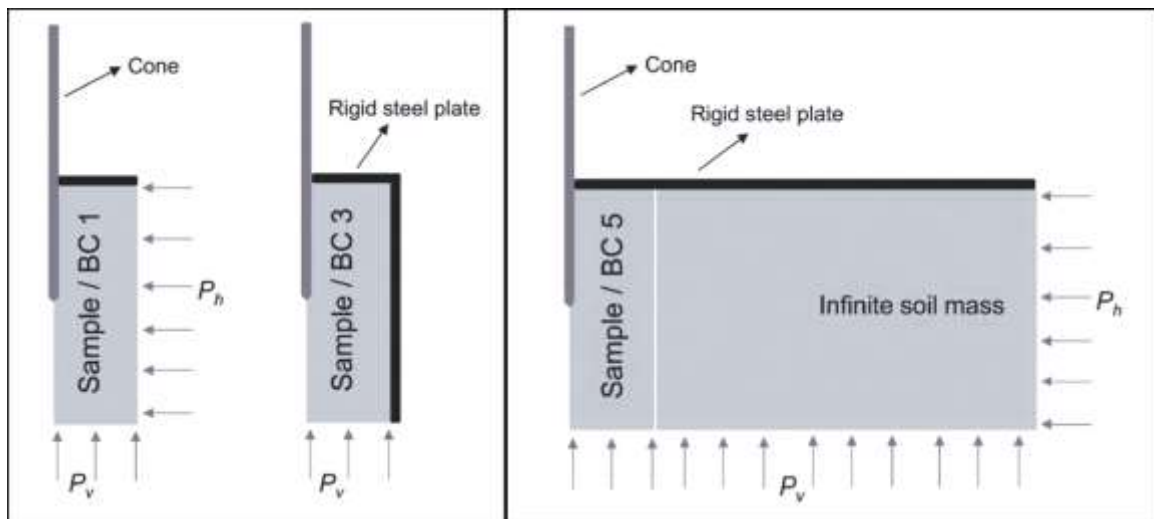


Figure 3.29: Illustration of different boundary condition mechanisms after Goodarzi et al. (2018)

Ghionna and Jamiolkowski (1991) addressed the concern of boundary conditions by realizing that building larger calibration chambers to avoid boundary effects can be very expensive for some projects and moreover, preparing such hefty soil specimens can often result in inaccuracy in terms of relative density especially for silty sands. However, besides observation, some studies extended their research in developing correction factors according to their own findings. By compiling over 640 CPT calibration chamber tests data on reconstituted quartz sands (with FC < 6%, $D_{50} = 0.15 - 1.0$ mm, $D_{10} = 0.1 - 0.7$ mm), Mayne and Kulhawy (1991) came up with the following correction factor for chamber size effect:

$$\frac{q_{c,corrected}}{q_{c,measured}} = \left(\frac{D_c/d_c - 1}{70} \right)^{-\frac{D_{rc}}{200}} \quad (3.6)$$

The above equation assumes that the effect of chamber boundaries disappears for $D_c/d_c \geq 70$. Based on calibration chamber experiments on Hokksund and Ticino sands, Been et al. (1987) proposed the following correction for chamber size effect as a function of state parameter (ψ) for different boundary conditions. The samples of this study correspond to $\psi = 0.012 - (-0.073)$ for which the effect of boundary conditions is negligible according to the following Figure 3.30. Tanizawa (1992) proposed another correction to estimate free field cone tip resistance after conducting CC CPT tests on Toyoura sand:

$$CF = a (D_r)^b \quad (3.7)$$

where, a and b are functions of D_c/d_c and D_r is the relative density of soil.

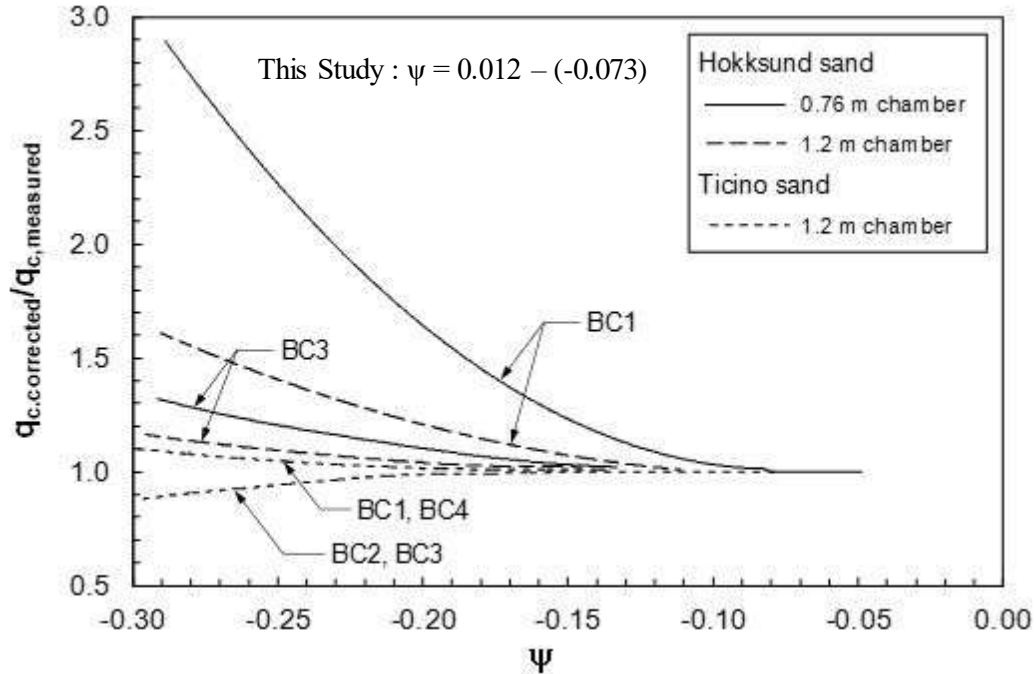


Figure 3.30: Correction for boundary effects based on state parameter by Been et al. (1987)

More recently, Jamiolkowski et al. (2001) suggested the following relationship to correct q_c for BC1 (flexible) boundary conditions:

$$\frac{q_{c,corrected}}{q_{c,measured}} = aD_{rc}^b \quad (3.8)$$

where a and b are empirical coefficients which depend on D_c/d_c .

Based on calibration chamber experiments on Ticino and Toyoura sands, Jamiolkowski et al. (2001) proposed specific values for a and b coefficients as a function of D_c/d_c . These parameters are determined for $D_c/d_c = 25$ (corresponding to this study) from the interpolation of those suggested by Jamiolkowski et al. (2001), where $a = 0.063$ and $b = 0.776$. The following Figure 3.31 presents the above equation for different D_c/d_c . According to this figure the data points from this study is shown in grey dots. The chamber

size effect appears for $D_{rc} > 45\%$ and the maximum correction factor is seen to reach almost 65% for the experiments of this study at 65%.

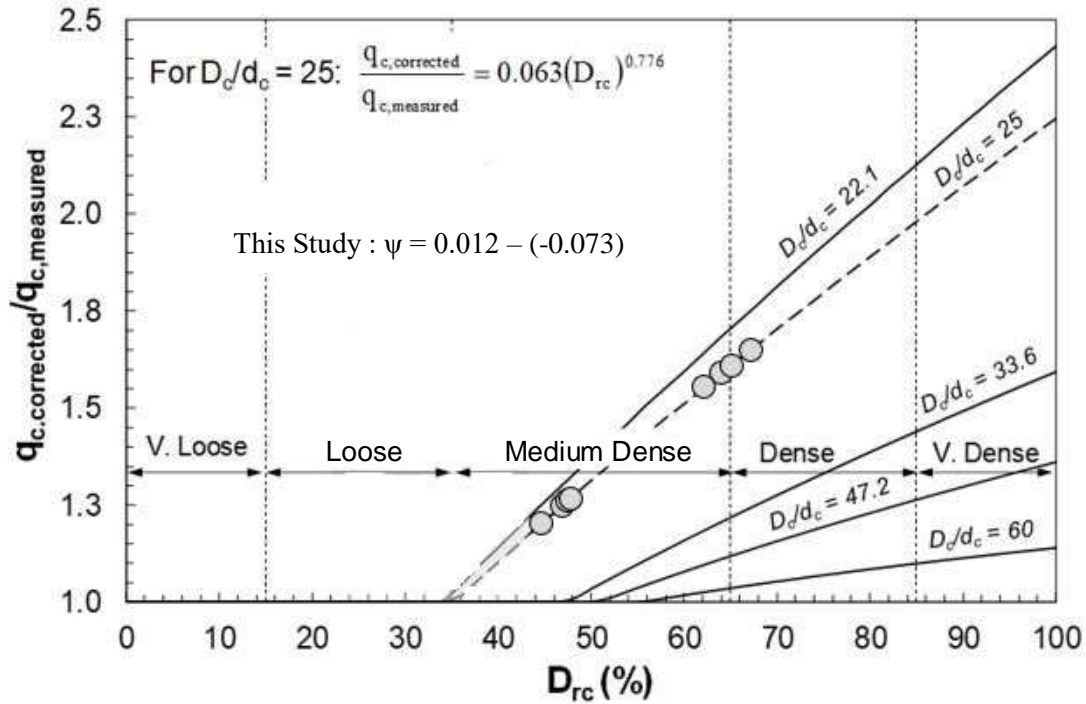


Figure 3.31: Correction for chamber size effect based on Jamiolkowski et al. (2001) empirical method

Based on 3D discrete element simulations of CPT with particles gradation of Ticino sand, Butlanska et al. (2010) arrived at the following parameters for Equation 3.8.

$$a = 9 \times 10^{-5} \left(\frac{D_c}{d_c} \right)^{2.02} \quad (3.9)$$

$$b = -0.565 \ln \left(\frac{D_c}{d_c} \right) + 2.59 \quad (3.10)$$

Nevertheless, 3D DEM analysis of cone penetration in sands showed that boundary effect diminished as $D_c/d_c > 22$ for $D_{rc} = 75\%$ (Butlanska et al. 2010). Based on the calibration chamber test results of Baldi et al. (1986) on Ticino and Hokksund sands, Jamiolkowski et al. (1988) suggested the following equation to account for boundary effects.

$$\frac{q_{c,corrected}}{q_{c,measured}} = \left\{ 1 + \frac{0.2[D_{rc}(\%) - 30]}{60} \right\} \quad (3.11)$$

Per this equation, there would be no boundary effect at $D_{rc} = 30\%$ for $D_c/d_c = 25$ (corresponding to this study). Accordingly, Wesley (2002) suggested an analytical procedure to account for the effective vertical stress reduction resulting from the insertion area of the cone. This procedure is applied for $D_c/d_c = 15, 25$ (this study), 50 and 75 in the following Figure 3.32.

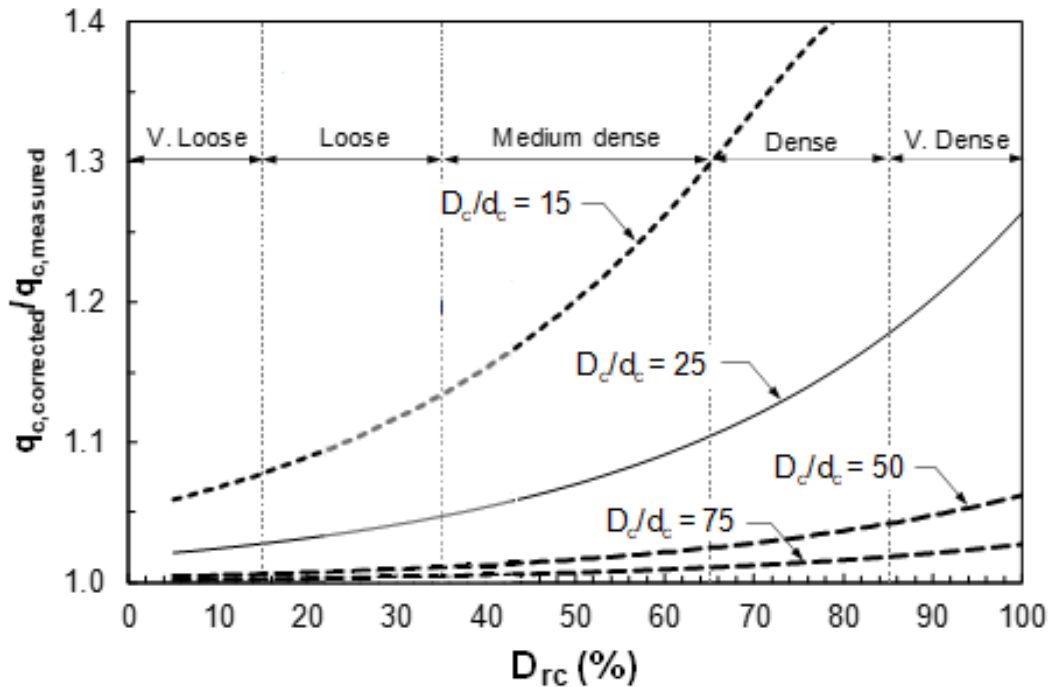


Figure 3.32: Chamber size effect resulting from the reduced vertical stress above the cone (from Wesley 2002)

Per the study of Wesley (2002), for a calibration chamber D/d_c ratio of 25, as in the current calibration chamber setup, the maximum q_c correction required for the current study, for tests at $D_{rc} = 65\%$, would be about 10% relative to measured q_c values. Despite some discrepancies, all methods generally indicate that penetration tests performed at small D_c/d_c ratios often have a lower penetration resistance than those at greater D_c/d_c ratios, and the effect of boundary condition on penetration resistance is generally more substantial with increasing relative density. In this study, the specimens were surrounded by a flexible membrane allowing a constant radial pressure and axial stress to be applied on the sample by the cell fluid pump and the piston pump, respectively. Hence, according to Table 3-1, a 'BC1' boundary condition was replicated in these tests.

A special testing program was designed and conducted in this study to examine the effect of boundary condition by changing the boundary condition from BC1 to BC3. This modification allowed us to compare cone penetration and sleeve frictional resistances between BC1 and BC3 boundary conditions. A unique approach was employed to produce a BC3 condition where the specimen was confined in the steel split mold. The steel mold provided a perfect rigid boundary while the piston pump was used to apply vertical consolidation to the sample. Hence, by applying a constant axial stress at the top and bottom boundaries and allowing no displacement in the radial direction, a 'BC3' condition was achieved during cone penetration. After assembling the triaxial chamber and the miniature cone, the sample was enclosed by the rigid boundary imposed by the steel mold and then was flushed and saturated with CO_2 and de-aired water similar to the other MCPTs.

Post saturation, the piston pump was used to apply the desired consolidation stress axially by uplifting the hydraulic piston beneath the specimen. The pore pressure sensor was connected to the specimen to measure any pore pressure changes inside the specimen. The other two (top and bottom) drainage lines were kept open to allow drainage during consolidation. The consolidation stress was maintained for about 30 minutes before the cone was pushed into the sample. The results recorded from these experiments were subsequently compared with those at BC1 conditions.

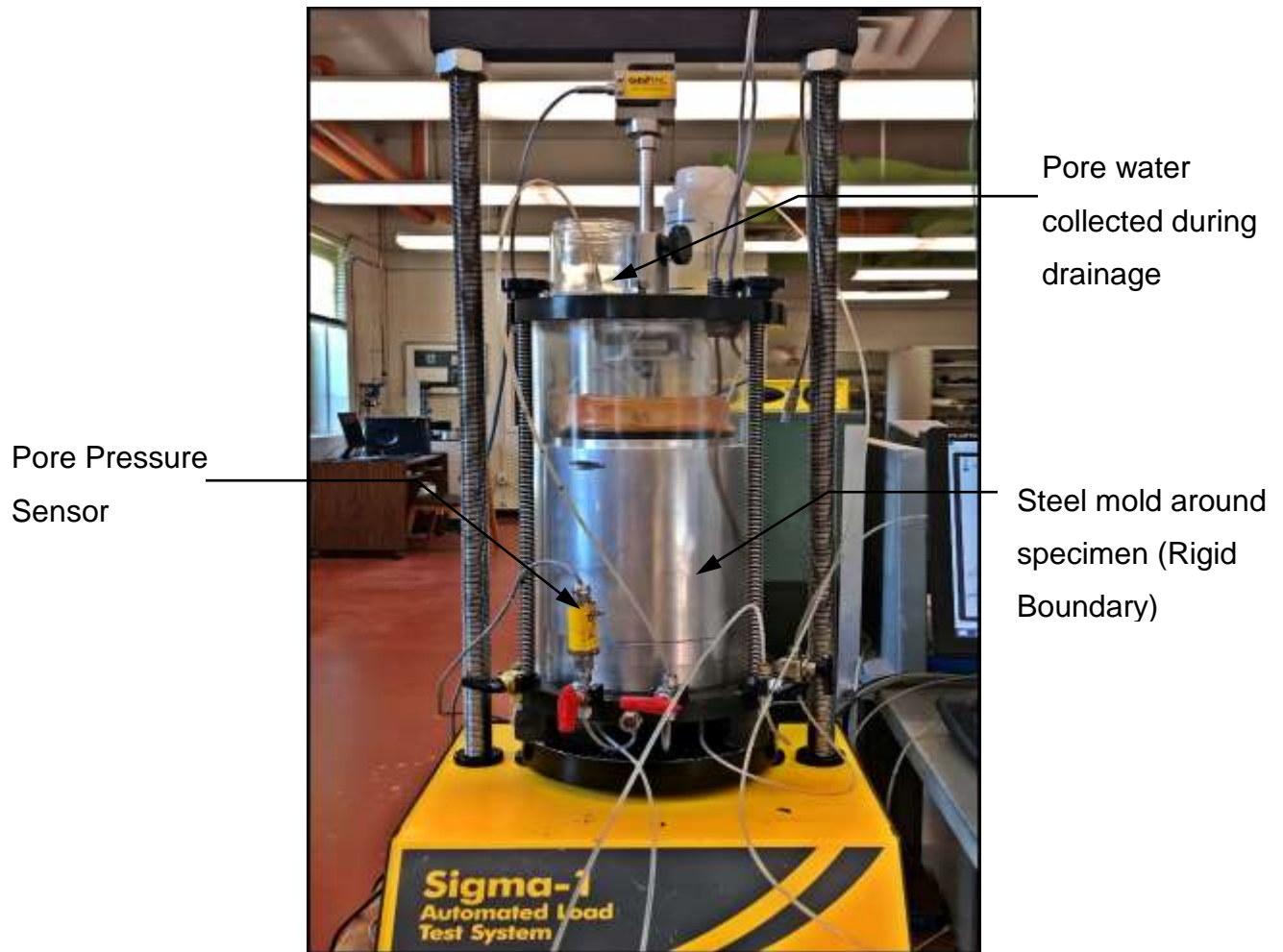


Figure 3.33: Setup of a BC3 MCPT

Previous research has shown that the influence of boundary condition is higher in dense specimens (Houlsby and Hitchman 1988; Mayne and Kulhawy 1991; Schnaid and Houlsby 1991; Salgado et al. 1998). Therefore, the goal was to test specimens which would exhibit the largest boundary effects. Three sets of tests were subsequently performed with the steel mold as the boundary constraint, on dense ($D_{rc} = 65\%$) specimens, on medium dense specimens ($D_{rc} = 45\%$) and another test on loose ($D_{rc} = 25\%$) specimens. The corresponding test results are compared with those subjected to BC1 condition in Figures 3.34 through 3.39.

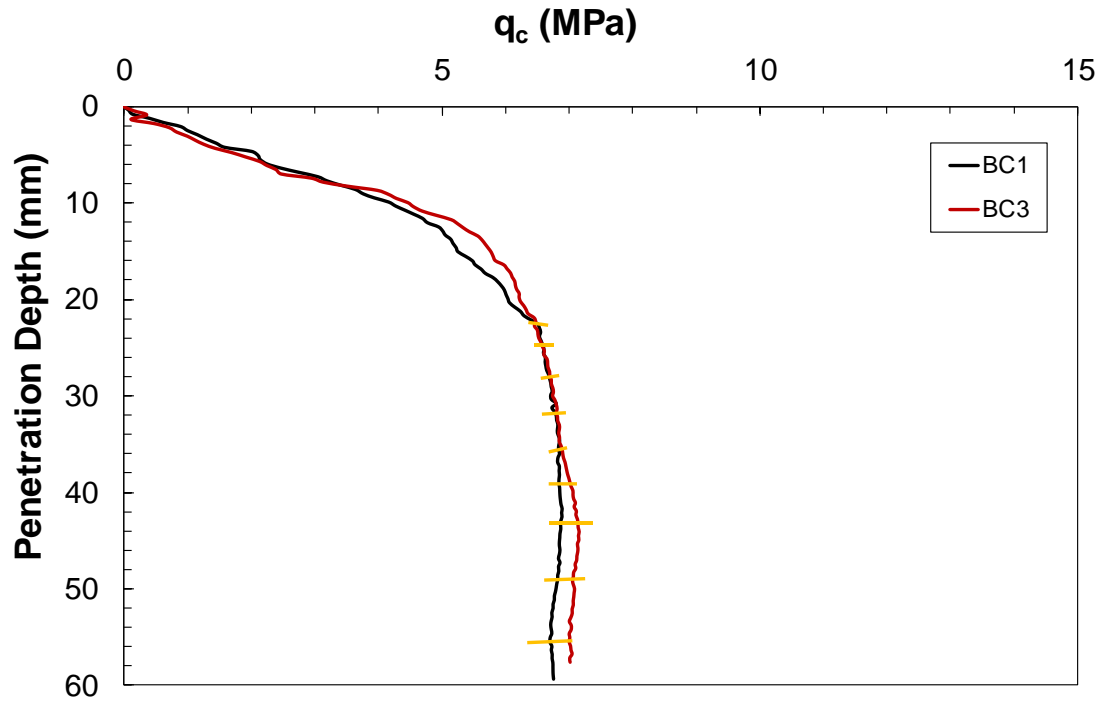


Figure 3.34: Comparison of q_c at BC1 and BC3 conditions for specimens $D_{rc} = 25\%$

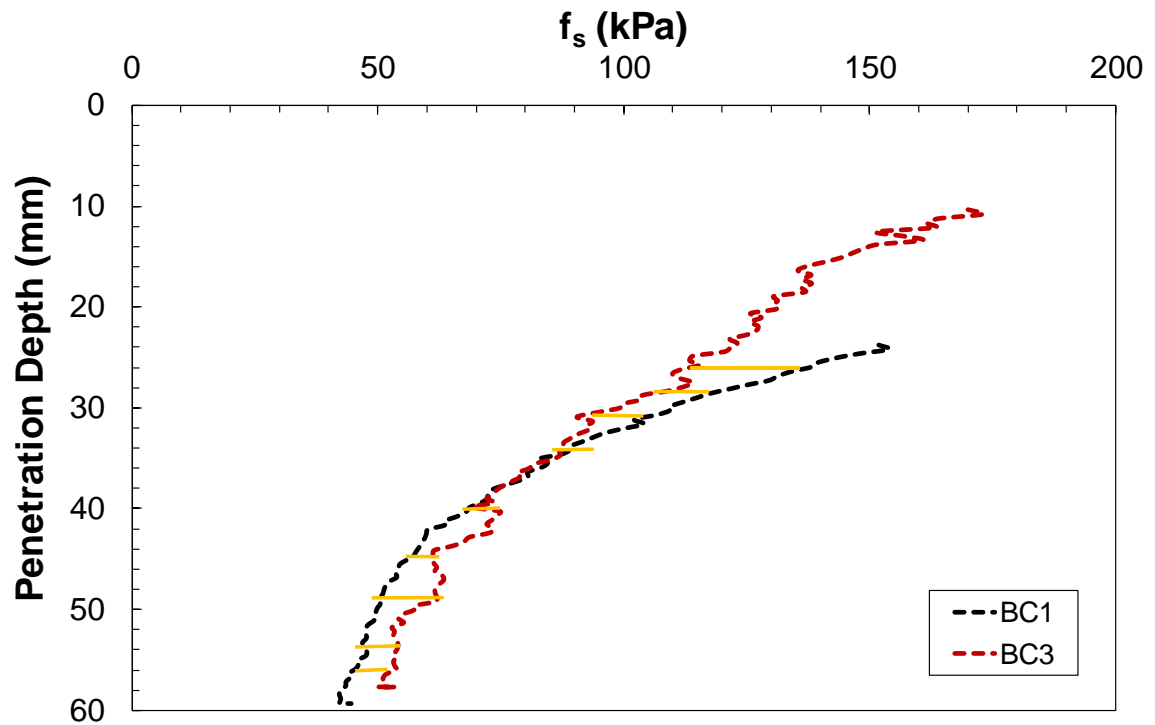


Figure 3.35: Comparison of f_s at BC1 and BC3 conditions for specimens $D_{rc} = 25\%$

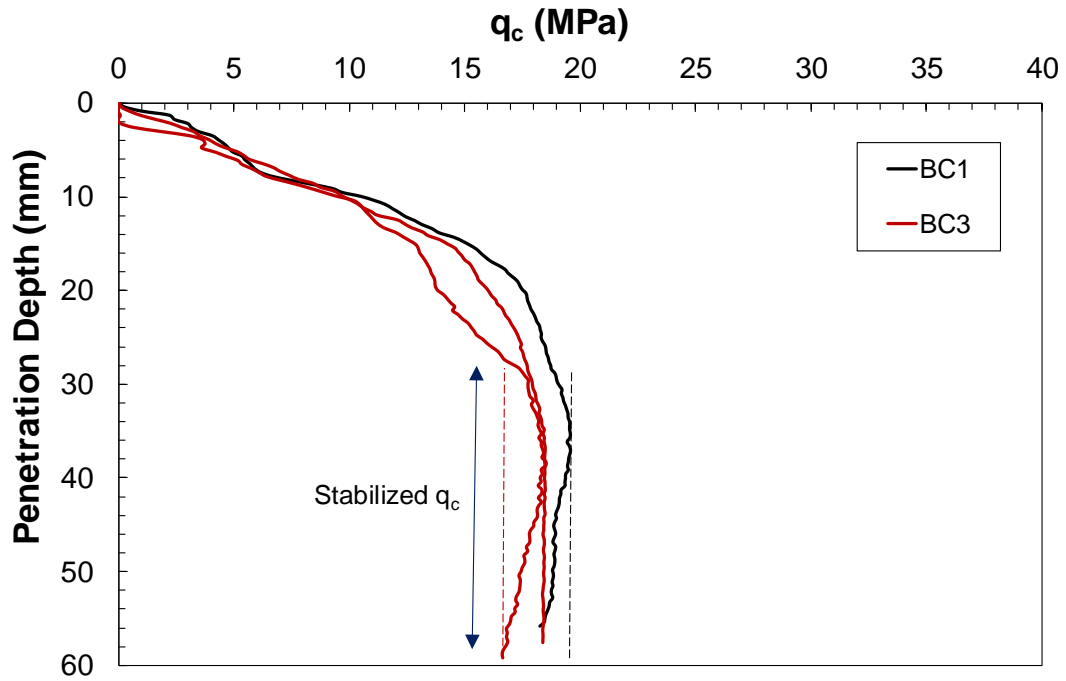


Figure 3.36: Comparison of q_c at BC1 and BC3 conditions for specimens $D_{rc} = 45\%$

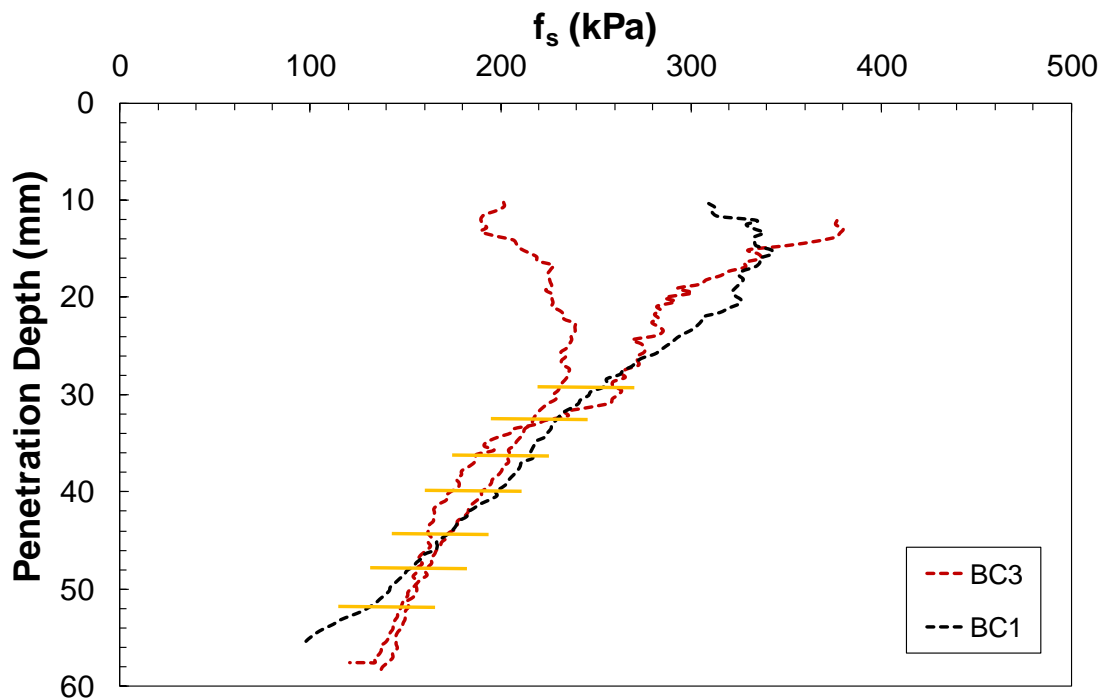


Figure 3.37: Comparison of f_s at BC1 and BC3 conditions for specimens $D_{rc} = 45\%$

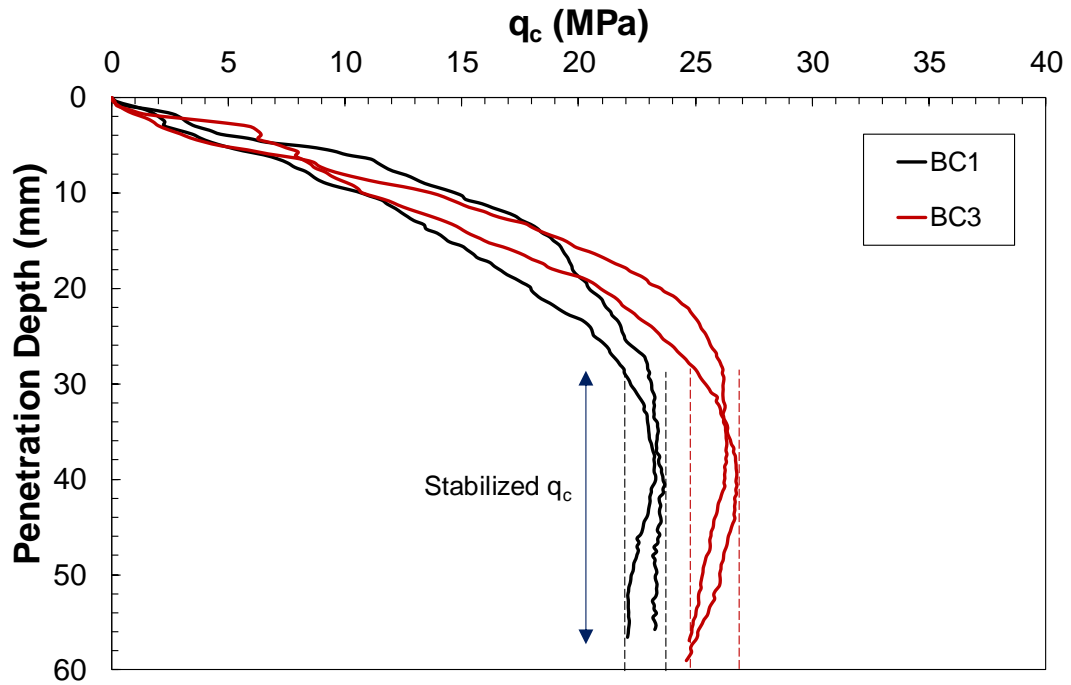


Figure 3.38: Comparison of q_c at BC1 and BC3 conditions for specimens $D_{rc} = 65\%$

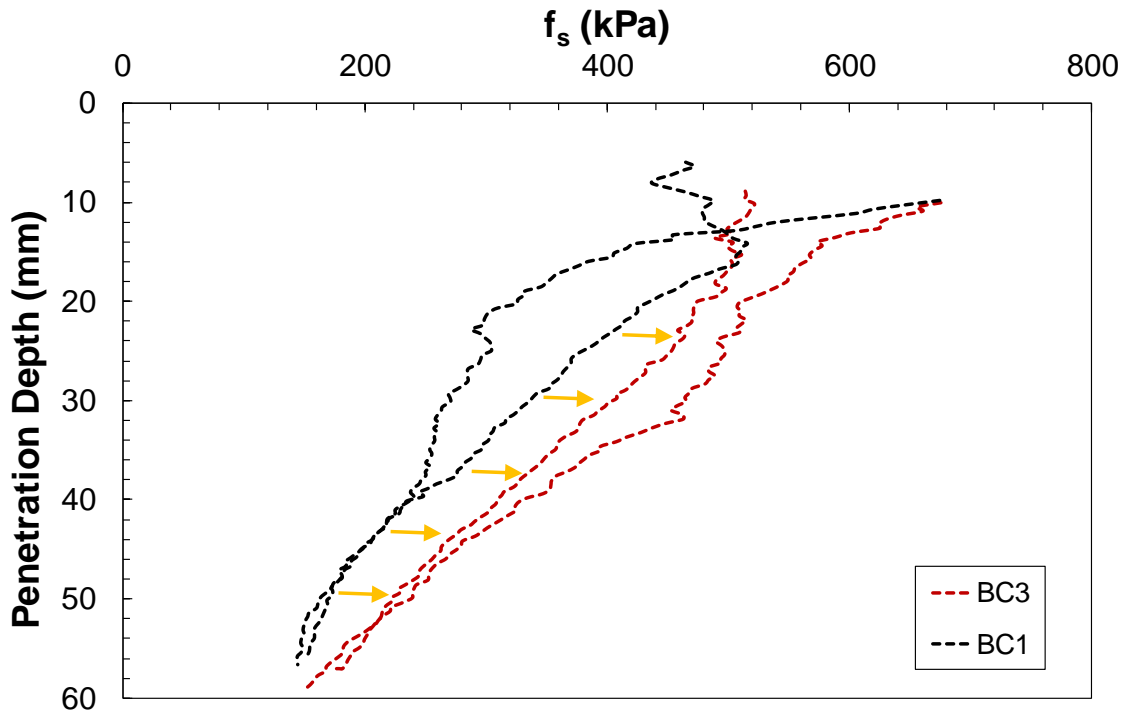


Figure 3.39: Comparison of f_s at BC1 and BC3 conditions for specimens $D_{rc} = 65\%$

The load response at the tip of the cone continues to increase with depth until a certain critical point, beyond which the cone penetration resistance seems to plateau. All values of cone tip resistance beyond this critical depth have been averaged to represent a unique magnitude of q_c for that particular test on a certain relative density and effective consolidation stress. Unlike q_c , magnitude of f_s continues to decrease as the surface area of the sleeve increases with increasing penetration depth. However, averaged value of f_s has been taken after the critical depth was observed for the corresponding q_c profile.

Table 3-2: Summary of CPT results at BC1 and BC3 boundary conditions

BC	D_{rc} (%)	σ'_{vc} (kPa)	q_c (MPa)	f_s (kPa)
BC1	27.2	99	6.78 (6.8 - 6.5)	73.7
BC3	24.7	105	6.94 (7.1 - 6.5)	76.8
BC1	47.8	406.1	19.1 (19.6 - 18.4)	185.9
BC3	43.7	400.4	17.78 (18.5 - 16.6)	173.2
BC3	44.5	402	18.41 (18.4 - 18.2)	172.9
BC1	67.2	402.51	23.35 (23.6 - 22.9)	231.4
BC1	65.7	405.06	22.69 (23.2 - 22.08)	222.2
BC3	68.2	400	25.78 (26.3 - 24.7)	283.4
BC3	67.4	405.07	26.09 (26.7 - 24.5)	278.7

As shown in Figures 3.34 through 3.39, there is little influence of boundary condition for loose and medium dense ($D_{rc} = 25\%$ and 45%) samples. However, for the dense samples ($D_{rc} = 65\%$) the cone tip resistance shows an increase of approximately 3 MPa in BC3 condition, corresponding to an increase of about 12.7%. Similarly, an average increase of 54 kPa is noticed for sleeve frictional resistances from BC1 to BC3 condition, which corresponds to an increase of 24%. The results achieved from these tests are summarized in Table 3-2. For loose and medium dense specimens, no such increment was noticed in the tests that were compared. It can be concluded that in this study, boundary condition was noticed for dense specimens at average $D_{rc} = 65\%$ for a $D_c/d_c = 25$.

Despite the 12.7% and 24% increase in q_c and f_s respectively from BC1 to BC3 conditions, an infinite (very far) boundary would be neither BC1 nor BC3 as these conditions simulate extreme limits of the most flexible and the most rigid boundaries. The actual in-situ boundary condition would be between BC1 and BC3 conditions, and probably somewhat closer to a BC1 condition. Hence, it is assumed that the actual difference between q_c and f_s measured in the experiments of this study (BC1) and the corresponding value from an in-situ test would be half of the difference between BC1 and BC3 conditions and thus q_c and f_s values measured in dense samples were increased by 6.35% for q_c and 12% for f_s to account for the effect of boundary condition and get a closer approximation of results at BC5. No correction was applied to q_c and f_s measured in loose and medium-dense samples as the q_c and f_s profiles were essentially the same at these densities as shown in Figures 3.34 through 3.37. The corrected cone tip resistance measurements established in this study are summarized in Table 3-3.

Table 3-3: Summary of measured and corrected q_c from this study

D_{rc} (%)	σ'_{vc} (kPa)	Measured q_c (MPa)	Corrected q_c (MPa)	Measured f_s (kPa)	Corrected f_s (kPa)
24.1	72.0	5.5	5.5	64.5	64.5
26.8	76.0	5.8	5.8	61.7	61.7
27.2	99	6.7	6.7	73.7	73.7
28.4	203.6	9.0	9.0	112.5	112.5
28.8	404.6	13.9	13.9	154.4	154.4
44.7	76.1	6.5	6.5	75.5	75.5
46.9	100.8	7.9	7.9	93.9	93.9
47.5	203.5	12.9	12.9	130.5	130.5
46.8	205.0	12.1	12.1	124.6	124.6
47.8	406.1	19.1	19.1	185.9	185.9
64.1	75.7	10.1	10.5	89.3	100.2
62.2	103.2	13.0	13.6	102.5	114.8
65.1	201.3	16.6	17.4	148.2	165.9
67.2	402.5	23.4	24.5	231.4	259.1
65.6	405.0	22.7	24.1	222.2	248.8

3.6 MCPT Results

A series of MCPTs were conducted in this study. Each test successfully measured cone tip resistance (q_c) and sleeve friction (f_s) over a wide range of effective consolidation stresses and relative densities.

3.6.1 Cone penetration

Cone tip resistances and sleeve frictional values were recorded throughout the penetration process at a rate of 1 reading per second, or one reading approximately every 0.4 mm of cone penetration. As shown in Figure 3.40, the cone tip resistance values began to stabilize after a penetration depth of about 25 mm and remained relatively constant until the end of penetration. Because of the free drainage nature of the clean sand used in this study and open drainage conditions of the sample during penetration, no excess pore water pressure was generated during penetration. However, the sleeve frictional resistances show a continuous decrease with penetration depth. This suggests that sleeve friction may not plateau at any point in time during the process of penetration, as the surface area of the cone penetrometer sleeve continues to increase with penetration, which as a result, decreases the sleeve friction values. The representative value of q_c was selected as an average after q_c reached a plateau. However, choosing a representative value for f_s was challenging as the magnitude of f_s kept decreasing with penetration depth. Hence, to maintain similarity in analysis, representative values of f_s were selected as the average after the point at which the q_c profile stabilized. In Table 3-4, the ranges of variation of q_c are shown alongside the average q_c . Owing to a higher degree of fluctuation compared to q_c , only the average f_s values are shown. Average cone penetration results, i.e. q_c and f_s are often normalized to account for changes in effective overburden stress. The method used to calculate overburden stress normalization parameters are discussed below.

Cone Tip Resistance normalized for overburden stress:

$$q_{c1} = q_c \left(\frac{Pa}{\sigma'_{vc}} \right)^n \quad (3.12)$$

where, $P_a = 100$ kPa (atmospheric pressure) and “n” is the stress normalization exponent.

Sleeve Friction normalized for overburden stress:

$$f_{s1} = f_s \left(\frac{P_a}{\sigma'_{vc}} \right)^x \quad (3.13)$$

where, $P_a = 100$ kPa (atmospheric pressure) and “x” is the stress normalization exponent.

Cone Tip Resistance normalized for dimension:

$$q_{cN} = \frac{q_c}{P_a} \quad (3.14)$$

Sleeve Friction normalized for dimension:

$$f_{sN} = \frac{f_s}{P_a} \quad (3.15)$$

Dimensionless, overburden stress normalized Cone Tip Resistance:

$$q_{c1N} = q_{cN} \left(\frac{P_a}{\sigma'_{vc}} \right)^n \quad (3.16)$$

Dimensionless, overburden stress normalized Sleeve Friction:

$$f_{s1N} = f_{sN} \left(\frac{P_a}{\sigma'_{vc}} \right)^x \quad (3.17)$$

Net Cone Tip Resistance:

$$q_{c,net} = q_c - \sigma_{vc} \quad (3.18)$$

where, σ_{vc} is the total vertical stress after consolidation

Net, overburden stress normalized Cone Tip Resistance:

$$q_{c1,net} = q_{c,net} \left(\frac{P_a}{\sigma'_{vc}} \right)^n \quad (3.19)$$

The detailed description and purpose of such normalization methods are highlighted in the subsequent sections of this chapter. The results of all MCPTs are summarized in Table 3-4, while Figures 3.40 through 3.42 present the cone tip and sleeve frictional resistance profiles developed in each test.

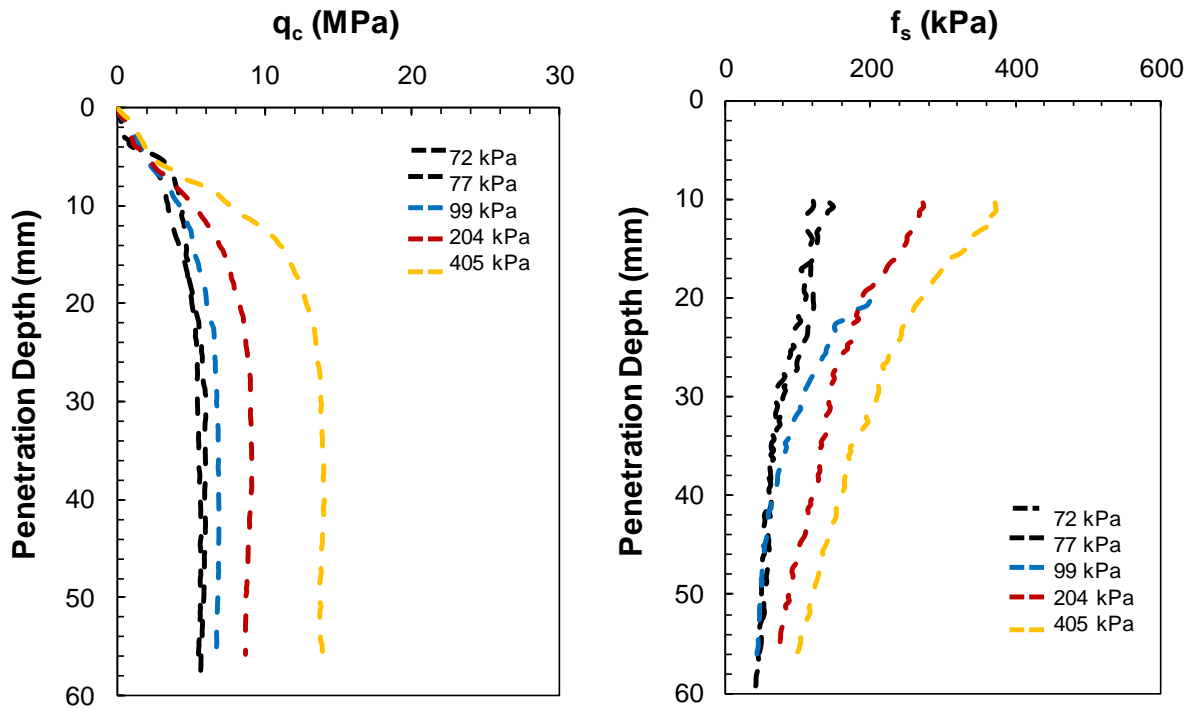


Figure 3.40: q_c and f_s profiles for specimens with an average $D_{rc} = 27.2\%$

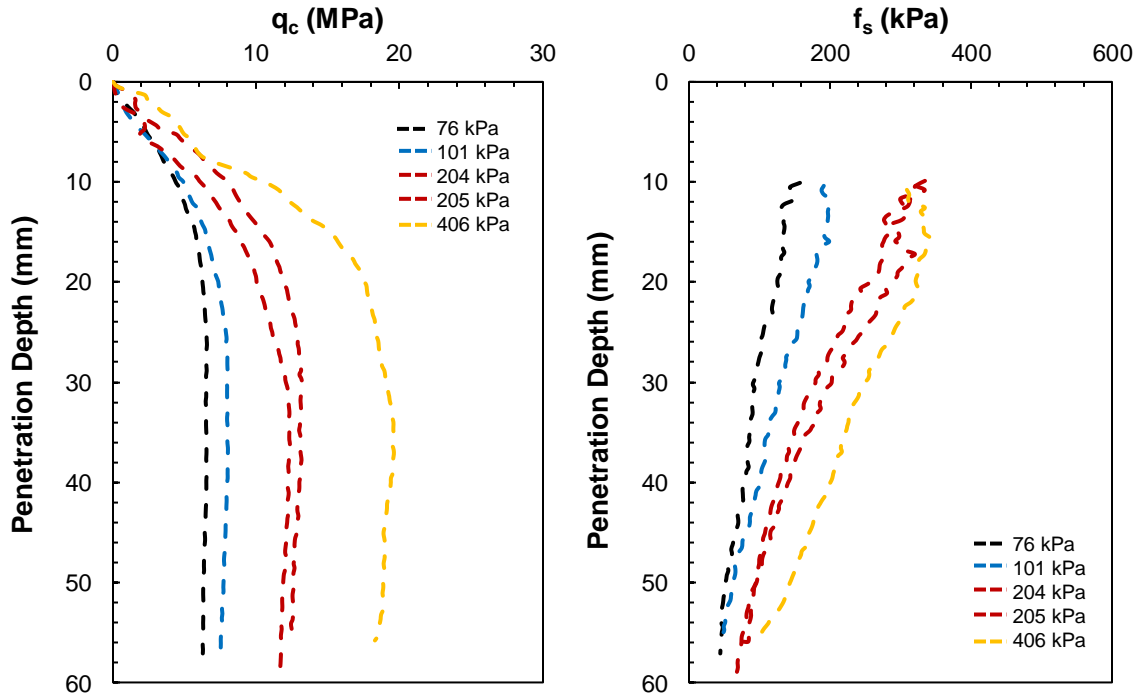


Figure 3.41: q_c and f_s profiles for specimens with an average $D_{rc} = 46.7\%$

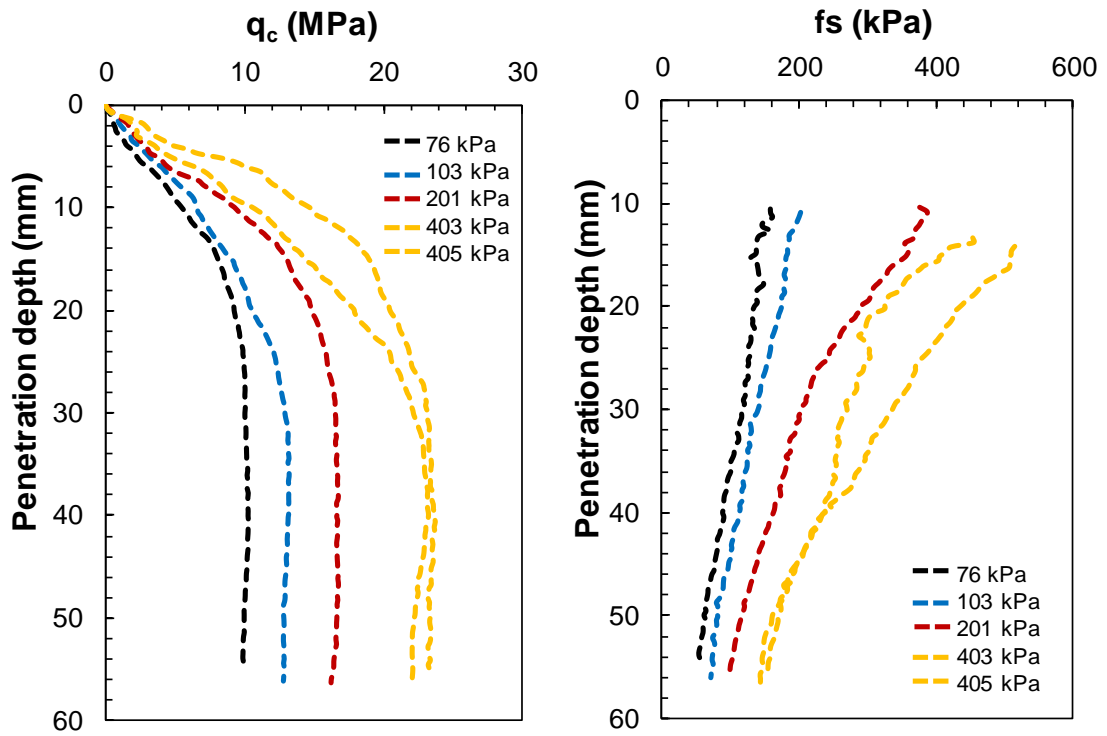


Figure 3.42: q_c and f_s profiles for specimens with an average $D_{rc} = 64.8\%$

Table 3-4: Summary of MCPT results completed in this study

	Test ID	D_{rc} (%)	e_c	σ'_{vc} (kPa)	K_c	Corrected q_c (MPa)	q_{cN}	Corrected f_s (kPa)	f_{sN}
BC1	CPT-25-1	24.1	0.768	72	0.51	5.5 (5.6 - 5.2)	55.1	64.5	0.6
	CPT-25-1(2)	26.8	0.759	76	0.48	5.8 (5.9 - 5.5)	58.2	61.7	0.6
	CPT-25-2	27.2	0.758	99	0.46	6.7 (6.8 - 6.5)	67.7	73.7	0.7
	CPT-25-3	28.4	0.754	203.6	0.51	9 (9.1 - 8.2)	89.5	112.5	1.1
	CPT-25-4	28.8	0.753	404.6	0.51	13.9 (14.0 - 13.7)	139	154.4	1.5
	CPT-45-1	44.7	0.702	76.1	0.52	6.5 (6.6 - 6.2)	64.7	75.5	0.8
	CPT-45-2	46.9	0.695	100.8	0.51	7.9 (8.01 - 7.5)	78.6	93.9	0.9
	CPT-45-3	47.5	0.693	203.5	0.56	12.9 (13.2 - 12.4)	128.9	130.5	1.3
	CPT-45-3(2)	46.8	0.695	205	0.54	12.06 (12.3 - 11.6)	120.6	124.6	1.25
	CPT-45-4	47.8	0.692	406.1	0.59	19.1 (19.6 - 18.4)	191	185.9	1.9
	CPT-65-1	64.1	0.64	75.7	0.54	10.5 (10.9 - 10.4)	107.1	100.2	1
	CPT-65-2	62.2	0.646	103.2	0.56	13.8 (14.06 - 13.6)	138.4	114.8	1.1
	CPT-65-3	65.1	0.637	201.3	0.5	17.6 (17.8 - 17.2)	176.3	165.9	1.6
	CPT-65-4	67.2	0.63	402.5	0.51	24.8 (25.2 - 24.4)	248.4	259.1	2.6
	CPT-65-4(2)	65.6	0.635	405	0.52	24.1 (24.7 - 23.4)	241.31	248.8	2.5
BC3	BC3-25-1	24.7	0.766	105		6.94 (7.1 - 6.5)	69.4	76.8	0.7
	BC3-45-1	44.4	0.703	402		18.41 (18.5 - 18.2)	184.1	173.2	1.7
	BC3-45-2	43.8	0.705	400		17.77 (18.5 - 16.6)	177.7	172.9	1.7
	BC3-65-1	68.1	0.627	400		25.78 (26.3 - 24.7)	257.8	283.4	2.8
	BC3-65-2	67.5	0.629	405		26.09 (26.7 - 24.5)	260.9	278.7	2.8

3.6.2 Repeatability

Repeatability of test results under the same conditions of density and stress is one of the major requirements of any reliable experiment, including the reduced-scale CPT of this study. In order to evaluate the repeatability of the CPT results, 5 tests were repeated with similar D_{rc} and σ'_{vc} conditions. These tests include results from three BC1 condition test and two BC3 condition tests. The summary of the repeated tests can be seen from Table 3-4 for Test IDs CPT-25-1 & CPT-25-1(2), CPT-45-3 & CPT-45-3(2), CPT-65-4 & CPT-65-4(2), BC3-45-1 & BC3-45-2 and BC3-65-1 & BC3-65-2. The repeated experiments show very similar average penetration resistances (q_c , f_s) after the critical depth, usually found to be in the range of 25-30 mm of penetration, and therefore confirm the repeatability

of the experiments. To quantify the differences in repeatability, the coefficient of variation among the results were calculated and COV_{q_c} ranged from 0.77 – 3.22% while COV_{f_s} ranged from 0.83 – 2.31%. The small differences in q_c and f_s measurements are inevitable and are associated with variations in specimen uniformity. The penetration resistance profiles with depth for the 3 repeated tests are presented in Appendix A.

3.7 Overburden Stress Normalization

Cone tip resistance and sleeve friction are essentially functions of effective stress level and sand relative density. Therefore, q_c and f_s measured in the same sand and at the same relative density can be very different at different penetration depths corresponding to different effective overburden stresses. To compare soil behaviour from different depths, the measured values are often normalized to a common effective overburden stress of 100 kPa. This correspond to test results at atmospheric pressure which is useful for comparing field and laboratory tests. A correction factor is typically multiplied by the obtained parameters which is denoted by C_q and C_f for q_c and f_s respectively.

$$C_q = \left(\frac{P_a}{\sigma'_{vc}} \right)^n \quad (3.20)$$

$$C_f = \left(\frac{P_a}{\sigma'_{vc}} \right)^x \quad (3.21)$$

where, $P_a = 100$ kPa (atmospheric pressure), “n” and “x” are the stress normalization exponents denoted in this study.

3.7.1 Normalization Exponent of Cone Tip Resistance

There have been extensive studies to interpret correction factors and determine the stress normalization exponent based on cone penetration data. For example, (Al-Akwati 1975; Fardis and Veneziano 1981) have found the normalization exponent to be in the range of

0.4 – 0.6. Jamiolkowski et al. (1985) performed several cone penetration tests on Edgar sand ($D_r = 31-70\%$), Ottawa sand ($D_r = 20-99\%$), Reid Bedford sand ($D_r = 24-81\%$), Ticino sand ($D_r = 11-95\%$), Hokksund sand ($D_r = 28-95\%$) and Melbourne sand ($D_r = 52-100\%$). The authors indicated a stress normalization exponent of 0.72 from their research. Similarly, Olsen (1994) reported that a stress normalization exponent of 0.7 represents a typical sand at medium dense to loose relative densities. Liao and Whitman (1986) and Tokimatsu and Yoshimi (1983) worked on clean quartz sand and in-situ sandy soil deposits respectively and found $n = 0.5$, which has proven to be widely used to determine C_q . Sadrekarimi (2017) through various MCPTs on reconstituted fine Ottawa Sand found $n = 0.612$. Robertson and Wride (1998) found that the exponent, n , varied from 0.5 for sands to 1.0 for clays.

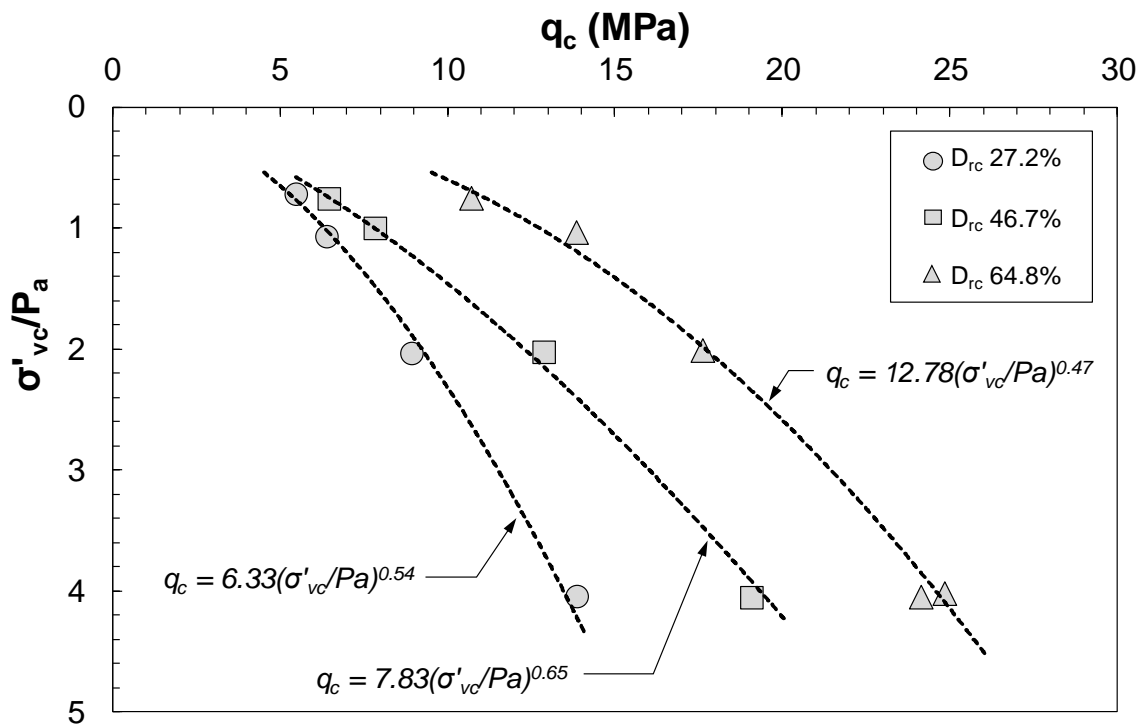


Figure 3.43: Variations of corrected q_c over normalized effective vertical stress

Figure 3.43 presents the stress normalization exponents from this study at different relative densities which range from 0.47 to 0.65, with an average value of 0.56. This value falls in the range of 0.4 – 0.6 as predicted by (Al-Akwati 1975; Fardis and Veneziano 1981; Tokimatsu and Yoshimi 1983; Liao and Whitman 1986) for sandy soils. Jones (2017) previously conducted MCPTs on Fraser River sand (clean sand) and found an average stress normalization exponent of 0.53 for cone tip resistance. Since this study is also based on a clean silica sand graded as Fraser River Sand, it can be confirmed that the normalization exponent derived from this study agrees with previous research.

3.7.2 Normalization Exponent of Sleeve Friction

The sleeve frictional resistances obtained from this study are also normalized to a reference atmospheric pressure of 100 kPa. Hence, to calculate the correction factor for normalization, the stress normalization exponent, “x” is determined from Figure 3.44.

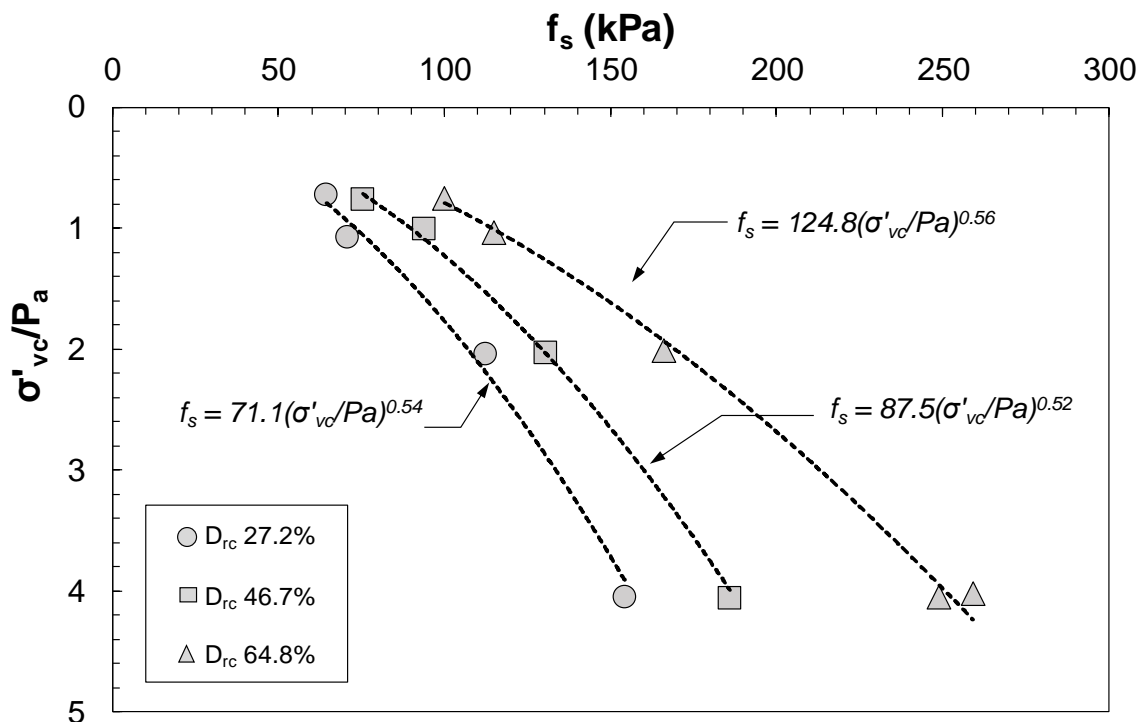


Figure 3.44: Variations of f_s over normalized effective stress

Figure 3.44 describes the variation of sleeve friction data at different relative densities and the corresponding stress normalization exponents obtained from the MCPT of this study. The stress normalization exponent for sleeve friction developed from this study lies in the range of 0.52 to 0.56, i.e. an average value of $x = 0.54$. For more precise comparisons of corrected cone tip and sleeve frictional resistances with other studies, the specific stress exponents derived at each relative density are used to normalize q_c and f_s , instead of the average values.

3.7.3 Stress Normalization Correction Factors

Several methods (Wroth 1984; Liao and Whitman 1986; Kayen et al. 1992; Robertson 1992, 2009; Idriss and Boulanger 2006; Moss et al. 2006) are suggested for converting the measured total cone tip resistance (q_c) or the net cone tip resistance ($q_{c,net}$) to a normalized magnitude in order to compare the obtained cone tip resistance or sleeve friction data to those that would have been measured if the CPT had been carried out at $\sigma'_{vc} = 100$ kPa. Therefore, these methods are described and compared to the test results obtained from this study subsequently in this chapter.

Table 3-5: CPT Overburden Stress Normalization methods

Cone Tip Resistance	Sleeve Friction	Reference
$q_{c1,net} = q_{c,net} \left(\frac{P_a}{\sigma'_{vc}} \right)^{0.5}$	–	Wroth (1984)
$q_{c1} = q_c \left(\frac{P_a}{\sigma'_{vc}} \right)^{0.5}$	–	Liao and Whitman (1986)
$q_{c1} = q_c \frac{1.8}{0.8 + \left(\frac{\sigma'_{vc}}{P_a} \right)}$	–	Kayen et al. (1992)

$q_{c1,net} = q_{c,net} \left(\frac{P_a}{\sigma'_{vc}} \right)^c$	$f_{s1} = f_s \left(\frac{P_a}{\sigma'_{vc}} \right)^c$	Olsen and Mitchell (1995)
$q_{c1} = q_c \left(\frac{P_a}{\sigma'_{vc}} \right)^c$	$f_{s1} = f_s \left(\frac{P_a}{\sigma'_{vc}} \right)^c$	Moss et al. (2006)
$q_{c1} = q_c \left(\frac{P_a}{\sigma'_{vc}} \right)^{0.784 - 0.521 D_{rc}}$	–	Idriss and Boulanger (2006)
$q_{c1,net} = q_{c,net} \left(\frac{P_a}{\sigma'_{vc}} \right)^c$	–	Robertson (2009)

where σ_{vc} and σ'_{vc} are the total and effective vertical stresses in kPa, P_a is the reference atmospheric pressure of 100 kPa and c is the stress normalization exponent for the corresponding study. The stress normalization methods adopted in this study are compared with those summarized in Table 3-5 in Figures 3.45 through 3.49. In these figures, q_c and $q_{c,net}$ have been normalized with stress normalization exponent values determined from this study

$$q_{c1} = q_c \left(\frac{P_a}{\sigma'_{vc}} \right)^n \quad (3.22)$$

$$q_{c1,net} = q_{c,net} \left(\frac{P_a}{\sigma'_{vc}} \right)^n \quad (3.23)$$

The magnitude of $q_{c,net}$ is generally determined by subtracting the total stress from the measured cone tip resistance, i.e. $q_{c,net} = q_c - \sigma_{vc}$. However, in this study, the effect of pore water pressure was neutralized by zeroing all stresses experienced by the load cells prior to the cone penetration process. Moreover, the magnitude of penetration-induced pore water pressure being extremely negligible compared to the magnitude of cone tip resistance, net cone tip resistance ($q_{c,net}$) was calculated taking the effective vertical stress into consideration.

$$q_{c,net} = q_c - \sigma'_{vc} \quad (3.24)$$

From Figure 3.45, the widely used stress normalization exponent of 0.5 by Liao and Whitman (1986) agrees well the data obtained for dense specimens ($D_{rc} = 65\%$) in this study. The stress normalization technique developed by Kayen et al. (1992) somewhat shows a comparison with the data obtained at $D_{rc} = 45\%$ but underestimates the q_{c1} values at $\sigma'_{vc} > 100$ kPa for the other two relative densities measured from this study. Based on a combination of theory and empirical relationships, Moss et al. (2006) suggested a stress normalization exponent for q_c as below.

$$c = 0.78 q_c^{-0.33} \left\{ \frac{\frac{f_s}{q_c} \times 100}{abs [Log (10 + q_c)^{1.21}]} \right\}^{-(-0.32 q_c^{-0.35} + 0.49)} \quad (3.25)$$

An average “c” exponent of 0.4 was interpreted from the above equation. Owing to a relatively low stress exponent, the method proposed by Moss et al. (2006) overestimates the q_{c1} values from this study beyond $\sigma'_{vc} > 100$ kPa.

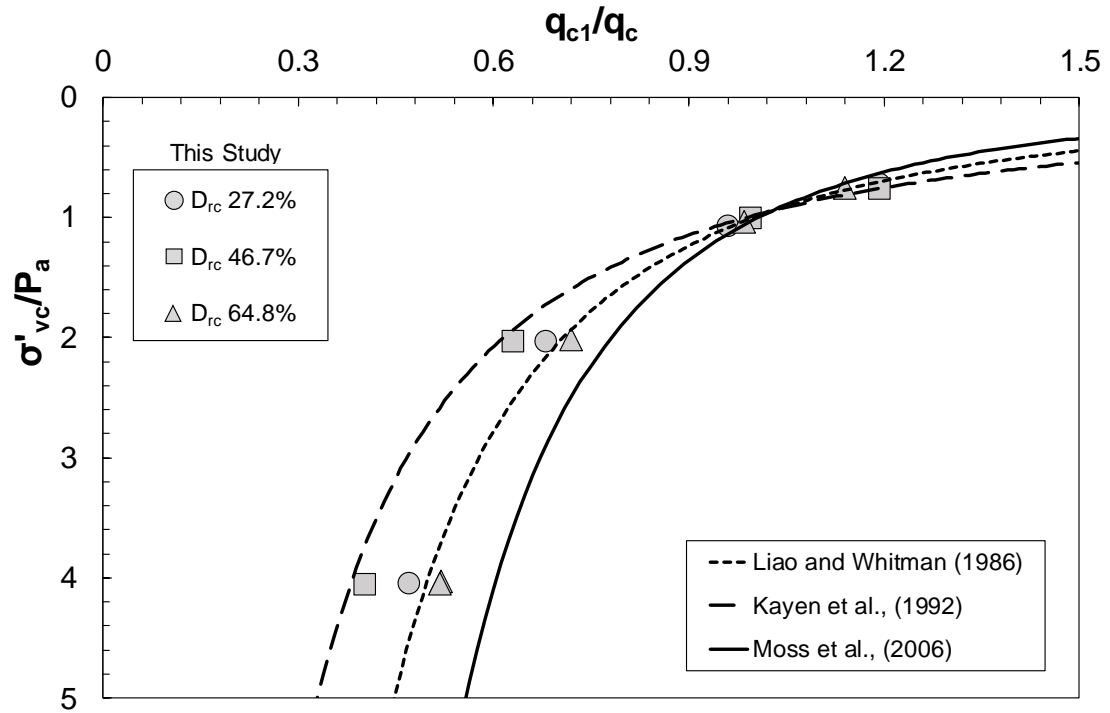


Figure 3.45: Comparison of C_q for q_{c1}

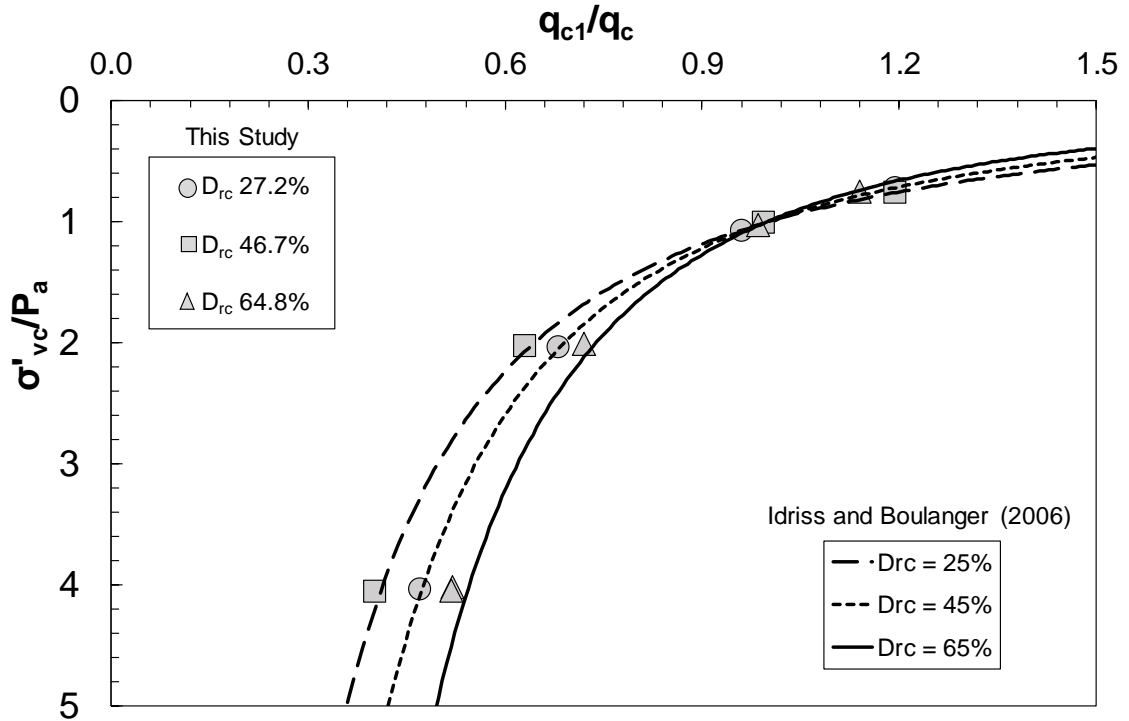


Figure 3.46: Comparison of C_q for q_{c1} with Idriss and Boulanger (2006)

However, the D_{rc} -based stress normalization technique suggested by Idriss and Boulanger (2006) provided a relatively better estimation to q_{c1}/q_c with the data points from this study. It is particularly seen to compare well with the data obtained from this study in case of dense samples ($D_{rc} = 65\%$). But beyond $\sigma'_{vc} > 100$ kPa, the .

Furthermore, the existing stress normalization techniques for $q_{c1,net}$ have also been compared with the obtained data from this study. Similarly, the overburden stress correction technique suggested by Wroth (1984) has shown to compare well with the present data for dense specimens ($D_{rc} = 65\%$). However, datapoints from tests on loose specimens ($D_{rc} = 25\%$) also seem to align well with the prediction of Wroth (1984) in Figure 3.47. One of the reasons being, the stress normalization exponent used by Wroth (1984) is 0.5 and the average stress normalization exponent derived from this study for q_c is 0.56.

More recently Robertson (2009) suggested an iterative method of determining stress normalization “c”, based on soil behaviour type (SBT) index I_c as below.

$$I_c = [(3.47 - \text{Log}Q_{tn})^2 + (\text{Log}F_r + 1.22)^2]^{0.5} \quad (3.26)$$

where, $Q_{tn} = \left(\frac{q_{c,net}}{P_a}\right) \left(\frac{P_a}{\sigma'_{vc}}\right)^c$ and $F_r = \frac{f_s}{q_{c,net}} \times 100\%$

If $I_c \leq 1.64$, then $c = 0.5$. If not, c is calculated as follows.

$$c = 0.381(I_c) + 0.05 \left(\frac{\sigma'_{vc}}{P_a}\right) - 0.15 \quad (3.27)$$

An average stress normalization exponent “c” of 0.73 was calculated by the described framework from Robertson (2009). From Figure 3.47, it is seen that such a relatively high magnitude of exponent underestimates the values of $q_{c1,net}$, especially at $\sigma'_{vc} > 100$ kPa.

Similarly, the D_{rc} -based stress normalization technique developed by Olsen and Mitchell (1995) is seen to overestimate the data points obtained from this study. However, at $D_{rc} = 45\%$, the data points seem to compare well the proposed method at the same relative density.

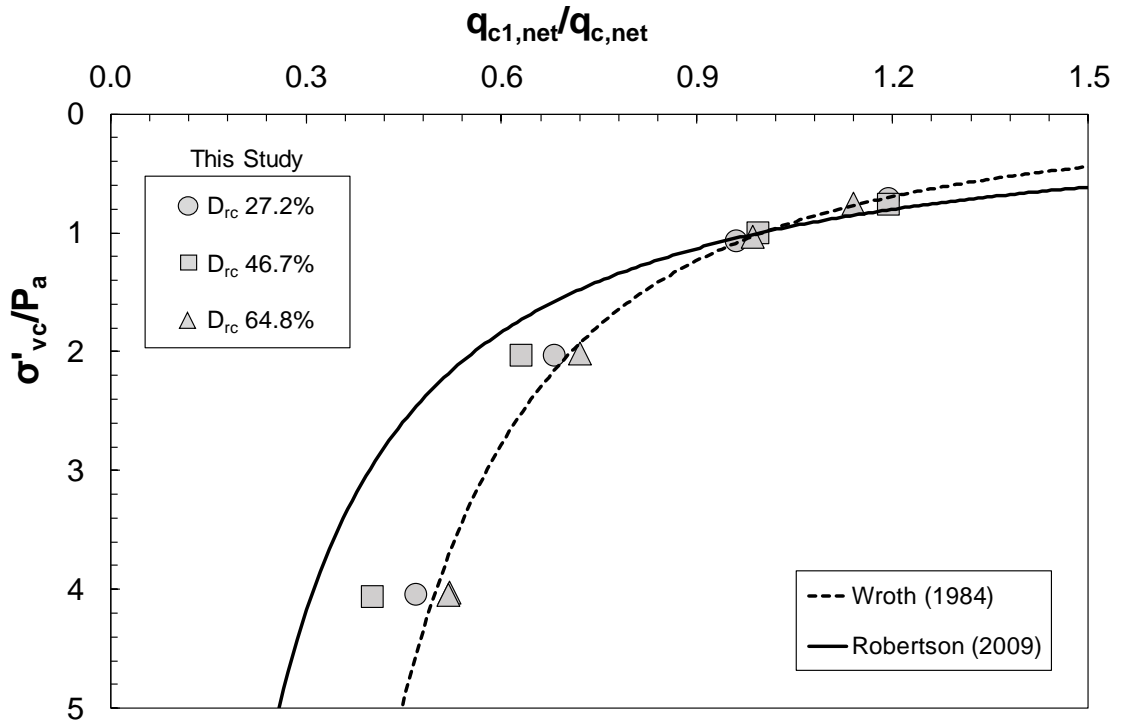


Figure 3.47: Comparison of stress normalization techniques for $q_{c1,net}$

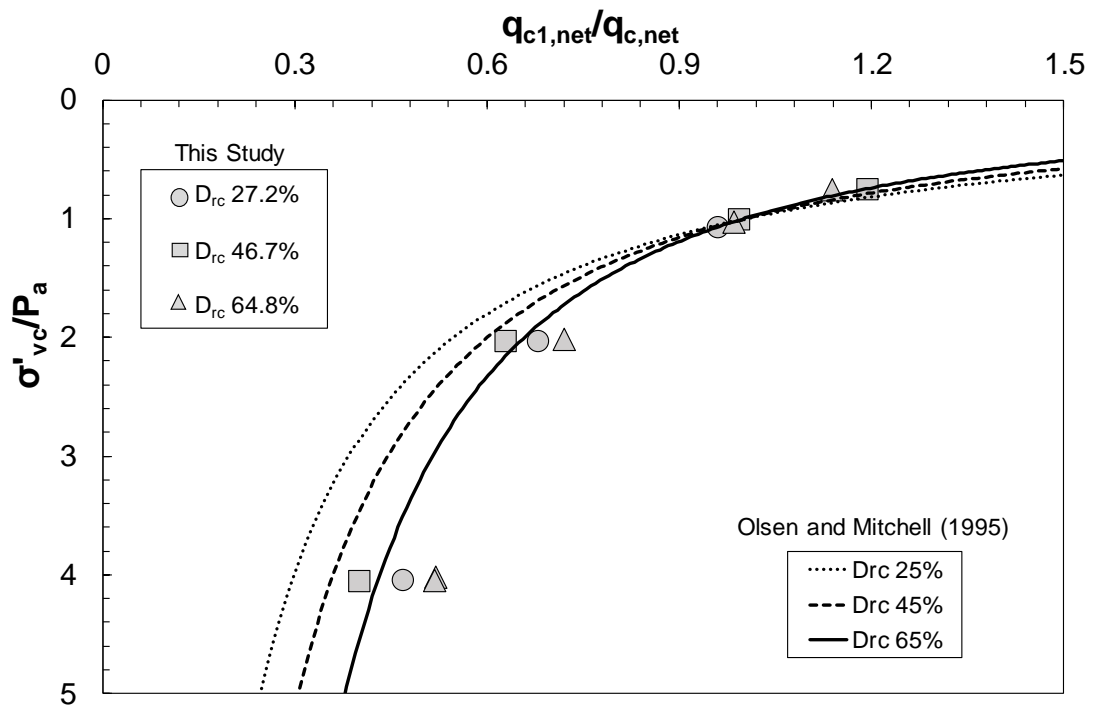


Figure 3.48: Comparison of stress normalization technique for $q_{c1,net}$ with Olsen and Mitchell (1995)

Olsen and Mitchell (1995) had collected over two decades of field data and an extensive database of CPT calibration chamber tests to derive an exponent as follows.

$$c = 1 - 0.007(D_{rc} - 10\%) \quad (3.28)$$

The above equation yields an exponent of $c \geq 0.8$ for loose specimens, which makes it underestimate the magnitude of $q_{c1,net}$. The variations observed during comparison can be accounted to possibilities such as the wide range of material used by Olsen and Mitchell (1995) which included clay, silt, sands and gravel. Pertaining to different particle shape and sizes, the stress normalization exponent often varies, for e.g., n approaches unity with increment of fines Robertson and Wride (1998). Therefore, the data points in this study obtained from clean silica sand specimens do not show a reasonable comparison with the method proposed by Olsen and Mitchell (1995).

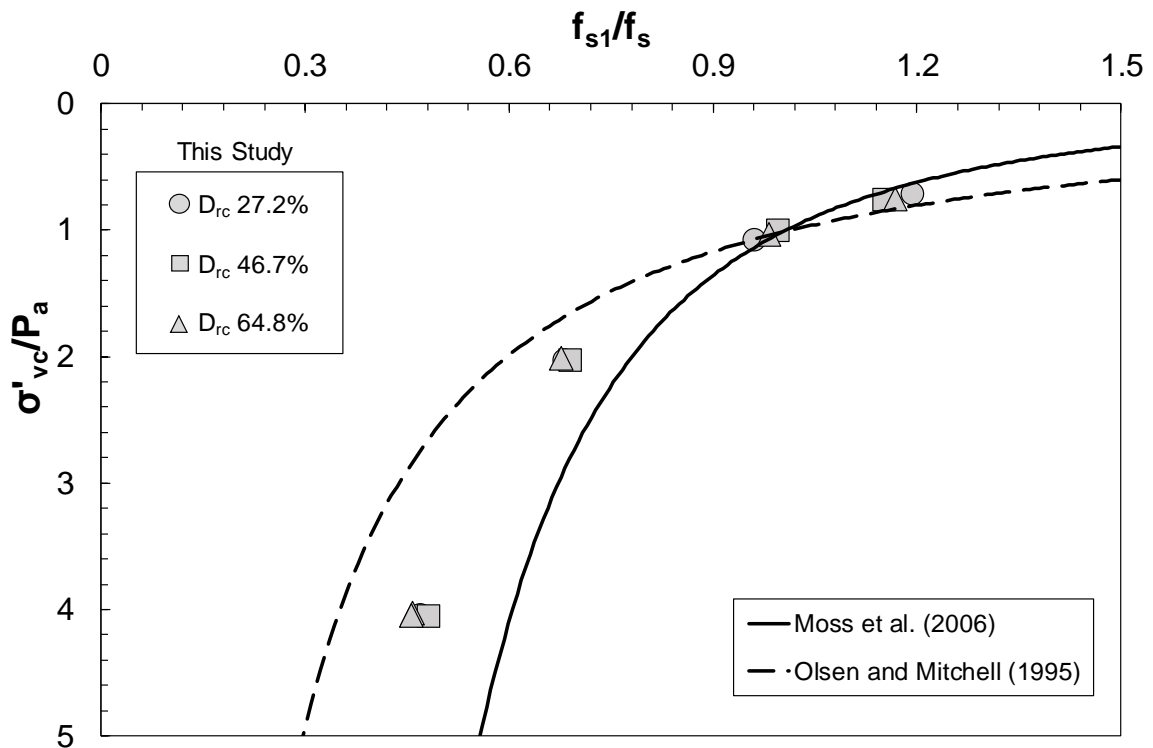


Figure 3.49: Comparison of stress normalization techniques for f_{s1}

Although majority of the studies have focussed on stress normalization methods for cone tip resistance, Olsen and Mitchell (1995) and Moss et al. (2006) have suggested stress normalization techniques for sleeve friction (f_s) as well. Figure 3.49 highlights some of the techniques and compares it with the data obtained from this study. Both the studies suggested using the similar stress normalization exponent “c” as calculated for normalizing q_{c1} and $q_{c1,net}$. Nevertheless, the stress normalization exponents for f_s from this study (0.54, 0.52, 0.57) derived at three different relative densities (25%, 45%, 65%), are used for calculating f_{s1} . In fact, the choice of stress normalization method has very minimal impact on the magnitude of f_{s1} for $\sigma'_{vc}/P_a = 0.5$ to 1.5. Beyond $\sigma'_{vc} = 150$ kPa, the stress normalization technique suggested by Olsen and Mitchell (1995) overestimates the magnitude of f_{s1} for this study, owing to a comparatively lower average stress normalization exponent ($c = 0.4$). On the other hand, the method suggested by Moss et al. (2006) underestimates the magnitude of f_{s1} for this study, owing to a comparatively higher average stress normalization exponent ($c = 0.75$) as shown in Figure 3.49.

3.8 Tip Resistance and Sleeve Frictional Resistance

The MCPTs in this study has produced a series of datapoints in terms of cone tip resistance (q_c) and sleeve frictional resistance (f_s) measured at different effective vertical stresses and relative densities. Therefore, the two obtained parameters have been plotted against each other to study and establish a general correlation. The correlation between q_c and f_s is generally investigated for development and comparison of soil classification methods (Eslami and Fellenius 1997; Mayne 2007; Robertson 2009). In fact, Robertson (2009) proposed to correlate q_c with friction ratio, F_r (%) in order to study soil classification, where F_r (%) is given by,

$$F_r = \frac{f_s}{q_{c,net}} \times 100\% \quad (3.29)$$

This study was performed only on clean silica sand specimens. Hence, comparison with existing soil classification methods does not seem reasonable. Test results on wide range of soils would provide better estimations with existing soil classification methods.

Robertson (1990) suggested using a soil behaviour chart based on friction ratio, as the author realized that friction ratio was generally more reliable than sleeve frictional resistance. The CPT penetration pore pressures (u_2) often suffers from lack of repeatability due to loss of saturation, especially when performed onshore at locations where the water table is deep and/or in very stiff soils. The sleeve resistance, f_s is often considered less reliable than the cone resistance, q_c due to variations in cone design Lunne et al. (1986). However, Boggess and Robertson (2010) provided recommendations on methods to improve the repeatability and reliability of sleeve resistance measurements by using cone designs with separate load cells, equal end-area sleeves and careful test procedures. Since soils are essentially frictional and both strength and stiffness increase with depth, and cone penetration tests have often been used to study end bearing and sleeve frictional resistance of pile foundations, correlations have been developed in this study to estimate sleeve friction from the more reliable parameter cone tip resistance. This is done by plotting the measured values of q_c and f_s from this study.

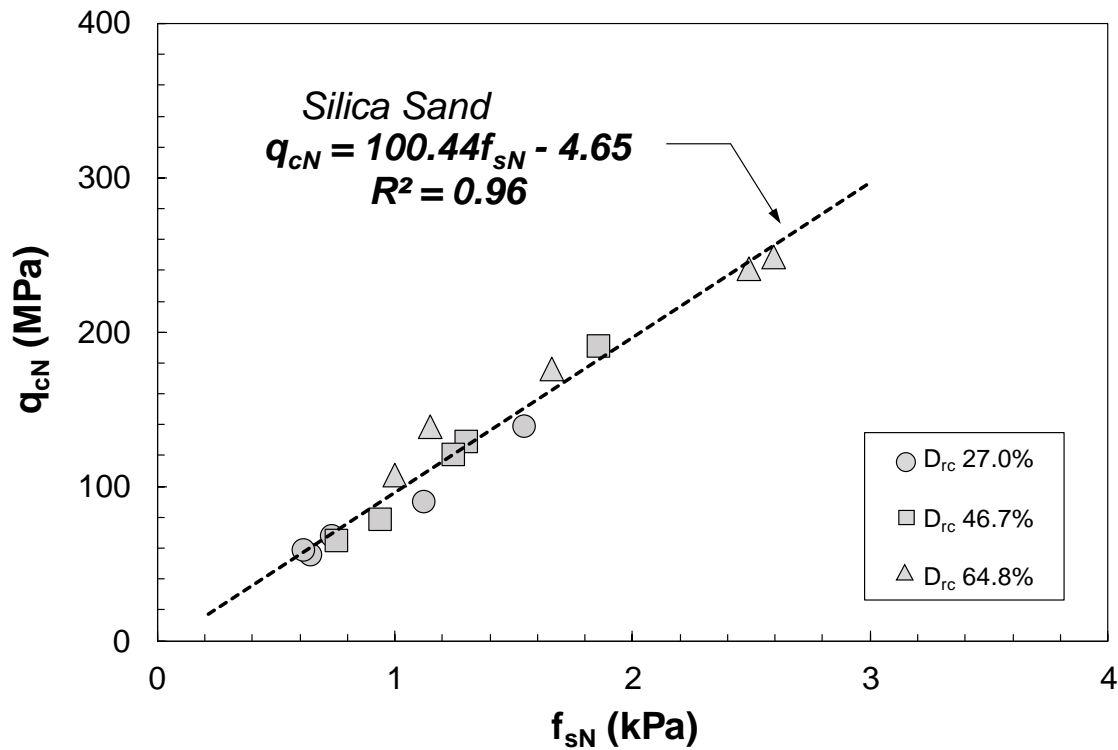


Figure 3.50: Correlation between Cone Tip Resistance and Sleeve Frictional Resistance for Silica sand

Figure 3.50 represents the $q_{cN} - f_{sN}$ and $q_{c1N} - f_{s1N}$ correlations. The locus of the data points is seen to plot along a linear function with coefficients of determination, $R^2 = 0.96$. With increasing relative density, both cone tip resistance and sleeve friction increase linearly for silica sand, shown in Equations 3.30.

$$q_{cN} = 100.44 f_{sN} - 4.65 \quad (R^2 = 0.96) \quad (3.30)$$

3.9 Evaluation of Soil Unit Weight

Soil unit weight is a critical parameter for calculating initial geostatic and overburden stresses for CPT data interpretation and estimating many other geotechnical engineering

parameters. The ideal process of estimating soil unit weight is by undisturbed sampling of in-situ soil by thin walled tube samplers, special block sampling or ground freezing techniques. However, such methods can be expensive, time consuming and highly labour intensive as they require expensive equipment to carry out the process. Therefore, indirect empirical correlations with CPT data or geophysical test data are often developed and used for quicker processing of preliminary geotechnical investigations. The soil unit weight can be calculated using fundamental index relationships as given in Equations 3.31 and 3.32.

$$\gamma_d = \gamma_w \frac{G_s}{1 + e_c} \quad (3.31)$$

$$\gamma_{sat} = \gamma_t = \frac{\gamma_w \cdot (G_s + e_c)}{(1 + e_c)}; \text{ assuming } S = 1 \quad (3.32)$$

where, γ_d = Dry unit of soil in kN/m^3 , γ_w = Unit weight of water, typically 9.8 kN/m^3 , γ_{sat} = Saturated unit weight of soil in kN/m^3 , G_s is the specific gravity of the tested material and e_c is the corresponding void ratio of the soil specimen after consolidation.

Mayne (2007) and Mayne et al. (2010) performed multiple regression analyses in both arithmetic and logarithmic scales to establish a direct correlation between unit weight of soil and CPT data. The following correlations were accordingly proposed as in Equations 3.33 and 3.34.

$$\gamma_d = 1.89 \log \left(\frac{q_c / P_a}{\left(\frac{\sigma'_{vc}}{P_a} \right)^{0.5}} \right) + 11.8 \quad (3.33)$$

$$\gamma_t = 1.81 \gamma_w \cdot \left(\frac{\sigma'_{vc}}{P_a} \right)^{0.05} \cdot \left(\frac{q_c - f_s}{P_a} \right)^{0.017} \cdot \left(\frac{f_s}{P_a} \right)^{0.073} \cdot (B_q + 1)^{0.16} \quad (3.34)$$

where, γ_t and γ_d are in kN/m^3 , B_q is the normalized pore water pressure parameter and is given by,

$$B_q = \frac{\Delta u_2}{q_{c,net}} \quad (3.35)$$

Figure 3.51 compares these correlations with the data obtained from this MCPT study conducted at $\sigma'_{vc} = 74.6, 103.9, 202.8, 404.4$ kPa and $D_{rc} = 27.2, 46.7$ and 64.6% .

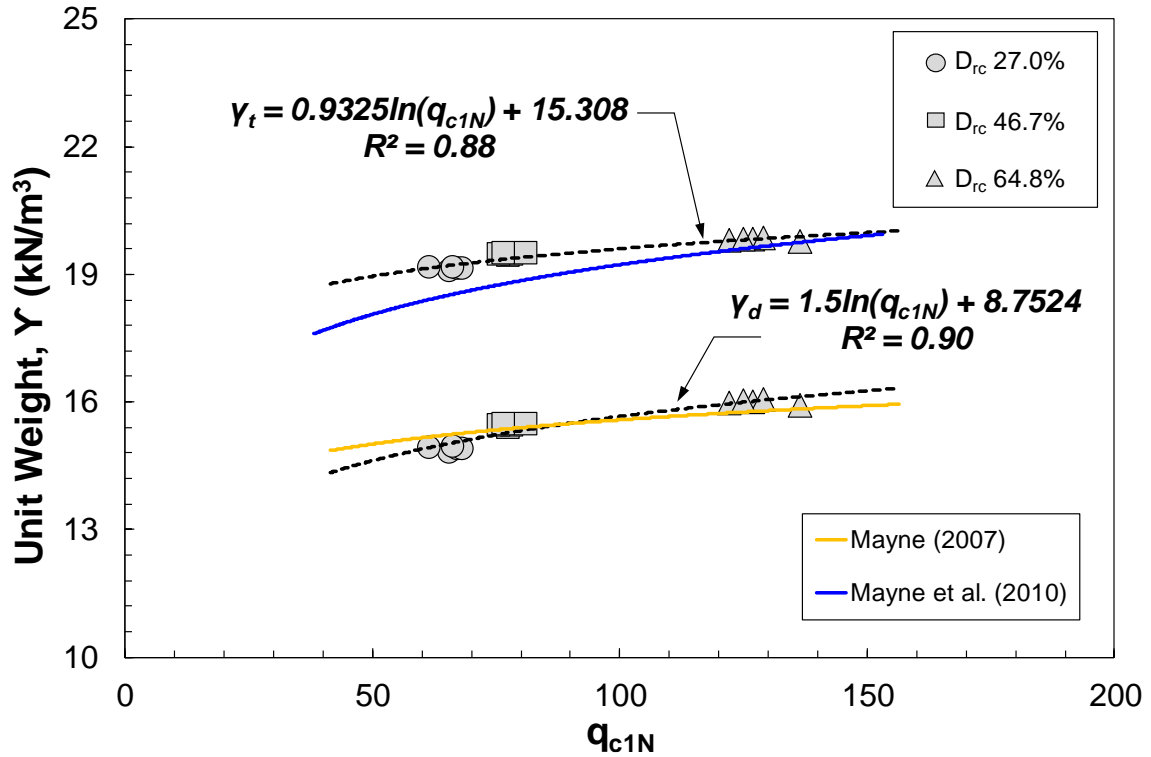


Figure 3.51: Comparison of unit weight and q_{c1N} correlation from this study with Mayne (2007) and Mayne et al. (2010)

Mayne (2007) developed the correlation given in Equation 3.33 after compiling a large database of calibration chamber-based cone penetration studies on sands, silts and clays. From Figure 3.51, that the correlation data set obtained from this study on silica sand compare well with the relationship suggested by Mayne (2007) for dry unit weight. But, later Mayne et al. (2010) developed the correlation suggested in Equation 3.34 after performing a regression analysis on CPT data obtained from different types of soil including clay and silt. Therefore, Figure 3.51 shows that the prediction by Mayne et al. (2010) somewhat underestimates the value of total unit weight relative to the trendline developed from the dataset in this study. Moreover, the consideration of sleeve friction (f_s)

in Equation 3.34 is a major difference in the two predictions. The fitted equations developed from this study between unit weight and normalized cone tip resistance are as below:

$$\gamma_d(kN/m^3) = 1.5 \ln(q_{c1N}) + 8.7524 \quad (R^2 = 0.90) \quad (3.36)$$

$$\gamma_t(kN/m^3) = 0.9325 \ln(q_{c1N}) + 15.308 \quad (R^2 = 0.88) \quad (3.37)$$

3.10 Evaluation of Sand Relative Density

The concept of relative density (D_r) was initially suggested by Burmister (1948) and it is till date one of the most extensively used geotechnical engineering parameter as an index of mechanical properties of coarse grained soils. Owing to uncertainties and extreme difficulties in retrieving good quality undisturbed cohesionless soil samples (Yoshimi et al. 1978; Hatanaka et al. 1988; Goto et al. 1992; Yoshimi 2000), geotechnical engineering practitioners often estimate relative density from penetration test results. Schmertmann (1976) through his pioneering work, was the first to correlate relative density and cone penetration test results after performing static cone penetration tests (CPT) in calibration chambers. Similarly, Jamiolkowski et al. (2001) performed 484 calibration chamber-based cone penetration tests on three silica sands (Ticino, Hokksund and Toyoura). Schmertmann (1976) suggested the following form of relationship for estimating D_{rc} :

$$D_{rc} = \frac{1}{C_2} \ln \left[\frac{q_c (\sigma'_{vc})^{C_1}}{C_0} \right] \quad (3.38)$$

where C_0 , C_1 , C_2 are empirical fitting parameters.

Modifying the similar model, Jamiolkowski et al. (2001) considered using normalized cone tip resistance and proposed the generalized form of Equation 3.38, shown in Equation 3.39,

$$D_{rc} = \frac{1}{C_2} \ln \left[\frac{q_c/P_a}{C_0 (\sigma'_{vc}/P_a)^{C_1}} \right] \quad (3.39)$$

where C_0 , C_1 and C_2 are empirical correlation factors and their values as proposed by Jamiolkowski et al. (2001), are 17.68, 0.50 and 3.10 respectively.

Besides these, there have been several other significant calibration chamber studies on different variety of sands, which explored the correlation between tip resistance and relative density. Baldi et al. (1986) studied this relationship on Ticino and Hokksund sand. Villet and Mitchell (1981) developed relative density-tip resistance correlations after performing calibration chamber tests on Monterey sand. Similarly Fioravante et al. (1991) and Kulhawy and Mayne (1990) extended their research on Toyoura quartz sand and quartz-silica sand respectively. Figure 3.52 compares the correlation trends developed from this MCPT study with the suggested correlation by Jamiolkowski et al. (2001) alongside correlation trends observed and reported by several other studies.

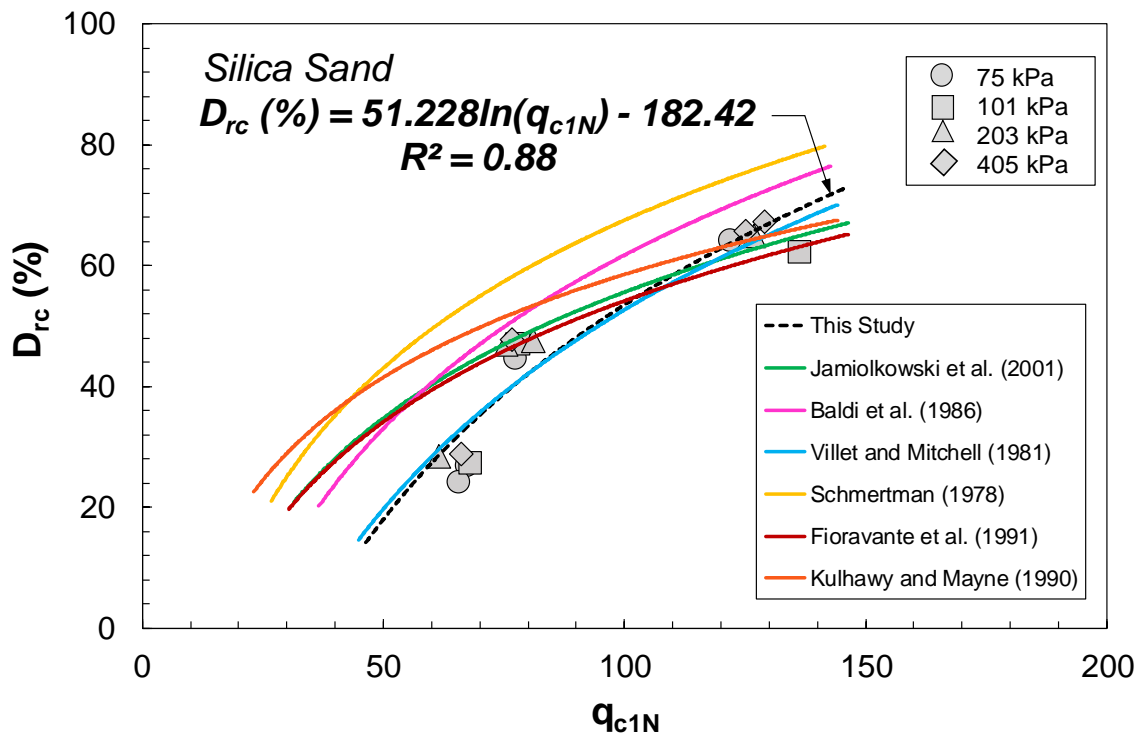


Figure 3.52: Comparison of D_{rc} and q_{c1N} correlation from this study with previous research

It can be inferred from Figure 3.52, that D_{rc} and q_{c1N} distributes over a wide range owing to different type of sands, particle size distribution or even fines content. Therefore, it can be realized that relative density and cone tip resistance correlation is sand specific. In Figure 3.52, that the correlation trendline (black) developed from the MCPT dataset in this study overall compares well with the calibration chamber study on Monterey sand by Villet and Mitchell (1981). Therefore, the sand specific correlation developed from this study is given by Equation 3.40.

$$D_{rc} (\%) = 51.228 \ln(q_{c1N}) - 182.42 \quad (R^2 = 0.88) \quad (3.40)$$

However, correlation by Jamiolkowski et al. (2001) fairly overestimates the relative density for loose and medium dense specimens. Owing to this discrepancy, empirical correlation fitting parameters C_0 , C_1 and C_2 have been determined for MCPTs from this study, through an optimization process by minimizing the standard deviation between measured and calculated penetration resistance. Therefore, for silica sand tested in this study, the suggested empirical fitting parameters are $C_0 = 39.29$, $C_1 = 0.76$ and $C_2 = 0.51$. The correlation equation for MCPTs from this study after being adjusted by a curve fitting process to adopt the model proposed by Jamiolkowski et al. (2001) takes the form,

$$D_{rc} = \frac{1}{0.51} \log \left[\frac{q_c/P_a}{39.29 \left(\sigma'_{vc}/P_a \right)^{0.76}} \right] \quad (3.41)$$

Jamiolkowski et al. (2001) also suggested a modified form of Equation 3.42 after considering compressibility into account, which is shown as below:

$$D_{rc}(\%) = 26.8 \log \frac{q_c/P_a}{\left(\sigma'_{vc}/P_a \right)^{c_1}} - b_x \quad (3.42)$$

where $b_x = 52.5$, 67.5 and 82.5 for high, medium and low compressibility sands.

Figure 3.53 present a comparison of the above-mentioned correlations relative to the MCPT results from this study to determine the compressibility factor for silica sand.

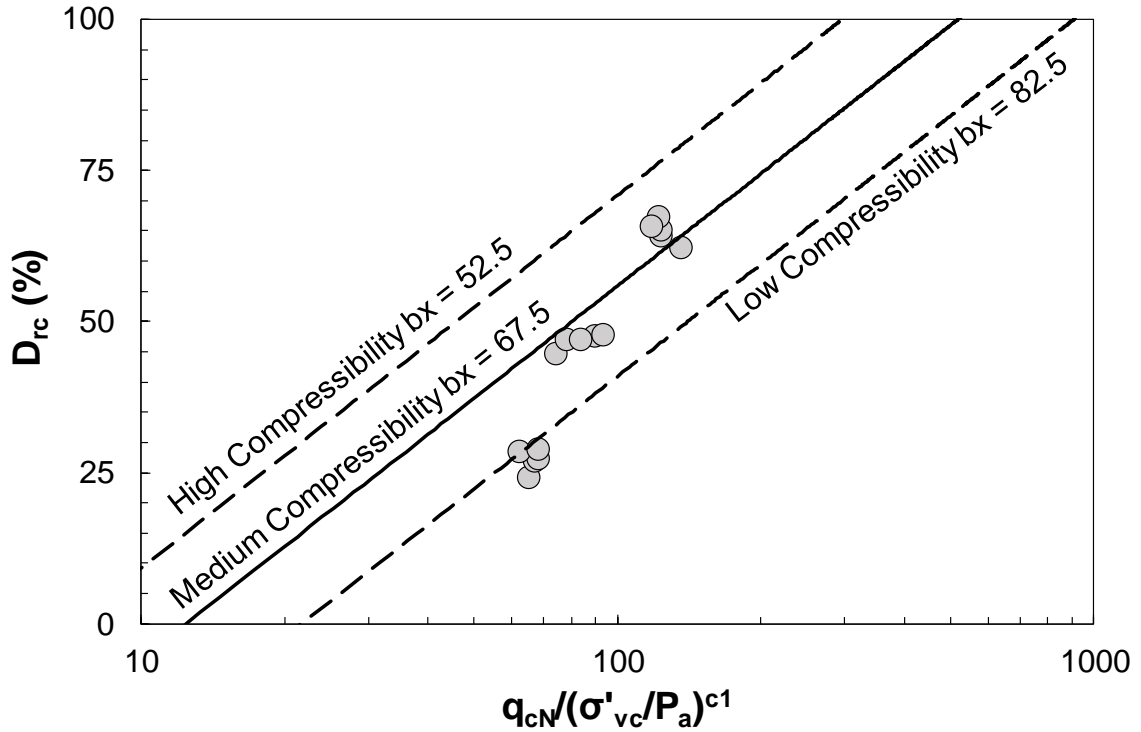


Figure 3.53: Comparison of D_{rc} from MCPT test of this study with suggested method by Jamiolkowski et al. (2001)

The dataset of MCPTs from this study appears to fall within the range of low to medium compressibility according to Figure 3.53.

Furthermore, this study focusses on the direct correlation between cone sleeve frictional resistance and relative density. This is important because sleeve friction being the one of the important parameters in a conventional test, can also be used to predict the relative density of in-situ soil. And as for silica sand of this study, the relationship is presented in Figure 3.54. The proposed correlation between normalized sleeve frictional resistance and relative density takes a logarithmic form as below:

$$D_{rc}(\%) = 88.55 (f_{s1N}) - 35.94 \quad (R^2 = 0.94) \quad (3.43)$$

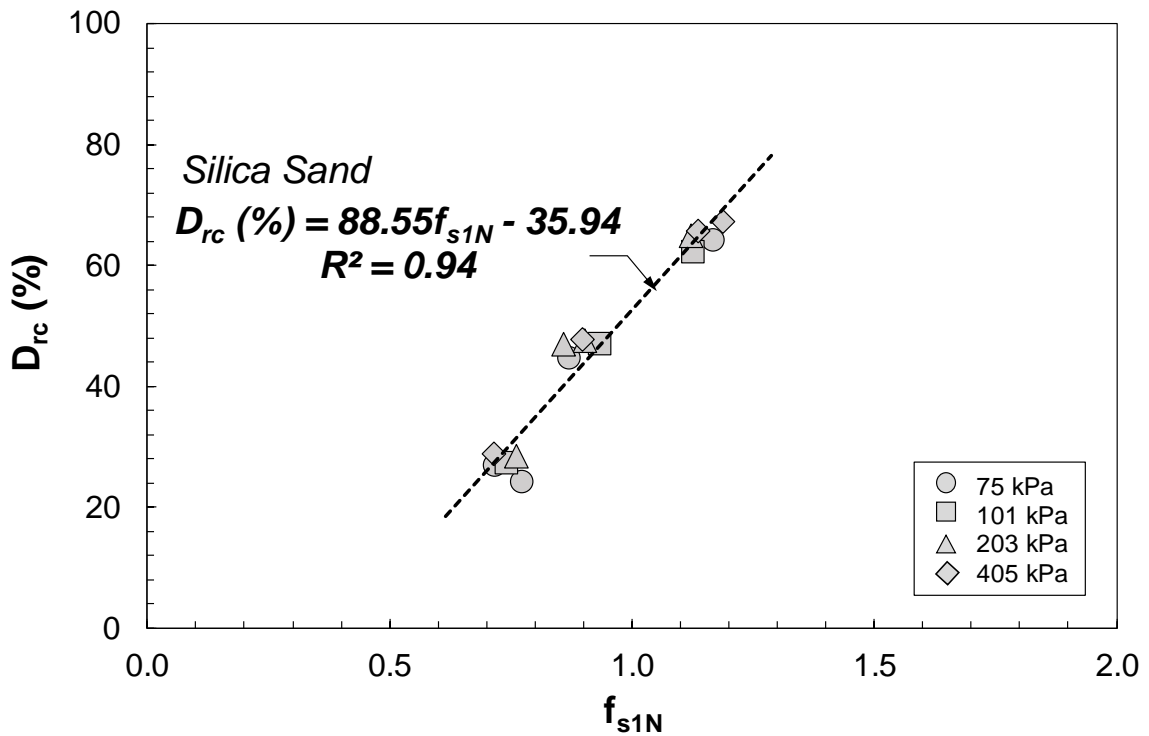


Figure 3.54: Correlation between D_{rc} and f_{s1N} for silica sand

3.11 Evaluation of Constrained Modulus

The cone penetration resistance in sands is a complex function of both strength and deformation properties and therefore several investigators have attempted to relate soil stiffness to cone penetration resistance (Schmertmann 1978; Tanaka and Tanaka 1998; Mayne 2007) from several calibration tests.

In this study, constrained modulus (M_D) was calculated for each individual test. For each MCPT, pairs of effective vertical stress (σ'_{vc}) and axial strain (ϵ_a) were fitted with a polynomial function. A third order polynomial function often provided the best fit to the σ'_{vc} - ϵ_a data, resulting in the following function:

$$\epsilon_a = a.(\sigma'_v)^3 + b.(\sigma'_v)^2 + c.(\sigma'_v) \quad (3.44)$$

Constrained modulus (M_D) was subsequently calculated by the differential of the polynomial function with respect to σ'_{vc} as below:

$$M_D = \frac{\Delta\sigma'_{vc}}{\Delta\varepsilon_a} \quad (3.45)$$

$$\frac{1}{M_0} = \frac{\delta\varepsilon_a}{\delta\sigma'_v} = 6a \cdot (\sigma'_v) + 2b \quad (3.46)$$

According to the above function, M_D could be calculated for each test at any σ'_{vc} .

Some of the most significant correlations between modulus M_D and dimensionless cone tip resistance parameter, q_{cN} are compared with the results of this study in Figure 3.55. For example, Veismanis (1974) performed laboratory calibration chamber tests on Edgarr and Ottawa sand and studied the correlation between M_D and q_c . Similar studies were conducted by Chapman and Donald (1981) on Frankston sand, and by Robertson and Campanella (1983) which summarized all the correlations along with their own proposed correlation between M_D and q_c . Table 3-6 summarizes the correlations examined in this study.

Table 3-6: M_0 - q_{cN} correlation ranges proposed by previous studies

$M_D = 0.3 q_{cN} - 1.1 q_{cN}$	Veismanis (1974)
$M_D = 0.3 q_{cN} - 0.4 q_{cN}$	Chapman and Donald (1981)
$M_D = 0.15 q_{cN} - 0.4 q_{cN}$	Robertson and Campanella (1983)

where q_{cN} is the dimensionless cone tip resistance parameter.

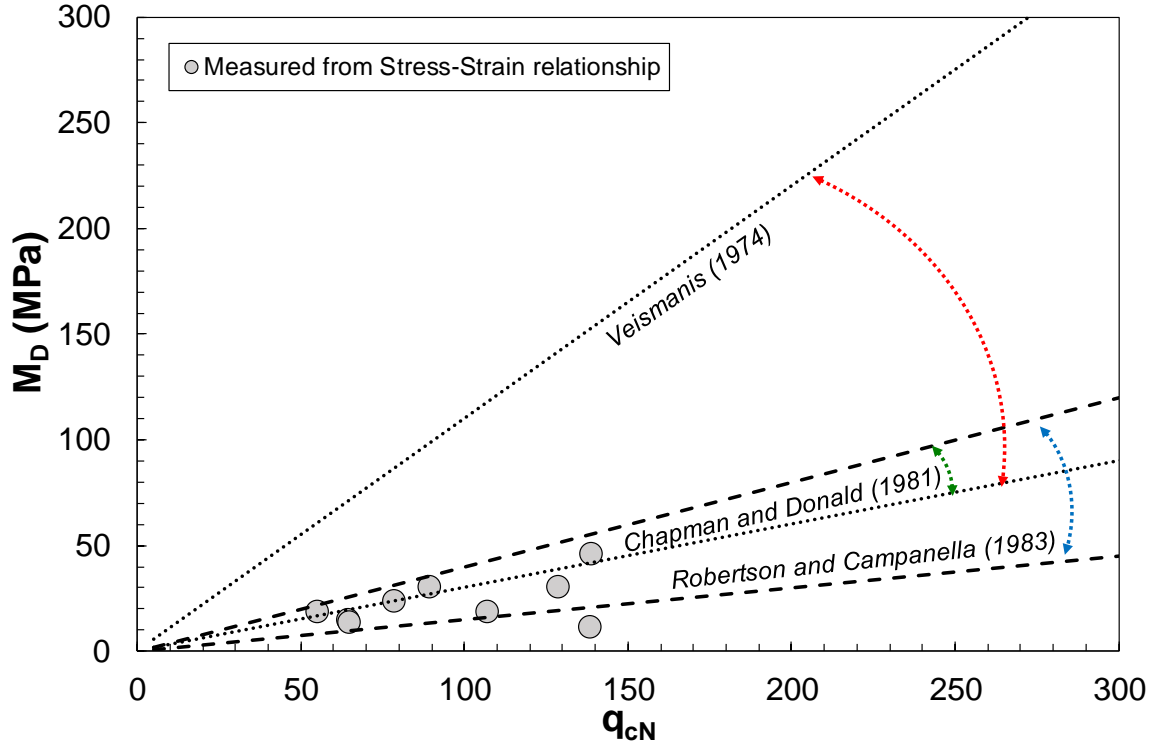


Figure 3.55: Comparison of M_D - q_{cN} correlation with previous studies

The dataset from this study agrees with the ranges prescribed by Chapman and Donald (1981) and Robertson and Campanella (1983). The upper bound of the correlation range proposed by Veismanis (1974) largely overestimates the constrained modulus at higher penetration resistances. Hence, the ranges developed by Chapman and Donald (1981) and Robertson and Campanella (1983) through their individual studies on calibration chambers, seem to be reasonable for the silica sand tested in this study. A small-strain constrained modulus (M_{max}) can also be determined from the small-strain shear modulus (G_{max}) calculated from shear velocity measurements (V_s) using bender elements as below:

$$G_{max} = \rho \cdot (V_s)^2 \quad (3.47)$$

From G_{max} , the maximum constrained modulus (M_{max}) can be calculated using the following equation after Lambe and Whitman (1969).

$$M_{max} = \frac{2 G_{max} (1 - \nu)}{1 - 2\nu} \quad (3.48)$$

where ν = Poisson's ratio.

To estimate small strain maximum constrained modulus (M_{max}) from large strain measurements like q_c , a correlation has been provided in this study. The proposed correlation is given by,

$$M_{max} = 3.26q_{cN} + 84.5 \quad (3.49)$$

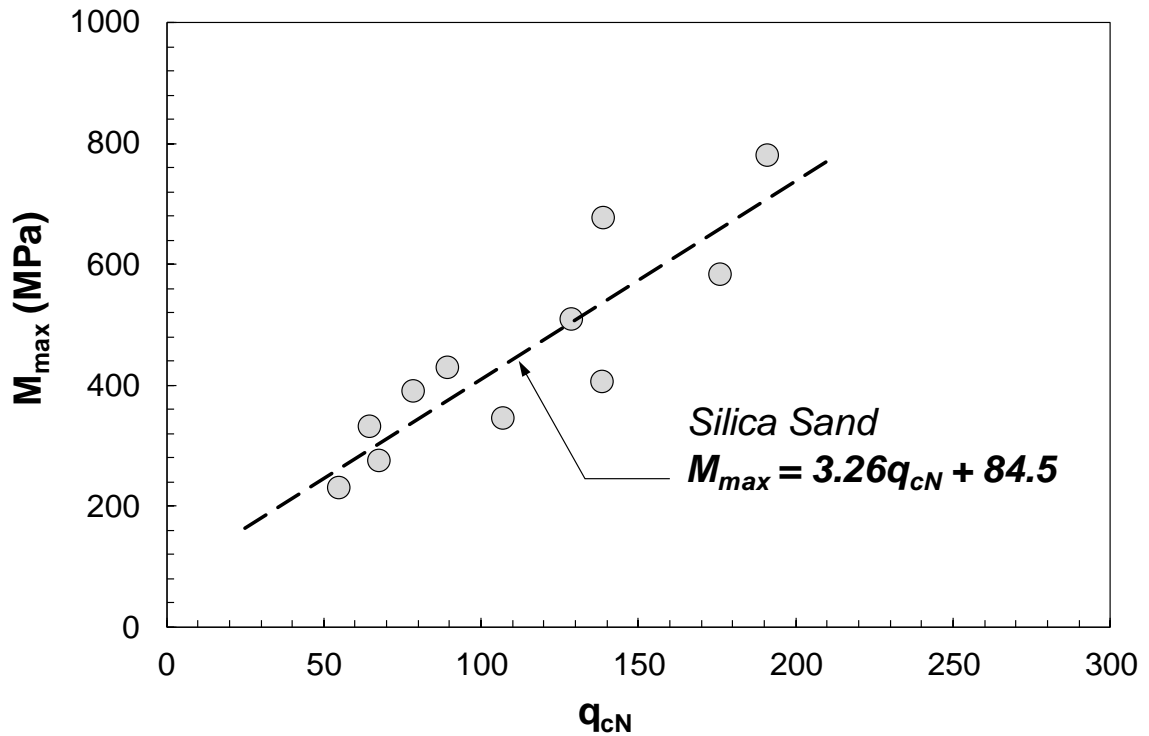


Figure 3.56: M_{max} – q_{cN} correlation for silica sand

3.12 Comparison with State Parameter

In the previous chapter, a detailed account of previous calibration chamber studies was highlighted so that all such studies can be used as a reference to compare and validate the results obtained from this MCPT study. Comparing the results from calibration chambers with in-situ tests is challenging as q_c is highly dependent on void ratio (e) and effective consolidation stress (σ'_{vc}) and the former is highly unlikely to be known in-case of in-situ tests. Furthermore, prior studies performed in calibration chambers have been conducted under different consolidation void ratio and effective consolidation stresses. The results of calibration chamber tests performed at different stress levels and densities can be compared by combining the effect of these parameters using the critical state parameter (ψ_{cs}) (Been et al. 1987) and a dimensionless cone tip resistance (Q_p).

The state parameter reflects the void ratio difference between the initial consolidation state and that on the critical state line at the same consolidation stress. The mathematical equation for ψ_{cs} is described as below:

$$\psi_{cs} = e_c - e_{cs} \quad (3.50)$$

where e_c = consolidation void ratio and e_{cs} = void ratio on the critical state line at the same consolidation stress level as e_c . Figure 3.57 presents the graphical illustration of critical state parameter.

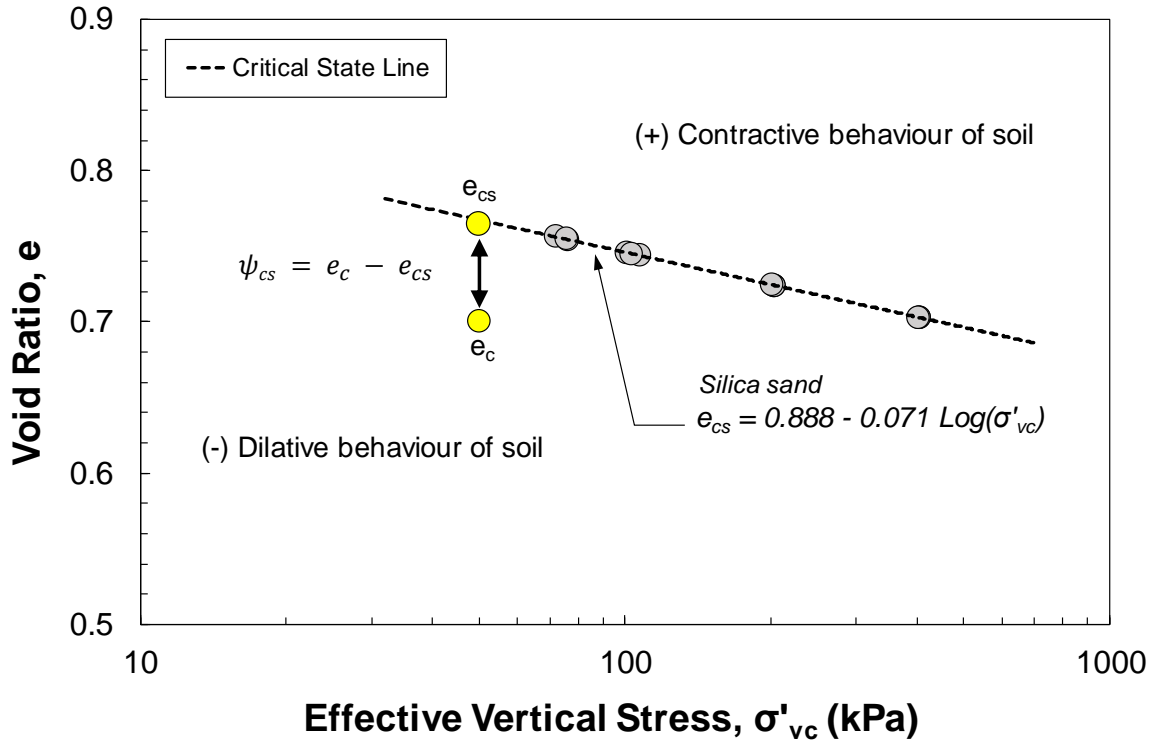


Figure 3.57: CSL for Silica sand from Boler Mountain (Mirbaha 2017)

A series of direct simple shear tests on Boler sand was performed by Mirbaha (2017) and a correlation was developed to calculate critical state void ratio (e_{cs}) in terms of effective consolidation stress as below:

$$e_{cs} = 0.888 - 0.071 \text{Log}(\sigma'_{vc}) \quad (3.51)$$

Equation 3.51 was used to calculate the critical state void ratio (e_{cs}) and therefore ψ_{cs} for each test in this study. Q_p , on the other hand is a dimensional cone tip resistance which is calculated as below:

$$Q_p = \frac{q_c - p_c}{p'_c} \quad (3.52)$$

where p_c and p'_c are total and effective mean consolidation stresses respectively.

For the current study, since the load cells that measure cone penetration resistances were zeroed before the beginning of the penetration and no excess pore pressure developed during cone penetration, p_c can be considered to be equal to p'_c . Been et al. (1987) proposed an exponential function for the relationship between ψ_{cs} and Q_p as below:

$$Q_p = k * \exp(-m\Psi_{cs}) \quad (3.53)$$

where k and m are the fitting parameters for the $Q_p - \psi_{cs}$ correlation.

Been et al. (1987) collected data from a wide range of calibration chamber tests on different sands such as Hokksund, Ticino, Ottawa sands, Monterey, Reid Bedford, etc. and also performed calibration chamber based CPTs on Erksak sand. Figure 3.58 compares the results of the $Q_p - \psi_{cs}$ correlation for the current study with many of the calibration chamber studies reported by Been et al. (1987).

Equation 3.54 presents the $Q_p - \psi_{cs}$ correlation for silica sand based on the form proposed by Been et al. (1987).

$$Q_p = 83.461 \exp(-5.674\psi_{cs}) \quad (R^2 = 0.67) \quad (3.54)$$

Overall, the correlation of $Q_p - \psi_{cs}$ for silica sand was found to compare well for denser test specimens with other calibration chamber studies, however, for looser specimens, Q_p values were found to be higher than in most studies. This discrepancy is most likely due to the difference in sand characteristics, i.e. particle shape, mineralogy and gradation. Moreover, Been et al. (1987) mentioned that test data for states looser than $\psi_{cs} = -0.05$ were not available and the trendlines shown in Figure 3.58 primarily pertain to medium dense and dense specimens. This is one of the reasons why the comparison is slightly off for the data points corresponding to state parameter beyond 0, relative to the other trendlines.

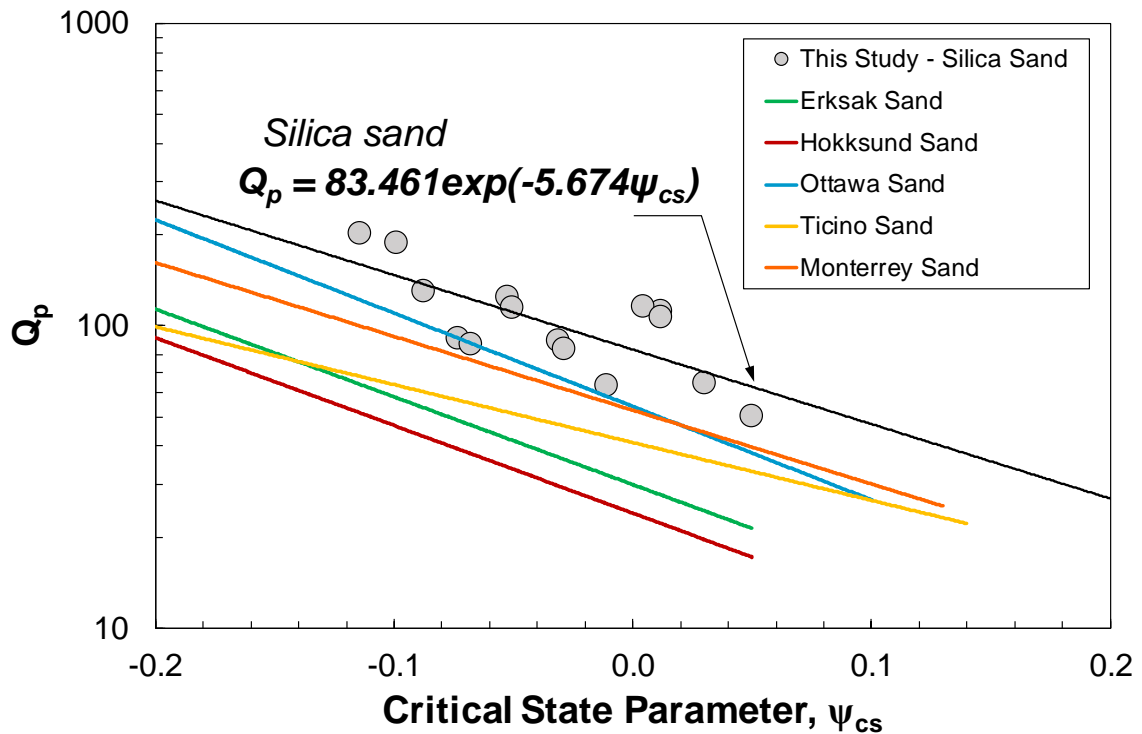


Figure 3.58: Correlation of Q_p - ψ_{cs} for silica sand in comparison with previous studies

Jefferies and Been (1995) mentioned that the dependence of k and m on the slope of CSL is the weakest point of Equation 3.53. Been et al. (1987) suggested that a unique relationship exists between logarithmic Q_p and ψ_{cs} for various sands. However, Sladen (1989) found that a stress level bias exists in the basic $Q_p - \psi_{cs}$ correlation. After investigating test results on normally consolidated Ticino Sand by Been et al. (1987), Sladen et al. (1989) highlighted some of the observations in his study which are as follows:

- (a) For a given stress level, there exists a linear relationship between log of Q_p and ψ_{cs} .
- (b) The stress level is however, not unique, rather, it varies with variation in mean stress level.
- (c) The slope of the series of linear relationships corresponding to each stress level is much flatter than the mean linear trendline.
- (d) The intercept “ k ” of the projections of these lines on the $\psi_{cs} = 0$ axis decreases with increasing stress.
- (e) Even for a given range

of mean stress level, there is a scatter in experimental data which is significant in for some sands. (f) There is a dearth test results on low stress levels and high values of state parameter. Owing to this, the scatter of the data based on which correlations have been developed can be misleading. Hence, Sladen (1989) concluded by mentioning that the state parameter approach is not a reliable way of comparing chamber test data with field situations for a different deposit. As shown in Figure 3.59, there is a substantial difference in $Q_p - \psi_{cs}$ correlations between tests at low and high effective consolidation stresses and moreover at different relative densities.

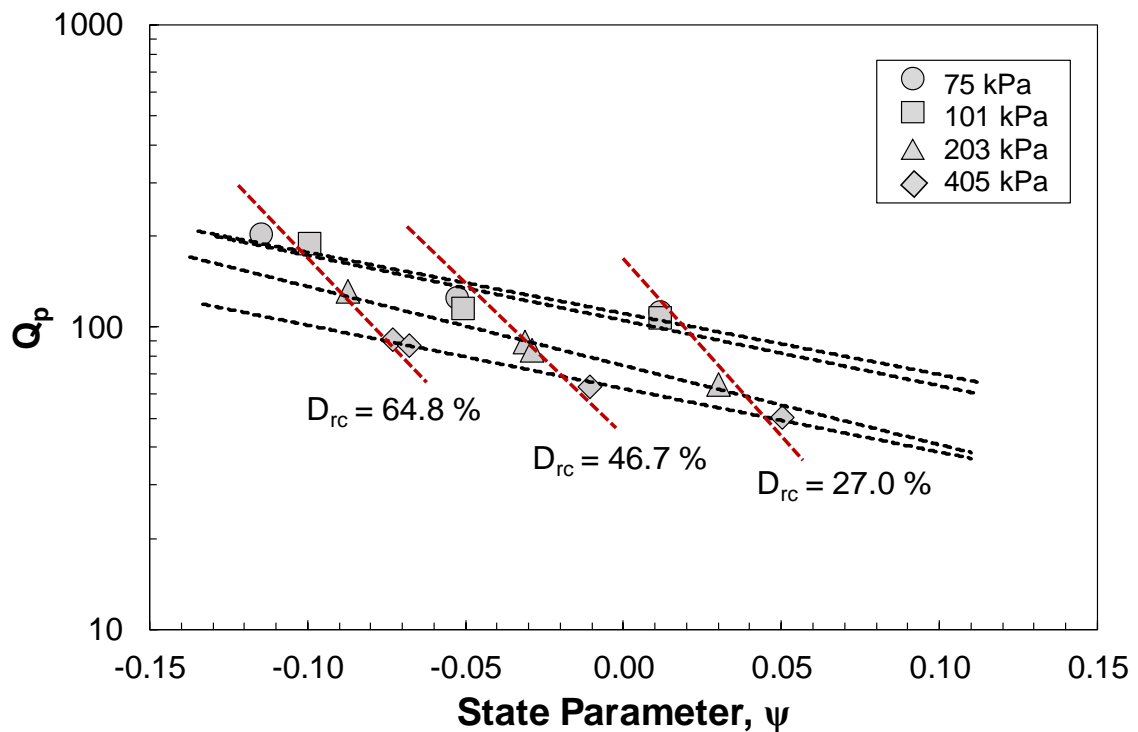


Figure 3.59: Illustration of stress level bias highlighted in this study

The stress level bias shown in Figure 3.59 is one of the shortcomings of the state parameter approach as it can be seen that the magnitude of cone tip resistance is lower in case of

higher effective consolidation stress ($\sigma'_{vc} = 404.4$ kPa) compared to lower consolidation stresses ($\sigma'_{vc} = 74.6$ kPa). Moreover, for future studies, it would be helpful to complete MCPTs on different sands, particularly in a loose condition and at a variety of consolidation stresses, as this may give a more accurate comparison of expected calibration chamber test results in these conditions relative to the compared studies shown in Figure 3.59.

3.13 Conclusion

In this study a series of MCPTs were completed in a calibration chamber using a miniature cone penetrometer to determine the behaviour of a silica sand collected from the Boler Mountain in London, Ontario. The tested material was characterized based on conventional CPT parameters like cone tip resistance (q_c) and sleeve friction (f_s). As discussed, earlier in this chapter, the calibration chamber was developed at Western University after modifying a conventional triaxial cell and load frame. Moreover, the triaxial setup was upgraded by Jones (2017) and it therefore had the capability to impose K_0 anisotropic consolidation for each test to replicate in-situ stress conditions. Silica sand specimens were tested at three relative densities (25%, 45% and 65%) and at four different consolidation stresses (75 kPa, 100 kPa, 200 kPa and 400 kPa). This provided a valuable means to validate the current calibration chamber test results across a wide range of relative densities and consolidation stresses with other studies.

- a. Several concerns related to the mechanism of using a miniature cone penetrometer and a reduced scale calibration chamber, rather than conventional in-situ methods, were investigated with other studies of similar nature. Some of the concerns were: scale effect, particle crushing, cone penetration rate and calibration chamber boundary effects. Based on literature review of past research, it was concluded that the only reasonable concern was the calibration chamber boundary effects. The remaining concerns were investigated and mitigated based on design and procedural aspects of the calibration chamber and the tested material. The concern regarding boundary effects was studied in detail and after reviewing several other studies (Huang and Hsu 2005; Goodarzi et al. 2018), a reasonable approach for

converting the measured cone tip resistance to that in a free-field soil deposit was used to correct the magnitude of cone tip resistances.

- b. All the obtained parameters were normalized to a reference pressure of 100 kPa. This is was done to negate the influence of initial geostatic stresses acting on the soil. Stress normalization was carried out using stress normalization exponent derived for each parameter at a given relative density level. The average stress normalization exponents for q_c and f_s were found to be 0.56 and 0.54, respectively. These exponents were found to be comparable with those established by other studies.
- c. Cone tip resistance and sleeve frictional resistance were correlated in this study and a linear function was developed between q_c - f_s and q_{c1} - f_{s1} .
- d. Several other evaluations were completed in this study such as with soil unit weight, relative density, constrained modulus, and comparison with state parameter.
- e. Predictive models for soil unit weight proposed by Mayne (2007) and Mayne et al. (2010) were used to compare correlations developed between unit weight and penetration resistance evaluated in this study. The results compared well with the reviewed studies especially for dry unit weight. The relationship of unit weight and shear wave velocity were found to be comparable for dense specimens with Burns and Mayne (1996). The correlations developed in this study are presented and can be used to estimate unit weight for silica-carbonate sand in case of difficulties in obtaining undisturbed soil samples.
- f. Predictive models for estimating D_{rc} from CPT data were also reviewed. The correlation trendlines between D_{rc} and q_{c1N} compared well with the reviewed studies. The trendlines showed better agreement with the correlation trendline developed by Villet and Michell (1991).
- g. Constrained modulus (M_D) was determined from the relationship between vertical stress and axial strain for each relative density and was plotted against q_{cN} . The dataset developed in this study showed good agreement with the constrained

modulus correlations suggested by Robertson and Campanella (1983) and Chapman and Donald (1981).

- h. Finally, the current MCPT results were compared with previous calibration chamber studies by correlating Q_p to ψ_{cs} based on an equation suggested by Jefferies and Been (2006). The dataset obtained from this study compared well with most the previous studies however, for looser samples, the dataset was not in complete agreement with other trendlines. The phenomenon of stress level bias in such a mechanism has also been highlighted by individually plotting the cone penetration values against state parameter, which makes the viability of using state parameter as a general comparison tool questionable.

Chapter 4

4 Non-destructive Testing with Shear Wave Velocity and Electrical Resistivity Measurements on Silica Sand

This chapter presents the results of a series of Bender Element and Electrical Resistivity tests performed on silica sand at a different effective consolidation stresses ($\sigma'_{vc} = 75$ kPa, 100 kPa, 200 kPa, 400 kPa) and relative densities ($D_{rc} = 25\%$, 45%, 65%) and the measured shear wave velocity (V_s), electrical resistivity of pore fluid (ρ_f) and bulk electrical resistivity of saturated specimens of silica sand (ρ_b). The results are presented alongside a wide range of correlations established between these parameters as well as the MCPT results from Chapter 3.

4.1 Introduction

Shear wave velocity is often used in constitutive models to determine the small-strain response of soils, estimate the in-situ stress state of cohesionless soils (Robertson et al. 1995), predict ground deformation, seismic site classification, to characterize site-response for evaluating seismic hazard, and assessing liquefaction potential in cohesionless soils (Andrus et al. 2004; Clayton 2011). It can also be used to determine a variety of geotechnical properties including soil classification (Mayne (2007), physical soil properties (Richart et al. 1970; Mayne 2007), and liquefaction triggering analysis (Andrus and Stokoe 2000; Kayen et al. 2013). Shear wave velocity represents a measure of soil stiffness in terms of the maximum shear modulus (G_{max}), which is calculated in Equation 4.1. Shear wave velocity and G_{max} are two of the most fundamental parameters for characterizing soils in geotechnical engineering design practice.

$$G_{max} = \rho \cdot V_s^2 \quad (4.1)$$

where, G_{max} is the maximum shear modulus (expressed usually in MPa) corresponding to very small values of strain ($\gamma < 10^{-5}$), V_s (m/sec) is the measured shear wave velocity and ρ (kg/m^3) is the density of the soil. The low strain shear modulus, G_{max} is an important

parameter to determine site response characteristics for seismic events. Shirley and Hampton (1978) performed the first study to use bender elements in soil testing for determining shear modulus. Commonly used laboratory devices like triaxial shear (Bates 1989; Brignoli et al. 1996; Jones 2017), direct simple shear (Dyvik and Madshus 1985; Jones 2017; Mirbaha 2017), and ring shear apparatuses (Youn et al. 2008; El Takch et al. 2016) were modified to record shear wave velocity measurements alongside the conventional test results from the devices. Bender elements are installed in standard testing devices, used to generate and detect shear motion. When an input waveform voltage is applied on the S-wave transmitter, one piezoceramic sheet extends and the other contracts, leading the transmitter to bend and generate a shear wave signal. The S-wave receiver bends when the shear wave arrives, propagating an electrical signal that can be visualized and measured by a data logger. The operation of bender elements for S-wave transmission was well described by other researchers (Dyvik and Madshus 1985; Lings and Greening 2001; Lee and Santamarina 2005; Camacho Tauta et al. 2012). During bender element testing, both the transmitted and received signals are recorded to determine the travel time, t , of the shear wave through a sample. The shear wave velocity, V_s , can then be calculated from the tip-to-tip travel length between the bender elements, L_{tt} , and travel time, t , as follows (Viggiani and Atkinson 1995):

$$V_s = \frac{L_{tt}}{t} \quad (4.2)$$

There are many studies done previously which showcase research on various time and frequency domain models to interpret shear wave velocity (Lee and Santamarina 2005; Camacho-Tauta et al. 2015). The time domain methods determine the travel time directly from the time lag between the transmitted and received signals. Referring to different characteristic points, the time domain methods can be classified into “arrival-to-arrival” method, “peak-to-peak” method and “cross correlation method” according to literature. In this study, shear wave velocity has been calculated according to the peak-to-peak method. In this method, time delay between the peak of transmitted signal and the first major peak of received signal is regarded as the travel time (Clayton et al. 2004; Ogino et al. 2015). The difficulties in test interpretation have been noticed previously and various strategies

for minimizing any form of error were proposed by several studies (Brignoli et al. 1996; Viggiani and Atkinson 1995). A common feature of all of these works was the identification and mitigation of source near-field effects. Further works by Arulnathan et al. (1998) and Blewett et al. (1999) introduced new considerations but near-field effects are still held as a central to uncertainties of test results (Kawaguchi et al. 2001). Past studies have also proposed setting the maximum wavelength of the shear waves (λ) to less than twice that of the bender elements tip to tip distance (i.e. the height of the specimen minus the height of the bender elements) to avoid near-field effects (Marjanovic and Germaine 2013). Pennington et al. (2001) pointed out that when the L_{tt}/λ values range from 2 to 10, a good signal can be obtained. Wang et al. (2007) advocated a ratio greater than or equal to 2 to avoid the near field effect. Similarly, a value of 3.33 was recommended by Leong et al. (2005) to improve the signal interpretation. In this study, only the values of shear wave velocity corresponding to $L_{tt}/\lambda > 2$ has been considered for analysis.

Another geophysical technique to characterize in-situ soil is by measuring soil electrical resistivity ρ (ohm·m). Electrical conduction in saturated cohesionless granular sediments occurs through the interstitial water as the soil grains have extremely high orders of resistivity. Electrical resistivity is therefore determined by the amount of water present in the soil-water medium, its salinity and the distribution of water in the medium. The porosity of the medium determines the amount of water that can be present in the system. However, salinity can be different in different types of soil-water formations depending on the concentration of conductive materials present in the water. To compare resistivities of different samples, it is therefore necessary to normalize the resistivity values in order to eliminate the influence of salinity. This is generally done by calculating the formation factor (FF) which is defined as the ratio of bulk electrical resistivity (ρ_b) of the sample to the electrical resistivity of the pore fluid (ρ_f).

$$FF = \frac{\rho_b}{\rho_f} \quad (4.3)$$

Archie (1942) presented a strong empirical evidence towards the correlation of formation factor and porosity as shown below:

$$FF = n^{-m} \quad (4.4)$$

where “n” is the porosity fraction of the soil and “m” is the slope of the line representing the relationship under discussion.

Archie (1942) described “m” to be dependent on the pore volume geometry. The equation comes with a boundary condition that at 100% porosity, formation factor will be equal to unity. Existing studies (Keller and Frischknecht 1966; Parkhomenko 1967; Arulanandan and Muraleetharan 1988; Mazac et al. 1990; Thevanayagam 1993) have found that for soils, electrical resistivity depends on many factors such as porosity, electrical resistivity of the pore fluid, composition of the solids, degree of saturation, particle shape and orientation, and pore structure. A comprehensive geophysical well logging was completed through 1961 by Dakhnov (1962) who summarized the factors that affect electrical resistivity of a porous media, which were: amount of clay/silt in the sediment, the porosity of the sediment, the degree of saturation of the sediment, temperature of the sediment, cation exchange capacity of the soil minerals and resistivity of the interstitial water. All these reasons made several investigators develop more correlations involving formation factor and porosity. Winsauer et al. (1952) introduced the generalized form the Archie’s first equation which is given by,

$$FF = a . n^{-m} \quad (4.5)$$

This equation has been termed the Archie – Winsauer equation. In this equation, Winsauer et al. (1952) introduced a tortuosity factor “a” which is a function of pore volume tortuosity. This factor generally decreases with an increase in compaction, consolidation, age or cementation of a soil mass. There are several other mathematical models involving formation factor and porosity developed by investigators according to their material and testing conditions. Not only field tests, but also some laboratory tests were performed to investigate the formation factor-porosity relationship (Erchul and Nacci 1971).

4.2 Design of the Non-destructive Testing Chamber

The chamber designed and used in this study was modified at Western University, London Ontario, Canada, from a large triaxial compression testing chamber which was used for miniature cone penetration tests (described in chapter 3) has been used for the non-destructive tests in this chapter as well. The triaxial cell used for this study was able to fit a specimen height of 190 mm and a diameter of 150 mm. For electrical resistivity measurements, the top acrylic cap used in the MCPTs, was replaced with a modified cap which could accommodate a portable electrical resistivity probe that housed 4 parallel stainless-steel electrodes. The resistivity probe known as the “Hydra-probe” was manufactured by Stevens Water Monitoring Systems Inc., Portland USA. The University Machine Shop at Western University fabricated the specimen cap to hold the electrode assembly at its center as shown in Figure 4.1.

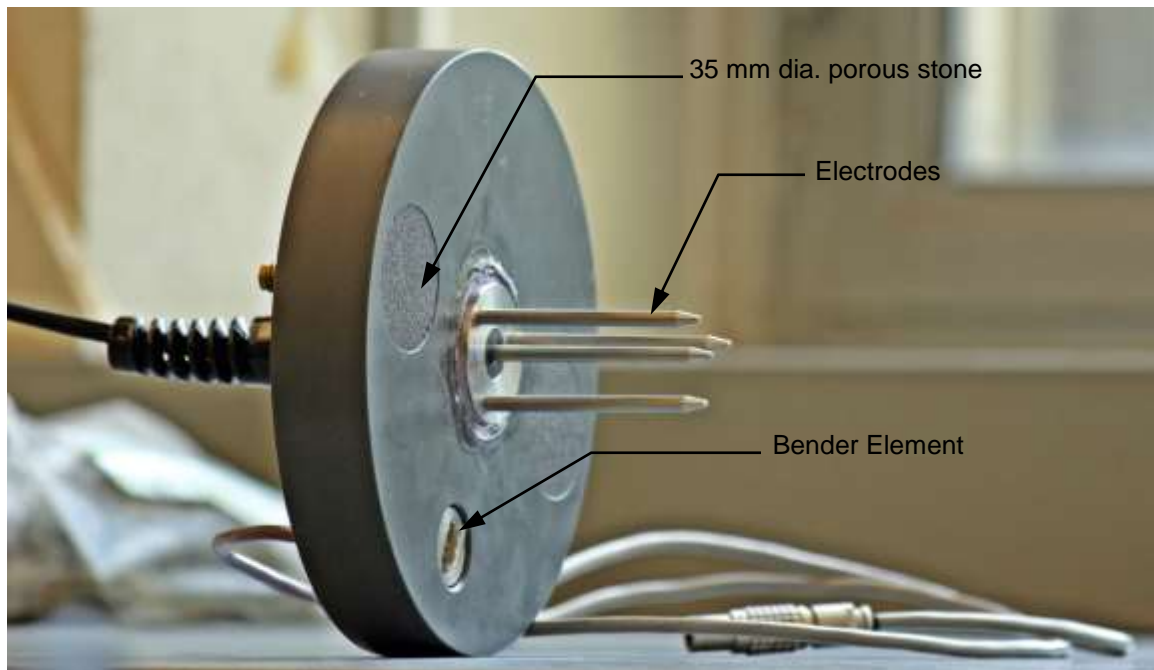


Figure 4.1: Modified top cap for electrical resistivity measurement

The chamber assembly consists of a circular metallic base platen on which a finely machine polished acrylic cell (412 mm in height and 190 mm internal diameter) was placed and finally a metallic top cap on the acrylic cell. The base platen and the top cap on either end of the acrylic cylindrical cell were held together tightly by three threaded rods to ensure that the acrylic cell is tightly fit in between the two plates. Two well-greased O-rings were placed at the junctions of the acrylic cell and the two plates so that the rubber gaskets prevent any form of leakage during the test.

During the tests, the acrylic cell was filled with 100% pure silicone oil to generate cell pressure. Oil, instead of water was used in this study to prevent the electrical connections and the Hydra-probe from any electrical short cuts. An external fluid pressure pump as describe in chapter 3, was used for to generate cell fluid pressure inside the testing chamber. On top of the base platen, a 150 mm diameter acrylic bottom disk was placed above a hydraulic piston. The base platen was equipped with a hydraulic piston to enable the application of vertical stress on the specimen to develop an anisotropic consolidation state or, a K_0 consolidation state. K_0 represents the ratio of horizontal stress (σ'_{hc}) to that of vertical stress (σ'_{vc}) after consolidation, during which, the specimen undergoes zero lateral strain. This stress anisotropy and boundary condition was an attempt to replicate an in-situ stress condition. The hydraulic piston was controlled by another fluid pressure pump like that of the cell fluid pump, mentioned above. The fluid from the pressure pump flowing into the piston generated hydraulic pressure and ultimately enabled uplift of the bottom disk situated above the piston. The description of the hydraulic piston and the corresponding calibration tests to determine its internal uplift friction has been described in detail in chapter 3.

The metallic base platen was equipped with 6 pressure line connections to control drainage, pore water pressure, cell pressure and piston pressure. A 50 mm in diameter porous disc was embedded into the bottom loading cap to provide drainage for the specimen.

A 0.5 mm thick latex rubber membrane held in place by multiple O-rings around the bottom disk, surrounded the specimen, therefore creating a flexible boundary. The membrane was long enough to enclose the entire height of the specimen as well as the bottom and top

acrylic caps. The top cap that sat on the specimen was specially designed for the top of the specimen, which was equipped with the housing of the electrode assembly at its center. These electrodes penetrate the soil sample until the bottom surface of the top cap rested on the specimen. The other side of the top cap had the cable propagating from the electrodes to the outside of the Hydra-probe chamber. At this juncture, the cable was fixed with ferrules and nuts to prevent any form of leakage from the chamber shown in Figure 4.3.



Figure 4.2: Illustration of the electrode cable on the upper side of the top cap

Two 35 mm diameter porous stones were installed in the inner surface of the top acrylic disk on either side of the electrode, to connect the specimen to drainage lines. The two porous stones were again internally connected so that the distribution of pressure throughout the specimen is uniform. Like the bottom disk, the top cap was also clamped by two O-rings to seal the latex membrane tightly against the walls of the cap. The upper surface of the top cap is shown in Figure 4.2.

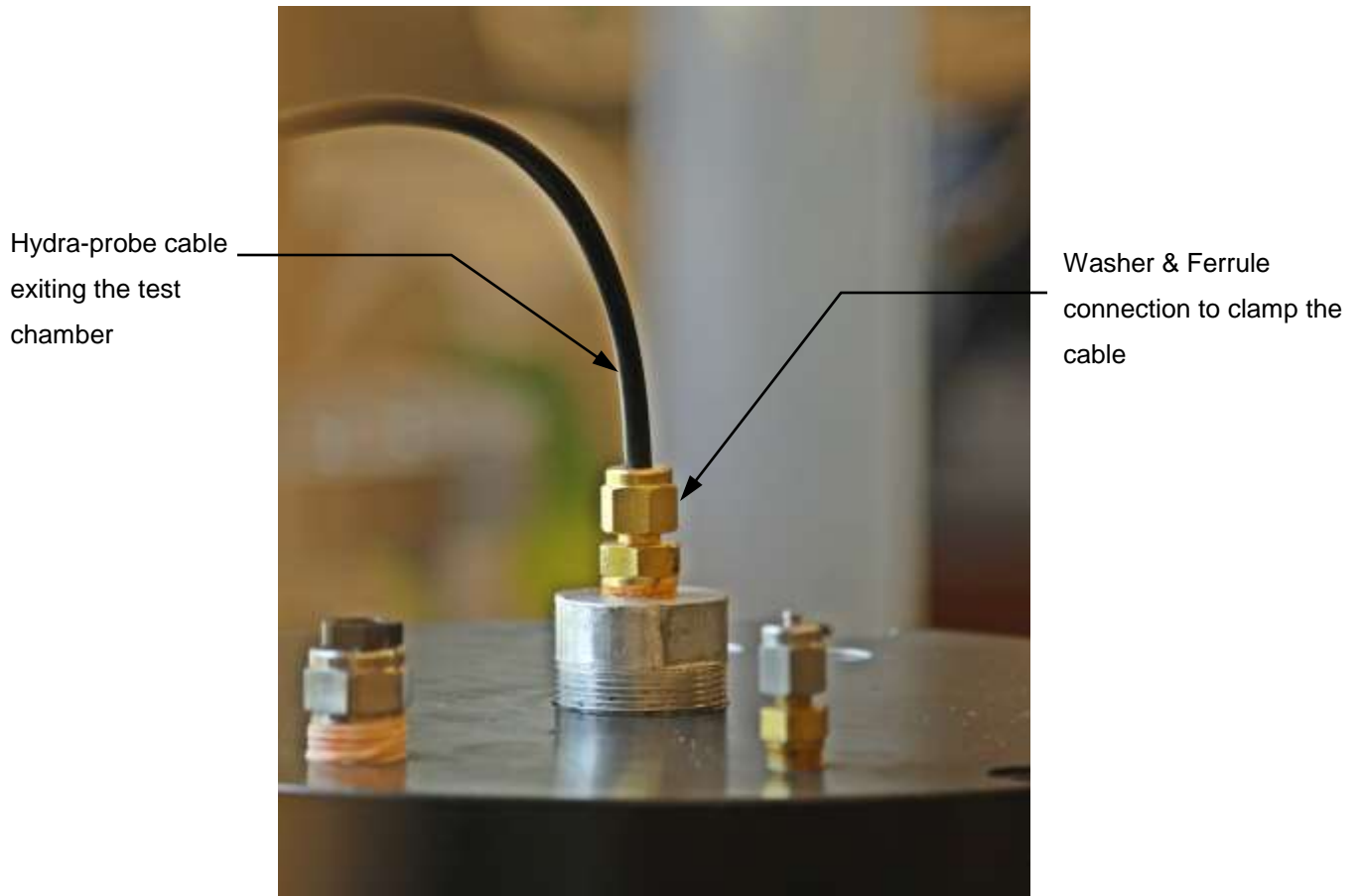


Figure 4.3: Special connection for the Hydra-probe to prevent leakage

A cylindrical hollow acrylic spacer cut axially into two pieces were placed on top of the specimen, resting on the top acrylic cap inside the Hydra-probe chamber. The spacer was built in a way to allow accessibility for the drainage lines around it and the cable of the resistivity probe housing. The purpose of this spacer was to provide axial reaction force to the specimen. Initially, at the beginning of the test, a small gap exists between the top of the acrylic spacer and the top metallic cap of the triaxial chamber. As the pressure inside the piston cavity increased and upward movement of the specimen was initiated, the gap minimized. Ultimately, after a point in time, the acrylic spacer came in contact with the top cap of the chamber. This phenomenon is called “docking”, as the spacer was then docked to the roof of the chamber. Hence, during anisotropic consolidation, further pressure from

the piston cavity would axially compress the specimen generating a vertical stress. A graphical representation of acrylic spacer is provided in Figure 3.8, Chapter 3.

One of the most significant features of this modified Hydra-probe chamber is the addition of embedded piezo-electric bender elements on both the top and bottom acrylic disks that confine the specimen. The bender elements, used to send and receive shear waves, are developed by GDS Instruments, United Kingdom. A data acquisition and processing unit was also used to record and interpret the shear waves generated by the bender elements. The top and bottom disks were modified to tightly fit 20 mm diameter cylindrical metal inserts that hold the cantilever type bender elements. The bender elements themselves are small metal pieces which were approximately 2.8 mm in height, 11.7 mm in length, and 1.5 mm in width, held together by a silicone sealing product to prevent leakage around the bender element through the insert. The metal inserts were installed in the acrylic disks in a way that the top of the inserts was flush with the surface of the disk. Hence, the bender elements were completely embedded inside the specimen. Narrow grooves were machined on the cylindrical surface of the metal inserts to hold O-rings at the bottom and mid-level, that would provide a complete seal between the metal inserts and the cut-out hole in the acrylic disk (refer to Figure 4.4) An electric current was transmitted through the bender elements, causing it to vibrate transversely relative to its fixed support. The vibrations caused a sinusoidal wave pattern to be emitted from one bender element which propagated through the specimen and was finally received by the other bender element on the opposite acrylic disk. A high signal voltage of ± 14 mV was used to generate strong shear waves and reduce the effect of noise on the wave pattern. The data processing unit then analyzed the incipient wave and the received wave with regards to time and travel distance to produce the shear wave velocity of the soil, V_s (m/sec) as shown below:

$$V_s \text{ (m/sec)} = \frac{L_{tt}}{\Delta t} \quad (4.6)$$

where, Δt (sec) is the time difference between the first positive peak of the received wave and the first positive peak of the incipient wave. L_{tt} denotes the distance from one tip of a bender element to the another.

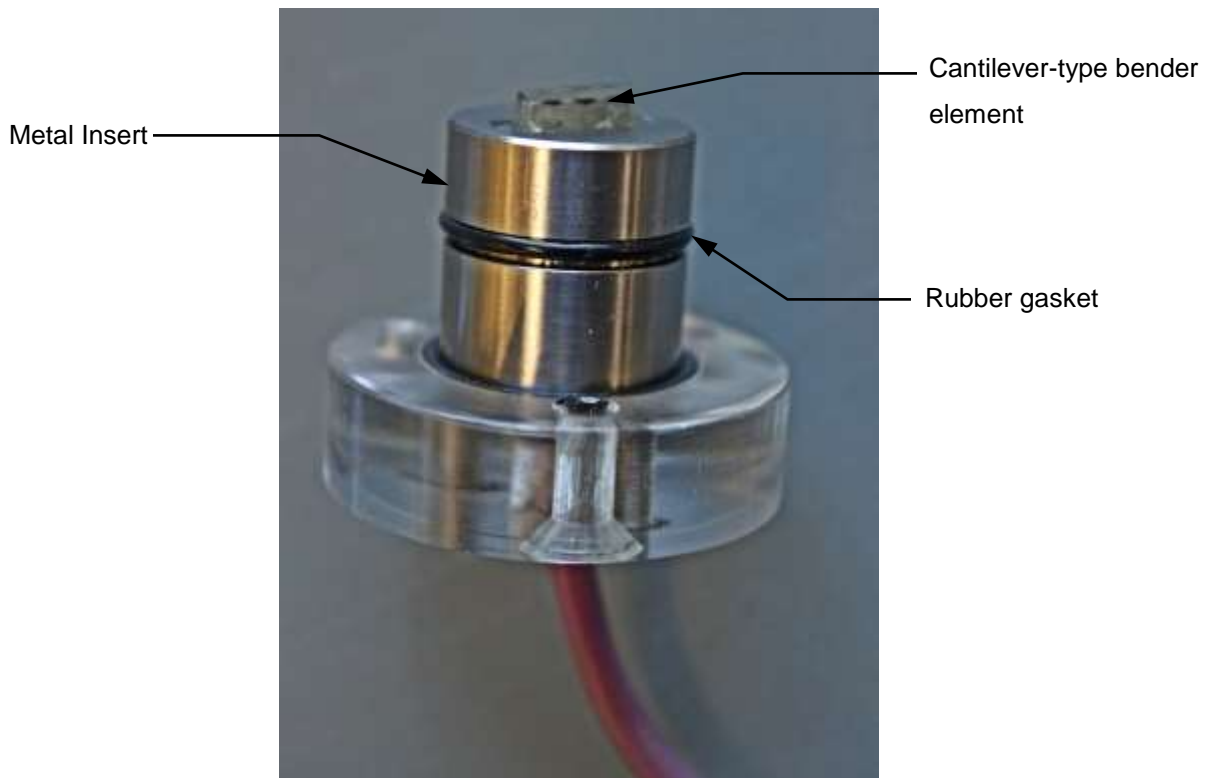


Figure 4.4: Piezo-electric bender element

As discussed previously, a portable electrical resistivity probe, namely “Hydra-probe” was used in this study to measure electrical resistivity. The Hydra-probe consists of four parallel stainless-steel electrodes spaced at a center-to-center distance of 13 mm. Each electrode is 55 mm long and 4 mm in diameter with an apex angle of 33°. The probe introduced a low frequency (50 Hz) alternating electric current of known intensity (I) into the soil sample at a certain depth through the electrodes and measured the potential voltage difference (V) in the soil adjacent to the electrodes. A battery unit was connected to a computer/any hand-held device and the Hydra-probe. A graphical user interface named Stevens Hydra Mon (1.5) software was used in this study to command the resistivity mechanism. The graphical interface was used to command the battery power unit to generate an electric current to the probe. The casing which housed the electrodes has an in-built microprocessor which could

translate the returning signal from the electrodes to a voltage reading. The graphical interface therefore, with its calibration factors converted the voltage reading into decipherable values of soil parameters. One such recorded parameter is soil conductivity, κ (S/m) which was inversed manually to achieve the bulk electrical resistivity, ρ (Ohm·m) of the specimen.

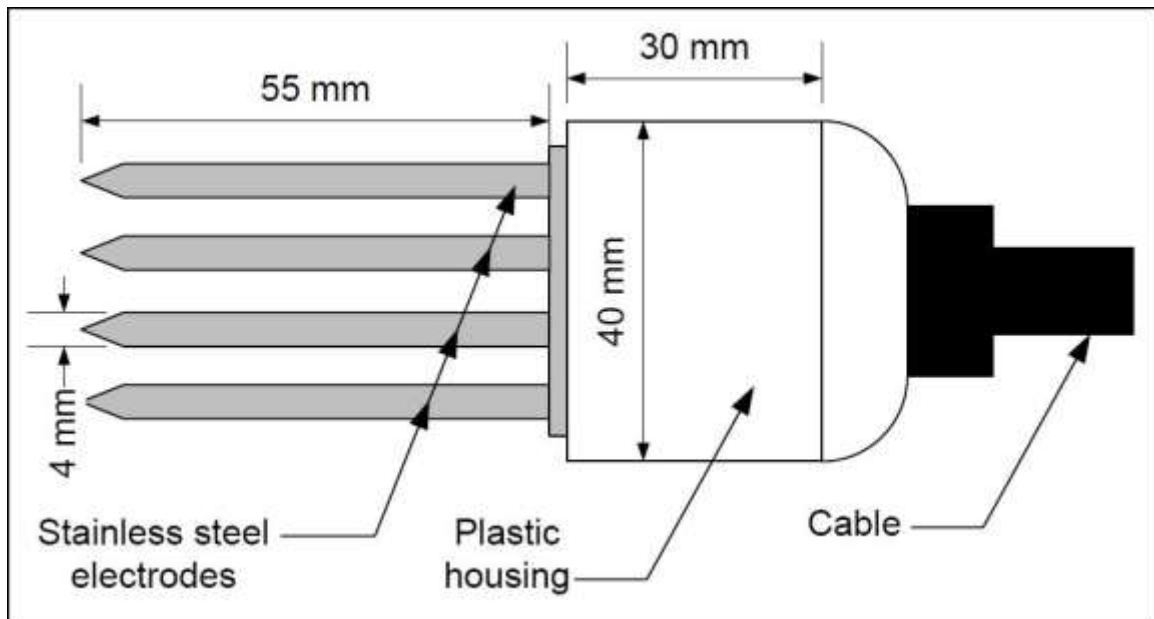


Figure 4.5: Schematic shape and dimensions of the Hydra-probe used in this study (Al-qaysi and Sadrekarimi 2015)

4.3 Tested Material

Reconstituted specimens of a local silica sand were prepared and tested in this experimental program. This sand is termed as “Boler Sand” as it was collected from Boler Mountain in London, Ontario. The natural Boler sand contains 11% fine particles (Mirbaha 2017). However, for the experiments of this study, the segregated particles of Boler sand were re-graded according to the gradation of Fraser River sand, following the ASTM Standard procedures ASTM D6913/D6913M-17 (2017). The Fraser River sand collected by

GeoPacific Consultants Ltd., from a site near the north arm of Fraser River in Richmond, B.C., had shown a fines content of approximately less than 1% (Jones 2017). Hence, to focus on the behaviour of clean sands, the Boler sand was graded according to Fraser River sand. The gradation curves are presented in Figure 4.7.



Figure 4.6: Sample image of silica sand from Boler Mountain

A specific gravity (G_s) of 2.67, maximum (e_{max}) and minimum (e_{min}) void ratios of respectively 0.845 and 0.525 were recorded following ASTM Standard procedures (ASTM D854-14 2014; ASTM D4253-16 2016; ASTM D4254-16 2016) According to the Unified Soil Classification System (USCS), Boler sand was classified as poorly-graded (SP). Scanning Electron Microscopic images and X-Ray Diffraction analyses were carried out previously by Mirbaha (2017) to determine the particle shape and mineralogy of the sand. The tests had shown that Boler sand is primarily composed of quartz (SiO_2) minerals with sub-angular to angular particle shapes.

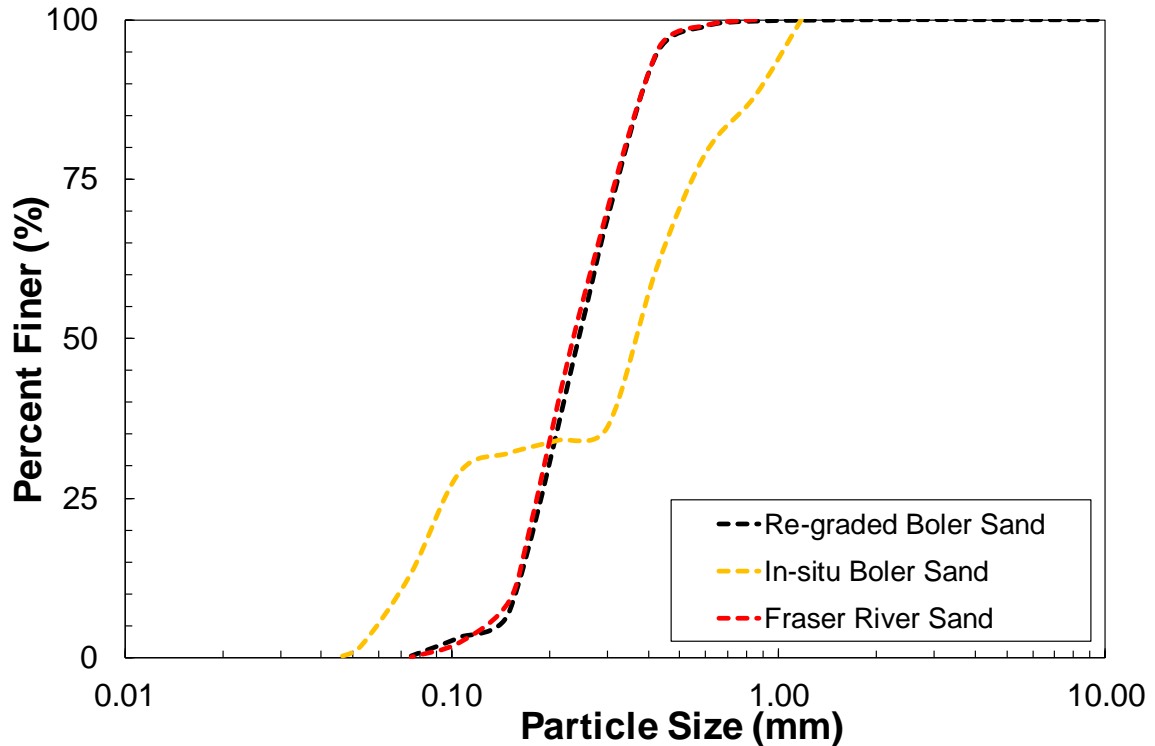


Figure 4.7: Particle size distribution of silica sand re-graded as Fraser River sand

An acid dissolution method was carried out to determine the carbonate content in the tested sand material. 50 gm of sand was soaked in 200 mL of hydrochloric acid for 24 hours. Tests were performed using both concentrated HCL, and 1N HCL. Overall, 13% of carbonate content was determined at the end of the tests. One of the primary highlights in the X-Ray Diffraction graphical presentation in Figure 4.8, is the content of Iron in the material. The importance of the presence of Iron in the sand material is directly related to its contribution to the electrical properties of the saturated media and this phenomenon will be further discussed in this chapter.

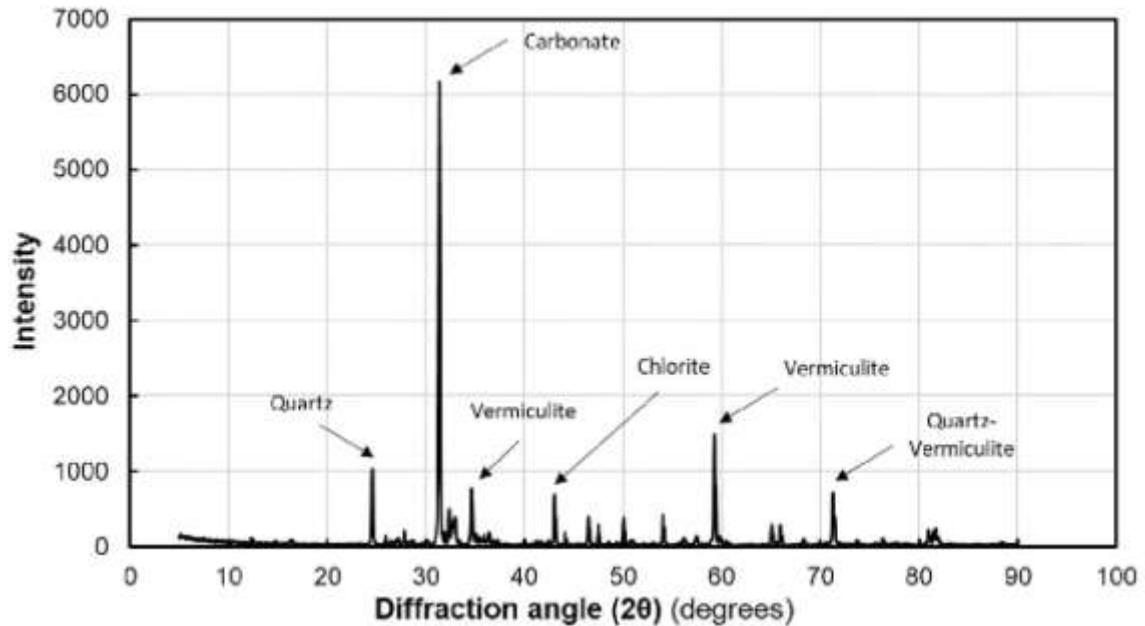


Figure 4.8: X-Ray Diffraction analyses on Boler Sand by Mirbaha (2017)

Due to a commanding presence of Quartz (SiO_2), this sand has been named silica sand for this study. But it is also highlighted in Figure 4.8, that minerals like Chlorite, Vermiculite and Quartz-Vermiculite share a certain percentage of the tested material as well. The Chlorite group, $(\text{Fe}, \text{Mg}, \text{Al})_6(\text{Si}, \text{Al})_4\text{O}_{10}(\text{OH})_8$ and the Vermiculite group $\text{Mg}_{0.7}(\text{Mg}, \text{Fe}, \text{Al})_6(\text{Si}, \text{Al})_8\text{O}_{20}(\text{OH})_{4.8}\text{H}_2\text{O}$, both consists of Iron in their compositions.

4.4 Mechanism of Non-destructive Testing

4.4.1 Specimen Preparation

All specimens prepared in this study had a height of 190 mm and a diameter of 150.2 mm excluding the 0.5 mm thickness of the latex membrane. The thickness of the membrane conforms to the ASTM Standards for triaxial shear tests ASTM D7181-11 (2011) to provide minimum restraint to the specimens. “Boler” sand specimens tested in this study

were prepared by the process of under-compaction as suggested by Ladd (1978) as the desired goal was to achieve a uniform density throughout the dimension of the specimen. Specimen preparation in this study was done exactly the way it was prepared for MCPTs described in chapter 3. An under-compaction ratio of 10% was used to prepare the specimen which were premoistened to a 5% moisture content and was laid in 10 layers each tamped to height of 19 mm, i.e. a total height of 190 mm. The specimen was prepared inside a steel split mold equipped with a suction mechanism (refer to Figure 3.17, chapter 3). The diameter and height were carefully measured at the end of specimen preparation to achieve an accurate initial void ratio (e_i) and relative density (D_{ri}). Specimens were prepared to three different initial relative densities (D_{ri}), the average values of which are – loose 24.2%, medium dense 46.4% and dense 64.2%. The specimens were attempted to prepared slightly looser, to account for the densification of the specimens during consolidation. After the specimen was prepared, the assembly was transported on to the load frame. The suction around the latex membrane was turned off and the split mold was carefully taken off. The acrylic cylinder was placed around the specimen on a properly greased O-ring. The metallic top chamber cap was placed after allowing the Hydra-probe cable to exit the chamber. The cable escaped the calibration chamber through a screwed housing equipped with ferrules and washers to prevent leakage at high cell fluid pressures (shown in Figure 4.3). Therefore, after preparing the specimen and assembling the cell, the entire length of the electrodes penetrated the sample enough for the top cap to rest on the surface of the specimen. Finally, the acrylic cylinder was filled with dyed silicone oil, through which the specimen was subjected to confining pressure. The non-conductive property of silicone oil made it a suitable fluid to be used in the cell to protect the electricity carrying wires and cables inside the chamber against electrical short circuits.

4.4.2 Seating, Docking, Flushing, Saturation

After the entire chamber had been assembled and the cell filled with dyed silicone oil, a seating pressure of 15 kPa was applied to maintain a uniform volume of the specimen during the subsequent stages of docking, flushing and saturation. The seating pressure was ramped to 15 kPa in 15 mins to ensure that the pressure build up is gradual and not sudden.

Soon after the seating pressure reached its target value, water was pumped into the piston cavity below the specimen from an external pump, to initiate uplift of the piston. The piston was uplifted to initiate docking, the point at which the acrylic spacers sitting on top of the specimen touches the metallic roof of the chamber cap. The entire process of docking and its associated friction and height calibration test details are described in words as well as graphically, in section 3.4.2, chapter 3). Post docking, the specimens were flushed with carbon dioxide (CO₂) for 45 minutes. Carbon dioxide being denser than air and highly soluble in water is an ideal agent to push air out of the sample. Subsequently, the specimens were flushed with saline water with a concentration 3 gm/L to achieve the highest degree of saturation with salt solution possible. The salt solution is the medium for conducting electrical current around the soil particles. The influence of the concentration of salt solution was later nullified by normalizing the measured parameters (discussed later). Once no air bubbles were seen to be flowing out of the drainage lines, and the pore water pressure inside the specimen was observed to be stable, the flushing stage was done. During these stages, the cell pressure was maintained at a constant value and any changes in cell volume were used to calculate specimen volume change. As soon as the flushing was completed, the cell pressure and back pressure were ramped to high pressures like 500 – 600 kPa, to achieve a pore pressure coefficient i.e., B value of at least 0.96. This ensured that the specimens were properly saturated. The change in volume of the back pressure pump was monitored during this stage to accurately determine specimen volume changes.

4.4.3 K_0 consolidation

Many research works have been carried out in the past to modify commonly used laboratory apparatuses to achieve a K_0 consolidation state. These involved K_0 -triaxial tests (Fedá 1984; Eliadorani 2000) and even calibration chambers as discussed earlier (Hsu and Lu 2008; Kumar and Raju 2009). These modifications were often done by fitting lateral strain gauges along the walls of the specimen to monitor zero-lateral strain conditions Hsu and Lu (2008).

The current study used a novel approach to induce K_0 consolidation state through the installation of the hydraulic piston beneath the bottom disk on which the specimen rests. This modification was done by Jones (2017). The consolidation was carried out using a volume control mode by extracting a certain volume of water from the specimen and simultaneously subjecting it to a specific axial deformation using the hydraulic piston. During this process, the cell pressure around the specimen was maintained at a constant value that was achieved at the end of back pressure saturation. Under such conditions equal volumetric strain, ε_v and axial strain, ε_a was maintained throughout the process, thus mimicking in-situ K_0 conditions.

$$\varepsilon_v = 2\varepsilon_r + \varepsilon_a \quad (4.7)$$

$$\text{If } \varepsilon_r = 0, \varepsilon_v = \varepsilon_a$$

Where ε_r , ε_a , and ε_v are the lateral, axial, and total volumetric strains applied to the specimen respectively during consolidation. A graphical representation of the phenomenon from one of the tests in this study is shown as an example in Figure 4.9.

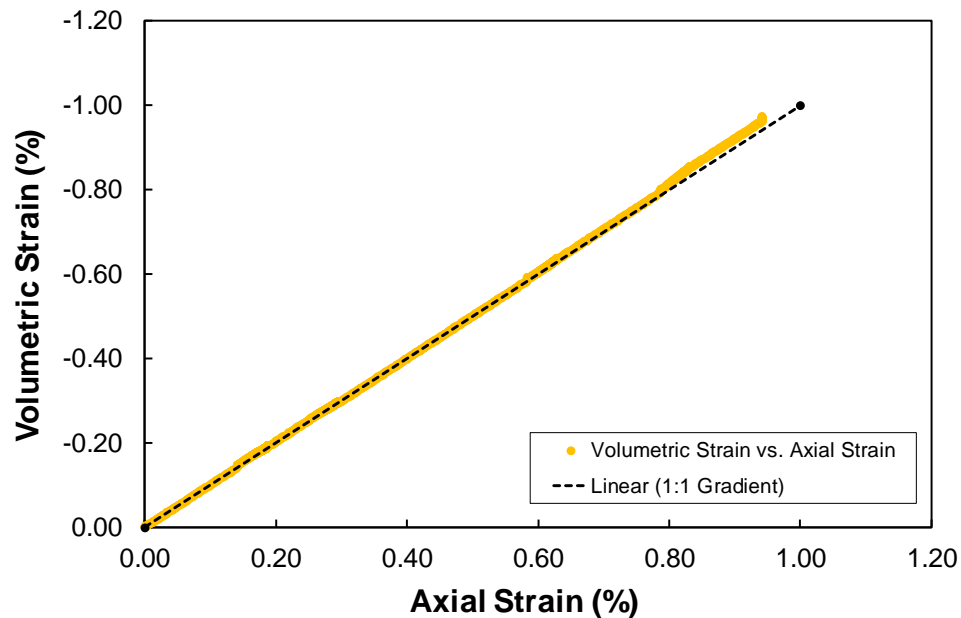


Figure 4.9: Graphical representation of K_0 consolidation for Test ID ND-45-4

This process of consolidating the specimen also meant that, instead of targeting a specific effective stress, a specific void ratio was being targeted. Both volume control functions were continued until a desired void ratio was reached. Because of the specimen's pore water pressure being decreased and the piston pressure being increased with respect to a constant cell pressure, consolidation stress was produced. The respective changes in the volume of the pore pressure pump and the piston pressure pump, volume and height changes of the specimen were calculated. The predetermined change of volume that was needed to be applied to reach a certain void ratio, was calculated by the following Equations 4.8 and 4.9.

$$\Delta V_{pore} = \frac{e_i - e_c}{1 + e_0} (V_{sp}) \quad (4.8)$$

$$\Delta V_{piston} = \frac{e_i - e_c}{1 + e_0} (18.051)(h) \quad (4.9)$$

where ΔV_{pore} and ΔV_{piston} are changes in the pore pump volume and piston pump volume respectively, e_i is the initial void ratio, V_{sp} is the specimen volume, h is the specimen height, and the value 18.051 is a calibration factor for height change (Jones 2017). After an initial adjustment period in the beginning of the consolidation, the K_0 stress state slowly begins to reach a certain constant value as the consolidation stage proceeds. This constant magnitude of K_0 represents the stress state of the specimen for the following stages of the test. Graphical presentations of pressure variation, specimen and piston volume changes during a typical consolidation stage is shown in Figures 3.25 and 3.26, Chapter 3. Figure 4.10 represents a typical stage-wise consolidation stress development during K_0 consolidation.

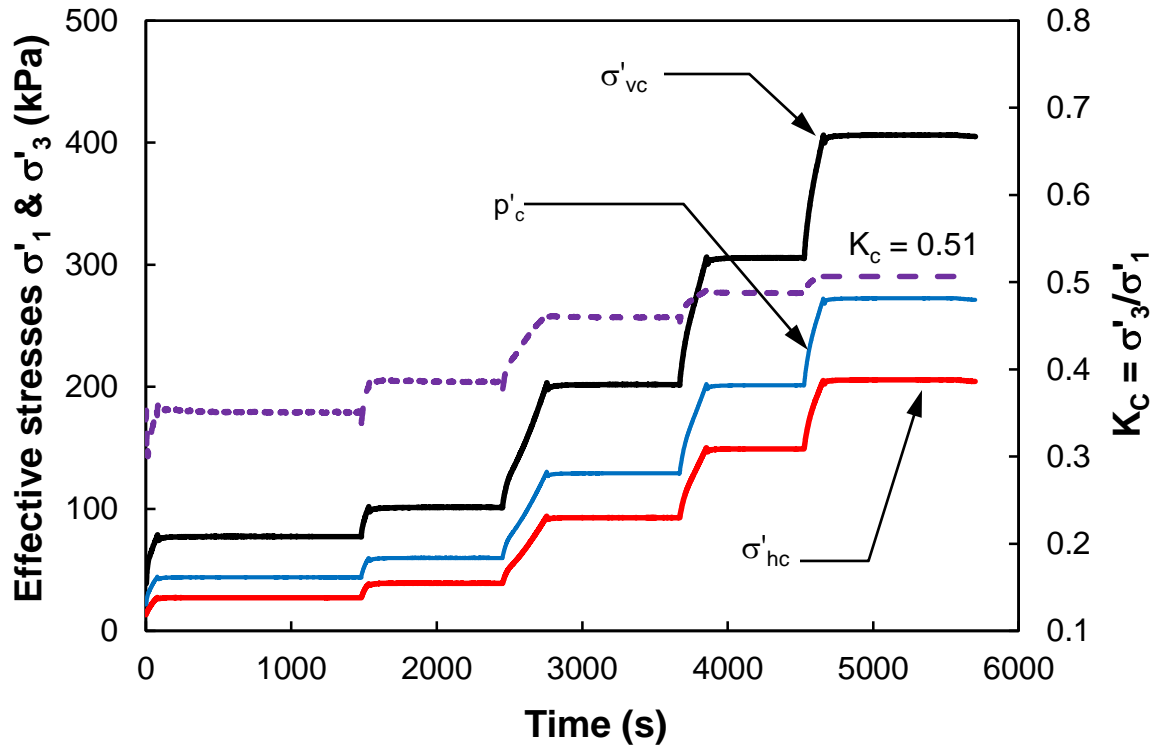


Figure 4.10: Illustration of the development of effective stresses for Test ID ND-65-4

4.4.4 V_s and ER Measurements

After a particular target void ratio was reached, i.e., at each stress level, the consolidation pressure was maintained for 30 minutes to allow the consolidation stresses to stabilize. Shear wave velocity measurements have been recorded using piezo-electric bender elements installed in the top and bottom acrylic disks on either side of the specimen. 30-45 minutes post consolidation, shear waves were triggered across the specimen through a graphical user interface. The signal processing unit recorded the incipient and the transmitted waves to determine the shear wave velocity in the specimen. Five signal frequencies (5 kHz, 3.33 kHz, 2.5 kHz, 2 kHz, 1.67 kHz) were employed to generate a large database of shear waves for each test and prevent the presence of any near field effect. After that, electrical resistivity measurements were made using the parallel electrodes.

4.5 Test Results

Silica specimens were consolidated to three different relative densities the average values of which are – loose (D_{rc} 25.9%), medium dense (D_{rc} 47.6%) and dense (D_{rc} 65.1%). At each relative density state, specimens were tested at four consolidation stress levels, the average values of which are, $\sigma'_{vc} = 74.52$ kPa, 102.08 kPa, 203.39 kPa and 411.83 kPa. A total of 12 tests were completed in this study and therefore compiled in Table 4-2.

4.5.1 Shear Wave Velocity

Results of the shear wave velocity measurements are summarized below through Figures 4.11 to 4.13 for each set of four tests performed at a constant relative density and signal frequency (f). A high signal voltage of ± 14 mV was used to generate strong shear waves and reduce the effect of noise on the wave pattern. While only signal frequencies which were clear and consistent throughout the four tests are presented, shear wave velocity measurements were taken at various applicable signal frequencies (5 kHz, 3.33 kHz, 2.5 kHz, 2 kHz, 1.67 kHz) for each test and averaged. To minimize the influence of near field effect, signal frequencies which produced a (L_t/λ) ratio of greater than 2, were considered. This averaged shear wave velocity measurement is what is presented in Table 4-2. The magnitude of λ has been calculated in this study as follows:

$$\lambda \text{ (mm)} = \frac{V_s \text{ (m/sec)}}{f \text{ (kHz)} \times 1000} \times 1000 \quad (4.10)$$

where, f = signal frequency.

The peak-to-peak time of the first transmitted and received signals was used to measure travel time (Δt) and determine V_s . Several researchers have suggested that this methodology can provide the most accurate measurement of V_s (Viggiani and Atkinson 1995; Brignoli et al. 1996; Jovicic et al. 1996; Lee and Santamarina 2005; Yamashita et al. 2010; Camacho-Tauta et al. 2015) as it holds a strong agreement in V_s results obtained from other laboratory techniques (e.g., resonant column tests, acceleration measurements, etc).

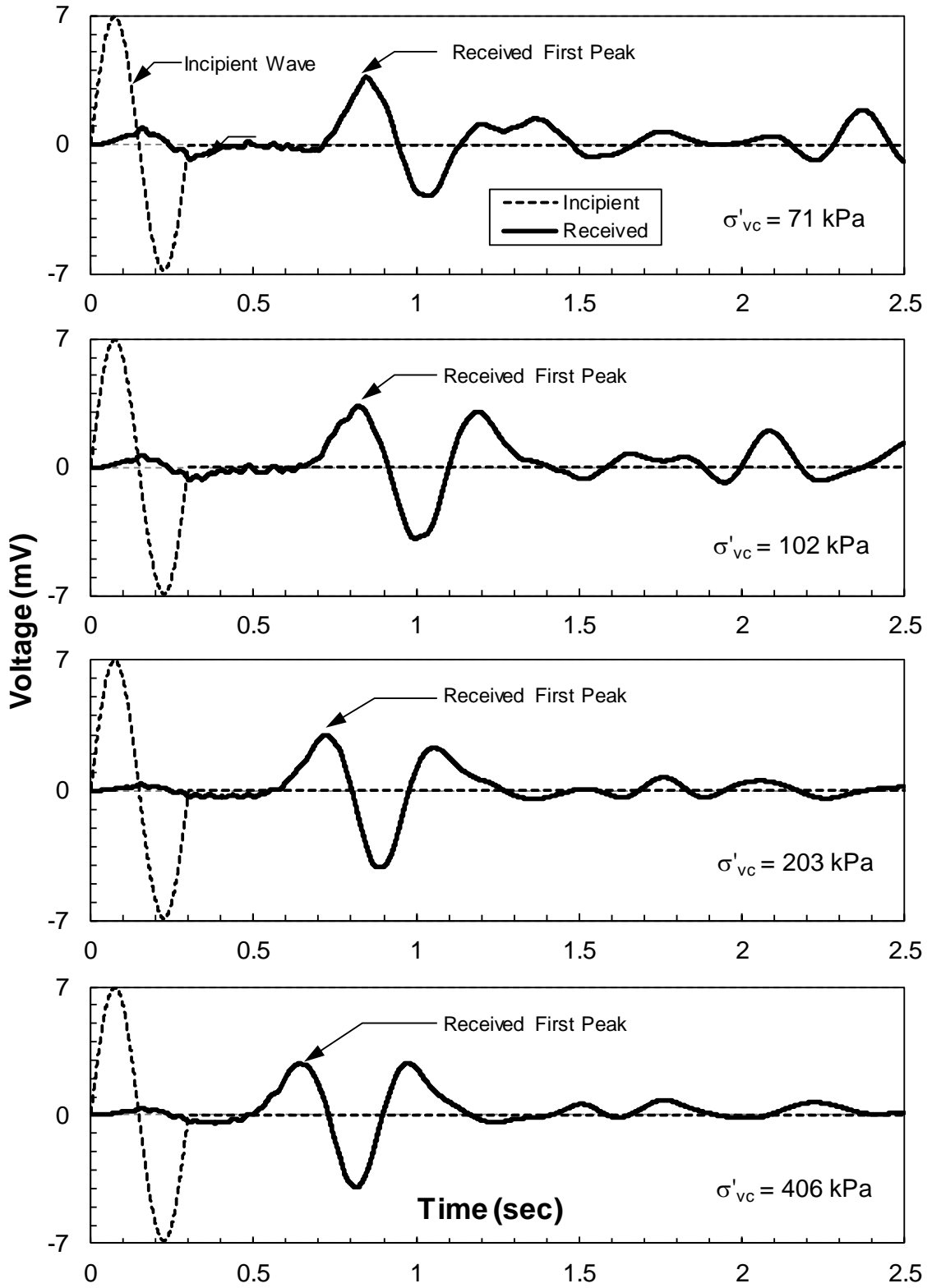


Figure 4.11: Shear wave signal time history at $D_{rc} = 25.9\%$ and $f = 3.3 \text{ kHz}$

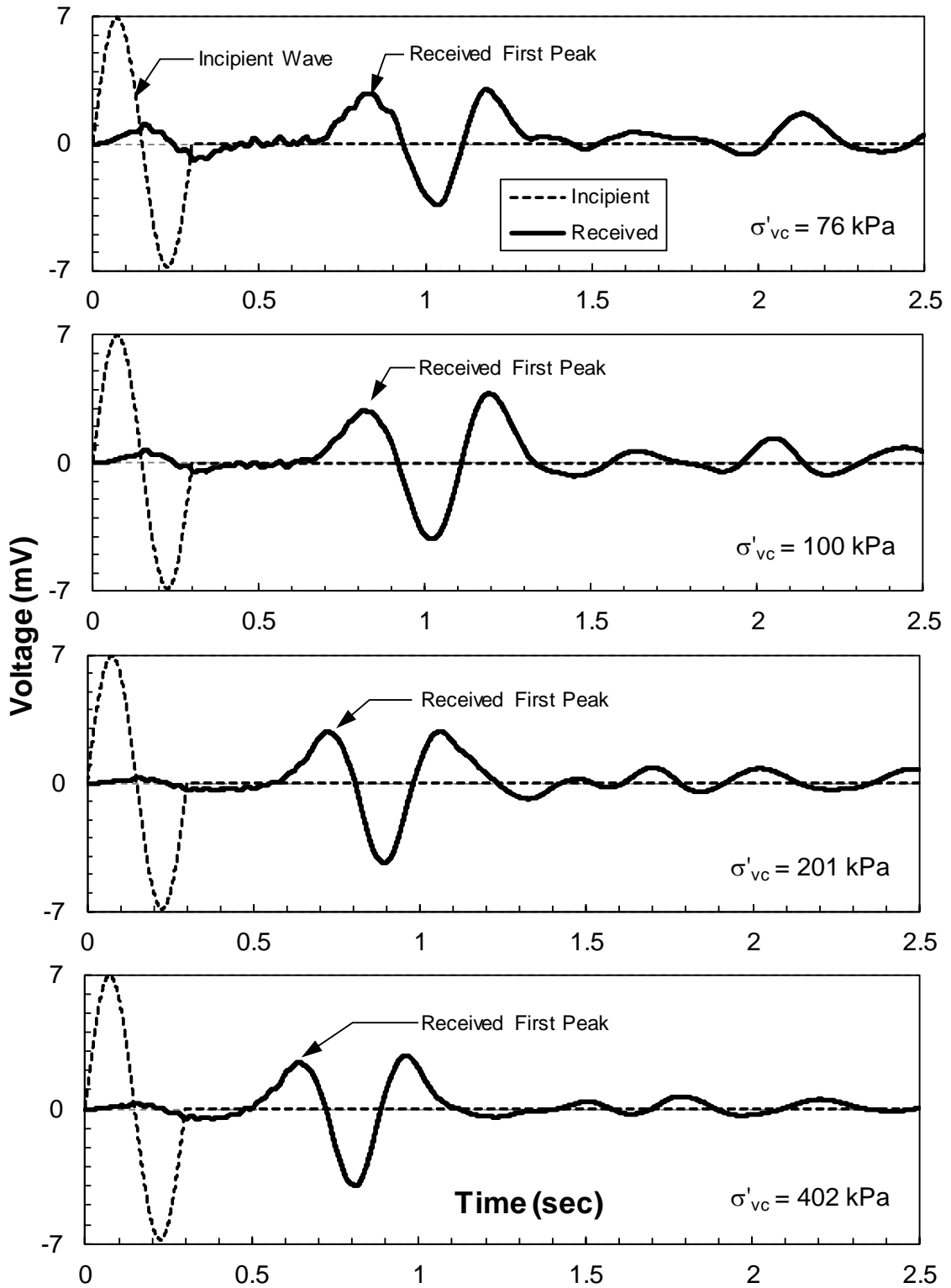


Figure 4.12: Shear wave signal time history at $D_{rc} 47.6\%$ and $f = 3.3 \text{ kHz}$

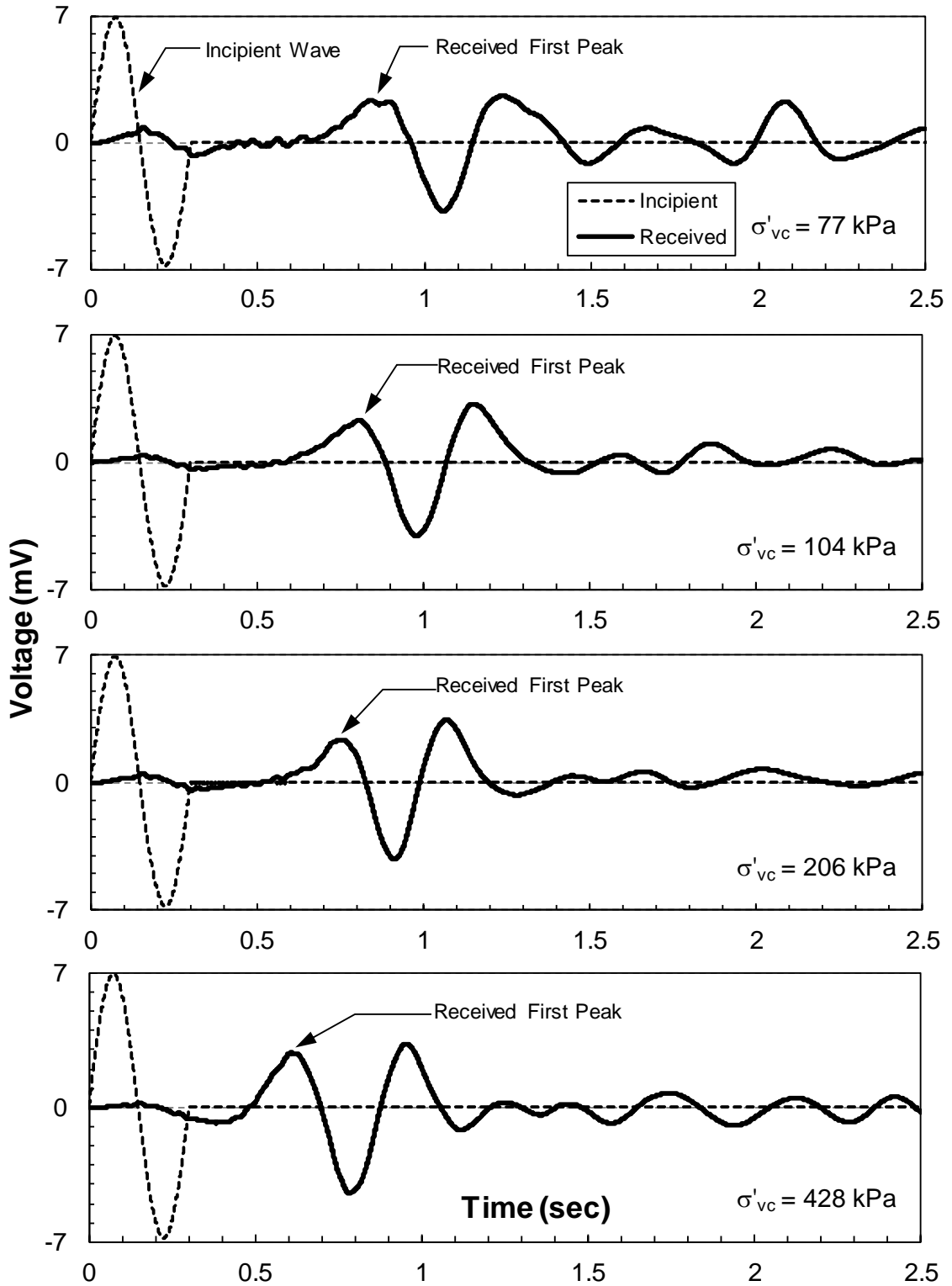


Figure 4.13: Shear wave signal time history at $D_{rc} = 65.1\%$ and $f = 3.3 \text{ kHz}$

4.5.2 Pore Fluid Electrical Resistivity

A set of calibration tests were completed in this study to determine the functionality of the Hydra-probe and the pore fluid electrical resistivity (ρ_f) was recorded. The specimens tested in this study were saturated with saline water with a salt concentration of 3 gm/L. Concentration of salt affects the performance of electrical conductivity strongly. In order to estimate field performance from the correlations developed from electrical resistivity tests, the salinity of pore fluid was chosen carefully. The natural ground water salinity varies from place to place. For e.g., Mayer et al. (2005) reported that natural groundwater salinity often varies from 0.5 to 3 gm/L and sea water salinity is generally more than 35 gm/L. The salinity of a particular site can be completely different than what is shown in this study. Due to this inconsistency in salinity of natural groundwater, even between electrolytic concentrations of different laboratory tests, the influence of salt concentration is eliminated, or in other words, the bulk electrical resistivity of the soil is normalized by measuring formation factor. Therefore, for this study, a representative solution with 3 gm/L salt concentration was prepared in a container and the electrical resistivity measurements were recorded. At first, a set of readings were taken while the Hydra-probe was out in the open, i.e. to measure electrical resistivity in air. Secondly, measurements were recorded with the Hydra-probe dipped in distilled water. Finally, measurements were recorded with the Hydra-probe dipped in a prepared saline solution with 3 gm/L salt concentration. The recorded measurements are summarized in Table 4-1.

Table 4-1: Calibration tests to determine pore fluid electrical resistivity

Medium	κ , Conductivity (S/m)	ρ , Resistivity (Ohm·m)
Air	0.001	1000
Distilled Water	0.004	250
Distilled Water + 3 gm/L NaCl	0.475	2.105

Several measurements were recorded for each medium and the averaged value is presented in Table 4-1. From these recordings, the pore fluid electrical resistivity was measured to be 2.105 Ohm·m. It was found to be comparable with the similar result obtained by Al-qaysi and Sadrekarimi (2015). The reviewed study observed a pore fluid electrical resistivity of 2.127 Ohm·m. Moreover, for the calibration tests in this study, a dielectric constant (ϵ_r) of air was recorded to be 1.47, whereas 82.423 in distilled water. Similar observations have been recorded by Rowlandson et al. (2013) who reported a dielectric constant of air to approximately 1 and that of water to be 80. Therefore, it can be concluded that the Hydra-probe was properly calibrated. However, to determine the exact value of Formation Factor, the pore fluid electrical resistivity was measured by taking measurements on the electrolyte solution that directly was in contact with the tested material. A test program was developed in this study to determine if the sand contributed to any variability in the conductive properties of the pore water. A batch of sand approximately identical to the amount of sand that is required in each test, was soaked in a container of the electrolyte solution i.e. distilled water mixed with 3 gm/L of salt. The sand was allowed to soak by leaving the container for 24 hours. The sand-soaked water was then collected in a beaker and the sand particles were separated from the interstitial water. Electrical resistivity measurements were subsequently conducted on this effluent water which is identical to the actual pore water during a real test. The electrical resistivity of the effluent has been measured to be 1.855 Ohm·m. The reduction in electrical resistivity from 2.105 to 1.855 Ohm·m confirms the contribution of the tested material in altering the conductive properties of the pure electrolyte solution. As discussed in section 4.3, the presence of Iron can be accounted for in the increase of electrical conductivity of the pore fluid, which in turn decreases electrical resistivity.

Therefore, it appears reasonable to consider 1.855 Ohm·m as the representative of the pore water electrical resistivity in this study to calculate Formation Factor. Illustrations of the above-mentioned test to measure pore fluid electrical resistivity is shown in Figures 4.14 and 4.15.



Figure 4.14: Image showing the effluent water after soaking Boler sand

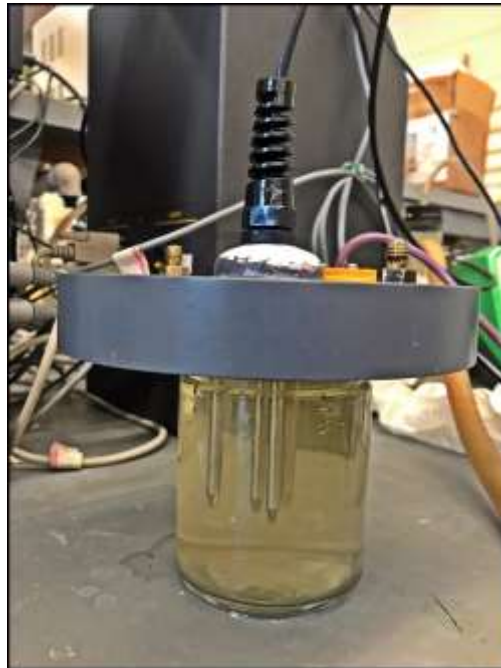


Figure 4.15: Electrical resistivity measurements being taken on pore water

4.5.3 Summary of Results

Table 4-2 summarizes the data obtained in this study at each relative density and effective vertical consolidation stress. ER readings were recorded multiple times at a fixed time interval, however, only the averaged value of the multiple readings have been tabulated here as a representative measurement.

Table 4-2: Summary of ER and V_s Measurements

Test ID	σ'_{vc} (kPa)	Measured κ (S/m)	ρ_b (O.m)	ρ_f (O.m)	Formation Factor	e_c	D_{rc} (%)	V_s (m/sec)
ND-25-1	71.02	0.203	4.926	1.855	2.656	0.771	23.1	183.70
ND-25-2	102.44	0.202	4.950	1.855	2.669	0.767	24.3	200.40
ND-25-3	202.71	0.200	5.000	1.855	2.695	0.759	26.8	250.60
ND-25-4	405.58	0.199	5.025	1.855	2.709	0.751	29.3	314.50
ND-45-1	75.91	0.189	5.291	1.855	2.852	0.699	45.6	218.40
ND-45-2	100.16	0.188	5.319	1.855	2.867	0.696	46.5	236.50
ND-45-3	201.32	0.186	5.376	1.855	2.898	0.691	48.1	270.30
ND-45-4	401.76	0.185	5.405	1.855	2.914	0.685	49.9	334.70
ND-65-1	76.62	0.175	5.714	1.855	3.080	0.641	63.7	220.80
ND-65-2	103.65	0.174	5.747	1.855	3.098	0.639	64.3	239.90
ND-65-3	206.15	0.173	5.780	1.855	3.116	0.636	65.3	286.90
ND-65-4	428.15	0.171	5.848	1.855	3.153	0.631	66.8	350.80

Formation Factor has been calculated using equation 4.3.

4.6 Overburden Stress Normalization

Shear wave velocity is essentially a function of effective stress level and sand relative density. Therefore, V_s measured in the same sand and at the same relative density can be very different at different penetration depths corresponding to different effective overburden stresses. To compare soil behaviour from different depths, V_s is often normalized to a common effective overburden stress of 100 kPa. This correspond to test results at atmospheric pressure which is highly beneficial for comparison of field and laboratory tests. A correction factor (C_v) is typically multiplied to V_s , determined as shown below:

$$C_v = \left(\frac{P_a}{\sigma'_{vc}} \right)^\beta \quad (4.11)$$

where, $P_a = 100$ kPa (atmospheric pressure) and “ β ” is the stress normalization exponent for shear wave velocity.

4.6.1 Normalization Exponent of Shear Wave Velocity

The shear wave velocity data obtained from bender element tests have been normalized to a reference atmospheric pressure of 100 kPa. Hence, to calculate the correction factor for normalization, the stress normalization exponent, “ β ” has been determined from the following graph (Figure 4.16).

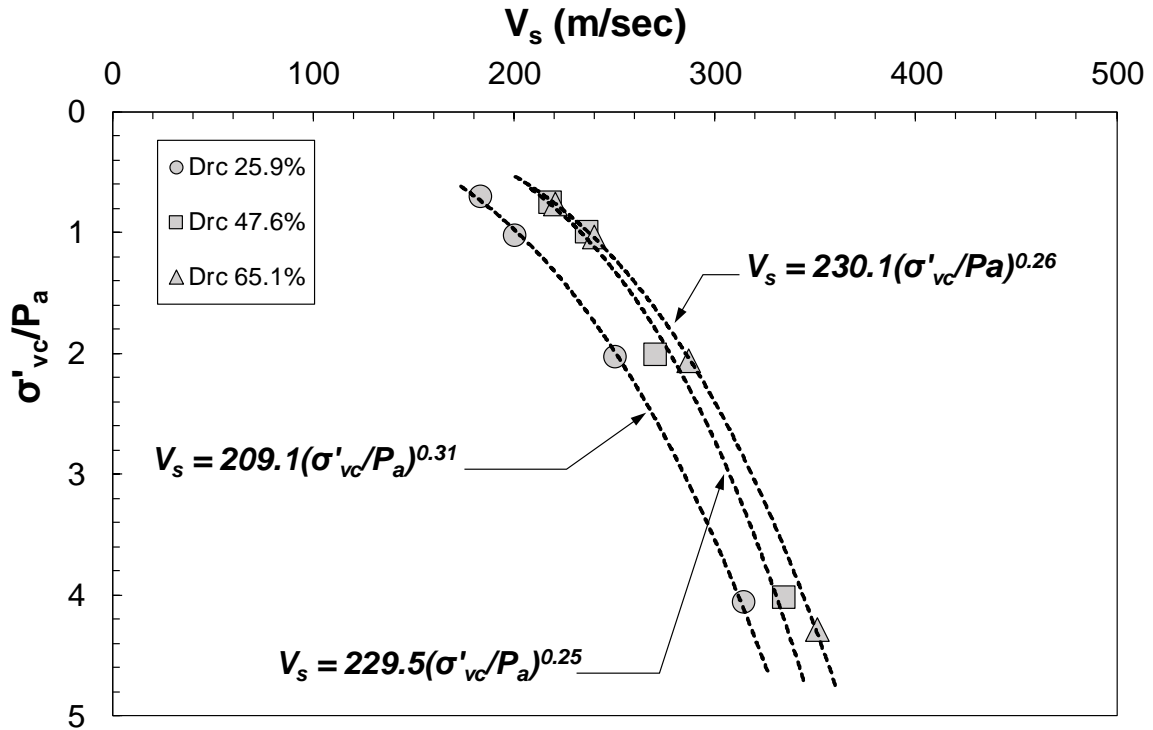


Figure 4.16: Variations of V_s over normalized effective vertical stress

Figure 4.16 describes the variation of shear wave velocity measured at different relative densities and the corresponding stress normalization exponent developed from each curve. The average stress normalization exponent produced in this study is 0.27. The globally accepted normalization exponent value for V_s measurements in sand is 0.25 which has been widely used in several studies (Hardin and Richart Jr. 1963; Hardin and Drnevich 1972; Thomann and Hryciw 1990; Kayen et al. 1992; Robertson et al. 1992; Hussien and Karray 2016) and for V_s -based liquefaction triggering analysis (Andrus and Stokoe 2000; Kayen et al. 2013). However, for this study each individual stress normalization exponents derived from their corresponding V_s profile at a certain relative density state, has been used to determine normalized shear wave velocity.

4.6.2 Correction Factor (C_v) for Shear Wave Velocity

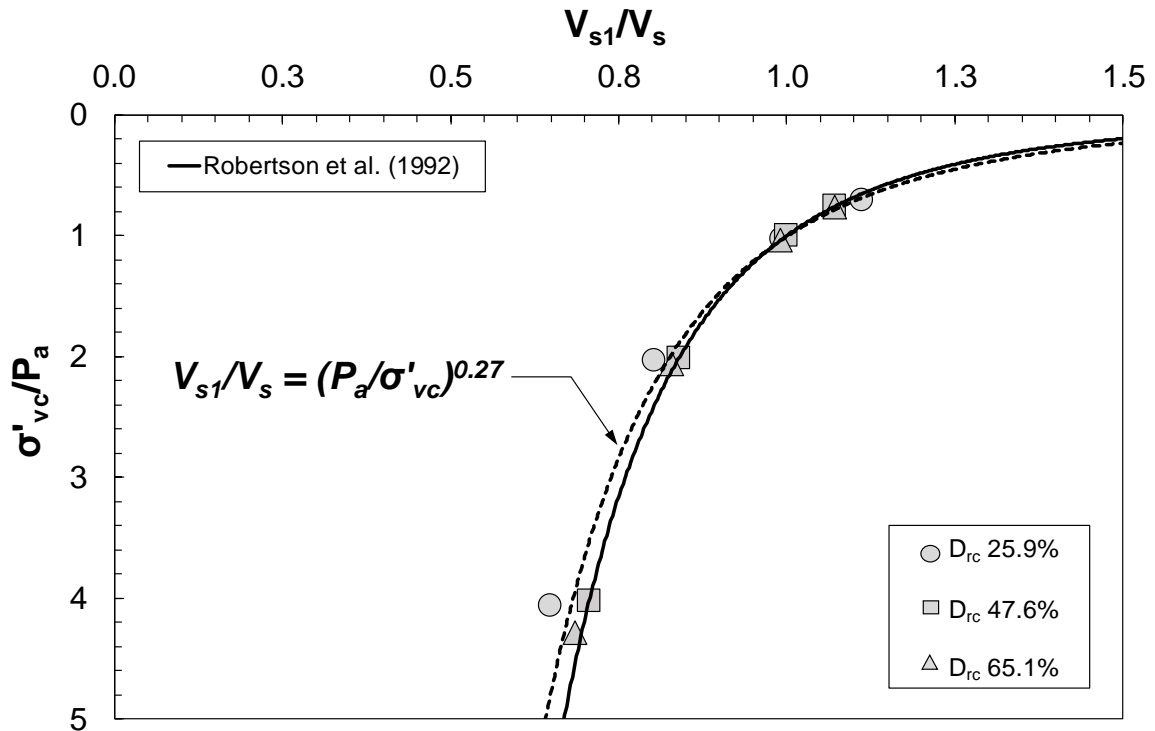


Figure 4.17: Comparison of stress normalization correction factor for V_{s1} with Robertson et al. (1992)

As discussed previously, several researchers (Hardin and Richart Jr. 1963; Yu and Richart 1984; Robertson et al. 1992; Kokusho and Yoshida 1997; Andrus and Stokoe 2000; Hussien and Karray 2016) normalized shear wave velocity for calculating V_{s1} using a stress normalization exponent, $\beta = 0.25$. However, the individual stress normalization exponents for their corresponding relative density levels from this study ($\beta = 0.31, 0.25, 0.26$) is used for calculating V_{s1} .

$$V_{s1} = V_s \left(\frac{P_a}{\sigma'_{vc}} \right)^\beta \quad (4.12)$$

The comparison of stress normalization correction factors for calculating V_{s1} is shown in Figure 4.17. The correction factors calculated from V_s for each individual stress level and relative density level in this study has been compared with Robertson et al. (1992) where a stress exponent of 0.25 was considered for normalizing shear wave velocity. It is seen that the two trendlines hold a reasonable agreement, especially for data points corresponding to medium dense ($D_{rc} = 47.5\%$) and dense specimens ($D_{rc} = 65.1\%$).

4.7 Influence of Stress on Formation Factor

The formation factor measured for each test in this study corresponds to a specific effective vertical stress and a specific relative density. Therefore, in order to investigate different correlations with formation factor, it is important to understand the behaviour of the parameter relative to effective vertical stress and relative density. Arulmoli et al. (1985) mentioned that formation factor being dependent on mineralogy of sands, may differ at different stress conditions due to the change in particle and contact orientation within the soil specimen. However, Erchul and Nacci (1971) after performing specialized tests on marine sediments, clean sands and clay, found that consolidation stress did not affect the measurements of formation factor as much as relative density did. Atkins and Smith (1961) explains that fitting parameter “m” changes with increasing overburden stress on sand matrix. Glanville (1959) studied Tuscaloosa and Pennsylvanian sandstones with and without overburden pressure and observed negligible effect of overburden stress on Tuscaloosa sandstone but a considerable effect on Pennsylvanian sandstone. Salem (2001) explains that sand matrix with a predominance of plate like shaped particles are likely to be influenced by overburden stress more than rounded or sub-rounded particles. The variation of formation factor for silica sand in this study is shown in Figure 4.18. In Figure 4.18, the broken black lines represent the three relative densities and the red broken lines represent the four effective vertical stresses that the specimens have been tested at, in this study. The datapoints along each relative density state is seen to increase with change in relative density (see black broken lines), while on a particular relative density state, the data points do not increase significantly with increasing effective vertical stress (see red

broken lines). It can therefore be inferred, that the primary variation in the magnitude of formation factor is due to the change in relative density.

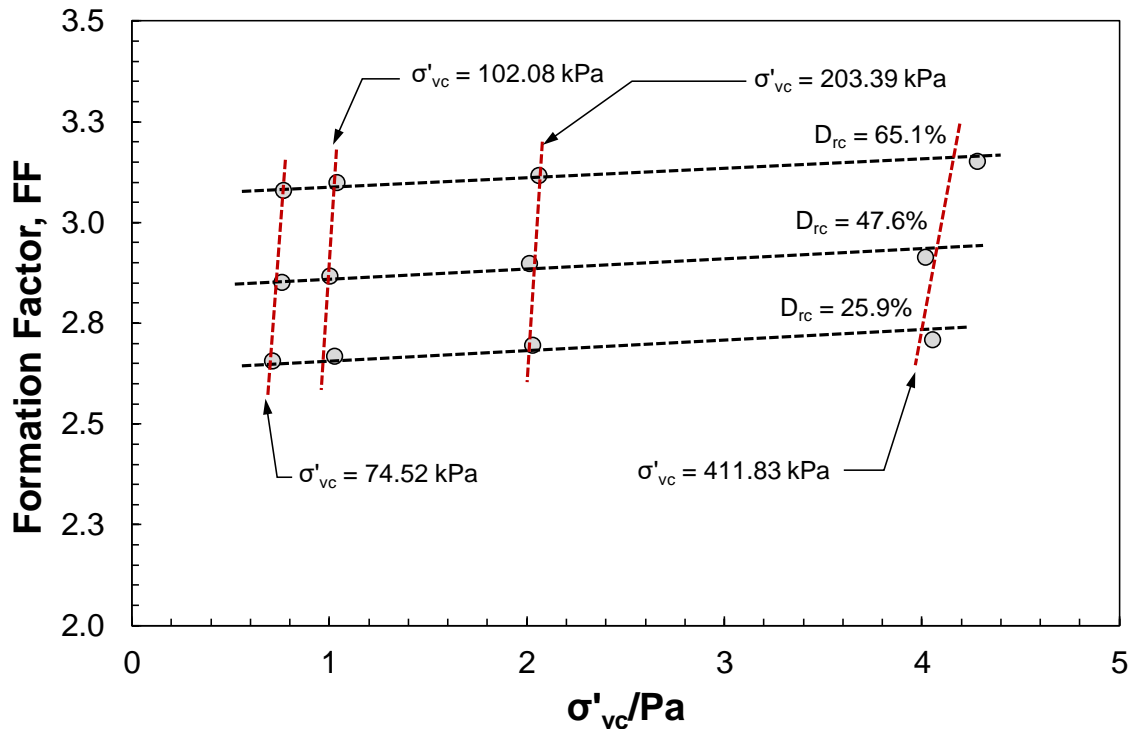


Figure 4.18: Influence of effective stresses and relative densities on formation factor

Moreover, when a certain specimen is exposed to an incremental stress level from 75 to 400 kPa, the specimen is compressed, and the relative density increases. Therefore, at any particular relative density level, the inappreciable increment in formation factor is also due to the change in void ratio of the specimen. Scanning Electron Microscopic images and X-Ray Diffraction analyses were carried out previously by Mirbaha (2017) to determine the particle shape and mineralogy of the sand. The tests had shown that “Boler” sand is primarily composed of silica minerals with sub-angular to angular particle shapes. Therefore, it can be concluded like Salem (2001) in terms of particle shape, that effective

consolidation stresses have minimal effect on formation factor measured in angular to sub-angular sand particles.

4.8 Correlations and Comparisons

The parameters measured from the miniature cone penetration tests (q_c and f_s) and the parameters measured from the non-destructive test series (V_s and FF) are correlated to each other and several other engineering properties of soil, to analyse how these parameters compare relative to each other.

4.8.1 Analysis of V_s – FF correlation

The two primary parameters obtained from this study of non-destructive testing, are shear wave velocity (V_s) and Formation and Factor (FF). There has not been much research that has correlated these two parameters besides Pulido et al. (2004) who proposed a correlation between formation factor derived porosity and shear wave velocity. However, this particular study was conducted on saturated carbonate rocks and quite reasonably, the predicted shear wave velocity was very high.

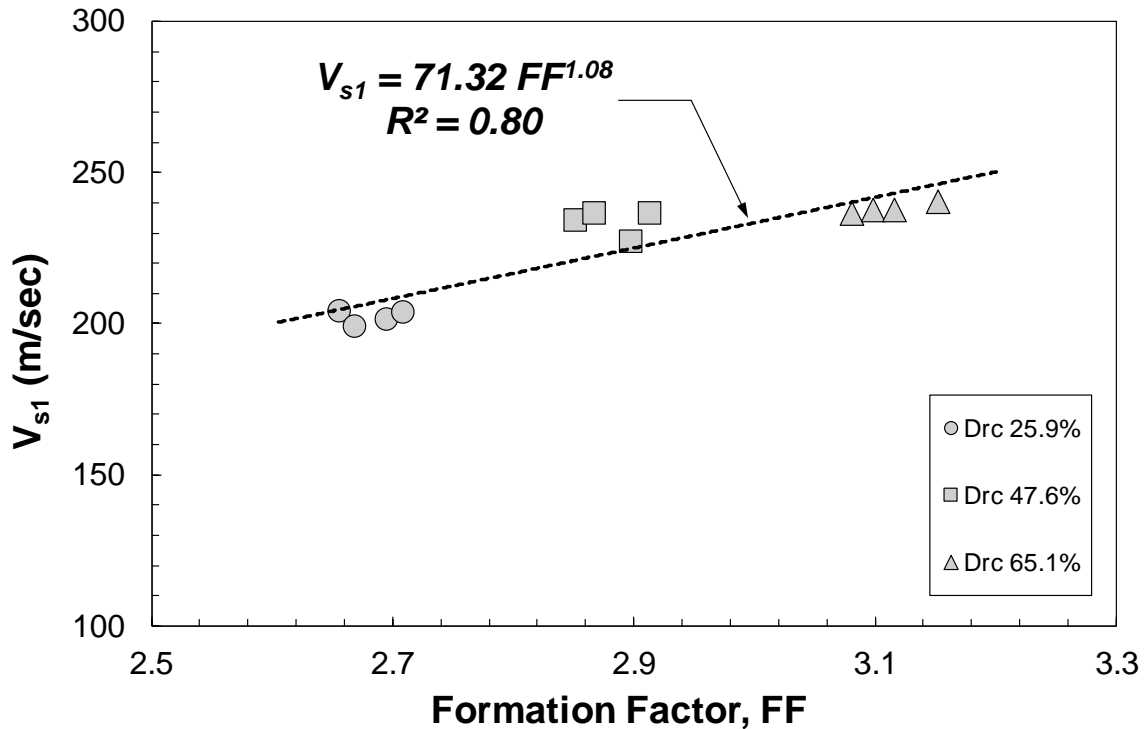


Figure 4.19: V_{s1} – FF correlation for silica sand

Figure 4.19 demonstrates the correlation between normalized shear wave velocity and formation factor and the corresponding data points at individual stress levels. The normalized shear wave velocity for each data point was calculated using the individual stress normalization exponents “ β ” determined for each level of relative density according to Equation 4.12. A power function has been used to correlate the two parameters.

Mitchell (1981) had proposed that the magnitude of shear wave velocity usually increases with increase in the cementation factor “ m ” developed from formation factor – porosity correlation. From Figure 4.19, it can be interpreted that the magnitude of shear wave velocity, rather normalized shear wave velocity increases with increase in formation factor. Electrical conduction around the soil grains gradually decrease with increasing relative density and consolidation stress as the soil densifies, leaving lesser space for the interstitial water to conduct electricity. Therefore, the resistivity increases and in turn, formation factor increases due to the densification. Similarly, shear wave velocity increases with

increase in relative density and consolidation stress. The behaviour shown in Figure 4.19 is therefore completely in agreement with the theoretical basis. The proposed correlation therefore can be formulated as below:

$$V_{s1} = 71.32 \cdot FF^{1.08} \quad (4.13)$$

4.8.2 Analysis of $V_s - q_c$ correlation

MCPT results, i.e. cone tip resistance and sleeve frictional resistance from Chapter 3 are used in this chapter for developing empirical correlations with the obtained parameters like shear wave velocity and formation factor. Often due to unavailability of instrumentation or labour, the seismic cone penetration tests cannot be used in-situ by engineers. Therefore, the indirect estimation of shear wave velocity from conventional CPT results is useful. Figure 4.20 presents a comparison between $V_{s1} - q_{c1N}$ relationship developed from this study and previous research. As discussed earlier, V_{s1} was calculated using the derived individual stress normalization exponents from this study, $\beta = 0.31, 0.25, 0.26$. In this relationship, q_{c1N} represents a dimensionless magnitude of the normalized cone tip resistance. Some applications of CPT analysis require a stress normalization of q_c as suggested by Robertson and Wride (1998) and it is expressed in Equations 4.14 and 4.15,

$$q_{c1N} = q_{cN} \left(\frac{P_a}{\sigma'_{vc}} \right)^n \quad (4.14)$$

$$\text{where, } q_{cN} = \frac{q_c}{P_a} \quad (4.15)$$

P_a is the reference pressure equal to 100 kPa and n is the stress normalization exponent derived from the MCPTs in Chapter 3.

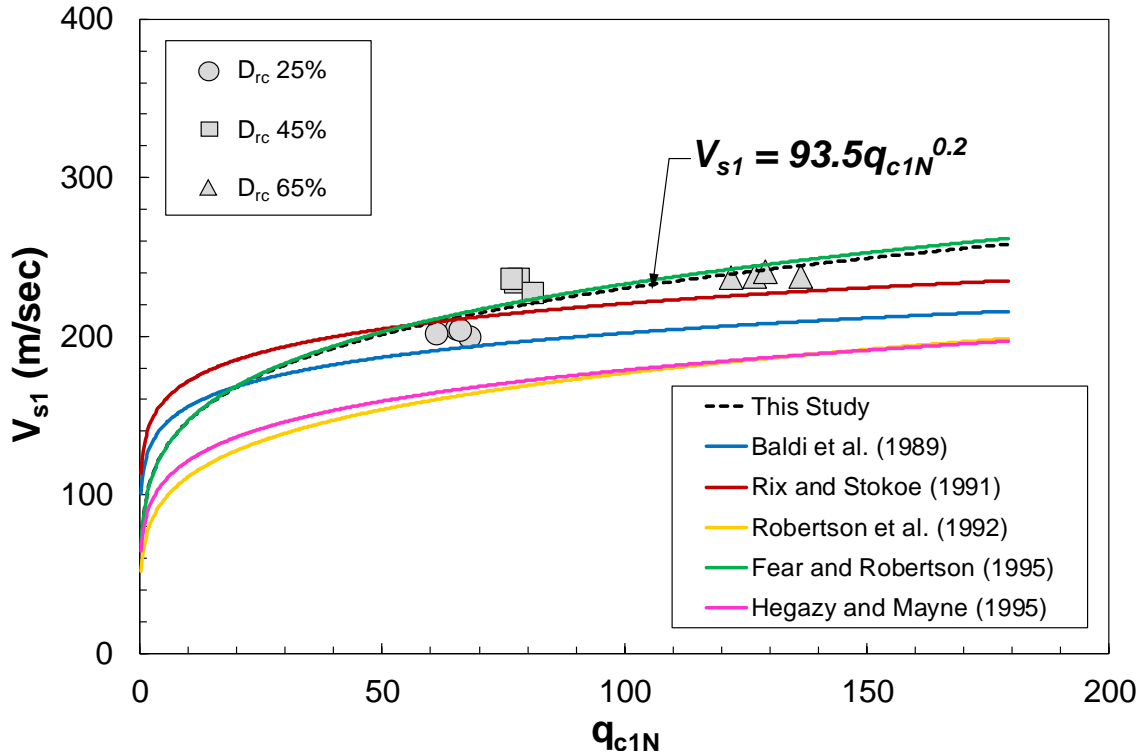


Figure 4.20: Comparison of $V_{s1} - q_{c1N}$ correlation with other studies

Baldi et al. (1989) used CPT calibration chamber and V_s from resonant column tests to develop a relationship between shear wave velocity and cone tip resistance for freshly deposited silica sand from Ticino, Italy. Rix and Stokoe (1991) carried out similar tests on freshly deposited washed mortar sand with a fines content of less than 1%. They also performed seismic crosshole and CPT tests on three different Holocene sand deposits in the Imperial Valley of Southern California. Robertson et al. (1992) and Fear and Robertson (1995) developed correlations using SCPT measurements in young, uncemented silica sand from Fraser River Delta region, BC. Hegazy and Mayne (1995) performed SCPT, crosshole, downhole, SASW tests on 24 sand sites to develop correlations between V_s and q_c . The correlations developed by each of the studies were collected and presented in their normalized form by Andrus et al. (2007) which are as follows.

Table 4-3: Summary of $V_{s1} - q_{c1N}$ correlations reported by Andrus et al., (2007)

Normalized $V_{s1} - q_{c1N}$ correlation	Reference
$V_{s1} = 110 q_{c1N}^{0.13}$	Baldi et al. (1989)
$V_{s1} = 123 q_{c1N}^{0.125}$	Rix and Stokoe (1991)
$V_{s1} = 60.3 q_{c1N}^{0.23}$	Robertson et al. (1992)
$V_{s1} = 79.5 q_{c1N}^{0.23}$	Fear and Robertson (1995)
$V_{s1} = 72.8 q_{c1N}^{0.192}$	Hegazy and Mayne (1995)

The profiles developed from the above-mentioned equations are plotted in Figure 4.20 alongside the dataset developed from this study. It can be observed that with increase in the normalized cone tip resistance values, the normalized shear wave velocity increases. This is theoretically correct as both shear wave velocity and cone tip resistance increase with increasing density and effective pressure. When a shear wave is triggered the wave form travels along the grains by being transmitted through grain to grain contacts. Therefore, with higher grain contact at dense conditions or under high effective pressure, shear wave velocity increases. Similarly, the tip of the cone experiences higher resistance from a densely packed soil matrix than a looser one. The $V_{s1} - q_{c1N}$ profile developed from this study (shown in black broken line) shows a very strong agreement particularly with the study conducted by Fear and Robertson (1995) on young, uncemented silica sand from Fraser River delta. As described in section 4.3, the silica sand used in this study was re-graded according to Fraser River Sand. Jones (2017) reported a D_{50} value of 0.23 mm while a $D_{50} = 0.24$ mm was measured in this study after re-grading the Boler sand. This shows that the relationship between shear wave velocity and cone tip resistance is highly influenced by the particle gradation and median particle diameter.

However, the study conducted by Hegazy and Mayne (1995) is not very comparable to this study. This contradiction can be due to the various material properties used by Hegazy and

Mayne (1995) who studied SCPT, crosshole, downhole, SASW tests on 24 sand sites to develop correlations between V_s and q_c . Nevertheless, the correlation developed from this study is presented in Equation 4.16,

$$V_{s1} = 93.5 q_{c1N}^{0.2} \quad (4.16)$$

It has been previously discussed in this study, that one of the most important engineering properties required in characterization of in-situ soil is the maximum shear modulus (G_{max}) which is calculated from low-strain shear wave velocity measurements as shown in Equation 4.1.

In this context, an improved correlation is presented in this study to indirectly estimate G_{max} of an in-situ cohesionless soil deposit by performing a cone penetration test. To do so, the measured G_{max} was normalized to G_{max1} for overburden stress, and a mean stress normalization exponent of 0.56 was determined in this process. Figure 4.21 denotes the different stress normalization exponents of $B = 0.63, 0.50$ and 0.54 at $D_{rc} = 25.9\%, 47.6\%$ and 65.1% respectively, the mean stress exponent being 0.56. Therefore, G_{max} has been normalized using the derived exponents to produce G_{max1} , in order to correct for overburden stress effects. Moreover, it is be noted, that in this study, the stress normalization exponent for G_{max} is found to be equal to the stress normalization exponent of q_c , both being 0.56. (Here, stress exponent for G_{max} is denoted as “B”)

$$G_{max1} = G_{max} \left(\frac{Pa}{\sigma'_{vc}} \right)^B \quad (4.17)$$

Therefore, a logarithmic correlation is seen to develop between G_{max1} and q_{c1} in Figure 4.22 with $R^2 = 0.72$. This is important because, a parameter which is a measure of strength of soil (q_c) can also produce a parameter which is measure of soil stiffness (G_{max}). The correlation between the two, is developed as shown below:

$$G_{max1} = 42.5 \ln(q_{c1}) + 8.70 \quad (4.18)$$

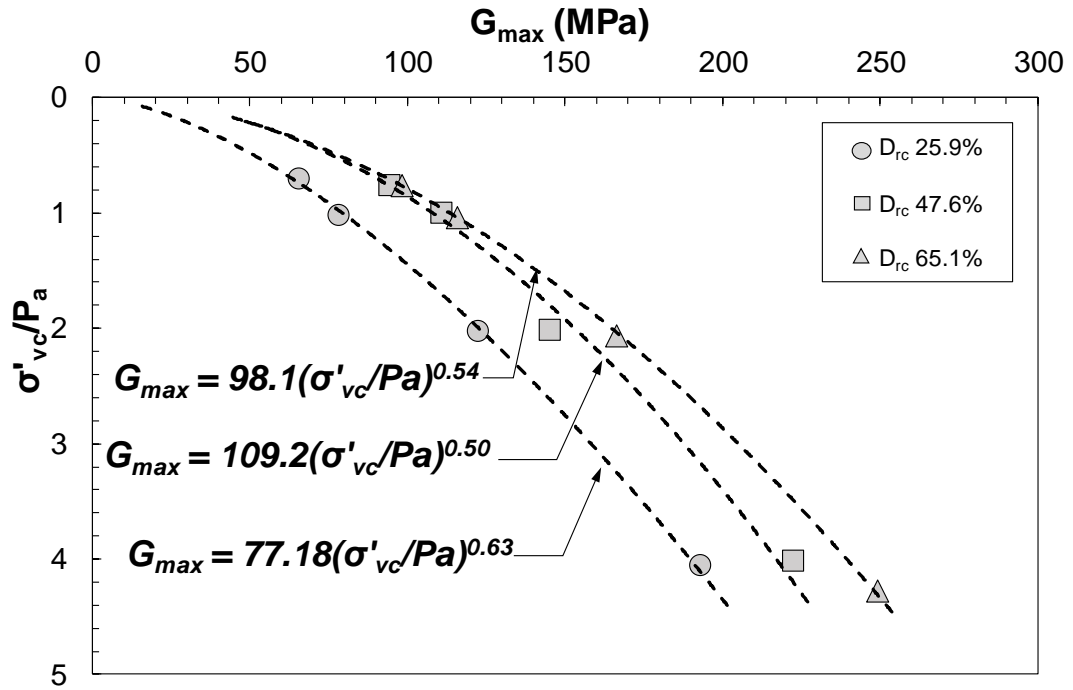


Figure 4.21: G_{max} vs. Normalized effective stress

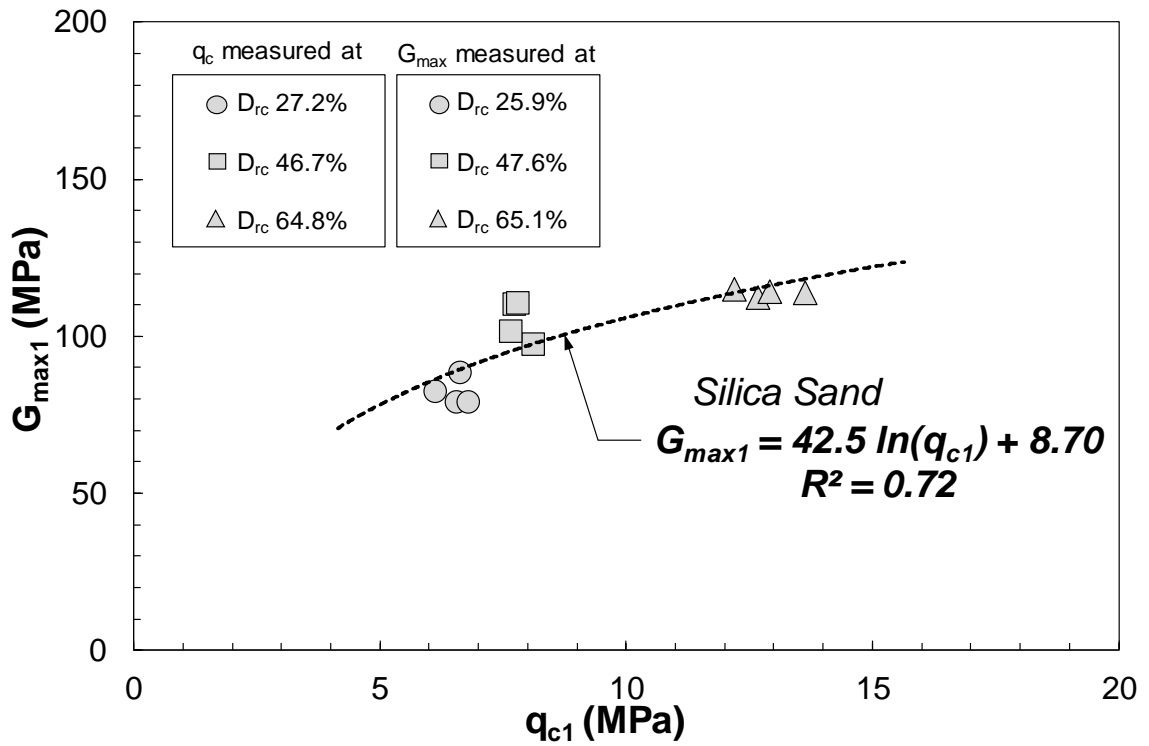


Figure 4.22: $G_{max1} - q_{c1}$ correlation for silica sand

4.8.3 Analysis of $V_s - f_s$ correlation

Not many studies have attempted to correlate shear wave velocity and sleeve frictional resistance before, but a very useful correlation is developed between the two in this chapter. In Figure 4.23, a power function best fits the data obtained from V_s and sleeve friction measurements.

$$V_{s1} = 231.09 \cdot f_{s1N}^{0.35} \quad (4.19)$$

Often, seismic cone penetration tests (SCPT) are not available in various sites. Therefore, using a conventional CPT and measuring q_c and f_s can indirectly help in estimating shear wave velocity for specific geotechnical engineering analysis.

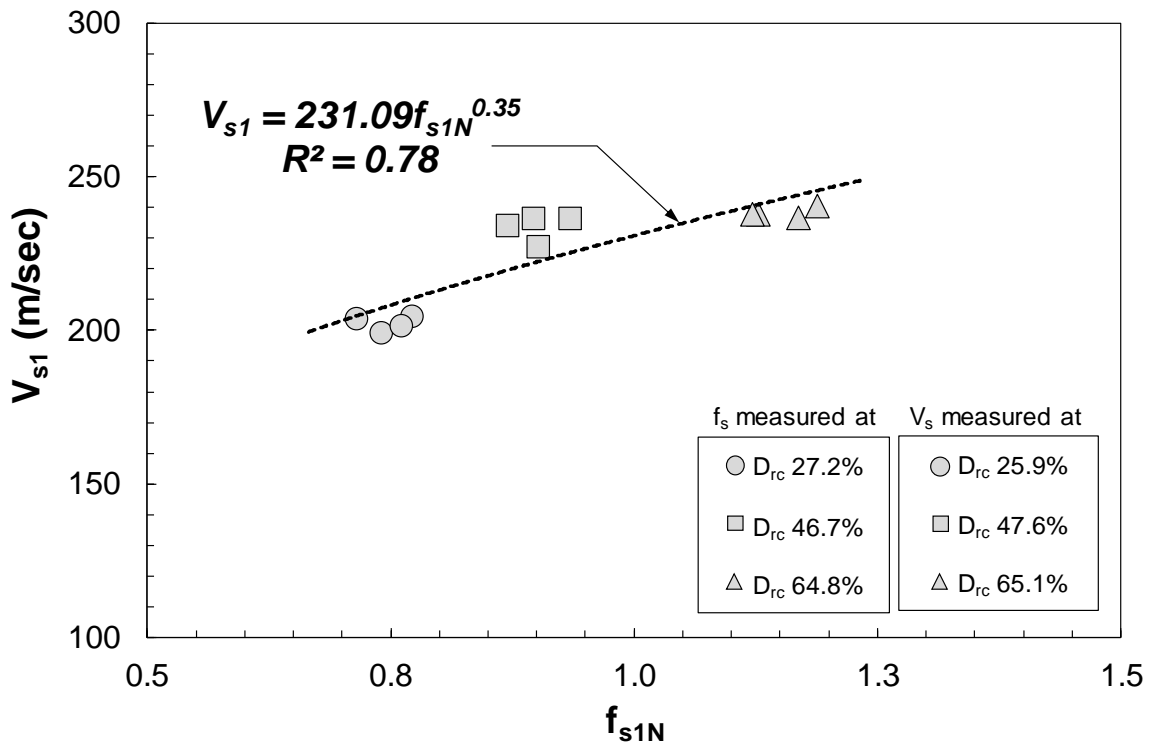


Figure 4.23: $V_{s1} - f_{s1N}$ correlation for silica sand

4.8.4 Analysis of FF – q_c correlation

A correlation between the results from electrical resistivity tests and the MCPT results from chapter 3 is developed in this study. The primary parameter that is calculated from the electrical resistivity tests is the formation factor which is highly influenced by the effect of soil grain-to-grain contacts. On the other hand, cone tip resistance, is a function of effective consolidation stress and relative density. Hence a unique correlation involving the two parameters would provide a useful tool that can be used in characterizing a silica sand.

In order to develop this correlation, formation factor is plotted against the normalized cone tip resistance i.e. q_{c1N} that eliminates the influence of overburden pressure and a unique trendline is thus developed as shown below.

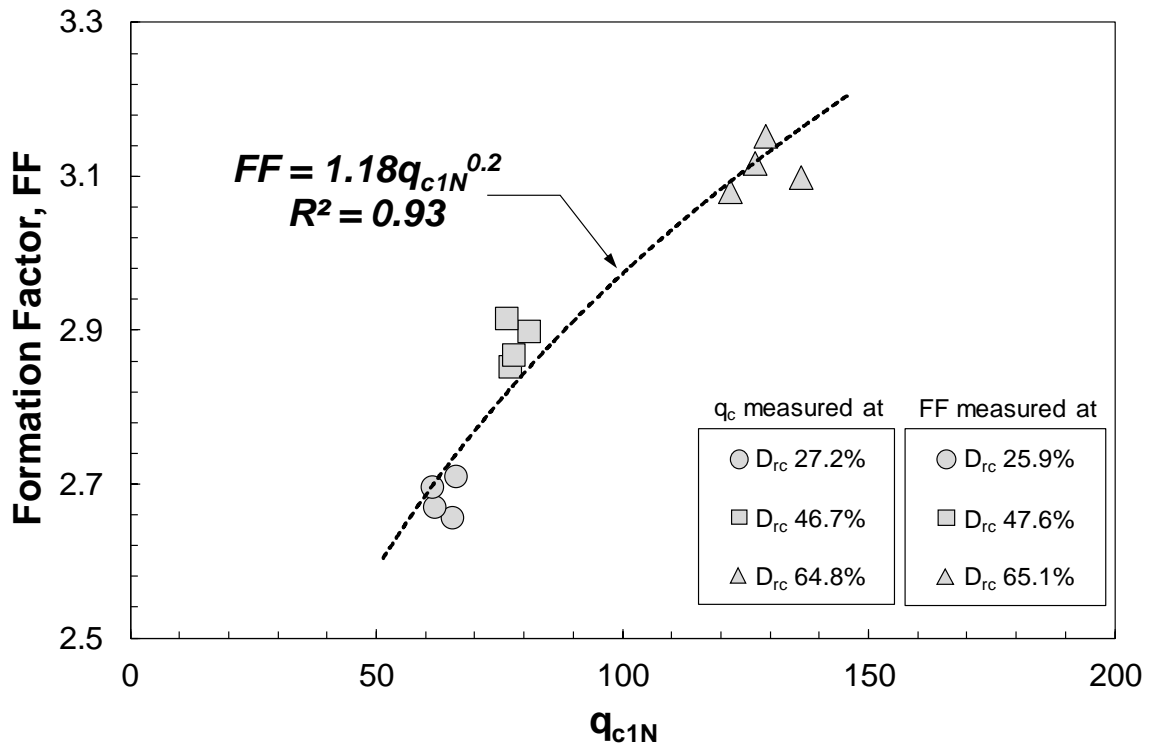


Figure 4.24: FF- q_{c1N} correlation for silica sand

In Figure 4.24, it is seen that a power function best fits the data points corresponding to individual cone tip resistance and formation factor values. Since the cone tip resistance is normalized for overburden pressure, the variation in the cluster of data points is due to the influence of relative density of the soil specimens. With increase in relative density, both q_{c1N} and FF is seen to increase which is reasonable. The average relative density levels at which individual tests were performed are shown in Figure 4.24. The developed correlation therefore is given by,

$$FF = 1.18 \cdot q_{c1N}^{0.20} \quad (4.20)$$

In the absence of any site specific data, the proposed correlation could be employed to determine the formation factor of a silica sand indirectly from cone penetration tests.

4.8.5 Estimation of Porosity

The relationship between electrical properties and porosity has been a very important subject of investigation in the oil and gas/petroleum industry for many years. It has also been proven to be of fundamental importance for geotechnical engineers for in-situ ground characterization. In this section, Archie's and the Archie-Winsauer mathematical models, which were used primarily for correlating formation factor and porosity, are discussed in further detail. The objective of this paper is to establish a formation factor – porosity correlation which will be unique for a silica sand. Figure 4.25 presents the formation factor – porosity correlation for silica sand developed in this study according to the general equation or the Archie – Winsauer mathematical model. The proposed correlation for silica sand is presented in terms of both the cementation factor “a” and shape factor “m”.

Some prominent laboratory-controlled electrical resistivity test results from previous literature has been reviewed and plotted in comparison with the dataset obtained from this study in Figure 4.25. Erchul and Nacci (1971) performed electrical resistivity tests on various soil samples ranging from clean sands to marine sediments to clay. They successfully performed the tests by developing an electrical resistivity cell which had a loading piston which would facilitate K_0 consolidation and the cell had provisions for

drainage during consolidation. Out of their several correlations developed for each type of soil, the test results on clean Ottawa sand and Glacial sand free from fine content was selected for comparison in Figure 4.25. Similarly, Arulmoli et al. (1985) performed electrical resistivity tests on Monterey 0/30 sand which was made free of fine sediments. They determined an average formation factor based on vertical and horizontal electrical resistivity measurements on Monterey sand specimens. The specimens were anisotropically consolidated and subsequently correlation models were developed between formation factor and cyclic stress ratio. Jackson et al. (1978) used a four-electrode device to measure electrical resistivity measurements on eight marine sands and plotted the derived results on an FF-n space based on the first equation (Equation 4.4) proposed by Archie (1942). Out of such eight sand samples, a batch of quartz and gravel was reported to be free from fine particles, which eventually has been presented in Figure 4.25 for comparison. In Figure 4.25, it is seen that the formation factor generally decreases with increase in porosity as looser specimens have more pore fluid around the soil grains to conduct electricity. The dataset from this study was developed at different consolidation stress levels ($\sigma'_{vc} = 74.52 \text{ kPa}, 102.08 \text{ kPa}, 203.39 \text{ kPa}$ and 411.83 kPa) as well as different relative densities ($D_{rc} = 25.9\%, 47.6\%$ and 65.1%). The factor “a” has been found to be 0.82 and the factor “m” has been found to be 1.4. The correlation was achieved with a very high coefficient of determination, i.e. $R^2 = 0.99$ and it takes the form of:

$$FF = 0.82 n^{-1.4} \quad (4.21)$$

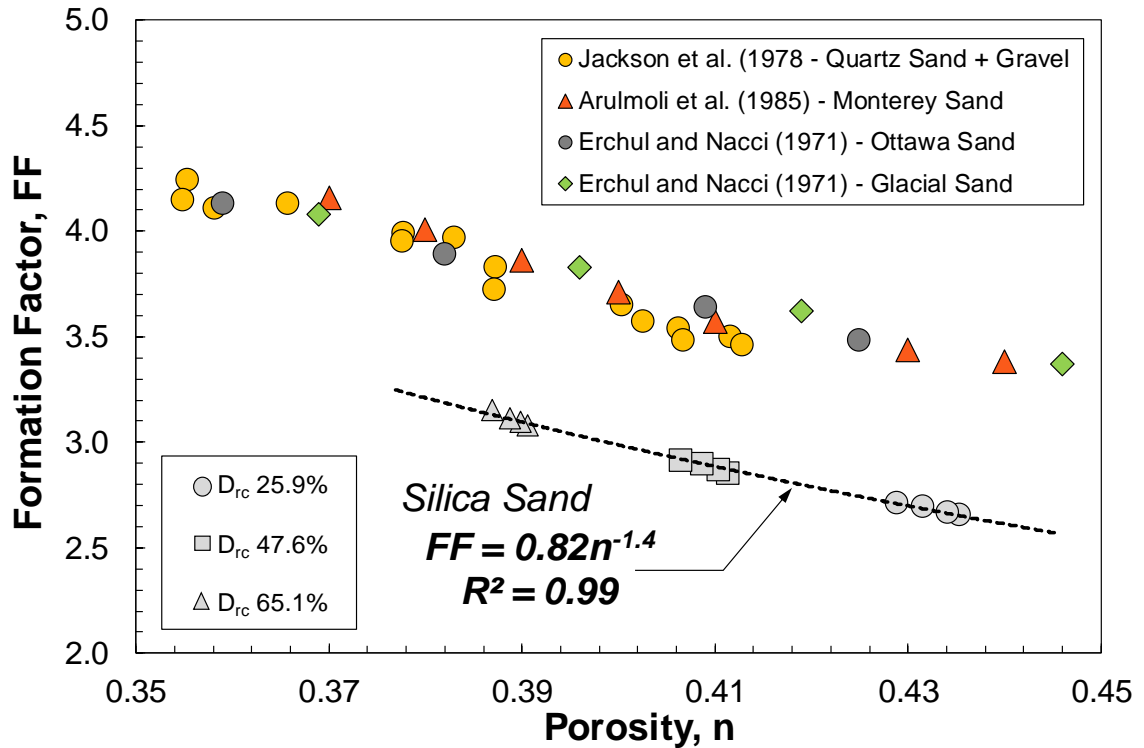
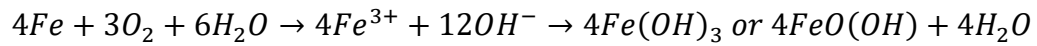


Figure 4.25: Formation factor – porosity correlation for silica sand in comparison with other studies

Section 4.5.2 in this chapter described the experiments that were conducted to measure pore fluid electrical resistivity used in this study. It was observed that distilled water mixed with 3 gm/L of salt solution produced an electrical resistivity of 2.105 Ohm.m. However, when a batch of silica sand was left saturated in a container with distilled water mixed with 3 gm/L for 24 hours, the effluent of the sand-water medium produced an electrical resistivity of 1.855 Ohm.m. The reduction in the value of resistivity can be directed towards the contribution of the sand particles to increase the conductivity of the interstitial water. Earlier, it was mentioned that the tested material comprised of a certain percentage of Chlorite and Vermiculite, both of which have Iron (Fe) in their chemical structure. Iron is often termed as the principal constituent of igneous rocks especially those containing basic silicate minerals. Iron in presence of water, is subject to a hydrolysis reaction releasing complex ions in the aqueous solution that exist either in free state or in the form of a

hydroxide. The ions released in the water acts a conductor of electricity. A general hydrolysis reaction takes the form,



Presence of iron can also be traced from the change in colour of the water that kept the sand saturated for 24 hours. Besides, during flushing of the specimens with salt solution to achieve a high degree of saturation, in each test of this study, the outcoming water from the specimen was yellowish-brown in colour. An illustration of the phenomenon is presented in Figure 4.26.



Figure 4.26: Presence of iron in outcoming water from a typical silica sand specimen

An enhanced conductivity of the pore water during a general test, reduces the bulk electrical resistivity of the specimen. No matter it being normalized by the true value of the pore fluid electrical resistivity, the measured formation factor would decrease. This phenomenon can be attributed as one of the primary reasons for the formation factor being lower in Boler sand relative to the other studies shown in Figure 4.25.

By equating formation factor in Equations 4.20 and 4.21, it can be demonstrated that from cone penetration tests one can indirectly estimate the in-situ porosity of a soil medium. Such a correlation is capable of solving the issue of measuring in-situ porosity of cohesionless soil as it can be extremely difficult to collect undisturbed cohesionless soil samples. Equation 4.22 therefore, presents the correlation for estimating soil porosity from normalized dimensionless cone tip resistance for silica sand developed in this study.

$$n = \frac{1}{(1.4 q_{c1N}^{0.2})^{1/1.4}} \quad (4.22)$$

Hence, the above-proposed correlations in Equations 4.21 and 4.22 could be employed to measure in-situ porosity of silica sand from CPT tests or electrical resistivity tests in case of absence of any site-specific data.

4.8.6 Estimation of Void Ratio

Some correlations are widely used in engineering practices as they are globally recognized through extensive research. For example, both experimental results and theoretical considerations have shown that V_s is primarily a function of void ratio (e_c) and effective confining stress (p'_c). Therefore, based on this understanding, Hardin and Richart Jr. (1963) proposed the empirical correlation given in Equation 4.23.

$$V_s = A F(e) (p'_c)^B \quad (4.23)$$

where $F(e)$ is the function of void ratio, A and B are material constants for a particular sand and σ'_{pc} refers to the effective confining stress experienced by the soil. B has generally found to be 0.25 (Hussein and Karray 2015). The effective confining pressure or the mean effective confining stress for any isotopically consolidated triaxial testing is generally determined by the following equation.

$$p'_c = \frac{(1 + 2K_o) \sigma'_{vc}}{3} \quad (4.24)$$

The effect of vertical effective stress is often removed using an overburden correction factor (Skempton 1986; Sykora 1987; Karray et al. 2011). In other words, V_s is normalized for vertical effective stress, σ'_{vc} as has been done in the studies for the evaluation of liquefaction potential (Youd et al. 2001).

$$V_{s1} = V_s \left(\frac{P_a}{\sigma'_{vc}} \right)^{0.25} \quad (4.25)$$

By substituting Equation 4.23 into Equation 4.25, the modified relationship in terms of normalized shear wave velocity is shown in Equation 4.26.

$$V_{s1} = A.F(e).p'_c{}^B \left(\frac{P_a}{\sigma'_{vc}} \right)^{0.25} \quad (4.26)$$

Furthermore, substituting Equation 4.24 into Equation 4.26, Hussein and Karray (2015) developed the correlation as follows,

$$V_{s1} = A.F(e) \cdot \left\{ \frac{100}{\left(\frac{3}{1 + 2K_o} \right)} \right\}^{0.25} \quad (4.27)$$

where, P_a has been substituted by 100 kPa atmospheric pressure.

(Sasitharan et al. 1994; Robertson et al. 1995) suggested a modified correlation using the relationship,

$$e = \frac{A}{B} - \frac{V_s (P_a)^{na + nb}}{B (\sigma'_{vc})^{na} (K_o \sigma'_{vc})^{nb}} \quad (4.28)$$

where na and nb are given stress exponents, typically $na = nb = 0.125$.

Moreover, measured values of V_s are mostly corrected for overburden effective stress which takes the form as in Equation 4.29 suggested by Cunnings et al. (1995).

$$V_{s1} = V_s \left(\frac{P_a}{\sigma'_{vc}} \right)^{na + nb} \quad (4.29)$$

Combining and simplifying Equations 4.28 and 4.29, Cunnings et al. (1995) suggested the relationship which takes the form as follows,

$$V_{s1} = (A - B e_c) K_o^{0.125} \quad (4.30)$$

$$F(e_c) = V_{s1} K_o^{0.125} \quad (4.31)$$

K_o is included in the Equation 4.31 to account for the substitution of effective confining stress. Similarly, there are some more mathematical models that have tried to correlate V_{s1} and void ratio. In this study, it has been attempted to develop a correlation between normalized shear wave velocity and void ratio after consolidation. The correlation between V_{s1} and e_c is seen to adopt a linear function as shown in Figure 4.27.

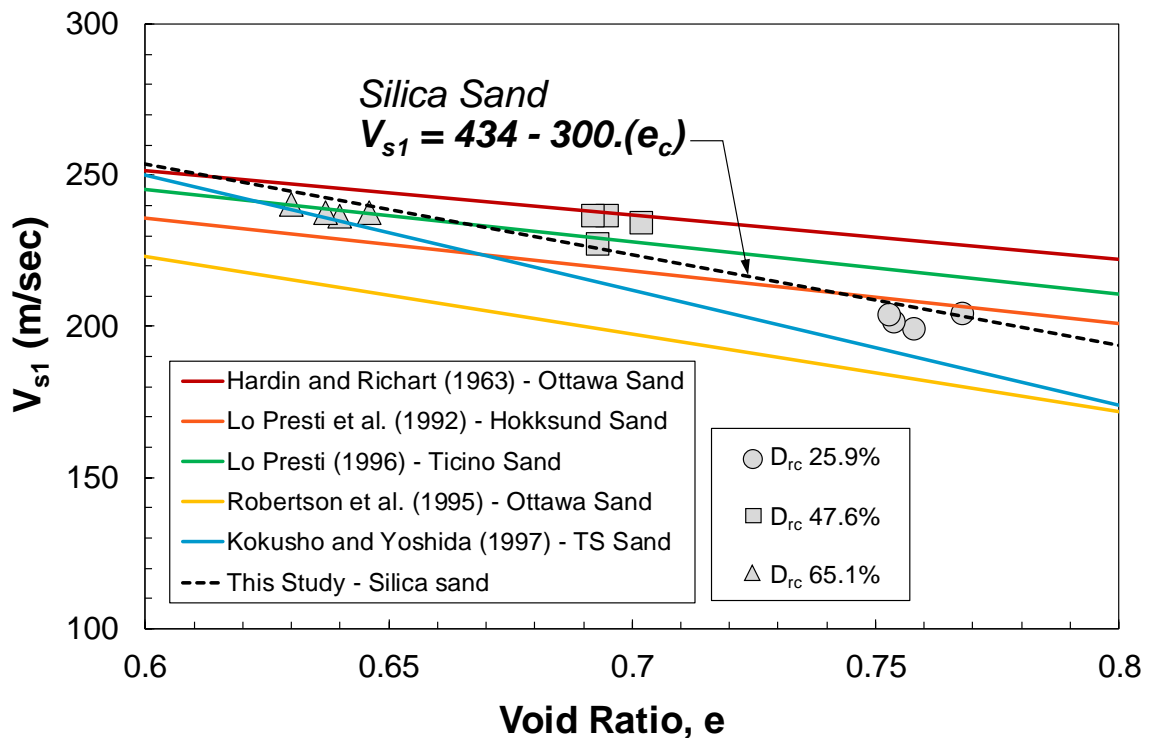


Figure 4.27: Correlation of consolidation void ratio (e_c) with V_{s1}

Figure 4.27 highlights the correlation developed between consolidation void ratio e_c , and the normalized shear wave velocity for this study on silica sand.

$$V_{s1} = 434 - 300 (e_c) \quad (4.32)$$

To verify this result, several other studies which measured V_s on sandy soils have been reviewed to draw a comparison on the behavior of our material relative to others. However, not all studies have been performed under similar testing conditions and equipment. For example, Hardin and Richart (1963) measured shear wave velocities on Ottawa Sand and quartz sand using Resonant Column tests. Robertson et al. (1995) performed bender element tests on Ottawa Sand, Syncrude Sand and Alaska Sand in a triaxial testing chamber after the sand specimens were subjected to isotropic consolidation. Overall, the trendline developed from this study shown in black broken line compares quite well with a number of studies (Lo Presti 1987; Lo Presti et al. 1992).

The dependence of shear wave velocity on void ratio is the very reason why shear wave velocity is such a highly recommended parameter in analysis of liquefaction resistance. Liquefaction resistance too, depends on void ratio and relative density of in-situ soil.

Following Equation 4.31 suggested by Cunning et al. (1995), normalized shear wave velocity as a function of void ratio has been plotted in Figure 4.28 along with some relevant previous studies.

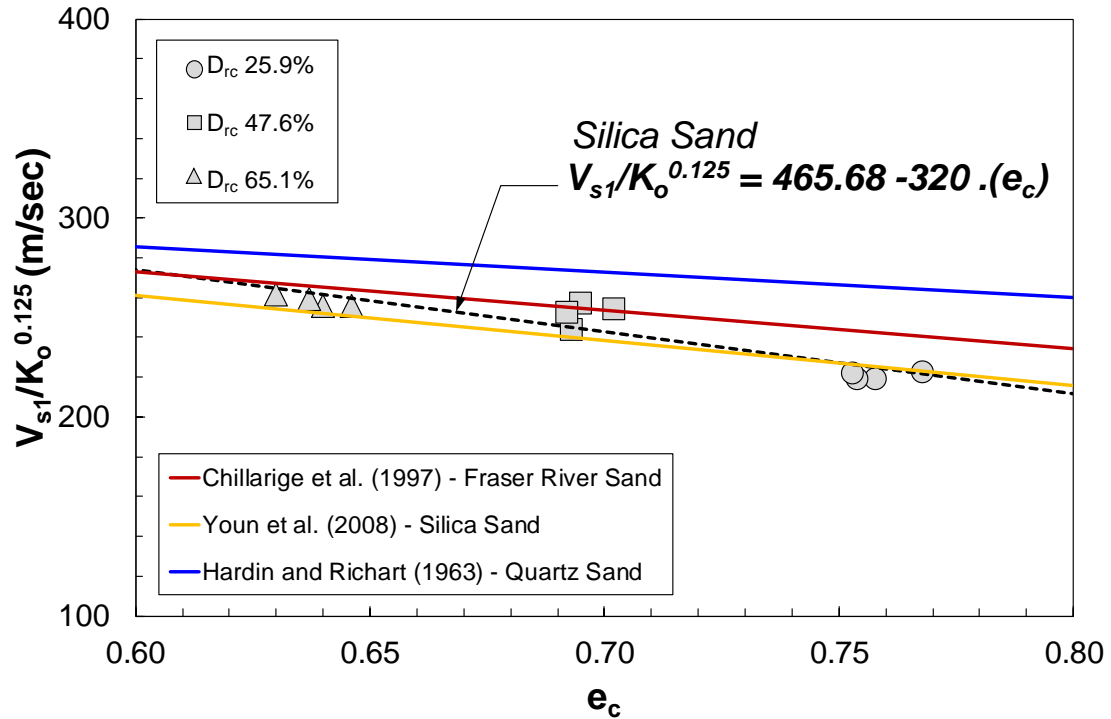


Figure 4.28: Correlation of consolidation void ratio (e_c) with $F(e_c)$

Figure 4.28 highlights the correlation developed between consolidation void ratio e_c , and the function of void ratio, $F(e_c)$ for this study on silica sand.

$$\frac{V_{s1}}{K_o^{0.125}} = 465.68 - 320.(e_c) \quad (4.33)$$

Chillarige et al. (1997) performed SCPT tests on Fraser River region and simultaneously performed undrained and drained isotropic triaxial tests and bender element tests on Fraser River Sand in the laboratory. Youn et al. (2008) measured V_s in Resonant Colum tests and Torsional Shear tests on silica sand samples. Nevertheless, Figure 4.28 provides some validation that the correlation obtained from this study reasonably compares with some of the reviewed previous research. As a matter of fact, the trendlines developed from the studies by Youn et al. (2008) and Chillarige et al. (1997) provides a very close comparison to the present study.

Along with shear wave velocity (V_s), small-strain shear modulus (G) is also a fundamental parameter in characterising soil behaviour. On one hand shear wave and its velocity gives a direct measure of soil elasticity and maximum shear modulus G_{max} , on the other hand maximum shear modulus G_{max} provides an understanding of stiffness and rigidity of the continuum material as depicted by Hussien and Karray (2015).

$$G_{max} = \rho V_s^2 \quad (4.34)$$

where G_{max} is in Pascal, ρ is the total mass density of the tested material in kg/m^3 .

Several investigations have been conducted on shear wave velocity and shear modulus of sandy soils and in the establishment of their correlations with soil characteristics like relative density, consolidation void ratio and confining pressure (Hardin and Black 1966; Iwasaki et al. 1978; Kokusho 1980; Robertson et al. 1995; Lo Presti et al. 1997). The predominant material tested in most of these studies were silica and quartz sand. Like $V_{s1} - e_c$ correlation, a normalized correlation between G_{max} and e_c has also been investigated and compared with relevant studies. These correlations are often generalized in a form represented by the Equation 4.35 after Hardin and Richart (1963).

$$\frac{G_{max}}{P_a} = A F'(e_c) \left(\frac{p'_c}{P_a} \right)^B \quad (4.35)$$

where $F'(e_c)$ is the function of consolidation void ratio and B is the stress normalization exponent which is often equal to $B = 2 \times n$ and n being the stress normalization exponent derived from Figure 4.16. The stress exponent, n , has often been taken to be around 0.5 (Hardin and Richart Jr. 1963; Hardin and Drnevich 1972; Shibuya and Tanaka 1996). However, the exact stress normalization exponent for this study is calculated and used accordingly. The average stress normalization exponent derived for V_s is 0.27. Therefore, $B = 2 \times 0.27 \approx 0.56$.

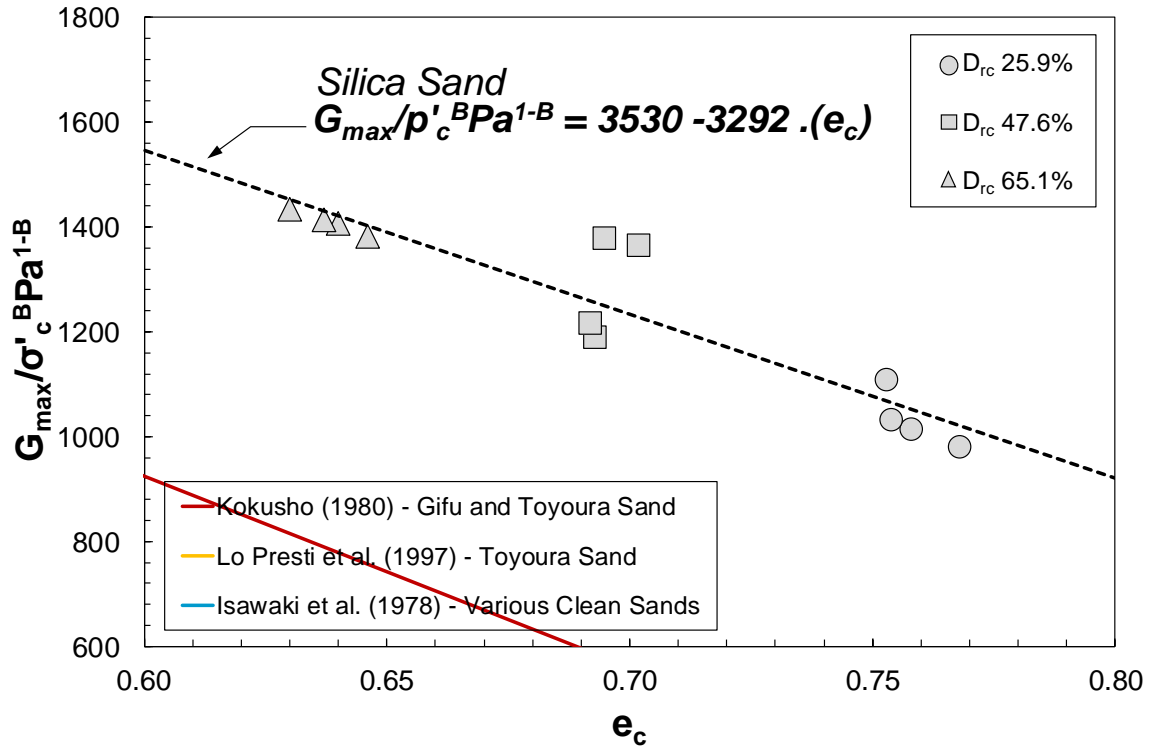


Figure 4.29: Correlation of consolidation void ratio (e_c) with $AF'(e_c)$

The correlation developed from the current study and its comparison with other relevant research is shown in Figure 4.29. To verify this result, several other studies which calculated G_{max} on sandy soils have been reviewed to draw a comparison on the behavior of our material relative to others. It is however seen from Figure 4.29, denser specimens from this study on silica sand have estimated relatively higher values of the function of void ratio that incorporate maximum shear modulus, compared to other studies. The reviewed tests have been performed in different testing conditions and equipment like resonant column tests, triaxial shear tests and cyclic simple shear tests. For example, Kokusho (1980) performed bender element tests in modified triaxial testing chamber on saturated and compacted specimens of Gifu and Toyoura sand after isotropic consolidation. Lo Presti et al. (1997b) performed bender element tests on Toyoura sand in both modified triaxial tests and resonant column tests. Iwasaki et al. (1978) collected various sands like Toyoura, Ban-nosu, Iruma, Kinjo-1, Kinjo-2, Ohgi-Shima, Monterey sand and measured

shear wave velocity in resonant column tests and torsional shear tests on the sand specimens.

The correlation developed from this study is shown in Equation 4.36.

$$\frac{G_{max}}{p'_c{}^B Pa^{1-B}} = 3530 - 3292(e_c) \quad (4.36)$$

Despite the nonlinear nature of soil behavior in general, the importance of soil stiffness in the range of very small shear strains ($\gamma = 10^{-6} - 10^{-5}$) has attracted increasing interest. Conventional laboratory tests like oedometer tests and triaxial tests measure stiffness only in a range of intermediate to large strains. Large strain dependent stiffness models have been widely studied (Hardin and Drnevich 1972; Ishibashi and Zhang 1993; Oztoporak and Bolton 2013), while the prediction of small strain stiffness is still quite challenging and studied intensively by (Hardin and Richart 1963; Iwasaki and Tatsuoka 1977; Senetakis et al. 2012; Wichtmann et al. 2015; Payan et al. 2017). Much like the empirical model between small-strain shear modulus as a function of void ratio, a well-recognized and widely used correlation is used for the prediction of small-strain constrained modulus (M_{max}) modelled as a function of void ratio.

M_{max} which is generally obtained from P-wave velocities can also be calculated from S-wave measurements. At very small strains, M_{max} can be directly calculated from G_{max} by the following equation,

$$M_{max} = \frac{2G_{max}(1 - \nu)}{1 - 2\nu} \quad (4.37)$$

where, ν = Poisson's ratio of soil, usually 0.3 for cohesionless soil.

The same form of Equation 4.36 was re-designed in terms of M_{max} by several authors including (Wichtmann and Triantafyllidis 2010; Senetakis et al. 2017; Panuska and Frankovska 2018) given by,

$$\frac{M_{max}}{Pa} = A \cdot F''(e_c) \cdot \left(\frac{p'_c}{Pa}\right)^B \quad (4.38)$$

where A is a material constant, $F''(e_c)$ is the function of consolidation void ratio and B is the stress normalization exponent which is often equal to $B = 2 \times n$ and n being the stress normalization exponent derived from Figure 4.16. The stress exponent, n, has often been taken to be around 0.5 (Hardin and Richart 1963; Hardin and Drnevich 1972; Shibuya and Tanaka 1996). However, the exact stress normalization exponent for this study is calculated and used accordingly. The average stress normalization exponent derived for V_s is 0.27. Therefore, $B = 2 \times 0.27 \approx 0.56$.

A linear correlation is seen to develop in Figure 4.30 between M_{max} as the function of void ratio and void ratio after consolidation. The correlation takes the form,

$$\frac{M_{max}}{p'_c{}^B Pa^{1-B}} = 12356 - 11521(e_c) \quad (4.39)$$

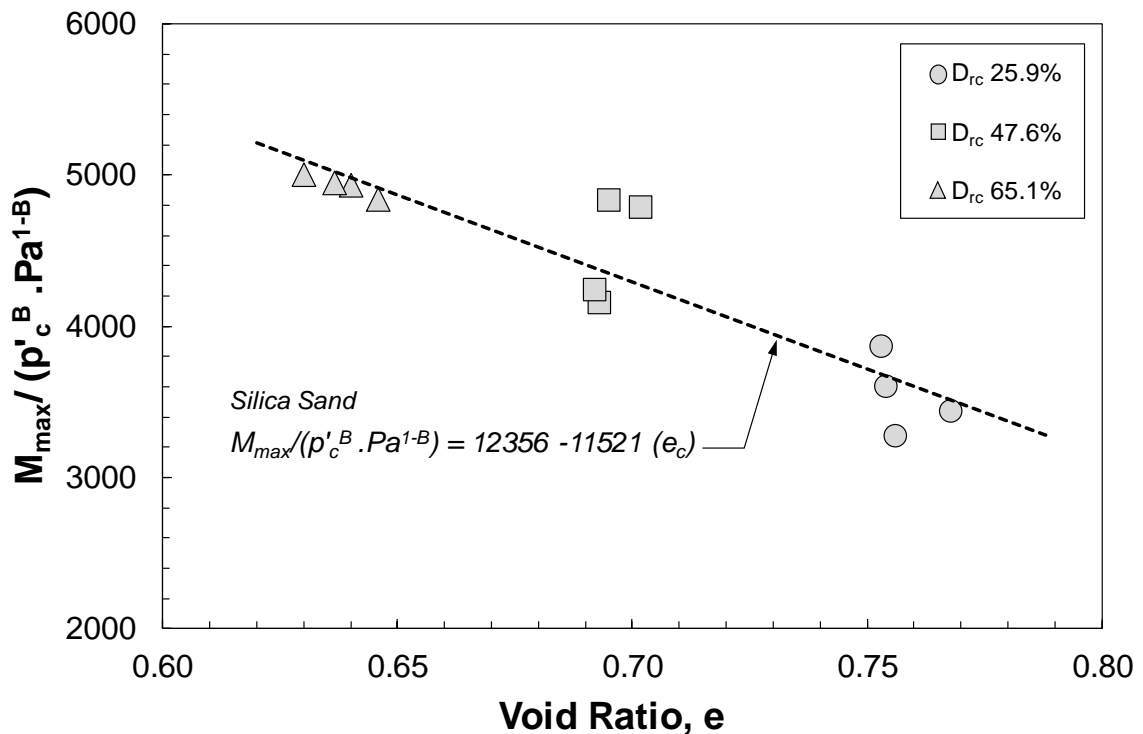


Figure 4.30: Correlation of consolidation void ratio (e_c) with $AF''(e_c)$ for this study on silica sand

Formation factor has however, shown to correlate with void ratio with a power function at a very high coefficient of determination ($R^2 = 0.99$). With increasing void ratio, i.e. decreasing relative density, formation factor is seen to decrease as looser specimens can hold more interstitial water which enhance the electrical conductivity. Figure 4.31 describes the correlation between formation factor and void ratio which will be used later in this chapter for evaluating techniques of determining in-situ state of silica sand. The developed correlation to estimate void ratio from formation factor measurements in silica sand is given in Equation 4.40, where e_c is the void ratio post consolidation.

$$FF = 2.14 \cdot e_c^{-0.83} \quad (4.40)$$

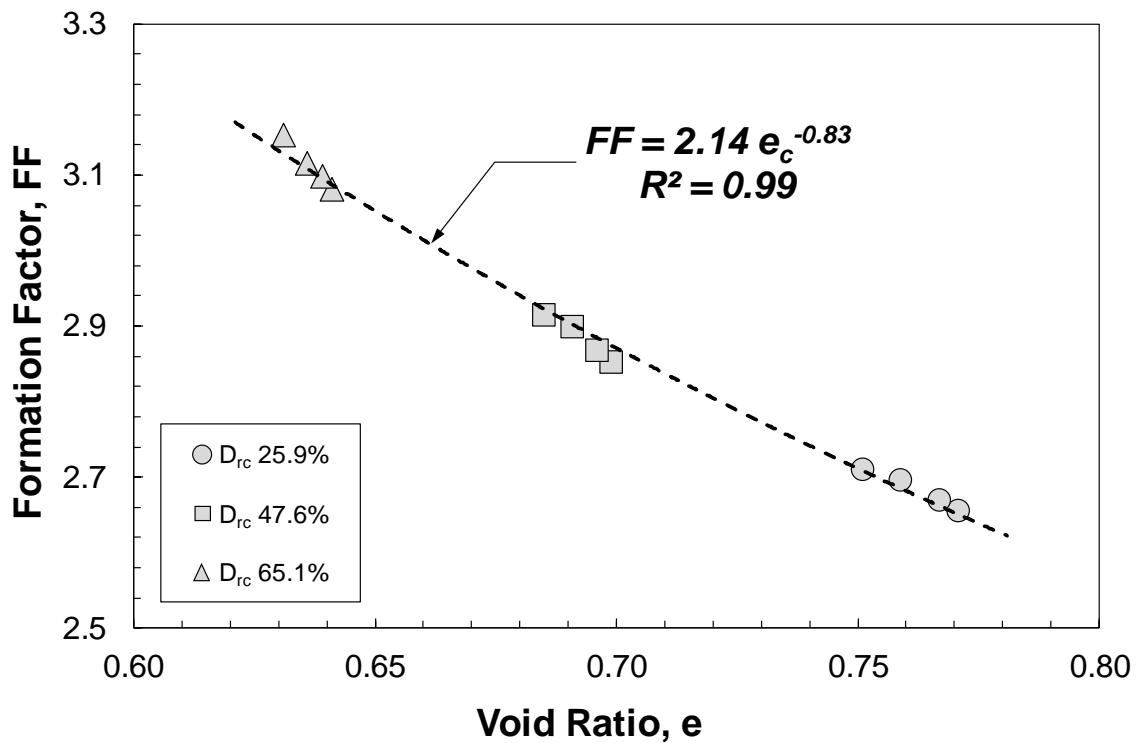


Figure 4.31: FF- e_c correlation for silica sand

4.8.7 Estimation of Relative Density

The concept of relative density (D_r) was initially suggested by Burmister (1948) and it is to date one of the most extensively used geotechnical engineering parameters as an index of mechanical properties of coarse grained soils. Owing to uncertainties and extreme difficulties in retrieving good quality undisturbed cohesionless soil samples (Yoshimi et al. 1978; Hatanaka et al. 1988; Goto et al. 1992; Yoshimi 2000), geotechnical engineering practitioners adopted the new way of estimating relative density from penetration test results. Schmertmann (1976) and later, Jamiolkowski et al. (2001) investigated the correlations between relative density and cone tip resistance. Empirical correlations based on MCPT results and relative density have been produced in chapter 3. In this chapter, shear wave velocity and formation factor are utilized to develop and compare correlations with relative density of soil, as both of these parameters are highly dependent on relative density.

Shear wave velocity (V_s) is often expressed as a function of void ratio, $F(e)$. But some researchers have also attempted to correlate V_s directly to relative density of soil. In the early 1970's, Seed and Idriss (1970) proposed a relationship between shear wave velocity and relative density of soil which was later re-arranged and simplified by Karray and Lefebvre (2008) as,

$$V_{s1} = 25.8 + (D_r + 25)^{0.5} \quad (4.41)$$

Despite several correlations that have tried to investigate V_s - e relationship, some studies have proposed recommendations on using soil grain characteristics and gradation while predicting V_s . On the other hand, another group of researchers claim that variation in void ratio at a macro level is enough to estimate V_s . For example, (Hardin and Richart 1963; Hardin and Drnevich 1972) after several resonant column tests on round grained Ottawa sand and angular grained crushed quartz sand, reported that particle size affects the magnitude of V_s but only through influencing the void ratio function. According to them, more than particle size, it is the density of the soil medium that influences the magnitude of shear wave velocity. Wichtmann and Triantafyllidis (2009) tested sands of 25 different grain size distributions of quartz sand on RC tests and their experimental data suggested

that V_s is independent of D_{50} . However, there have been many studies based on the influencing factors for shear wave velocity which claim that not only relative density, but soil grain size also influences measurements. Kulhawy and Mayne (1990) and Cubrinovski and Ishihara (1999) showed that with not only relative density, but with a change in D_{50} (mm) alters measured parameters like N-SPT, q_c -CPT and V_s . Iwasaki and Tatsuoka (1977) using resonant column tests on normally consolidated reconstituted sands of different C_u and D_{50} , reported that V_s is strongly affected by increasing fines content however, for poorly graded sands without fines, V_s does not depend on D_{50} . Chang and Ko (1982) had a similar observation after testing 23 medium – loose sand specimens. Ishihara (1996) after collecting results from different gradation of sands and gravels concluded particle characteristics might influence V_s . Rollins et al. (1998) confirmed that V_s increases with gravel content. Menq and Stokoe (2003) after performing several RC tests on reconstituted specimens of natural river sand reported that D_{50} influences V_s strongly.

All of these investigations led Hussein and Karray (2015) to develop an empirical correlation between V_s and relative density which includes D_{50} . The correlation takes the form,

$$V_{S1} = 5.68 (\ln(D_{50}) + 4.84) + \sqrt{D_r + 25} \quad (4.42)$$

However, this equation is valid for a range of D_{50} , 0.2 to 10 mm. The tested material in this study has a D_{50} of 0.24 mm, which comfortably falls within the prescribed range.

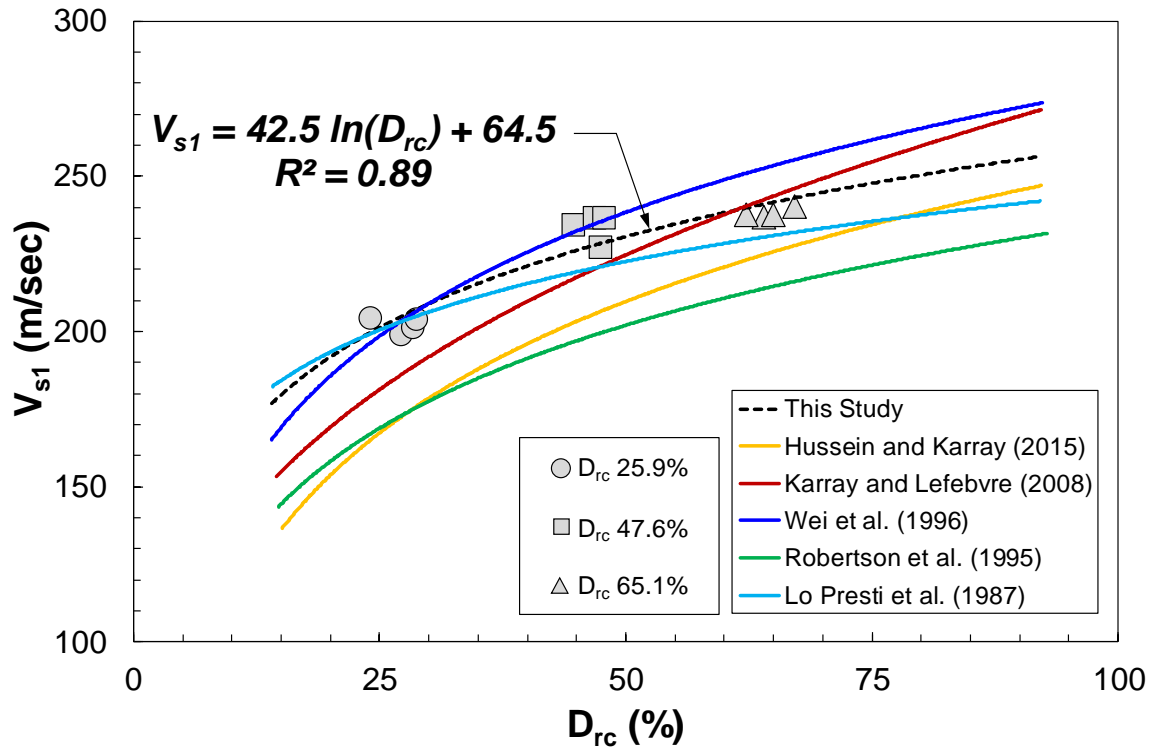


Figure 4.32: Comparison of correlations between V_{s1} and D_{rc} from this study with (Karray and Lefebvre 2008; Hussein and Karray 2015)

Figure 4.32 presents the correlation developed from this study on silica sand in comparison with previous studies. The predictive models by Karray and Lefebvre (2008) and Hussein and Karray (2015) have also been plotted alongside the dataset. Wei et al. (1996) measured shear wave velocity on fine, medium and coarse sands collected from New Madrid Seismic zone. Robertson et al. (1995) developed correlations with shear wave velocity on Ottawa sand. Lo Presti et al. (1987) measured shear wave velocities on Ticino sand by RC tests. Overall, the correlation trendline for silica sand compared decently with quite a few numbers of studies especially with that of Lo Presti et al. (1987).

For the tests on loose and medium dense specimens, silica sand is seen to predict higher values of V_{s1} than both (Karray and Lefebvre 2008; Hussein and Karray 2015). One of the reasons that can explain such a behaviour is that, these studies developed their correlations based on multiple data collected for numerous soil types. Supposedly, a particular soil type

which consists of significant amount of fines content would bring the magnitude of shear wave velocity down. This study has been performed on clean silica sand after eliminating fines content which can exhibit a higher magnitude of V_{s1} . A logarithmic function is seen to correlate V_{s1} and relative density with a coefficient of determination (R^2) of 0.89. The specific correlation for silica sand is therefore,

$$V_{s1} = 42.5 \ln(D_{rc}) + 64.5 \quad (4.43)$$

The correlation does not include D_{50} as all the tests in this study has been conducted on the same material which has a $D_{50} = 0.24$.

However, the influence of D_{50} (mm) is found reasonable by the current study as it was seen in Figure 4.20, that the relationship between V_{s1} and q_{cIN} showed particular agreement with the study by Fear and Robertson (1995) on young, uncemented Fraser River sand. The silica sand used in this study was re-graded according to Fraser River Sand. Jones (2017) reported a D_{50} value of 0.23 mm while a $D_{50} = 0.24$ mm was measured in this study after re-grading the Boler sand. This shows that the relationship between shear wave velocity and cone tip resistance is highly influenced by the particle gradation and median particle diameter.

From Figure 4.33, it can be inferred that the predicted V_{s1} from the method of Karray and Lefebvre (2008) seems to be generally closer to the measured values of V_{s1} with a slight underestimation.

Relative density of any soil is important both for laboratory and in-situ tests for geotechnical investigations. It is significant in understanding the state of the soil. For example, Jefferies and Been (2006) highlighted that cohesionless soils with state parameter (ψ) values more than -0.05 are much prone to a liquefaction event, where state parameter is a function of both relative density and effective stress. If laboratory tests on a specific soil material under a controlled environment can produce significant empirical correlations to estimate engineering properties of the soil, it eliminates the problem of collecting undisturbed soil samples. Moreover, if in-situ tests are not feasible at a particular site,

empirical correlations developed from such laboratory tests can be used to characterize the subsurface.

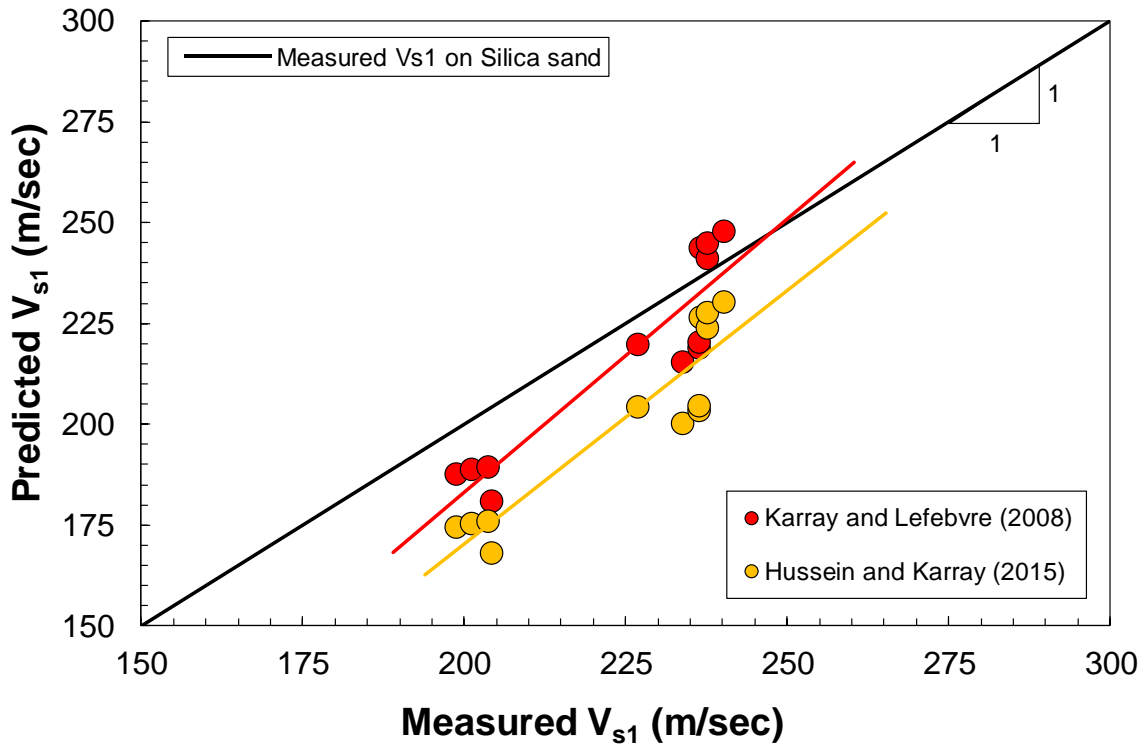


Figure 4.33: Comparison of V_{s1} predictive models proposed by (Karray and Lefebvre 2008; Hussein and Karray 2015)

It was discussed earlier in this chapter, that the measured formation factor values have shown significant variation with changes in the state of relative density. The tests have been performed at average $D_{rc} = 25.9\%$, 47.6% and 65.1% and from Figure 4.34 one can easily identify the three stages of relative density through which formation factor has varied. In section 4.8.6, correlations have been developed for estimating porosity from electrical resistivity tests in case of silica sand. Therefore, Figure 4.34 presents the correlation developed for estimating relative density of silica sand indirectly from formation factor.

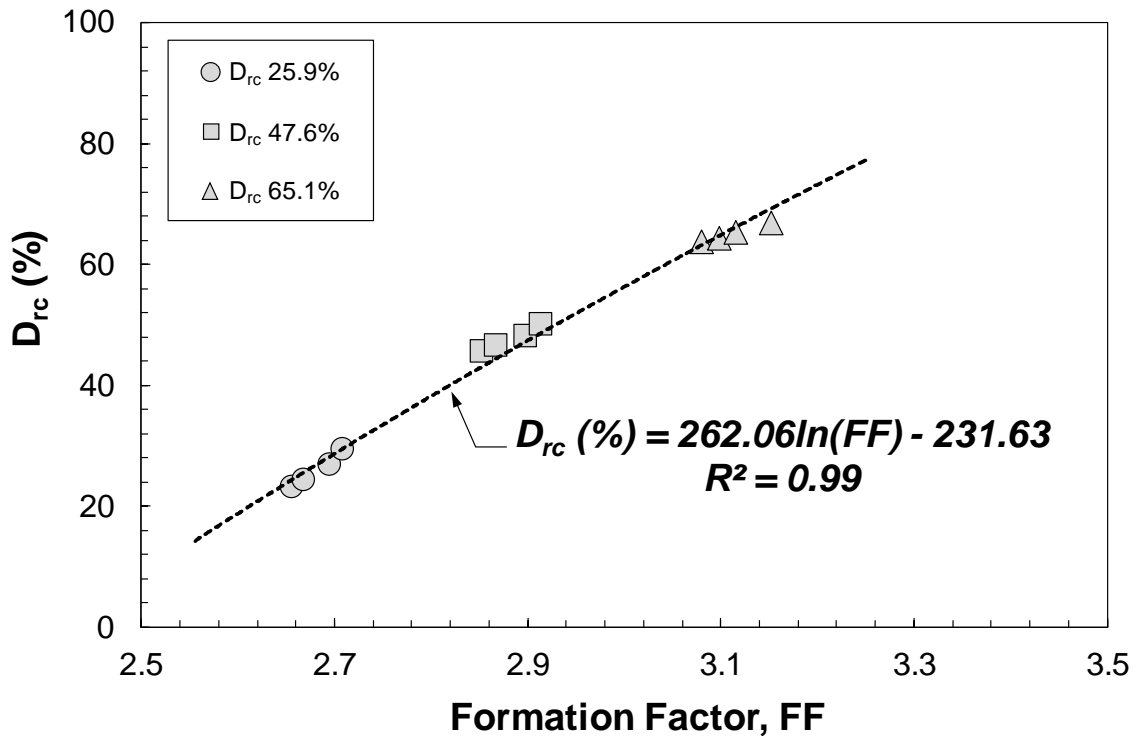


Figure 4.34: FF – D_{rc} correlation for silica sand

With a very high coefficient of determination, $R^2 = 0.99$, the two parameters are seen to correlate with each other in a logarithmic function. The three clusters of datapoints correspond to each relative density level shown in Figure 4.34. The proposed correlation is given by,

$$D_{rc}(\%) = 262.06 \ln(FF) - 231.63 \quad (4.44)$$

It is also acknowledged that formation factor is a better representative of in-situ state more than relative density. Relative density is a function of the spatial distribution of void ratio in a soil medium. Moreover, the correlation between $D_{rc} - q_{c1N}$ in chapter 3, showed that the correlation is sand specific as it distributes over a wide range owing to different type of sands, particle size distribution or even fines content. However, formation factor as discussed earlier, not only depends on the void ratio or porosity, but also on shape, size,

cementation characteristics, contact orientation of the soil particles (Archie 1942; Wyllie and Gregory 1953; Jackson 1975; Arulanandan and Kutter 1978; Kutter 1978; Arulmoli 1980, 1982) which most likely is a better parameter to predict in-situ state. However, future investigations in this context is required to strengthen this theory.

4.8.8 Estimation of Unit Weight

Soil unit weight is a critical parameter for calculating initial geostatic and overburden stresses for CPT data interpretation, analysis of shear wave velocity measurements and to estimate other geotechnical engineering parameters. The ideal process of estimating soil unit weight is by undisturbed sampling of in-situ soil by thin walled tube samplers, special block sampling or ground freezing techniques. However, such methods can be expensive, time consuming and highly labour intensive as they require expensive equipment to carry out the process. Therefore, indirect empirical correlations with CPT data or geophysical test data are often developed and used for quicker processing of preliminary geotechnical investigations. The soil unit weight can be calculated using fundamental index relationships as given in Equations 4.45 and 4.46.

$$\gamma_d = \gamma_w \frac{G_s}{1 + e_c} \quad (4.45)$$

$$\gamma_{sat} = \gamma_t = \frac{\gamma_w \cdot (G_s + e_c)}{(1 + e_c)}; \text{ assuming } S = 1 \quad (4.46)$$

A global and rudimentary relationship exists between V_s and unit weight of soils as shear wave velocity strongly depends on void ratio, effective stress state, fabric, structure, cementation, ageing (Tatsuoka and Shibuya 1992; Stokoe and Carlos Santamarina 2000; Mayne et al. 2010). Burns and Mayne (1996) compiled data from numerous field tests and laboratory tests on various soil types including rocks, gravels, sands, silts and clays, and established that total unit of weight of soil can be expressed a power function in terms of effective overburden stress and shear wave velocity, given in Equation 4.47.

$$\gamma_t(kN/m^3) = 6.87(V_s)^{0.227} \cdot (\sigma'_{vo})^{-0.057} \quad (4.47)$$

Figure 4.35 represents the comparison between the trendlines developed from the correlation of this study relative to the prediction suggested by Burns and Mayne (1996). The distinction between the trends of the current study and the one suggested by Burns and Mayne (1996) is about 1 kN/m³ on an average. The difference in material tested, mineralogy of the material tested, test equipment, volume of data used to develop correlations, etc. are some of the reasons which can be considered to justify the distinction. Burns and Mayne (1996) developed the regression model based on data collected from a variety of soil including clay and gravel. The power function produced from the dataset of the bender element tests is given by the following equation.

$$\gamma_t = 16.5 \cdot (V_s)^{0.029} \quad (4.48)$$

An alternative version to the above discussed empirical correlation by Burns and Mayne (1996), was suggested by Mayne (2007) in terms of normalized shear wave velocity. Mayne (2007) from a global database on numerous soils, suggested the correlation shown in Equation 4.49.

$$\gamma_{sat} = 4.17 \cdot \ln(V_{s1}) - 4.03 \quad (4.49)$$

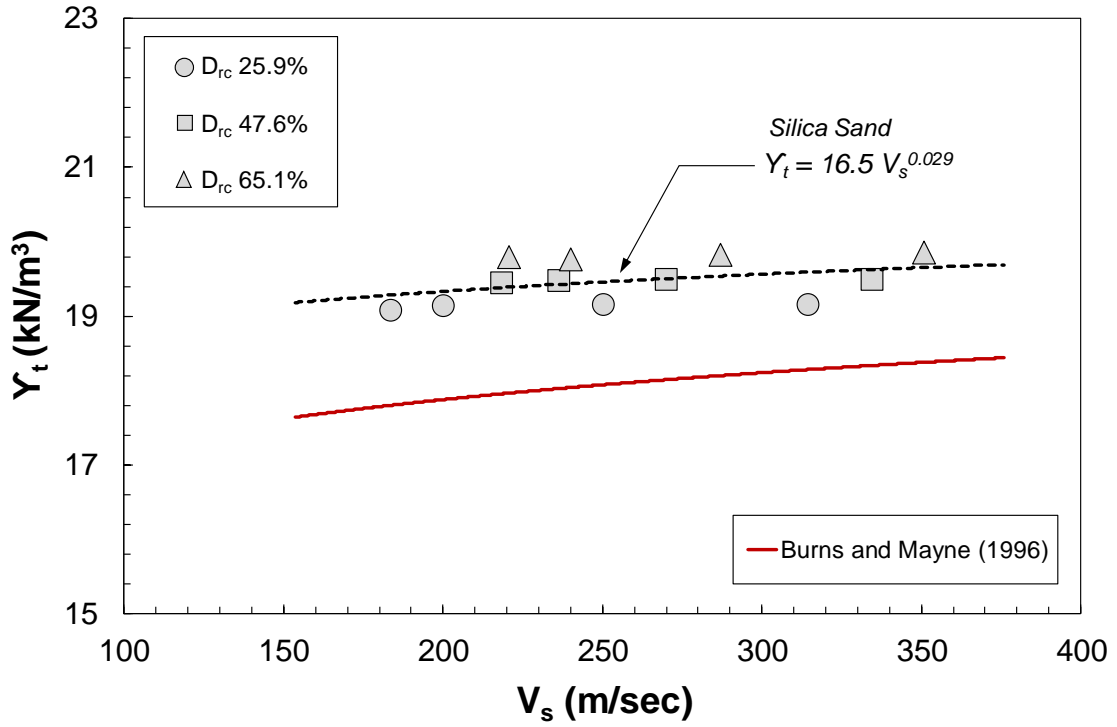


Figure 4.35: Comparison of $Y_t - V_s$ correlation with Burns and Mayne (1996)

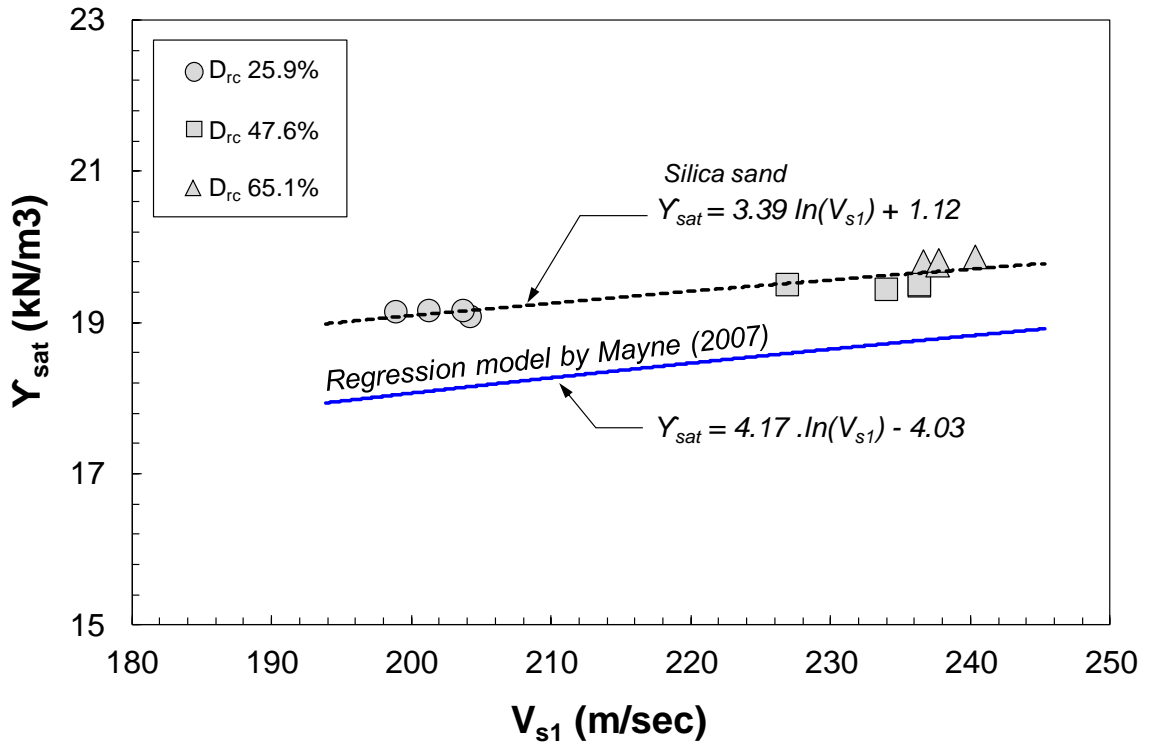


Figure 4.36: Comparison of $Y_{sat} - V_{s1}$ correlation with Mayne (2007)

In Figure 4.36, alongside the regression model proposed by Mayne (2007), the dataset obtained from the bender element tests in this study has been plotted. A logarithmic correlation is seen to develop between saturated unit weight of silica sand and shear wave velocity which is given by,

$$\gamma_{sat} = 3.39 \ln(V_{s1}) + 1.12 \quad (4.50)$$

For dry soils above the water table and no capillary effects, a similar relationship was developed by Mayne (2007) from RC tests on four batches of reconstituted quartz sand performed by Richart et al. (1970). The correlation takes the form of a linear equation given by,

$$\gamma_d = 2 + 0.06V_{s1} \quad (4.51)$$

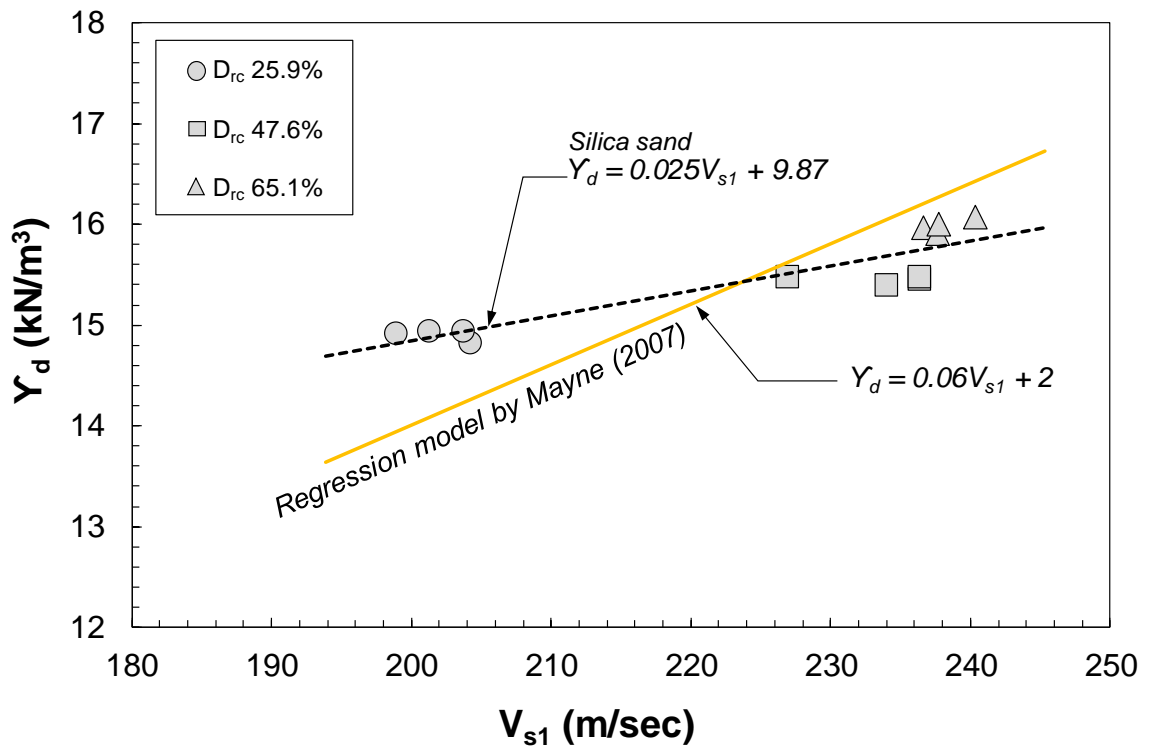


Figure 4.37: Comparison of $\gamma_d - V_{s1}$ correlation with Mayne (2007)

In Figure 4.37, the regression model proposed by Mayne (2007) for dry unit weight and normalized shear wave velocity underpredicts the dry unit weight for loose silica sand. However, the comparison is better for medium dense and dense silica sand with a slight over prediction of dry unit weight. Depending on material behaviour, type of tests conducted, particle size and shape distribution, each type of sand will tend to develop its own locus of datapoints. Therefore, considering all such datapoints, a mean correlation was developed by Mayne (2007) in the form of Equation 4.51. But specifically, for silica sand, the linear correlation takes the form as shown below in Equation 4.52:

$$\gamma_d = 0.025 \cdot V_{s1} + 9.87 \quad (4.52)$$

Overall, the advantage of such correlations lies in the fact that one can predict dry and total unit weight of in-situ indirectly from geophysical test results which can further be used for characterizing the subsurface during a pre-design geotechnical investigation.

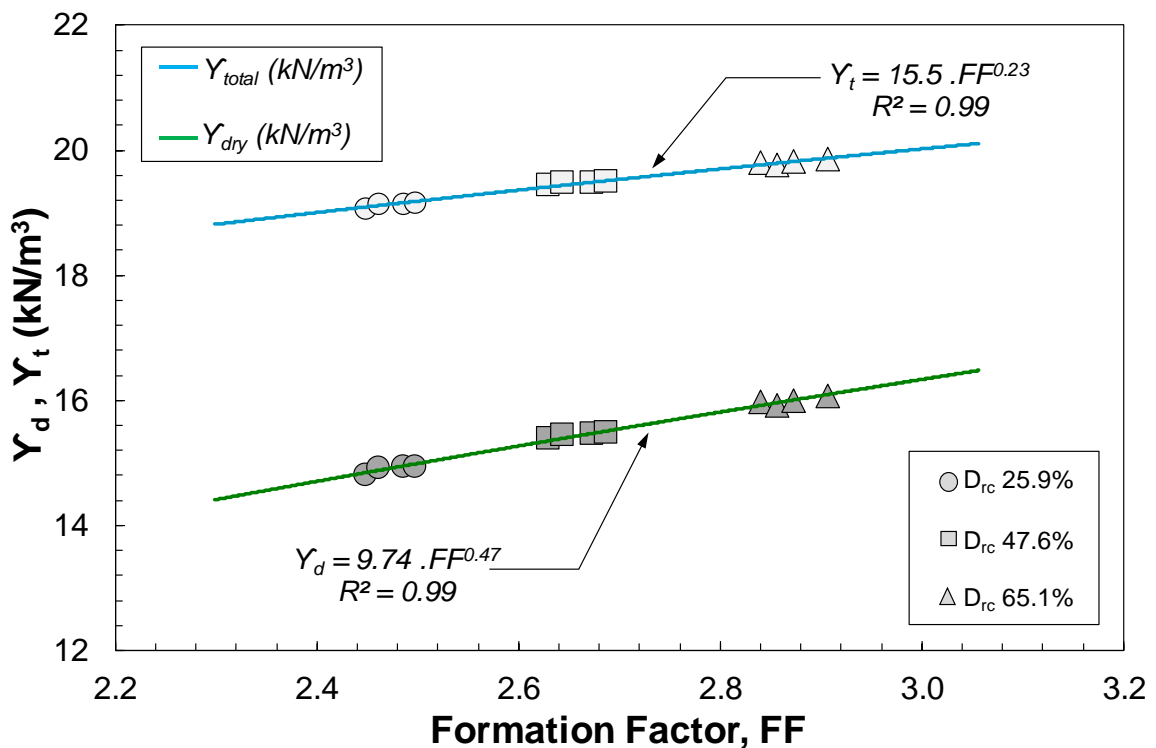


Figure 4.38: Y_d and Y_{total} – FF correlation for silica sand

Since formation factor generally is a good representative of in-situ state, utilizing it to estimate unit weight of soil creates an opportunity to propose a new correlation model between two very significant soil properties, to help characterize the silica sand. Figure 4.38 presents the correlation between dry and total unit weight of sand and formation factor derived from electrical resistivity tests. Unit weight and formation factor both are seen to increase as relative density increases.

Much like the $FF - n$ correlation, a power function with a very high coefficient of determination, $R^2 = 0.99$, is seen to correlate the two parameters. The proposed correlations are given in Equations 4.53 and 4.54.

$$\gamma_{total} = 15.5 \cdot FF^{0.23} \quad (4.53)$$

$$\gamma_{dry} = 9.74 \cdot FF^{0.47} \quad (4.54)$$

In cases of absence of any site-specific data or, inconvenience regarding in-situ tests, the proposed correlations can be used on silica sand material to indirectly estimate unit weight of soil.

4.9 Evaluation of In-Situ State

Been and Jefferies (1985) postulated that the behaviour of any sand may be characterized by a state parameter which combines the influence of void ratio and stress. The physical conditions for any state parameter must have a unique structure which is not influenced under the original test conditions. Therefore, Been and Jefferies (1985) defined state parameter as a description of physical conditions which combine the influence the void ratio and consolidation stress. The state parameter at critical state can be calculated from the following equation,

$$\psi_{cs} = e_c - e_{cs} \quad (4.55)$$

where e_c = consolidation void ratio and e_{cs} = void ratio at critical state and ψ_{cs} is the state parameter at critical state. The CSL or critical state line presents a boundary between strain-

softening (contractive) or strain hardening (dilative) behaviour of a soil where ψ is the difference between the current void ratio and the void ratio under critical state. Denser soils have a negative value of ψ while looser soils have a positive value of ψ . A series of monotonic drained and undrained simple shear tests on silica sand collected from Boler Mountain in London, Ontario was performed by Mirbaha (2017) and a correlation was developed to calculate critical state void ratio (e_{cs}) in terms of effective vertical consolidation stress which takes the form,

$$e_{cs} = 0.888 - 0.071 \text{Log}(\sigma'_{vc}) \quad (4.56)$$

Equation 4.56 was used to calculate critical state void ratio and therefore critical state parameter was determined for each individual test in this study. Figure 4.39 represents the unique CSL for silica sand developed by Mirbaha (2017).

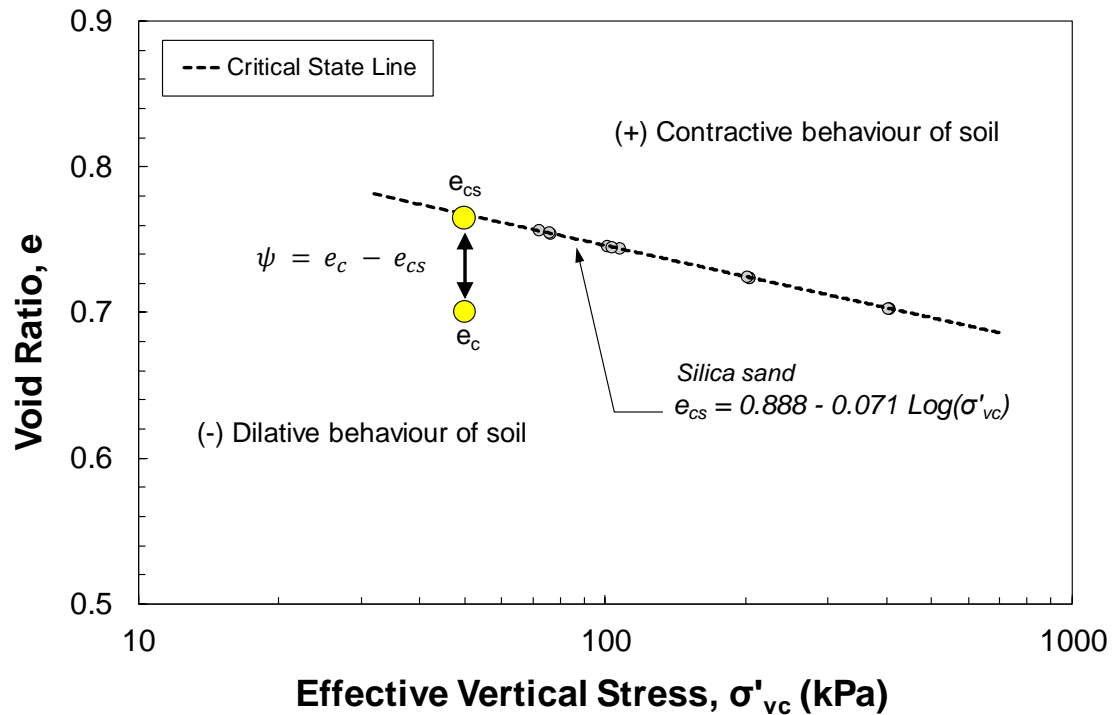


Figure 4.39: CSL for silica sand developed by Mirbaha (2017)

Figure 4.40 presents the correlation between V_{s1} and state parameter. Therefore, the distribution of the points after normalization remains primarily due to the change in relative density levels shown in different shapes. Negative values of state parameter refer to medium dense or dense specimens while positive values refer to the looser specimens. Shear wave velocity measured from in-situ tests on silica sand can indirectly estimate the state parameter from the developed correlation given in Equation 4.57. An exponential correlation was found to be the best representation of the data series.

$$V_{s1} = 214.55 \cdot \exp(-1.236 \psi) \quad (4.57)$$

A similar correlation between FF and state parameter could not be developed because of the fact that FF is seen to be mostly influenced by relative density and not stress level. However, state parameter involves the influence the void ratio and consolidation stress (Been and Jefferies 1985).

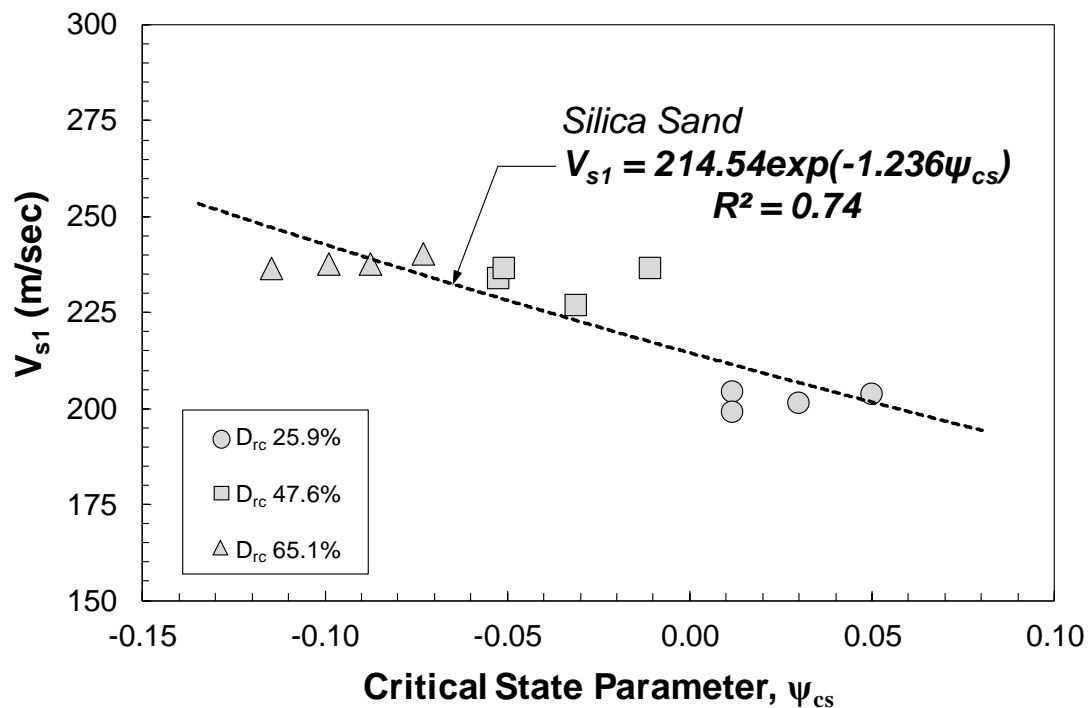


Figure 4.40: Normalized shear wave velocity vs. state parameter for silica sand

Been and Jefferies (1985) introduced the concept of state parameter to describe large strain behaviour of sand based on combined influences of void ratio and effective stress. Robertson et al. (1995) and Cunning et al. (1995) have shown that shear wave velocity can be used for determining in-situ state for a particular sand as it is influenced both by effective stress and relative density. The advantage of working with shear wave velocity is the ease at which it can be measured both in laboratory tests and field tests. Generally, no significant corrections are made on shear wave velocity measurements owing to boundary conditions or scale effect from field to laboratory tests, moreover, it can be easily normalized with stress normalization exponents that can be determined from data points at a particular relative density. Soil compressibility, which has a significant effect on CPT or SPT results, has little or no influence on shear wave velocity measurements. But fabric, cementation and aging play an important role in shear wave velocity measurements. However, when young, uncemented sands are being used to predict in-situ state, influences like cementation or age have very little to do. Robertson et al. (1995) reported very little effect of fabric on shear wave velocity for Ottawa sand.

In this study, the state parameter has been calculated in terms of effective vertical stress. The CSL in terms of void ratio can be defined as,

$$e_{cs} = \Gamma_{cs} - \lambda_{cs} \text{Log}(\sigma'_{vc}) \quad (4.58)$$

where, Γ_{cs} is the soil critical void ratio at σ'_{vc} (vertical effective stress) = 1 kPa and λ_{cs} is the slope of the critical state line in an $e - \log \sigma'_{vc}$ plane.

However, for evaluating the in-situ state of silica sand shear wave velocity and formation factor has been used. The state parameter as defined by Been and Jefferies (1985) is the difference between current void ratio and the void ratio at critical state/steady state, with same effective vertical stress (σ'_{vc}). Therefore, combining Equations 4.55 and 4.58,

$$\psi = e_c - [\Gamma_{cs} - \lambda_{cs} \text{Log}(\sigma'_{vc})] \quad (4.59)$$

Previously a correlation to estimate the current void ratio from formation factor measurements was developed in Figure 4.31. The correlation therefore being,

$$FF = 2.14 \cdot e_c^{-0.83} \quad (4.60)$$

Equation 4.60 can be re-arranged in terms of consolidation void ratio, e_c as,

$$e_c = \left(\frac{2.14}{FF} \right)^{0.83} \quad (4.61)$$

Shear wave velocity is usually normalized by using a stress normalization exponent developed from a particular relative density level and a reference atmospheric pressure of 100 kPa (Robertson et al. 1992; Hussein and Karray 2015). The stress normalization exponent β has been investigated earlier in this chapter for the individual relative densities and the average value of β was found to be 0.27.

$$V_{s1} = V_s \left(\frac{P_a}{\sigma'_{vc}} \right)^\beta \quad (4.62)$$

Equation 4.62 can be re-arranged in terms of effective vertical stress, σ'_{vc} as,

$$\sigma'_{vc} = P_a \cdot \left(\frac{V_s}{V_{s1}} \right)^{1/\beta} \quad (4.63)$$

In Figure 4.19 and Equation 4.13, a correlation between V_{s1} and FF was investigated, i.e.,

$$V_{s1} = 71.32 FF^{1.08} \quad (4.64)$$

Therefore, Equation 4.58 can be expressed in terms of V_s and FF using Equations 4.63 and 4.64, which is shown in Equation 4.65.

$$e_{cs} = \left[\Gamma_{cs} - \lambda_{cs} \text{Log} \left\{ P_a \cdot \left(\frac{V_s}{V_{s1}} \right)^{1/\beta} \right\} \right] \quad (4.65)$$

$$e_{cs} = \left[\Gamma_{cs} - \lambda_{cs} \text{Log} \left\{ P_a \cdot \left(\frac{V_s}{71.32 FF^{1.08}} \right)^{1/\beta} \right\} \right] \quad (4.66)$$

With both current void ratio (e_c) and void ratio at critical state (e_{cs}) being re-ordered in terms of shear wave velocity and formation factor, in-situ state of any silica based sand can be characterized. Using the values of e_c and e_{cs} from Equations 4.61 and 4.66, the final definition of state parameter in terms of V_s and FF is given in Equation 4.67.

$$\psi = \left(\frac{2.14}{FF}\right)^{0.83} - \left[\Gamma_{cs} - \lambda_{cs} \text{Log} \left\{ Pa \cdot \left(\frac{V_s}{71.32 FF^{1.08}} \right)^{1/\beta} \right\} \right] \quad (4.67)$$

Ideally, in order to evaluate in-situ strength and large-strain behaviour of sands, laboratory tests on high quality undisturbed specimens can be conducted. However, collecting such undisturbed specimens of cohesionless soil can be expensive due to ground freezing techniques, etc. But it is possible to estimate the large-strain behavior of a uniform loose sand deposit using shear-wave velocity measurements and also formation factor. Many studies have proposed methods of measuring in-situ shear wave velocity (Robertson et al. 1986; Stokoe and Hoar 1987; Woods 1987; Addo and Robertson 1992). Field resistivity probes can be used to measure in-situ salinity and electrical resistivity.

For a more detailed evaluation of a given sand, it should be possible to develop material specific behaviour among shear wave velocity, formation factor, void ratio and effective consolidations stress. Moreover, some monotonic simple shear tests or triaxial compression tests will be required to measure the influencing parameters like Γ_{cs} and λ_{cs} , which essentially remained unchanged even in the final re-arranged equation.

Therefore, for young, uncemented sandy deposits the above mentioned correlation can be useful as a reasonable tool to predict the in-situ state. For aged or cemented sands, the correlation might not be valid as in-situ shear wave velocity can be very sensitive towards aging and cementation. However, it is the young, uncemented sandy deposits that possess the higher risks of being affected by flow liquefaction. Robertson et al. (1995) explained that aging generally decreases the void ratio of a cohesionless soil and can result in a more dilatant response while cementation can increase the small strain stiffness of a soil. Therefore, this approach can be used for initial geotechnical investigations of in-situ state on such sandy deposits.

4.10 Conclusion

In this chapter, a total of 12 non – destructive tests were completed on silica specimens of 150 mm diameter and 190 mm height. Silica sand collected from Boler Mountain in London, Ontario, was re-graded according to Fraser River Sand to eliminate the maximum possible fines content from the natural state of sand. This enabled us to characterize clean silica sands. Specimens were prepared at loose, medium dense and dense conditions and anisotropically consolidated (K_0) to four effective consolidation stresses, the average values of which are, $\sigma'_{vc} = 74.52$ kPa, 102.08 kPa, 203.39 kPa and 411.83 kPa. Prior to consolidation specimens were saturated with brine solution having a concentration of 3 gm/L. At each effective vertical stress stages, shear wave velocity and electrical resistivity measurements were taken ultimately the minimum desired void was not reached. Shear wave velocity was measured with the help of the installed piezo-electric bender elements in the testing chamber, while electrical resistivity was measured with a four – electrode Hydra-probe used in this study. The influence of the brine concentration was however, diminished by normalizing the measured bulk electrical resistivity by the electrical resistivity of the pore fluid.

In this study a number of investigations were completed, which are hereby summarized. Firstly, a series of tests were completed to determine the calibration of the Hydra-probe and the electrical resistivity of the pore fluid. However, a specialized test was carried out to accurately determine the electrical resistivity of the pore fluid. In this process, it was found that the silica sand used in this study contributed to the electrical conduction of the interstitial water around the soil grains through hydrolysis of iron. X-ray diffraction results by Mirbaha (2017) showed that the sand composed of vermiculite and chlorite group of minerals which contain iron is sufficient quantity.

The shear wave velocity measured in this study was normalized for overburden stress using the individual stress normalization exponents $\beta = 0.31, 0.25$ and 0.26 produced from $V_s - \sigma'_{vc}/\text{Pa}$ plots for each relative density level. The measured bulk electrical resistivity of soil was normalized by the measured electrical resistivity of pore fluid and the ratio of the two parameters, i.e. formation factor was used further in this study for developing correlations.

The influence of relative density and stress level of formation factor was studied, and it was found that the change in effective stress level hardly impacted the magnitude of formation factor. On the other hand, the primary variation of formation factor was responsible because of the change in the state of relative density. The two primary parameters, V_s and FF were correlated, and a significant scatter was observed due to stress level bias. However, upon using V_{s1} , a unique correlation trendline was developed between V_{s1} and FF. This correlation which took form of a power function was later used in development of predictive models to evaluate in-situ state.

The measured parameters from MCPTs in chapter 3 (q_c , f_s) were used in this paper to develop further cross-correlations between the MCPT parameters and NDT parameters. The correlation between $V_{s1} - q_{c1N}$ was compared with several other studies and it was particularly comparable with the study by Fear and Robertson (1995) which is based on Fraser River sand. Since the tested material in this study was re-graded according to Fraser river sand, it proved that grain size distribution played an important role in the correlation of $V_{s1} - q_{c1N}$. The correlation between V_{s1} and f_s , showed that the stress normalization exponent " β " for V_s was exactly half of the stress normalization exponent of f_s , " x ". This finding can be used practically in case of in-situ tests on specific sands to predict and normalize sleeve frictional resistance from shear wave velocity data and vice-versa. New correlations were established in this study between formation factor and cone tip resistance and sleeve friction. All such correlations are proposed to be used in case of any site specific geotechnical investigation.

Due to the presence of iron, the data series in the formation factor – porosity space located slightly lower than the reviewed studies. Nevertheless, a unique correlation based on Archie – Winsauer mathematical model, was proposed to estimate in-situ porosity from formation factor. Similarly, shear wave velocity, small strain- shear modulus (G_{max}) and small-strain constrained modulus (M_{max}) were determined as functions of void ratio. Previous literature was reviewed in this context and reasonable agreement was found.

New empirical correlations were developed to estimate soil relative density and unit weight. Predictive models proposed by Hussein and Karray (2015) and Karray and

Lefebvre (2008) were reviewed for comparison with the present study. The predictive model proposed by Karray and Lefebvre (2008) showed better comparison than the other study. The influence of median grain size (D_{50}) on shear wave velocity, discussed by Hussein and Karray (2015) was not seen in case of this study. Regression models proposed by Mayne (2007) and Burnes and Mayne (1996) were used for comparison with the present study in estimation of soil unit weight. The correlations, owing to a huge database of soil types, did not show good comparison with the data series from this study.

Finally, using the improved correlations developed in this study, in-situ state was evaluated, and the state parameter model was expressed in terms of shear wave velocity and formation factor. For a more detailed evaluation of a given sand, it should be possible to develop material specific behaviour among shear wave velocity, formation factor, void ratio and effective consolidations stress. Moreover, some monotonic simple shear tests or triaxial compression tests will be required to measure the influencing parameters like Γ_{cs} and λ_{cs} , which essentially remained unchanged even in the final re-ordered equation.

Therefore, for young, uncemented sandy deposits all the improved correlations developed in this study for silica sand can be useful as a reasonable tool to characterize in-situ state.

Chapter 5

5 Conclusion

This chapter summarizes all the work that has been done in the previous chapters and also provides concluding remarks on each investigation carried out in this study. Besides, probable future investigations have also been proposed.

5.1 Fulfillment of Research Objectives

Research in Chapter 3 sought about the validation of the MCPT calibration chamber device in Western University as a novel tool to produce useful ground characterization parameters. This was achieved through the completion of a series of MCPTs on Boler sand or, silica sand at several different consolidation stresses and relative densities and comparing the results with various studies related to cone penetration tests. These comparisons included in-situ CPT tests, overburden stress normalization techniques, predictions of relative density, unit weight, constrained modulus and comparison with state parameter from MCPT results, calibration chamber studies or in-situ tests. Through these comparisons, as well as the series of tests, the validation of test results using the MCPT calibration chamber was confirmed for the recorded parameters of q_c and f_s . A comprehensive analysis on the influence of boundary conditions affecting cone penetration results as well as particle crushing effect was studied, and the measured parameters were accordingly corrected to account for such external influences.

The goal in chapter 4 was to investigate the application of geophysical techniques including shear wave velocity and electrical resistivity measurements for characterizing a silica-based sand. This was achieved by conducting experiments on saturated samples of a natural silica sand consolidated under a wide range of stress conditions and relative densities. The measured parameters of q_c and f_s were utilized in this chapter as well to develop improved correlations. Some correlations were compared with existing studies based on field tests or laboratory tests, while some new correlations were also proposed for better characterization of cohesionless soil deposits in case of any pre-design geotechnical investigation. An

analysis of in-situ state was re-modelled in terms of the measured parameters of FF and V_s . Through these comparisons, as well as the series of tests, the establishment of an improved method for characterizing a natural silica sand using geophysical techniques was confirmed. Therefore, for young, uncemented sandy deposits the correlations proposed in this chapter can be useful as a reasonable tool to predict the in-situ state.

5.2 Future Investigations

The current study presented a novel approach to the experimental testing of a soil for ground characterization, specifically in the domains of calibration chamber testing and geophysical testing. From this approach comes the possibility of other experimental testing that can be performed which would extend the research using calibration chamber, electrical methods and bender elements tests. Some of these suggestions for future investigations using these test apparatuses have been included within the study, however, they will be repeated in this section along with additional suggestions. These possible related research investigations are listed as below:

- I. In this study, lateral boundary effects were investigated. However, a testing mechanism can be employed to investigate axial boundary conditions as well.
- II. Using lateral strain gauges and circular rubber rings around a flexible boundary could help monitor the amount of deformation occurs during cone penetration. This would resemble BC5 condition, which provides the closest replica of in-situ stress state.
- III. Improved characterization with electrical resistivity methods could be employed on different types of sands with different percentages of fines content to investigate more into the concepts of shape factor and cementation factor.

Bibliography

- Abedin, M.Z. 1995. The characterization of unsaturated soil behaviour from penetrometer performance and the critical state concept, Newcastle. The University of Newcastle upon Tyne.
- Abedin, M.Z., and Hettiaratchi, D.R.P. 2002. SW—Soil and Water: State Parameter Interpretation of Cone Penetration Tests in Agricultural Soils. *Biosystems Engineering*, **83**(4): 469–479.
- Addo, K.O., and Robertson, P.K. 1992. Shear-wave velocity measurement of soils using Rayleigh waves. *Canadian Geotechnical Journal*, **29**(4): 558–568.
- Ahmadi, M.M. 2000. Analysis of Cone Tip Resistance in Sand. University of British Columbia.
- Al-Akwati, Z. 1975. On Problems of Soil Bearing Capacity at Depth. Duke University, Durham, North Carolina.
- Al-qaysi, Z., and Sadrekarimi, A. 2015a. Determination of the Porosity of Granular Soils Using Electrical Resistivity Measurements. *Canadian Journal of Exploration Geophysics*,: 7–11.
- Al-qaysi, Z., and Sadrekarimi, A. 2015b. Determination of the Porosity of Granular Soils Using Electrical Resistivity Measurements. *CANADIAN JOURNAL OF EXPLORATION GEOPHYSICS*,: 7–11.
- Andrus, R.D., Mohanan, N.P., Piratheepan, P., Ellis, B.S., and Holzer, T.L. 2007. Predicting shear-wave velocity from cone penetration resistance. *Proceedings of the 4th International Conference on Earthquake Geotechnical Engineering*, (1454): 12.
- Andrus, R.D., Piratheepan, P., Ellis, B.S., and Zhang, J. 2004. Comparing liquefaction evaluation methods using penetration-VS relationships. *Soil Dynamics and Earthquake Engineering*, **24**: 713–721. doi:10.1016/j.soildyn.2004.06.001.

- Andrus, R.D., and Stokoe, K.H. 2000. Liquefaction Resistance of Soils from Shear Wave Velocity. *Journal of Geotechnical and Geoenvironmental Engineering, ASCE*, **126**(11): 1015–1025.
- Archie, G.E. 1942. The electrical resistivity log as an aid in determining some reservoir characteristics. *Transactions of the American Institute of Mining and Metallurgical Engineers Petroleum Division*, **146**(1): 54.
- Arulanandan, K., and Kutter, B.L. 1978. A Directional Structure Index Related to Sand Liquefaction. *In Proceedings, ASCE Conference on Earthquake Engineering and Soil Dynamics*. pp. 213–230.
- Arulanandan, K., and Muraleetharan, K. 1988. Level Ground Soil Liquefaction Analysis Using In Situ Properties: I. *Journal of Geotechnical Engineering, ASCE*, **114**(7): 753–770.
- Arulmoli, K. 1980. Sand Structure Characterization for In Situ Testing. University of California.
- Arulmoli, K. 1982. Electrical Characterization of Sands for In Situ Prediction of Liquefaction Potential. University of California.
- Arulmoli, K., Arulanandan, K., and Seed, B. 1985. New Method for Evaluating Liquefaction Potential. *Journal of Geotechnical Engineering*, **11**(1).
- ASTM D4253-16. 2016. Standard test methods for maximum index density and unit weight of soils using a vibratory table. *ASTM International*,: 1–14.
doi:10.1520/D4253-16.
- ASTM D4254-16. 2016. Standard Test Methods for Minimum Index Density and Unit Weight of Soils and Calculation of Relative Density. *ASTM International*,: 9.
doi:10.1520/D4254-00R06E01.1.3.
- ASTM D5778-12. 2012. Standard Test Method for Electronic Friction Cone and Piezocone Penetration Testing of Soils. *ASTM International*, **04**(January).

doi:10.1520/D5778-12.agreed.

ASTM D6913/D6913M-17. 2017. Standard Test Methods for Particle-Size Distribution (Gradation) of Soils Using Sieve Analysis. ASTM International, West Conshohocken, PA, **04**: 1–35. doi:10.1520/D6913-04R09.2.

ASTM D7181-11. 2011. Standard test method for consolidated drained triaxial compression test for soils. ASTM International, 1–11. doi:10.1520/D7181-11.Copyright.

ASTM D854-14. 2014. Standard Test Methods for Specific Gravity of Soil Solids by Water Pycnometer. ASTM International, **2458000**: 1–7. doi:10.1520/D0854-10.2.

Atkins, E. R., J., and Smith. 1961. The significance of particle shape in formation factor-porosity relationships. *Journal of Petroleum Technology*, **13**(3): 285–291.

Balachowski, L. 2007. Size effect in centrifuge cone penetration tests. *Hydro-Engineering and Environmental Mechanics*, **54**(3): 161–181.

Baldi, G., Bellotti, R., Ghionna, V., Jamiokowski, M., and Pasqualini, E. 1981. Cone Penetration Testing in Dry N.C. and O.C. Sands. *In Cone Penetration Testing and Experience*. St. Louis, Missouri.

Baldi, G., Bellotti, R., Ghionna, V., Jamiolkowski, M., and Pasqualini, E. 1986. Interpretation of CPTs and CPTUs: Part II. *In Proc., Fourth Int. Geotech. Seminar on Field Instrumentation and Insitu Measurement*. Singapore. pp. 143–156.

Baldi, G., Bellotti, R., Ghionna, V.N., Engineering, G., Jamiolkowski, M., Engineering, G., Torino, P., Presti, D.C.F.L.O., Ph, D., and Torino, P. 1989. Modulus of sands from CPT ' s and DMT ' s.

Bates, C.R. 1989. Dynamic soil property measurements during triaxial testing. *Geotechnique*, **39**(4): 384–397.

Baxter, C. 2010. Mini-cone Penetration and Standard Penetration Tests. Narragansett.

- Been, K., Crooks, J.H.A., and Rothenburg, L. 1988. A critical appraisal of CPT Calibration chamber tests. *In Penetration Testing 1988*. Balkema, Rotterdam.
- Been, K., and Jefferies, M. 1985. A state parameter for sands. *Geotechnique*, **35**(2): 99–112.
- Been, K., Lingnau, B.E., Crooks, J.H.A., and Leach, B. 1987. Cone Penetration Test Calibration for Erksak (Beaufort Sea) Sand. *Canadian geotechnical journal*, **24**(4): 601–610. doi:10.1139/t87-074.
- Bellotti, R., and Pedroni, S. 1991. Design and development of a small calibration chamber for compressible sands. *In Proceedings of the 1st International Symposium on Calibration Chamber Testing*. Potsdam.
- Bellotti, R. 1985. Chamber size effects and boundary conditions effects. *In Seminar of cone penetration testing in the laboratory*, University of Southampton. pp. 26–29.
- Biella, G., and Tabbacco, I. 1981. The influence of grain size on the relations between resistivity, porosity, and permeability in unconsolidated formations. *Boll. Geofis. Teor. Appl*, **23**: 43–58.
- Bogess, R., and Robertson, P.K. 2010. CPT for soft sediments and deepwater investigations. *In In Proceedings International Symposium on Cone Penetration Testing, CPT'10*. Huntington Beach, California. pp. 1–17.
- Bolton, M.D., and Gui, M.W. 1993. The study of relative density and boundary effects for cone penetration tests in centrifuge.
- Boulanger, R.W., and Idriss, I.M. 2012. Probabilistic SPT-based liquefaction triggering procedure. *Journal of Geotechnical and Geoenvironmental Engineering ASCE*, **138**(10): 1185–1195.
- Bouma, A.H., Sweet, W.E., Chmelik, F.B., and Huebner, G.I. 1971. Shipboard and in-situ electrical resistivity logging of unconsolidated marine sediments. *In Proc. 3rd Annual Offshore Technology Conference*. p. pp 1351.

- Boyce, R.E. 1968. Electrical resistivity of modern marine sediments from the Bering Sea. *Journal of Geophysical Research*, **73**(14): 4759–4766.
- Brignoli, E.G.M., Gotti, M., and Stokoe, K.H. 1996. Measurement of shear wave in laboratory specimens by means of piezoelectric transducers. *Geotechnical Testing Journal*, **19**(4): 384–397.
- Brown, G.A. 1988. The formation porosity exponent — the key to improved estimates of water saturation in shaly sands. *In* Trans. SPWLA, 29th Annu. Logging Symp. San Antonio, Texas. pp. 1–24.
- Bryson, L.S., and Bathe, A. 2009. Determination of Selected Geotechnical Properties of Soil Using Electrical Conductivity Testing. *Geotechnical Testing Journal*, ASTM, **32**(3): 252–261.
- Burmister, D.M. 1948. The importance and practical use of relative density in soil mechanics. *In* Proceedings ASTM. p. 1249.
- Burns, S.E., and Mayne, P.W. 1996. Small- and high-strain measurements of in situ soil properties using the seismic cone penetrometer. *Transportation Research Record*, (1548): 81–88.
- Butlanska, J., Arroyo, M., and Gens, A. 2010. Size effects on a virtual calibration chamber. *In* Numerical Methods in Geotechnical Engineering – Benz & Nordal (eds). Taylor & Francis Group, London.
- Camacho-Tauta, J.F., Cascante, G., Viana Da Fonseca, A., and Santos, J. 2015. Time and frequency domain evaluation of bender elements system. *Geotechnique*, **65**(7): 548–562.
- Carothers, J.E. 1968. A statistical study of the formation factor relation. *Log Anal.*
- Carothers, J.E., and Porter, C.R. 1971. Formation factor - porosity relation derived from well log data. *The Log Analyst*, **12**(1): 16–26.

- Chang, N.Y., and Ko, H.Y. 1982. Effect of grain size distribution on dynamic properties and liquefaction potential of granular soils.
- Chapman, G.A., and Donald, I.B. 1981. Interpretation of static penetration tests in sand. *In* 10th International Conference on Soil Mechanics and Foundation Engineering. pp. 455–458.
- Chillarige, A.R. V., Robertson, P.K., Morgenstern, N.R., and Christian, H.A. 1997. Evaluation of the in situ state of Fraser River sand. *Canadian Geotechnical Journal*, **34**(4): 510–519. doi:10.1139/t97-018.
- Chmelik, F.B., Bouma, A.H., and Rezaei, R. 1969. Comparison of Electrical logs and Physical parameters of Marine sediment cores. *Trans. Gulf-Coast Association of Geological Societies*,.
- Clayton, C.R.I. 2011. Stiffness at small Strain: Research and Practice. *Geotechnique*, **61**(1): 5–37.
- Cubrinovski, M., and Ishihara, K. 1999. Empirical correlation between SPT N-value and relative density for sandy soils. *Soils and Foundations*, **39**(5): 61–71.
- Cui, X. 2011. Development and Calibration of an Electronic Miniature Cone Penetrometer for Design of Small Piles in Silty Clays. *Journal of Testing and Evaluation*, **39**(5): 103432. doi:10.1520/jte103432.
- Cunning, J.C., Robertson, P.K., and Segoo, D.C. 1995. Shear wave velocity to evaluate in situ state of cohesionless soils. *Canadian Geotechnical Journal*, **32**(5): 848–858. doi:10.1139/t95-081.
- Dakhnov, V.N. 1962. Geophysical Well Logging. *In* Q. Colorado Sch. Mines.
- Damavandi-Monfared, S., and Sadrekarimi, A. 2015. Development of a miniature cone penetrometer for calibration chamber testing. *Geotechnical Testing Journal*, **38**(6): 878–892. doi:10.1520/GTJ20150036.

- Dayal, U., and Allen, J.H. 1975. The Effect of Penetration Rate on the Strength of Remolded Clay and Sand Samples. *Canadian Geotechnical Journal*, **12**(3): 336–348.
- Donaldson, E.C., and Siddiqui, T.K. 1989. Relationship between the Archie saturation exponent and wettability. *SPE Formation Evaluation*, **4**: 359–362.
- Dyvik, R., and Madshus, C. 1985. Lab measurement of Gmax using bender elements. *In Proceedings of Advances in the Art of Testing Soils Under Cyclic Conditions*. Detroit.
- Ehrlich, R., Etris, E.L., Brumfield, D., Yuan, L.P., and Crabtree, S.J. 1991. Petrography and reservoir physics III — Physical models for permeability and formation factor. *Bull. Am. Assoc. Pet. Geol.*, **75**: 1579–1592.
- Eid, W.K. 1987. Scaling Effect in Cone Penetration Testing in Sand. Virginia Polytechnic Institute and State University.
- Eiksund, G., and Nordal, S. 1996. Dynamic model pile testing with pore pressure measurements. *In Proceedings of the 5th International Conference on the Application of Stress-Wave Theory to Piles*. Orlando.
- Eliadorani, A.A. 2000. The response of sands under partially drained states with emphasis on liquefaction. University of British Columbia.
- Erchul, R.A. 1972. The use of Electrical Resistivity to Determine Porosity of Marine Sediments. University of Rhode Island.
- Erchul, R.A., and Nacci, V.A. 1971. The use of marine electrical resistivity measurements to predict porosity of marine sediments. *In Proc., Int. Symp on Engineering properties of sea-floor 425 soils and the geophysical identification*. pp. 296–308.
- Erickson, S.N., and Jarrard, R.D. 1998. Porosity/formation-factor relationships for siliciclastic sediments from Amazon Fan. *Geophysical Research Letters*, **25**(13): 2309–2312.

- Eslami, A., and Fellenius, B.H. 1997. Pile capacity by direct CPT and CPTu methods applied to 102 case histories. *Canadian Geotechnical Journal*, **34**(6): 886–904. doi:10.1139/t97-056.
- Esquivel, E.R., and Silva, C. 2000. Miniature piezocone for use in centrifuge. *Journal of Geotechnical and Geoenvironmental Engineering ASCE*,.
- Falagush, O., McDowell, G.R., and Yu, H.-S. 2015. Discrete element modeling of cone penetration tests incorporating particle shape and crushing. *International Journal of Geomechanics*, **15**(6).
- Fardis, M.N., and Veneziano, D. 1981. Estimation of SPT-N and relative density. *Journal of the Geotechnical Engineering Division*, **107**(110): 1345–1359.
- Fear, C.E., and Robertson, P.K. 1995. Estimating the undrained strength of sand: a theoretical framework. *Journal of Geotechnical and Geoenvironmental Engineering ASCE*, **32**(5): 859–870.
- Feda, J. 1984. KO - Coefficient of sand in triaxial apparatus. *Journal of Geotechnical Engineering*, **110**(4): 519–524.
- Fioravante, V., Jamiolkowski, M., Tanizawa, F., and Tatsuoka, F. 1991. Results of CPT's in Toyoura quartz sand. *In Proc., First Int. Symp. on Calibration Chamber Testing (ISOCCT1)*. New York. pp. 135–146.
- Franzen, J.H. 2006. Cone penetration resistance in silt. University of Rhode Island.
- Ghionna, V. 1984. Influence of chamber size and boundary conditions on the measured cone resistance. *In Proc. Sem. Cone Penetration Testing in the Laboratory*, Univ. of Southampton.
- Ghionna, V.N., and Jamiolkowski, M. 1991. A critical appraisal of calibration chamber testing of sands. *Proceedings of the First International Symposium on Calibration Chamber Testing/ISOCCT1*, An-Bin Huang, Ed., Potsdam, New York,: 13–40.

- Givens, W.W. 1987. A conductive rock matrix model (CRMM) for the analysis of low-contrast resistivity formations. *The Log Analyst*, **28**: 138–151.
- Glanville, C.R. 1959. Laboratory Study Indicates Significant Effect of Pressure on Resistivity of Reservoir Rocks. *Journal of Petroleum Technology*,: 20–26.
- Goodarzi, M., Stähler, F.T., Kreiter, S., Rouainia, M., Kluger, M.O., and Mörz, T. 2018. Numerical simulation of cone penetration test in a small-volume calibration chamber: The effect of boundary conditions. *In Proceedings of the 4th International Symposium on Cone Penetration Testing, CPT 2018*. pp. 309–315.
- Goto, S., Suzuki, Y., Nishio, S., and Oh-Oka, H. 1992. Mechanical Properties of Undisturbed Tone-River Gravel obtained by In Situ Freezing Method. *Soils and Foundations*, **32**(3): 15–25.
- Gui, M.W. 1998. Guidelines for cone penetration tests in sand. *In Tokyo, Proceedings of the International Conference Centrifuge*.
- Hardin, B.O., and Black, W.L. 1966. Sand stiffness under various triaxial stresses. *Journal of Soil Mechanics and Foundation Division, ASCE*, **92**(2): 27–42.
- Hardin, B.O., and Drnevich, V.P. 1972. Shear modulus and damping in soils. *Journal of Soil Mechanics and Foundation Division, ASCE*, **98**(7): 667–692.
- Hardin, B.O., and Richart Jr., F.E. 1963. Elastic wave velocities in granular soils. *Journal of Soil Mechanics and Foundation Division, ASCE*, **89**(1): 33–65.
- Hatanaka, M., Suzuki, Y., Kawasaki, T., and Endo, M. 1988. Cyclic Undrained Shear Properties of High Quality Undisturbed Tokyo Gravel. *Soils and Foundations*, **28**(4): 57–68. Available from <http://www.mendeley.com/research/geology-volcanic-history-eruptive-style-yakedake-volcano-group-central-japan/>.
- Hegazy, Y.A., and Mayne, P.W. 1995. Statistical correlations between VS and cone penetration data for different soil types. *In Proceedings of the International Symposium on Cone Penetration Testing: CPT '95*. Linköping.

- Helander, D.P., and Campbell, J.M. 1966. The effect of pore configuration, pressure and temperature on rock resistivity. *In* Trans. SPWLA, 7th Annu. Logging Symp., pp. 1–29.
- Hill, N.M., and Milburn, E.D. 1956. Effect of Clay and Water Salinity on the Electrochemical Behavior of Reservoir Rocks. *Journal of Petroleum Technology*, **207**: 65–72.
- Holden, J.C. 1991. History of the first six CRB Calibration Chambers. *In* Calibration Chamber Testing. *Edited by* A.B. Huang. Elsevier Science Publishing Company.
- Houlsby, G.T., and Hitchman, R. 1988a. Calibration chamber tests of a cone penetrometer. (I).
- Houlsby, G.T., and Hitchman, R. 1988b. Calibration chamber tests of a cone penetrometer in sand. *Geotechnique*, **38**(1): 39–44.
- Hsu, H.-H., and Lu, C.-C. 2008. KO values of normally consolidated sand measured in calibration chamber. *In* Proceedings of the 21st Pacific Congress on Marine Science and Technology. Honolulu.
- Huang, A.B., and Hsu, H.H. 2005. Cone penetration tests under simulated field conditions. *Geotechnique*, **55**(5): 345–354. doi:10.1680/geot.2005.55.5.345.
- Hussein, M.N., and Karray, M. 2015. Shear wave velocity as a geotechnical parameter: An overview. *Canadian Geotechnical Journal*, **53**(2): 252–272. doi:10.1139/cgj-2014-0524.
- Huy, N.Q., Dijkstra, J., van Tol, A.F., and Holscher, P. 2005. Influence of loading rate on the bearing capacity of piles in sand. *In* Proceedings of the 16th International Conference on Soil Mechanics and Geotechnical Engineering. Osaka.
- Idriss, I.M., and Boulanger, R.W. 2006. Semi-empirical procedures for evaluating liquefaction potential during earthquakes. *Soil Dynamics and Earthquake Engineering*, **26**(2-4 SPEC. ISS.): 115–130. doi:10.1016/j.soildyn.2004.11.023.

- Ishibashi, I., and Zhang, X. 1993. Unified dynamic shear moduli and damping ratios of sand and clay. *Soils and Foundations*, **33**(1): 182–191.
- Ishihara, K. 1996. *Soil Behaviour in Earthquake Geotechnics*. Clarendon Press, Oxford.
- Iwasaki, T., and Tatsuoka, F. 1977. Effects of grain size and grading on dynamic shear moduli of sands. *Soils and Foundations*, **17**(3): 19–35.
- Iwasaki, T., Tatsuoka, F., and Takagi, Y. 1978. Shear moduli of sands under cyclic torsional shear loading. *Soils and Foundations*, **18**(1): 39–50.
- Jackson, P.D. 1975. An Electrical Resistivity Method for Evaluating the In-Situ Porosity of Clean Marine Sands. *Marine Geology*, **1**(2): 97–116.
- Jackson, P.D., Taylor-Smith, D., and Stanford, P.N. 1978. Resistivity-porosity-particle shape relationships for marine sands. *Geophysics*, **43**(6): 1250–1268.
- Jamiolkowski, M., Baldi, G., Bellotti, R., Ghionna, V., and Pasqualini, E. 1985. *Penetration Resistance and Liquefaction of Sands*. San Francisco.
- Jamiolkowski, M., Ghionna, V.N., Lancellotta, R., and Pasqualini, E. 1988. New Correlations of Penetration Tests for Design Practice. *In* Proceedings of the 1st International Symposium on Penetration Testing, Orlando, Florida, USA. pp. 263–296.
- Jamiolkowski, M., Lo Presti, D.C.F., and Manassero, M. 2001. Evaluation of Relative Density and Shear Strength of Sands from CPT and DMT. *Soft Ground Construction*, ASCE,.
- Jasinski, J.D. 2008. Mini cone chamber testing of silt. University of Rhode Island.
- Jefferies, M., and Been, K. 1995. Cone factors in sand. *In* Int Symposium of Cone Penetration Testing. Linkoping, Sweden.
- Jefferies, M., and Been, K. 2006. *Soil liquefaction: A critical state approach*. Taylor and Francis, New York.

- Jones, S. 2017. Liquefaction Susceptibility Analysis of Fraser River Sand in Miniature Cone Penetration Tests and Cyclic Direct Simple Shear Tests. University of Western Ontario.
- Jovicic, V., Coop, M.R., and Simic, M. 1996. Objective criteria for determining G_{max} from bender element tests. *Geotechnique*, **46**(2): 357–362.
- Karray, M., and Lefebvre, G. 2008. Significance and evaluation of Poisson's ratio in Rayleigh wave testing. *Canadian Geotechnical Journal*, **45**(5): 624–635.
- Karray, M., Lefebvre, G., Ethier, Y., and Bigras, A. 2011. Influence of particle size on the correlation between shear wave velocity and cone tip resistance. *Canadian Geotechnical Journal*, **48**(4): 599–615.
- Kayen, R., Mitchell, J., Seed, R., Lodge, A., Nishio, S., and Coutinho, R. 1992. Evaluation of SPT-, CPT-, and shear wave-based methods for liquefaction potential assessment using Loma Prieta data. *In U.S. National Center for Earthquake Engineering Research (NCEER). Proceedings from the fourth Japan-U.S. workshop on earthquake resistant design of lifeline facilities and countermeasures for soil liquefaction.* pp. 177–204.
- Kayen, R., Moss, R.E.S., Thompson, E.M., Seed, R.B., Cetin, K.O., Der Kiureghian, A., Tanaka, Y., and Tokimatsu, K. 2013. Shear-Wave velocity-based probabilistic and deterministic assessment of seismic soil liquefaction potential. *Journal of Geotechnical and Geoenvironmental Engineering*, **139**(3): 407–419. doi:10.1061/(ASCE)GT.1943-5606.0000743.
- Keller, G.V. 1982. Electrical properties of rocks and minerals. *In Handbook of Physical Properties of Rocks. Edited by R.S. Carmichael.* CRC Press, Boca Raton. pp. 217–293.
- Keller, G.V., and Frischknecht, F.. 1966. *Electrical methods in geophysical prospecting.* Pergamon Press, New York.
- Kermabon, A.J., Gehin, C., and P., B. 1969. A deep-sea electrical resistivity probe for

- measuring porosity and density of unconsolidated sediments. *Geophysics*, **34**: 534–571.
- Kim, J.H., Yoon, H.K., and Lee, J.S. 2011. Void Ratio Estimation of Soft Soils Using Electrical Resistivity Cone Probe. *Journal of Geotechnical and Geoenvironmental Engineering*, ASCE, **137**(1): 86–93.
- Kokusho, T. 1980. Cyclic triaxial test of dynamic soil properties for wide strain range. *Soils and Foundations*, **20**(2): 45–60.
- Kokusho, T. 2003. Current state of research on flow failure considering void redistribution in liquefied deposits. *Soil Dynamics and Earthquake Engineering*, **23**(7): 585–603. doi:10.1016/S0267-7261(03)00067-8.
- Kokusho, T., Ito, F., Nagao, Y., and Green, R. 2012. Influence of non/low-plastic fines and associated aging effects on liquefaction resistance. *Journal of Geotechnical & Geoenvironmental Engineering*, **138**(6): 747–756.
- Kokusho, T., and Yoshida, Y. 1997. SPT N-value and S-wave velocity for gravelly soils with different grain size distribution. *Soils and Foundations*, **37**(4): 105–113. doi:10.3208/sandf.37.4_105.
- Kulhawy, F.H., and Mayne, P.W. 1990. *Manual on Estimating Soil Properties for Foundation Design*. doi:EPRI-EL-6800.
- Kumar, J., and Raju, K.V.S.B. 2008. Correlation between miniature cone tip resistance and shear strength parameters of clean and silty sand using a conventional triaxial setup. *Geotechnical Testing Journal*, ASTM, **31**(3).
- Kumar, J., and Raju, K.V.S.B. 2009. Miniature cone tip resistance of sand with fly ash using triaxial setup. *Canadian Geotechnical Journal*, **46**(2): 231–240.
- Kutter, B.L. 1978. *Electrical Properties in Relation to Structure of Cohesionless Soils*. University of California.

- Ladd, R.S. 1978. "Preparing Test Specimens Using Undercompaction." *Geotechnical Testing Journal*, **1**(1): 16–23.
- Lambe, T.W., and Whitman, R. V. 1969. *Soil Mechanics*. John Willey and Sons, New York.
- Lee, J., and Santamarina, J.C. 2005. Bender elements: performance and signal interpretation. *Journal of Geotechnical and Geoenvironmental Engineering*, **131**(9): 1063–1070.
- Leong, E.C., Yeo, S.H., and Rahardjo, H. 2005. Measuring shear wave velocity using bender elements. *Geotechnical Testing Journal, ASTM*, **28**(5): 488–498.
- Liao, S.S.C., and Whitman, R. V. 1986. Overburden correction factors for SPT in sand. *Journal of Geotechnical Engineering*, **112**(3): 373–377.
- Lunne, T., Eidsmoen, T., Gillespie, D., and Howland, J.D. 1986. Laboratory and field evaluation on cone penetrometers. *In* Proceedings of the ASCE Specialty Conference In Situ'86: Use of In Situ Tests in Geotechnical Engineering. Blacksburg, ASCE. pp. 714–729.
- Marjanovic, J., and Germaine, J.T. 2013. Experimental study investigating the effects of setup conditions on bender element velocity results. *Geotechnical Testing Journal*, **36**(2): 187–197.
- Mayne, P.W. 2007. Invited overview paper: In-situ test calibrations for evaluating soil parameters. *In* Characterization & Engineering Properties of Natural Soils. pp. 1602–1652.
- Mayne, P.W., and Kulhawy, F.H. 1991. Calibration chamber database and boundary effects correction for CPT data. *In* Proceedings of the 1st International Symposium on Calibration Chamber Testing. Potsdam.
- Mayne, P.W., Peuchen, J., and Bouwmeester, D. 2010. Soil unit weight estimation from CPTs. *In* 2nd International Symposium on Cone Penetration Testing. p. 8.

doi:doi:10.1201/b10132-41 10.1201/b10132-41.

- Mazac, O., Cislerova M., Kelly, W.E., Landa, I., and Venhodova, D. 1990. Determination of Hydraulic Conductivities by Surface Geoelectrical Methods. *In* Geotechnical and environmental geophysics. *Edited by* S. Ward.
- Menq, F.Y., and Stokoe, K.H. 2003. Linear dynamic properties of sandy and gravelly soils from large-scale resonant tests. *In* In The 3rd International Symposium on Deformation Characteristics of Geomaterial. *Edited by* B.H. Di, T. Doanh, H. Geoffroy, and C. Sauzeat. Publishers, Rotterdam A.A. Balkema, Lyon, France. pp. 61–71.
- Mirbaha, K. 2017. Bi-directional Cyclic Behaviour and Liquefaction Analysis of a silica-carbonate sand. University of Western Ontario.
- Mitchell, B.J. 1981. Regional variation and frequency dependence of Q_s in the crust of the United States. *Bull. Seismol. Soc. Am.*, **71**: 1531–1538.
- Moss, R.E.S., Seed, R.B., and Olsen, R.S. 2006. Normalizing the CPT for overburden stress. *Journal of Geotechnical and Geoenvironmental Engineering*, **132**(3): 378–387. doi:10.1061/(ASCE)1090-0241(2006)132:3(378).
- Olsen, R.S. 1997. Cyclic liquefaction based on the cone penetrometer test. NCEER Workshop on Evaluation of Liquefaction Resistance of Soils, (February): 225–276.
- Olsen, R.S., and Mitchell, J. 1995. CPT Stress normalization and prediction of soil classification. *International Symposium on Cone Penetration Testing, CPT*, (January 1995): 257–262.
- Oztoporak, S., and Bolton, M.D. 2013. Stiffness of sands through a laboratory test database. *Geotechnique*, **63**(1): 54–70.
- Panuska, J., and Frankovska, J. 2018. Regression Analysis of Small Strain Shear and Constrained Modulus Measurements on Sands with Fines: Effect of Different Void Ratio Functions Used. *Slovak Journal of Civil Engineering*, **26**(4): 11–19.

- Park, J.Y. 1999. A Critical Assessment of Moist Tamping and Its Effect on the Initial and Evolving Structure of Dilatant Triaxial Specimens.
- Parkhomenko, E.I. 1967. Electrical Properties of Rocks. Plenum, New York.
- Parkin, A., Holden, J.C., Aamot, K., Last, N., and Lunne, T. 1980. Laboratory investigation of CPTs in sand.
- Parkin, A., and Lunne, T. 1982. Boundary effects in the laboratory calibration of a cone penetrometer in sand. *In* Proceedings of the 2nd European Symposium on Penetration Testing. Amsterdam, Netherlands.
- Payan, M., Senetakis, K., Khoshghalb, A., and Khalili, N. 2017. Effect of gradation and particle shape on small-strain young's modulus and poisson's ratio of sands. *International Journal of Geomechanics*, **17**(5): 1–14. doi:10.1061/(ASCE)GM.1943-5622.0000811.
- Porcino, D., and Marciano, V. 2010. Evaluating liquefaction resistance of a calcereous sand using the cone penetration test. *In* Proceedings of the 5th International Conference on Recent Advances in Geotechnical Earthquake Engineering and Soil Dynamics. San Diego.
- Pournaghiazar, M. 2011. The Cone Penetration Test in Unsaturated Sands. University of New South Wales, Sydney.
- Pournaghiazar, M., Russell, A.R., and Khalili, N. 2013. The cone penetration test in unsaturated sands. *Geotechnique*, **63**(14): 1209–1220.
- Lo Presti, D.C.F. 1987. Mechanical behavior of Ticino sand from resonant column tests. Politecnico di Torino, Turin, Italy.
- Lo Presti, D.C.F., Jamiolkowski, M., Pallara, O., and Cavallaro, A. 1997a. Shear modulus and damping of soils. *Geotechnique*, **47**(3): 603–617.
- Lo Presti, D.C.F., Pallara, O., and Cavallaro, A. 1997b. Damping Ratio of Soils from

Laboratory and in Situ Tests. *In Proceedings of the 14th International Conference on Soil Mechanics and Foundations Engineering.*

- Lo Presti, D.C.F., Pedroni, S., and Crippa, V. 1992. Maximum dry density of cohesionless soils by pluviation and by ASTM D 4253-83: a comparative study. *Geotechnical Testing Journal, ASTM*, **15**(2): 180–189.
- Pulido, N., Ojeda, A., Atakan, K., and Kubo, T. 2004. Strong ground motion estimation in the Sea of Marmara region (Turkey) based on a scenario earthquake. *Tectonophysics*, **4**: 357–391.
- Puppala, A.J., Acar, Y.B., and Tumay, M.T. 1991. Miniature CPT Tests in dense Monterey No. 0/30 in flexible double walled calibration chamber. *In Elsevier Science Publishing, Inc.*
- Ransom, R.C. 1984. A contribution toward a better understanding of the modified Archie formation resistivity factor relationship. *The Log Analyst*, **25**: 7–12.
- Richart, F.E., Hall, J.R., and Wood, R.D. 1970. *Vibrations of Soils and Foundations.* Prentice-Hall, Englewood Cliffs, N.J.
- Rix, G.J., and Stokoe, K.H. 1991. Correlation of initial tangent modulus and cone penetration resistance. *In Proc, 1 st International Symposium on Calibration Chamber Testing/ ISOCCT1.* Postdam, New York. pp. 351–362.
- Robertson, P.K. 1990. Soil classification using the cone penetration test. *Canadian Geotechnical Journal*, **27**(1): 151–158.
- Robertson, P.K. 1992. Seismic techniques to evaluate liquefaction potential. *In Proceedings of the 45th Canadian Geotechnical Conference.* Toronto.
- Robertson, P.K. 2009. Interpretation of cone penetration tests - A unified approach. *Canadian Geotechnical Journal*, **46**(11): 1337–1355. doi:10.1139/T09-065.
- Robertson, P.K., and Campanella, R.G. 1983. Interpretation of cone penetration tests.

- Part I: Sands. *Canadian Geotechnical Journal*, **20**(4): 734–745. doi:10.1139/t83-079.
- Robertson, P.K., Campanella, R.G., Gillespie, D., and Rice, A. 1986. Seismic CPT to measure in situ shear wave velocity. *Journal of Geotechnical Engineering*, **112**(2): 791–803.
- Robertson, P.K., Sasitharan, S., Cunning, J.C., and Segoo, D.C. 1995. Shear-wave velocity to evaluate in-situ state of Ottawa sand. *Journal of Geotechnical Engineering*, **121**(3): 262–273. doi:10.1061/(ASCE)0733-9410(1995)121:3(262).
- Robertson, P.K., Woeller, D.J., and Finn, W.D.L. 1992. Seismic cone penetration test for evaluating liquefaction potential under cyclic loading. *Canadian Geotechnical Journal*, **29**(4): 686–695.
- Robertson, P.K., and Wride, C.E. 1998. Evaluating cyclic liquefaction potential using the cone penetration test. *Canadian Geotechnical Journal*, **35**: 442–459. doi:10.1139/t99-102.
- Rollins, K.M., Evans, M.D., Diehl, N.B., and Daily, W.D. 1998. Shear modulus and damping relationships for gravels. *Journal of Geotechnical and Geoenvironmental Engineering*, **124**(5): 396–405.
- Rowlandson, T.L., Berg, A.A., Bullock, P.R., Ojo, E.R.T., McNairn, H., Wiseman, G., and Cosh, M.H. 2013. Evaluation of several calibration procedures for a portable soil moisture sensor. *Journal of Hydrology*, **498**: 335–344. Elsevier B.V. doi:10.1016/j.jhydrol.2013.05.021.
- Ruhovets, N. 1990. A log analysis technique for evaluating laminated reservoirs in the Gulf Coast area. *The Log Analyst*, **31**: 294–303.
- Sadrekarami, A. 2014. Effect of the mode of shear on static liquefaction analysis. *Journal of Geotechnical and Geoenvironmental Engineering*, **140**(12). doi:10.1061/(ASCE)GT.1943-5606.0001182.
- Sadrekarami, A. 2017. Evaluation of stress normalization methods for cone-penetration

- testing in quartz sands. *Journal of Geotechnical and Geoenvironmental Engineering*, **143**(6): 1–5. doi:10.1061/(ASCE)GT.1943-5606.0001675.
- Salem, H.S. 1992. A theoretical and practical study of petrophysical, electric, and elastic parameters of sediments. Kiel University, Germany.
- Salem, H.S. 2001. Determination of Porosity, Formation Resistivity Factor, Archie Cementation Factor, and Pore Geometry Factor for a Glacial Aquifer. *Energy Resources*, **23**(6): 589–596.
- Salem, H.S., and Chilingarian, G. V. 1999. The cementation factor of Archie's equation for shaly sandstone reservoirs. *Journal of Petroleum Science and Engineering*, **23**: 83–93.
- Salgado, R., Mitchell, J.K., and Jamiolkowski, M. 1998. Calibration chamber size effects on penetration resistance in sand. *Journal of Geotechnical and Geoenvironmental Engineering*, **124**(9): 878–888.
- Sasitharan, S., Robertson, P.K., Sego, D.C., and Morgenstern, N.R. 1994. State-Boundary Surface for Very Loose Sand and Its Practical Implications. *Canadian Geotechnical Journal*, **31**: 321–334.
- Sawansuriya, A. 2012. Wave Propagation Methods for Determining Stiffness of Geomaterials. INTECH Open Access Publisher,.
- Schmertmann, J.. 1976. DACW 38-76M 6646 - An updated correlation between relative density, Dr and Fugro-type electric cone bearing, qc. Vicksburg, Mississippi.
- Schmertmann, J.. 1978. Guidelines for Cone Penetration Test (Performance and Design). Washington D.C.
- Schnaid, F., and Houlsby, G.T. 1991. An assessment of chamber size effects in the calibration of in situ tests in sand. *Geotechnique*, **41**(3): 437–445.
- Seed, H.B., and Idriss, I.M. 1970. Soil moduli and damping factors for dynamic response

analyses.

- Sen, P.N., Scala, C., and Cohen, M.H. 1981. A self-similar model for sedimentary rocks with application to the dielectric constant of fused glass beads. *Geophysics*, **46**: 781–795.
- Senetakis, K., Anastasiadis, A., and Pitilakis, K. 2012. Small strain shear modulus and damping ratio of quartz and volcanic sands. *Geotechnical Testing Journal*, ASTM, **35**(6): 1–17.
- Senetakis, K., Sandeep, C.S., and Todisco, M.C. 2017. Dynamic inter-particle friction of crushed limestone surfaces. *In Tribology International*. pp. 1–8.
- Sharp, M.K., Dobry, R., and Phillips, R. 2010. CPT-based evaluation of liquefaction and lateral spreading in centrifuge. *Journal of Geotechnical and Geoenvironmental Engineering*, **136**(10): 1334–1346.
- Shibuya, S., and Tanaka, H. 1996. Estimate of elastic shear modulus in Holocene soil deposits. *Soils and Foundations*, **36**(4): 45–55.
- Shirley, D.J., and Hampton, L.D. 1978. Shear wave measurements in laboratory sediments. *Journal of the Acoustical Society of America*, **63**(2): 607–613.
- Skempton, A.W. 1986. Standard penetration test procedures and the effects in sands of overburden pressure, relative density, particle size, ageing and overconsolidation. *Geotechnique*, **36**(3): 425–447.
- Sladen, J.A. 1989. Problems with interpretation of sand state from cone penetration test. *Geotechnique*, **39**(2): 323–332.
- Smith, D.T. 1971. Acoustic and Electric Techniques for Sea-Floor Sediment Identification. *In Proceedings: The International Symposium on the Engineering Properties of Sea-floor soils and Their Geophysical Identification*. Washington D.C.
- Stokoe, K.H., and Carlos Santamarina, J. 2000. Seismic-wave-based testing in

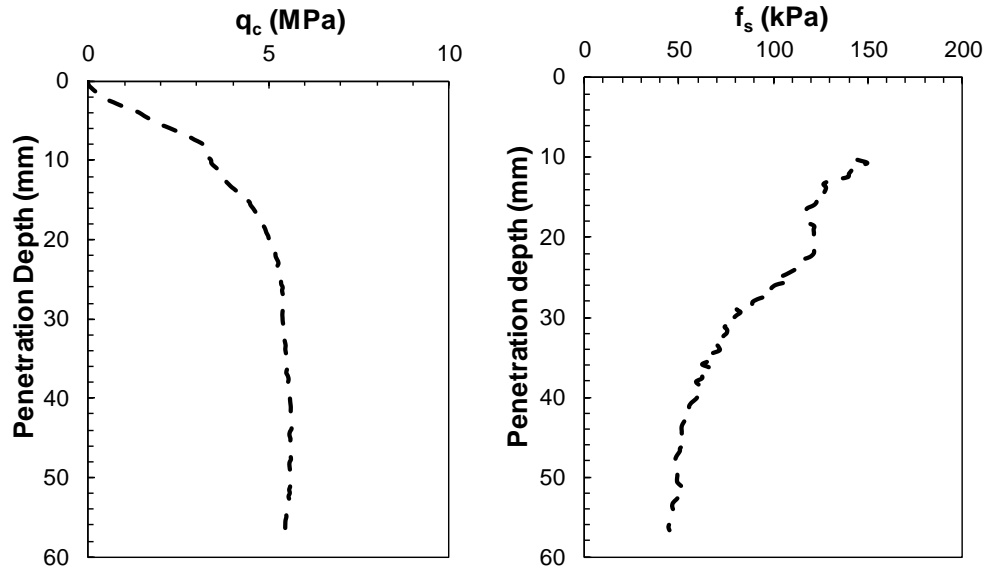
- geotechnical engineering. *In* ISRM International Symposium 2000, IS 2000.
- Stokoe, K.H., and Hoar, R.J. 1987. Variables affecting in situ seismic measurements. *In* Proceedings, Conference on Earthquake Engineering and Soil Dynamic. New York, ASCE Geotechnical Engineering Division. pp. 919–939.
- Sundberg, K. 1932. Effect of impregnating waters on electrical conductivity of soils and rocks. *Trans. American Institute of Mining and Metallurgical Engineers*, **79**: 367–391.
- Sykora, D.W. 1987. Examination of existing shear wave velocity and shear modulus correlations in soils. Department of the Army, Waterways Experiment Station, Corps of Engineers, Miscellaneous Paper GL-87-22.
- El Takch, A., Sadrekarimi, A., and El Naggar, H. 2016. Cyclic resistance and liquefaction behaviour of silts and sandy silts. *Journal of Soil Dynamics and Earthquake Engineering*, **83**: 98–109.
- Tanaka, H., and Tanaka, M. 1998. Characterization of sandy soils using CPT and DMT. *Soils and Foundations*, **38**(3): 55–65.
- Tanizawa, F. 1992. Correlations between cone resistance and mechanical properties of uniform clean sand. Milan.
- Tatsuoka, F., and Shibuya, S. 1992. Deformation characteristics of soils and rocks from field and laboratory tests. *In* Proceedings of the 9th Asian Regional Conference on SMFE. Bangkok. pp. 101–170.
- Thevanayagam, S. 1993. Electrical response of two-phase soil: Theory and Applications. *Journal of Geotechnical Engineering, ASCE*, **119**(8): 1250–1275.
- Thomann, T.G., and Hryciw, R.D. 1990. Laboratory measurement of small strain shear modulus under Ko conditions. *Geotechnical Testing Journal*, **13**(2): 97–105.
- Tiab, D., and Donaldson, E.C. 1996. Theory and Practice of Measuring Reservoir Rock

- and Fluid Transport Properties. *Petrophysics*,: 706.
- Tokimatsu, K., and Yoshimi, Y. 1983. Empirical correlation of soil liquefaction based on SPT N-value and fines content. *Soils and Foundations*, **23**(4): 56–74.
- Towle, G.H. 1962. An analysis of the formation resistivity factor-porosity relationship of some assumed pore geometries. *In* *Trans. SPWLA, 3rd Annu. Logging Symp.* Houston, Texas. pp. 1–13.
- Veismanis, A. 1974. Laboratory investigation of electrical friction-cone penetrometers in sand. *In* *Proceedings of the European Symposium on Penetration Testing, ESOPT I.* Stockholm.
- Viggiani, G., and Atkinson, J.H. 1995. Interpretation of bender element tests. *Geotechnique*, **45**(1): 149–154.
- Villet, W.C.B., and Mitchell, J.K. 1981. *Cone Resistance, Relative Density and Friction Angle.* Berkeley, California.
- Waxman, M.H., and Thomas, E.C. 1974. Electrical conductivities in shaly sands: I. The relation between hydrocarbon saturation and resistivity index. The temperature coefficient of electrical conductivity. *Journal of Petroleum Technology*, **26**: 213–225.
- Wei, B.Z., Pezeshk, S., Chang, T.S., Hall, K.H., and Liu, H.. 1996. An empirical method to estimate shear wave velocity of soils in the New Madrid seismic zone. *Soil Dynamics and Earthquake Engineering*, **15**(6): 399–408.
- Wesley, L.D. 2002. Interpretation of calibration chamber tests involving cone penetrometers in sands. *Geotechnique*, **52**(4): 289–293.
- Wheatcroft, R.A. 2002. In-situ measurements of near-surface porosity in shallow-water marine sands. *IEEE Journal of Oceanic Engineering*, **27**(3): 561–570.
- Wichtmann, T., Navarrete Hernández, M.A., and Triantafyllidis, T. 2015. On the

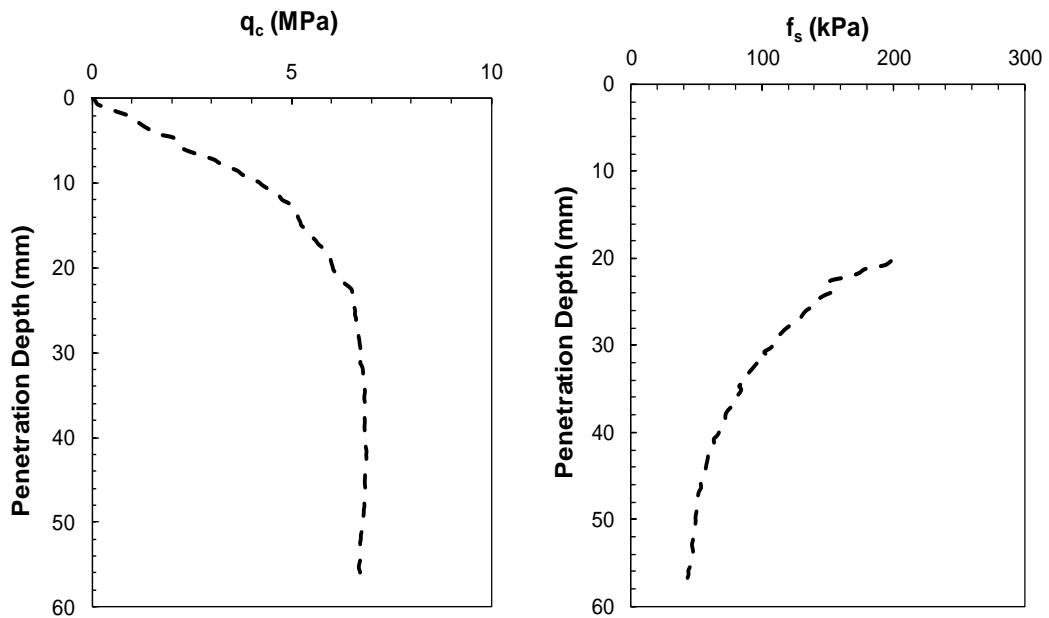
- influence of a non-cohesive fines content on small strain stiffness, modulus degradation and damping of quartz sand. *Soil Dynamics and Earthquake Engineering*, **69**: 103–114.
- Wichtmann, T., and Triantafyllidis, T. 2009. On the influence of the grain size distribution curve of quartz sand on the small strain shear modulus G_{max} . *Journal of Geotechnical and Geoenvironmental Engineering*, **135**(10): 1404–1408.
- Wichtmann, T., and Triantafyllidis, T. 2010. On the influence of the grain size distribution curve on P-wave velocity, constrained elastic modulus M_{max} and Poisson's ratio of quartz sands. *Soil Dynamics and Earthquake Engineering*, **30**(8): 757–766.
- Windle, D., and Worth, C.P. 1975. Electrical resistivity method for determining volume changes that occur during a pressure-meter test. *In ASCE Proc. Spec. Conf. on In-situ Measurements of Soil Properties*. Raleigh, NC. pp. 497–510.
- Winsauer, W.O., Shearin, H.M., Masson, P.H., and Williams, M. 1952. Resistivity of brine saturated sands in relation to pore geometry. *Bulletin of the American American Association of Petroleum Geologists*, **36**: 253–257.
- Wong, P., Koplik, J., and Tomatic, J.P. 1984. Conductivity and permeability of rocks. *Physical Review B*, **30**: 6606–6614.
- Woods, R.D. 1987. In situ tests for foundation vibration. *In Proceedings of the Specialty Conference on the Use of in situ Tests in Geotechnical Engineering*. Blacksburg, VA. pp. 336–375.
- Worthington, P.. 1993. The uses and abuses of the Archie equations, 1: The formation factor-porosity relationship. *Journal of Applied Geophysics*, **30**: 215–228.
- Wroth, C.P. 1984. The interpretation of in situ soil tests. *Geotechnique*, **34**(4): 449–489.
- Wu, W., and Ladjal, S. 2014. Scale effect of cone penetration in sand. *In 3Rd International Symposium on Cone Penetration Testing*. Las Vegas. pp. 459–465.

- Wyllie, M.R.J., and Gregory, A.R. 1953. Formation factors of unconsolidated porous media: Influence of particle shape and effect of cementation. *Trans. AIME*, **198**: 103–110.
- Wyllie, M.R.J., and Rose, W.D. 1950. Some theoretical considerations related to the quantitative evaluation of the physical characteristics of reservoir rocks from electrical log data. *AIME*, **189**: 105–118.
- Yamashita, C., Liu, H., and Chu, X. 2010. Gravity wave variations during the 2009 stratospheric sudden warming as revealed by ECMWF-T799 and observations. *Geophysical Research Letters*, **37**(22).
- Yoshimi, Y. 2000. A Frozen Sample that did not Melt. *In Proceedings of Conference on Development in Geotechnical Engineering*. Bangkok. pp. 293–296.
- Yoshimi, Y., Hatanaka, M., and Oh-Oka, H. 1978. Undisturbed Sampling of Saturated Sands by Freezing. *Soils and Foundations*, **8**(3). Available from https://www.jstage.jst.go.jp/article/bpb1993/17/11/17_11_1460/_pdf/-char/ja.
- Youd, B.T.L., Idriss, I.M., Andrus, R.D., Arango, I., Castro, G., Christian, J.T., Dobry, R., Finn, W.D.L., Jr, L.F.H., Hynes, M.E., Ishihara, K., Koester, J.P., Liao, S.S.C., Iii, W.F.M., Martin, G.R., Mitchell, J.K., Moriwaki, Y., Power, M.S., Robertson, P.K., Seed, R.B., and Ii, K.H.S. 2001. Liquefaction Resistance of Soils : Summary Report From the 1996 Nceer and 1998 Nceer / Nsf Workshops on Evaluation. *Journal of Geotechnical and Geoenvironmental Engineering*, **127**(10): 817–833. doi:10.1061/(ASCE)1090-0241(2001)127:10(817).
- Youn, J.U., Choo, Y.W., and Kim, D.S. 2008. Measurement of small-strain shear modulus G_{max} of dry and saturated sands by bender element, resonant column, and torsional shear tests. *Canadian Geotechnical Journal*, **45**(10): 1426–1438. doi:10.1139/T08-069.
- Yu, P., and Richart, F.E. 1984. Stress ratio effects on shear modulus of dry sands. *Journal of Geotechnical and Geoenvironmental Engineering*, **110**(3): 331–345.

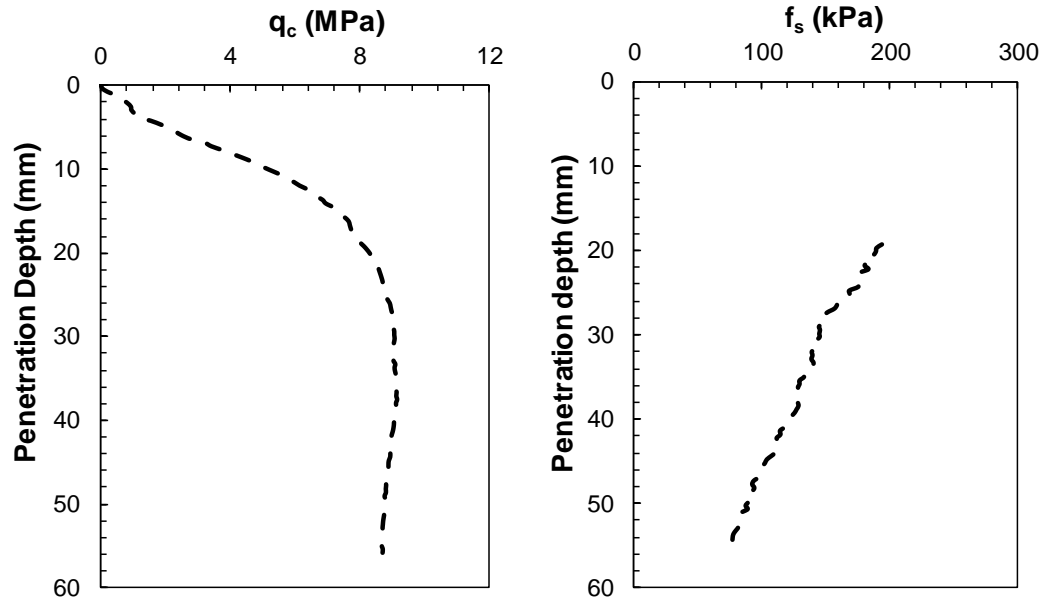
Appendix – A – MCPT Results



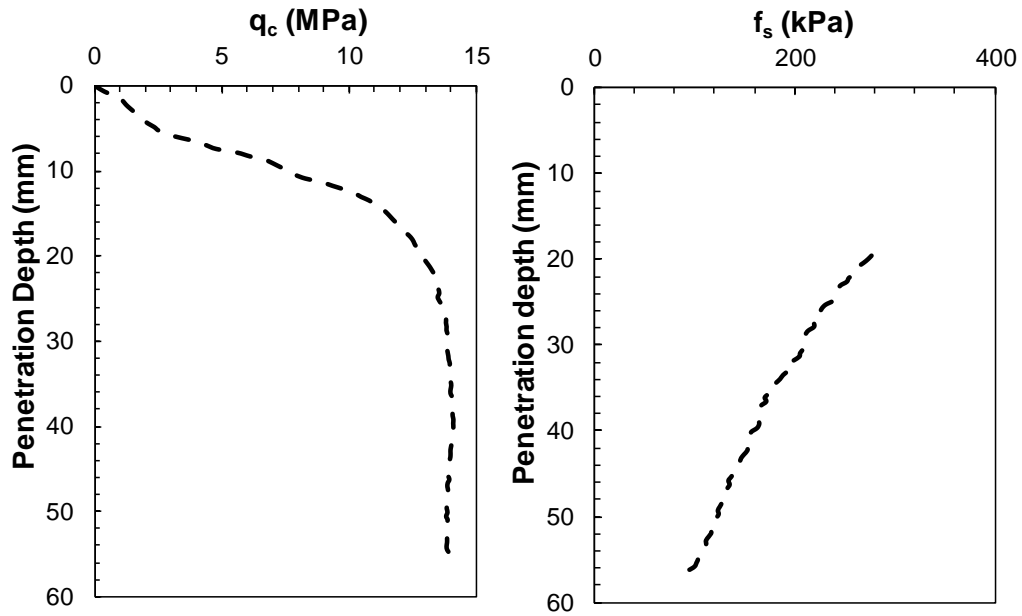
Appendix A-1: MCPT cone tip and sleeve frictional resistance profile at $D_{rc} = 24.06\%$ and $\sigma'_{vc} = 71.99$ kPa



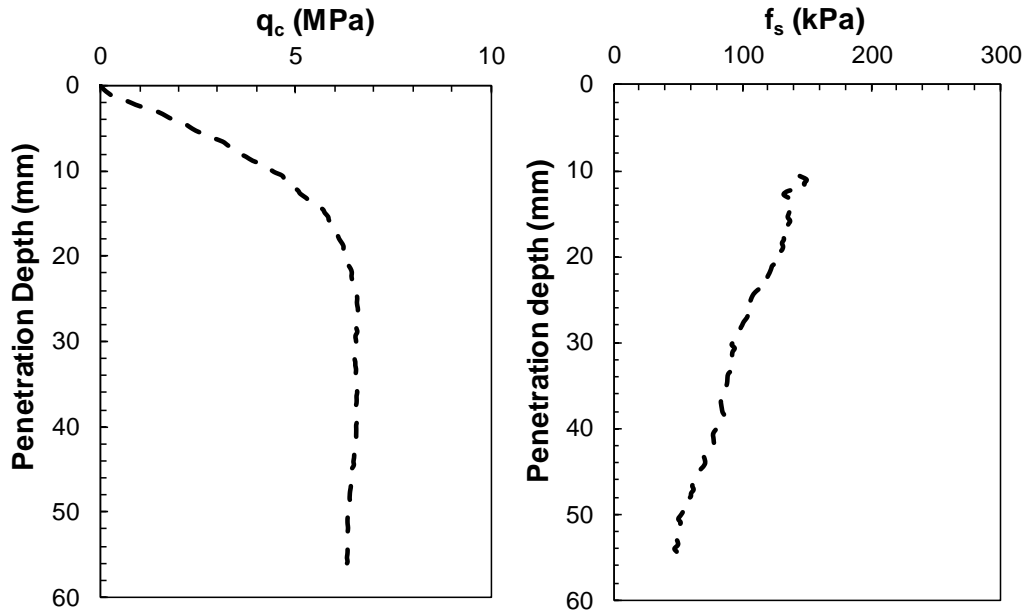
Appendix A-2: MCPT cone tip and sleeve frictional resistance profile at $D_{rc} = 27.19\%$ and $\sigma'_{vc} = 99$ kPa



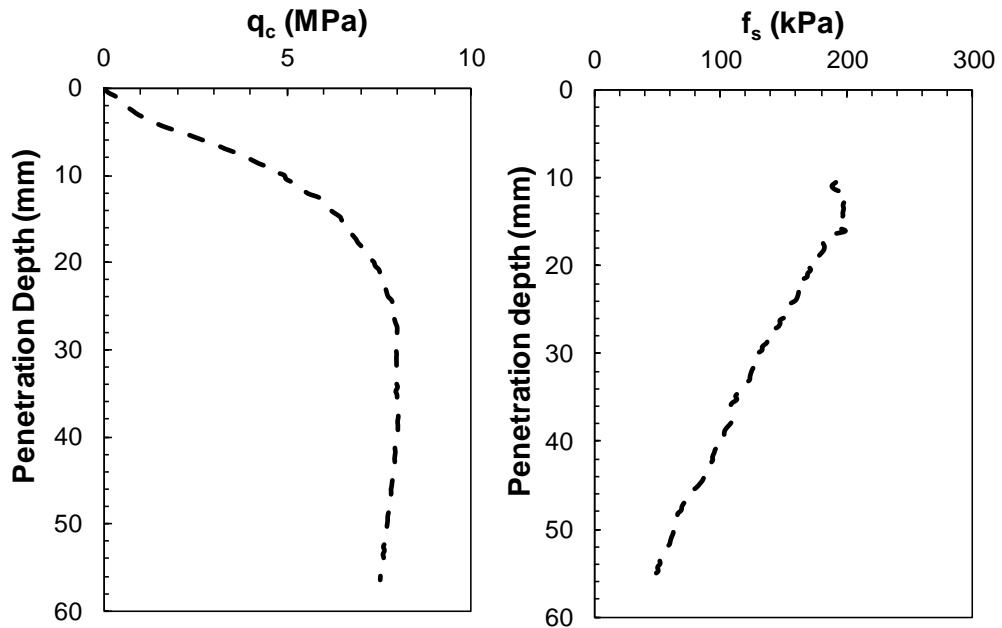
Appendix A-3: MCPT cone tip and sleeve frictional resistance profile at $D_{rc} = 28.44\%$ and $\sigma'_{vc} = 203.55$ kPa



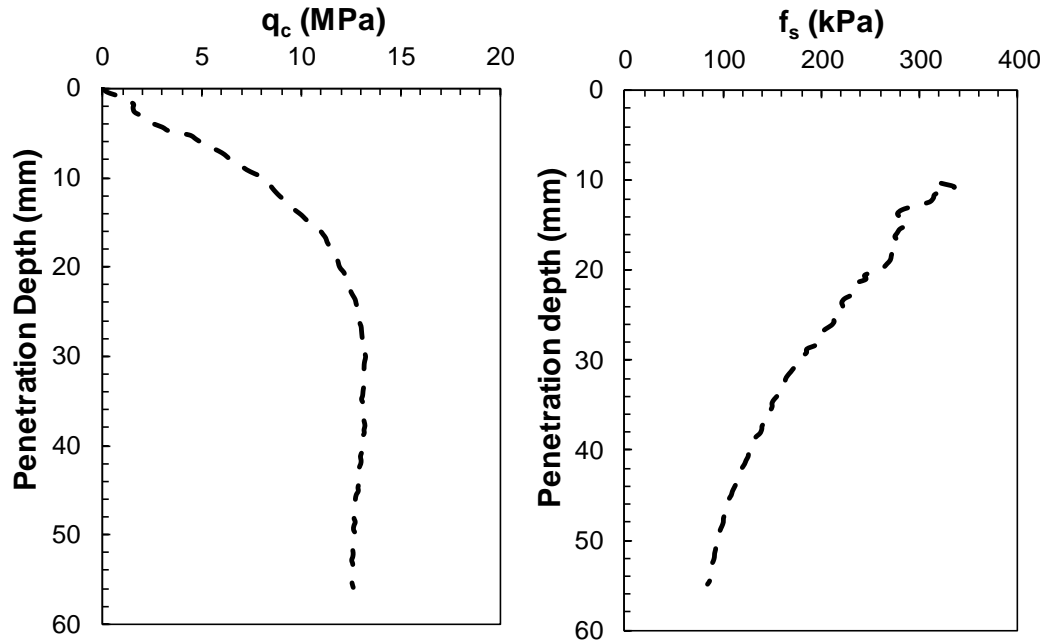
Appendix A-4: MCPT cone tip and sleeve frictional resistance profile at $D_{rc} = 28.75\%$ and $\sigma'_{vc} = 404.64$ kPa



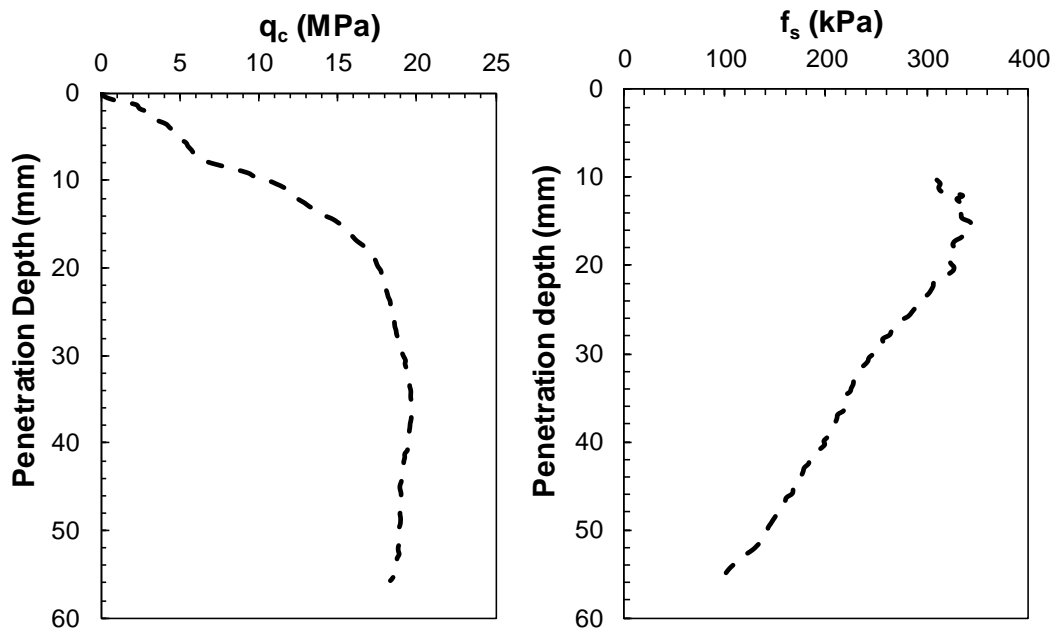
Appendix A-5: MCPT cone tip and sleeve frictional resistance profile at $D_{rc} = 44.69\%$ and $\sigma'_{vc} = 76.07$ kPa



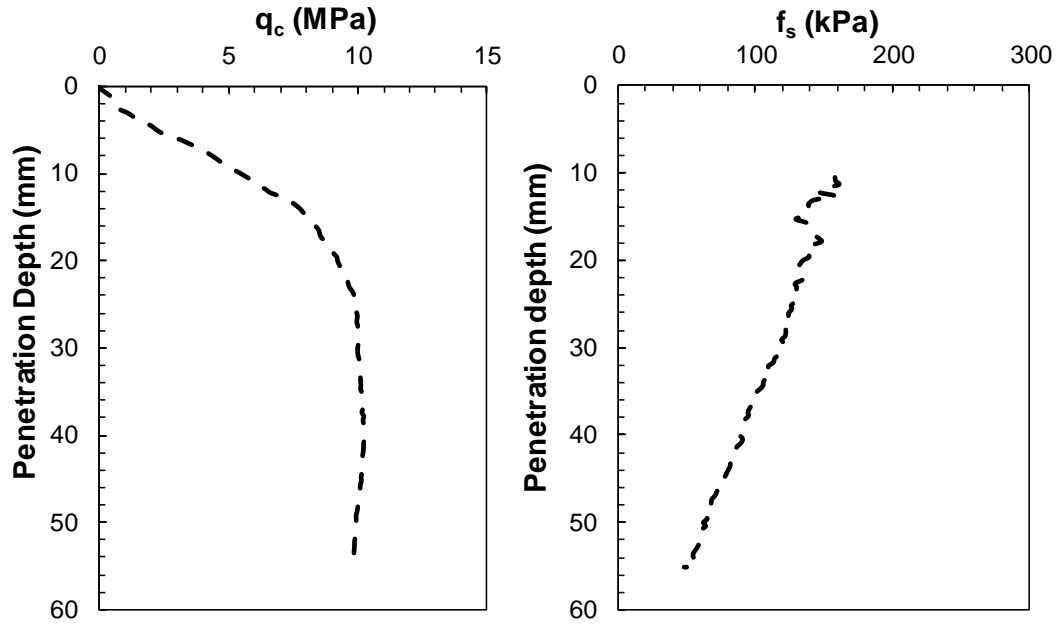
Appendix A-6: MCPT cone tip and sleeve frictional resistance profile at $D_{rc} = 46.88\%$ and $\sigma'_{vc} = 100.81$ kPa



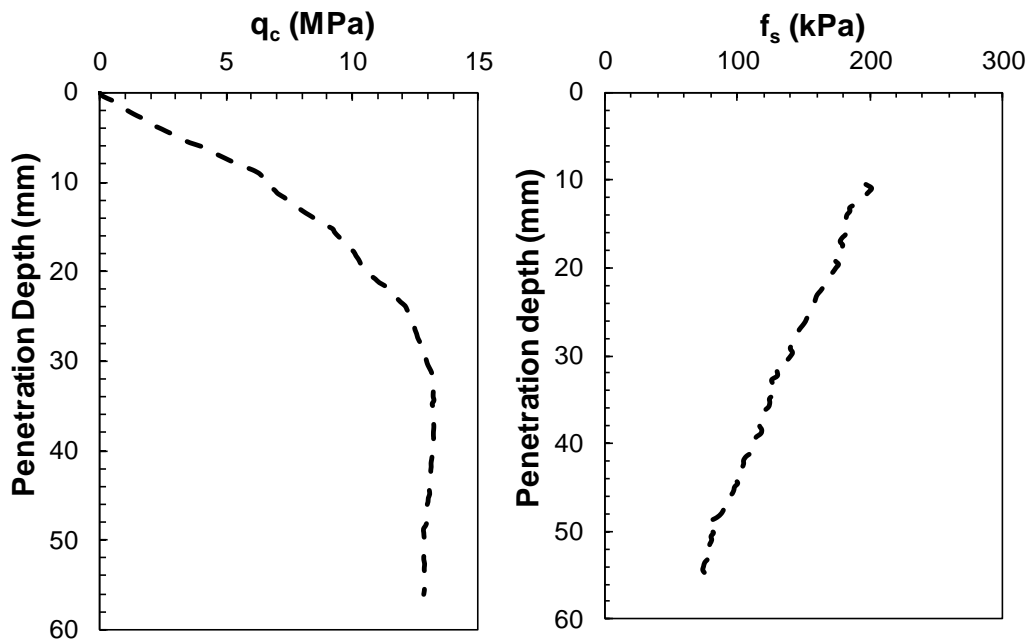
Appendix A-7: MCPT cone tip and sleeve frictional resistance profile at $D_{rc} = 47.50\%$ and $\sigma'_{vc} = 203.51$ kPa



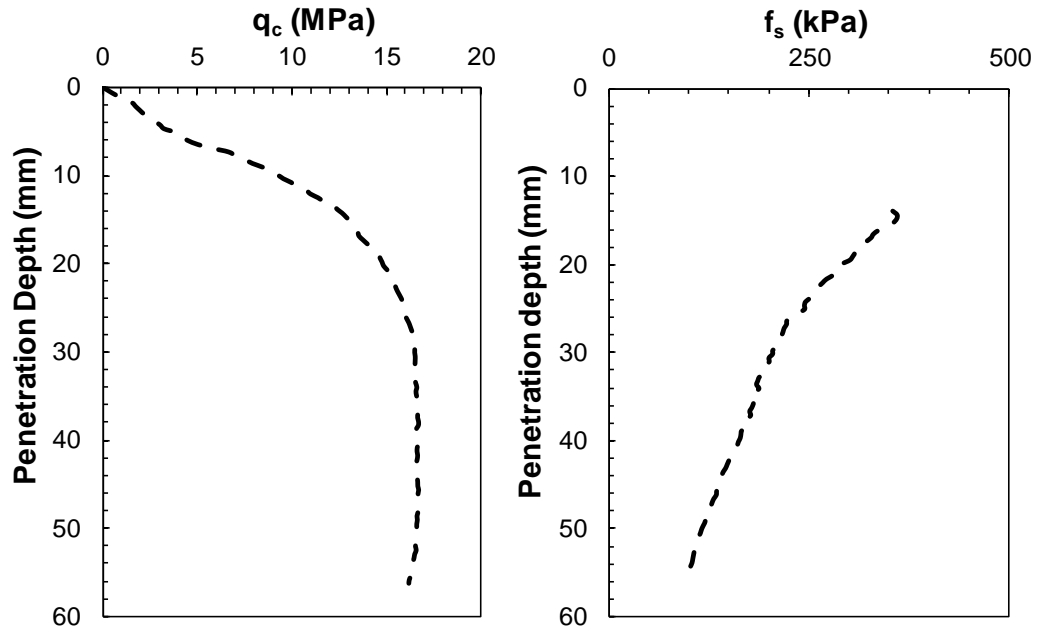
Appendix A-8: MCPT cone tip and sleeve frictional resistance profile at $D_{rc} = 47.81\%$ and $\sigma'_{vc} = 406.11$ kPa



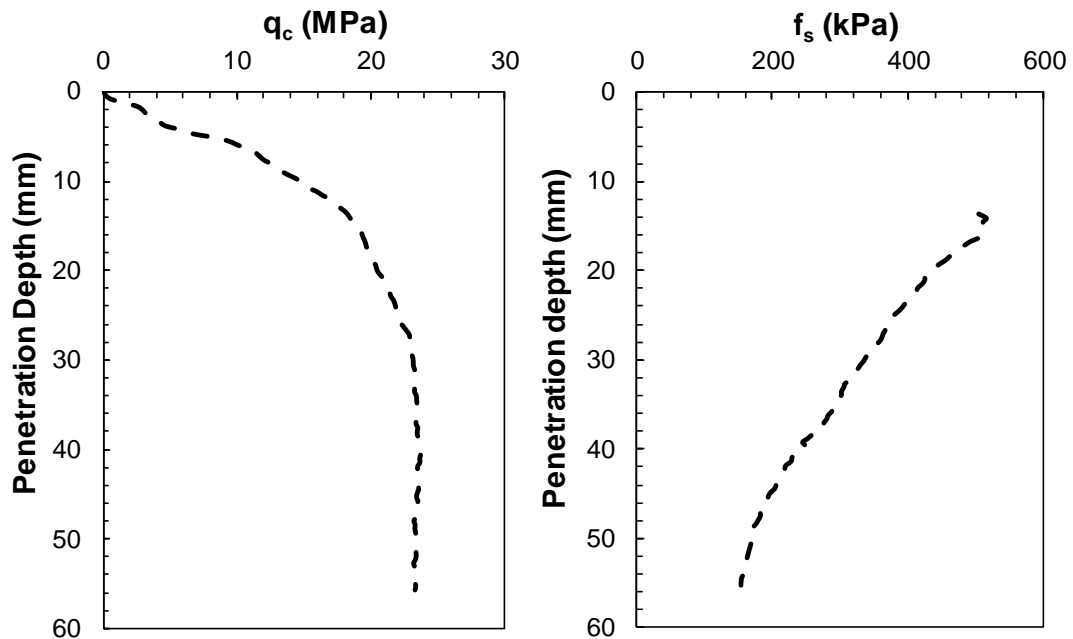
Appendix A-9: MCPT cone tip and sleeve frictional resistance profile at $D_{rc} = 64.06\%$ and $\sigma'_{vc} = 75.74$ kPa



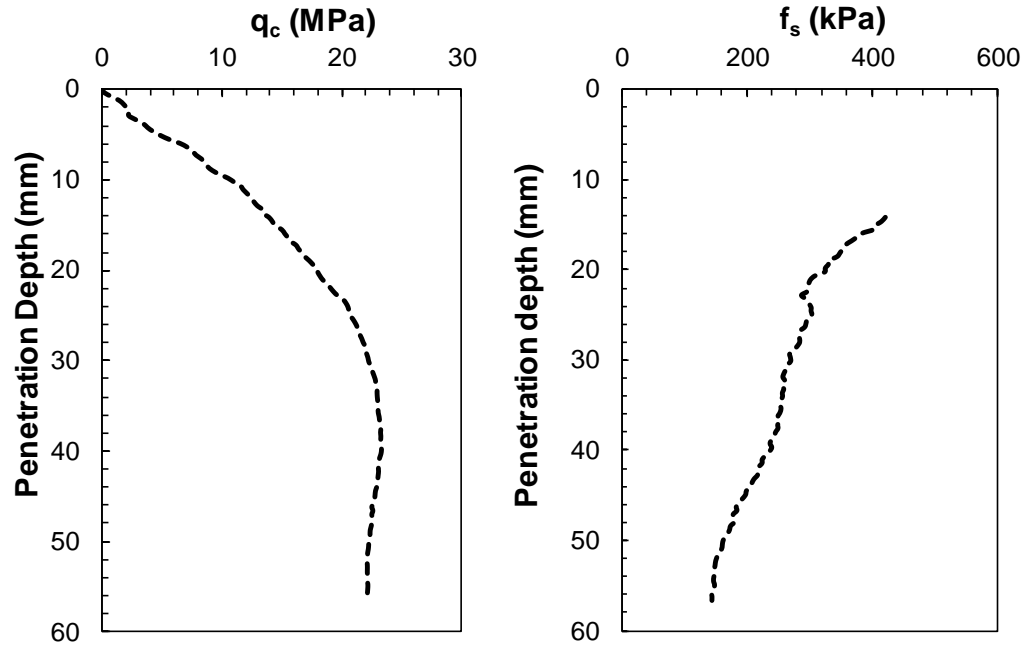
Appendix A-10: MCPT cone tip and sleeve frictional resistance profile at $D_{rc} = 62.19\%$ and $\sigma'_{vc} = 103.19$ kPa



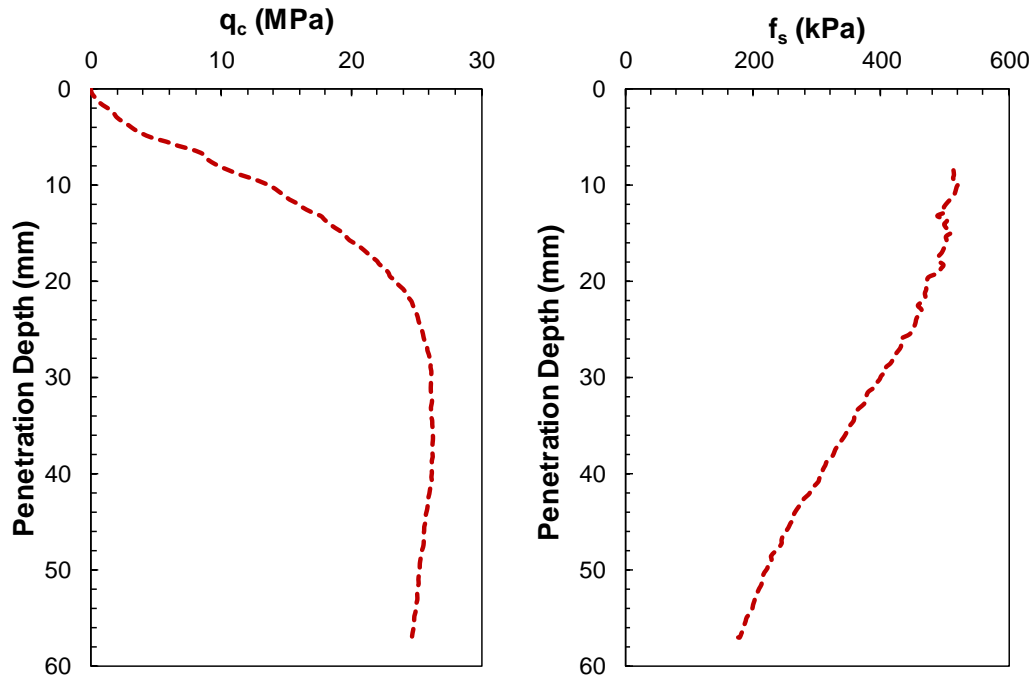
**Appendix A-11: MCPT cone tip and sleeve frictional resistance profile at $D_{rc} = 65\%$
and $\sigma'_{vc} = 201.26$ kPa**



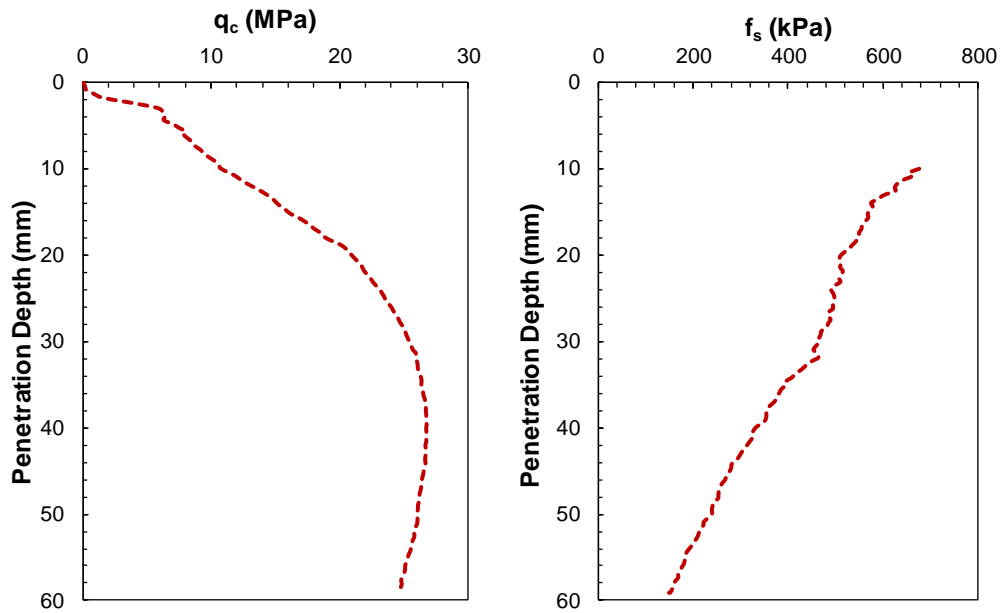
**Appendix A-12: MCPT cone tip and sleeve frictional resistance profile at $D_{rc} =$
 67.19% and $\sigma'_{vc} = 402.51$ kPa**



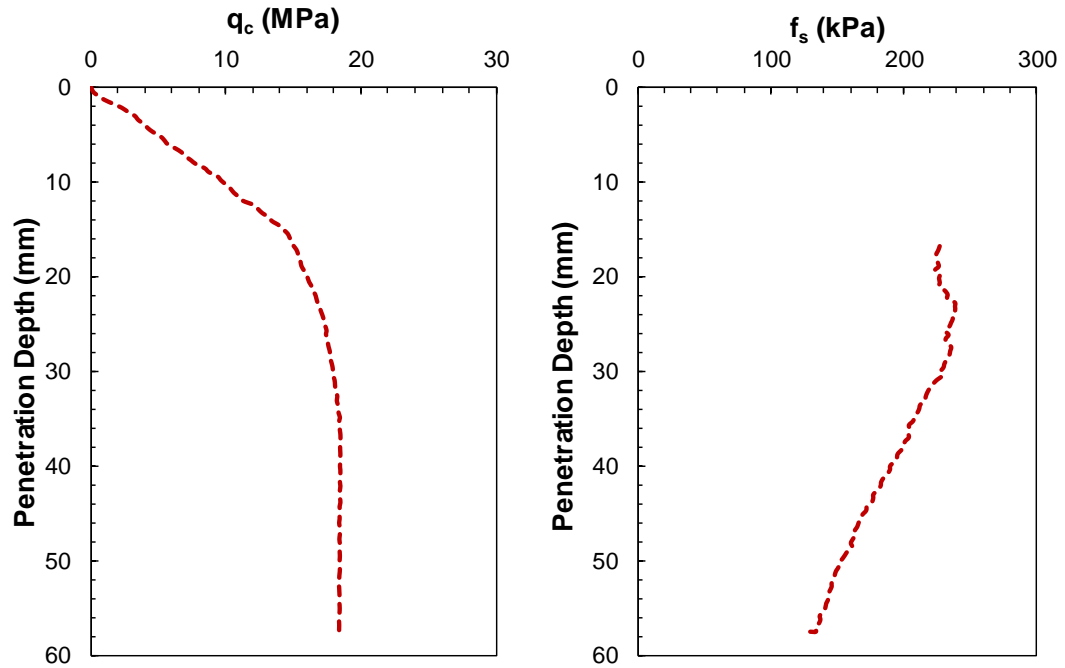
Appendix A-13: MCPT cone tip and sleeve frictional resistance profile at $D_{rc} = 65.63\%$ and $\sigma'_{vc} = 405.07$ kPa



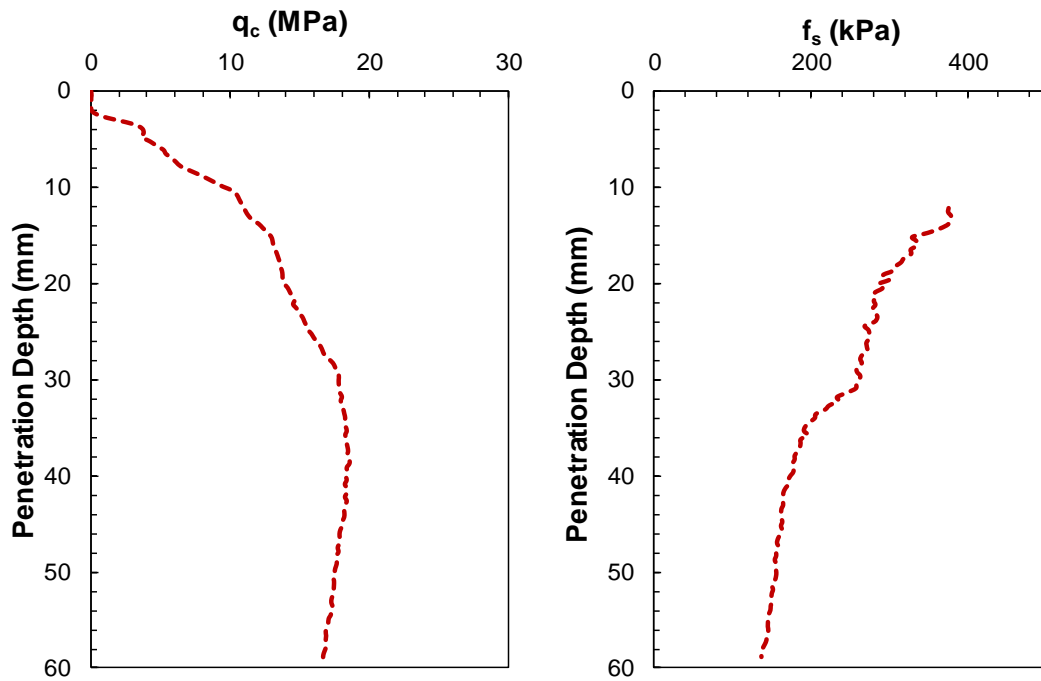
Appendix A-14: BC3-MCPT cone tip and sleeve frictional resistance profile at $D_{rc} = 68.1\%$ and $\sigma'_{vc} = 400$ kPa



Appendix A-15: BC3-MCPT cone tip and sleeve frictional resistance profile at $D_{rc} = 67.5\%$ and $\sigma'_{vc} = 405$ kPa



Appendix A-16: BC3-MCPT cone tip and sleeve frictional resistance profile at $D_{rc} = 44.4\%$ and $\sigma'_{vc} = 402$ kPa



Appendix A-17: BC3-MCPT cone tip and sleeve frictional resistance profile at $D_{rc} = 43.8\%$ and $\sigma'_{vc} = 400$ kPa

Curriculum Vitae

Name: Ronit Ganguly

Post-secondary Education and Degrees: KIIT University
Bhubaneswar, India
2012-2016 B.Tech.

The University of Western Ontario
London, Ontario, Canada
2017-2019 M.E.Sc

Honours and Awards: Western Graduate Research Scholarship
2018-2019, 2019-Present

Western Graduate Research Assistantship
2018-Present

R.M. Quigley Award 2019 (GRC Awards, Western University)

Related Work Experience Teaching Assistant
The University of Western Ontario
2018-2019

Research Assistant
Indian Institute of Technology
Bhubaneswar, India
2016-2017